Multi-scale physico-chemical phenomena in articular cartilage and subchondral bone

Multi-schaal fysisch-chemische verschijnselen in kraakbeen en subchondraal bot

(met een samenvatting in het Nederlands)

Proefschrift

ter verkrijging van de graad van doctor aan de Universiteit Utrecht op gezag van de rector magnificus, prof.dr. G.J. van der Zwaan, ingevolge het besluit van het college voor promoties in het openbaar te verdedigen op donderdag 23 november 2017 des middags te 4.15 uur.

door

Behdad Pouran

geboren op 18 december 1986 te Teheran, Iran

Promotor:	Prof. dr. ir. H. Weinans Prof. dr. ir. J. Malda
Copromotor:	Dr. A.A. Zadpoor

ISBN/EAN: 978-94-6233-772-5

b.pouran@gmail.com

This work was carried out in the *Department of Orthopaedics* of *University Medical Center Utrecht*. The research in this thesis was financially supported by: Dutch Arthritis Foundation (Grant No. 13-3-406).

Keywords: articular cartilage, subchondral bone plate, solute transport, osmolality, concentration, solute's charge, indentation, finite element modelling, pore-scale modelling, osteochondral interface

Printed in The Netherlands: Gilderprint.nl
Front cover graphic: Shutterstock.com
Back cover graphic: Shutterstock.com
Published by: Utrecht University Library

This PhD thesis is dedicated to my mother, my father, my brother and my fiancé for being supportive, encouraging and inspiring.

Table of Contents

Chapter 1

Introduction

1.1. **INTRODUCTION**

Articular cartilage (AC) and the subchondral bone plate (SBP) are two mechanically and structurally distinct components that are tightly connected, providing excellent shock-absorbing capabilities to diarthrodial joints [1]. The majority of AC consists of fixed negatively charged glycosaminoglycans (GAGs) entrapped in a collagen type II fibril network, which complex is immersed in interstitial water with varying composition from the superficial to the deep zone of the cartilage layer [2]. Unlike collagen type II fibrils, GAG molecules undergo continuous turnover, which process is governed by the chondrocytes [3]. The calcified cartilage, a highly mineralized compartment of AC, forms a bridge between the non-calcified hyaline cartilage to the SBP and acts as an interface between the non-matching mechanical properties of non-calcified cartilage and SBP [2]. In osteoarthritis, both AC and SBP undergo structural deterioration, which at micro-scale is associated with GAG loss and disrupted collagen fibrils in AC and increase/decrease in thickness and perforation of the SBP, depending on the stage of OA (Figure 1) [4, 5].

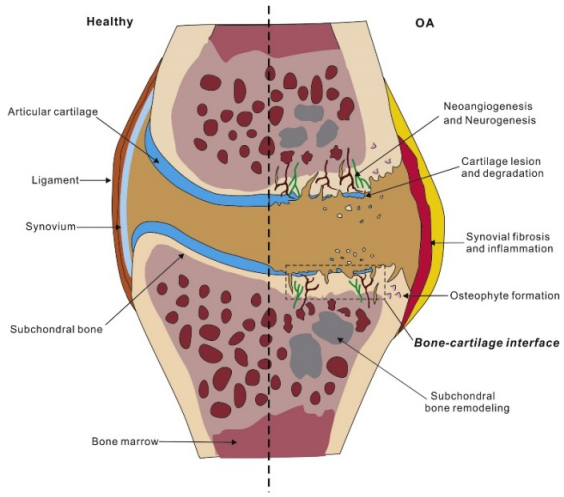

Figure 1.1. Cartilage and bone alterations occurring at tissue and micro-scale levels during osteoarthritis. These alterations inevitably affect the cross-talk between cartilage and subchondral bone plate (Adapted by permission from Elsevier: Osteoarthritis and cartilage).

In early osteoarthritis, gradual GAG loss and collagen fibril damage prevails, which leads to diminished net charge of the tissue and inferior compressive properties due to loss of water attraction and retention, and impaired tensile properties due to damage to the collagen fibrils [6, 7]. Beside changes in GAGs and collagens, increased water content can enhance the permeability of the tissue in late stage OA when the tissue features large fissures [8]. Therefore, it is likely that the transport properties of the tissue are affected in the various stages of OA. The decreased compaction of GAGs and disrupted collagen fibrils alter the solute-matrix interactions (steric-hindrance effects). Moreover, the alterations in electrostatic interactions due to diminished negative charges, result in slower penetration of positively charged solutes and faster penetration of negatively charged solutes [9]. Therefore, alterations in microstructure, charge, and water content play a key role in the diffusive properties of the tissue. This is of great importance, as the health status of the joint is linked to the cross-talk between the AC and SBP [10]. This cross-talk intrinsically depends on the cartilage matrix alterations and micro- and nano-topographic changes in the subchondral bone plate, namely pore characteristics and invasion of vasculature. Furthermore, the collagen-apatite space found typically in calcified cartilage could affect the transport between non-calcified cartilage and the SBP. The exact pathways by which the transport occurs between cartilage and the underlying bone is to date not fully understood. Therefore, one major aim of this thesis was to better identify factors affecting diffusion in AC and the SBP separately and in conjunction, using advanced experimental and computational platforms. Not only does this approach allow the prediction of the diffusive properties of cartilage and bone in health and/or disease, but it also may provide avenues to optimize delivery of e.g. therapeutic molecules or contrast agent.

Beside OA, ageing jeopardizes the health of bone and cartilage, mainly through accumulation of advanced-glycation end products (AGEs) [11-13]. AGEs are synthesized as a consequence of the reaction between arginine and lysine, amino acids from the collagen fibrils, and reducing sugars like glucose and threose. As a result of AGE formation and accumulation, the tissue

becomes less resilient and more prone to mechanical damage. Furthermore, formation of AGEs inevitably reduces spacing between collagen fibrils, thus. increasing steric hindrance, and increases the net charge of the tissue leading to increased electrostatic interactions. These two factors could substantially influence the transport within articular cartilage, particularly that of larger solutes. Because of demographic developments ageing and the related accumulation of AGEs currently pose increasing risks for the elderly population and therefore the other aim of this thesis was to interrelate the rate of chemical reactions between collagen fibrils and reducing sugars with external mechanical cues to help in developing anti-ageing strategies in articulating joints.

1.2. THESIS OUTLINE

The thesis consists of eleven chapters.

Chapter 1 (the current chapter) is meant to provide an introduction to the thesis with some information about the diffusion processes in cartilage and subchondral bone as well as about the mechano-chemcial processes involved in ageing and osteoarthritis. A short overview of each chapter then follows to give the reader an impression of the essential contents of the thesis.

Chapter 2: This chapter reviews the major imaging tools, namely fluorescent microscopy, computed tomography (CT) and magnetic resonance imaging (MRI) that are used to study the diffusion process in articular cartilage by adopting a multi-scale approach. Suggestions and recommendations are provided to optimally select proper imaging tools for the various diffusion applications.

Chapter 3: This chapter investigates the separate effects of osmotic swelling, external bath concentration and solute's charge on the solute transport across articular cartilage. Contrast-enhanced micro-computed tomographic is used in an experimental setup and finite element models are employed to address the roles of those factors in different zones of articular cartilage.

Chapter 4: A novel biphasic-solute finite element model to describe the diffusion process in different zones of articular cartilage is developed based on solute concentration versus time data that were obtained from contrast-enhanced micro-computed tomographic experiments. The developed multi-zone biphasic-solute model successfully predicts the diffusive properties of different cartilage layers when applying a neutral solute.

Chapter 5: A multi-zone multiphasic finite element model is developed based on the contrast-enhanced micro-computed tomographic experiments. This model allows the accurate description of the diffusive properties of articular cartilage in different layers when a charged molecule diffuses.

Chapter 6: A multiphysics platform is developed to assess the effects of size and stirring of the overlying bath in contact with the cartilage surface, as well as of formation of a stagnant layer at the bath-cartilage interface. This platform allows investigation of pivotal bath parameters affecting diffusion in cartilage and enables diffusion experiments to be performed in an optimal fashion.

Chapter 7: To investigate the cross-talk between cartilage and bone, the diffusion at the interface of cartilage and subchondral bone is characterized using contrast-enhanced micro-computed tomography. The diffusion is not only characterized for relatively small solutes in human and equine samples, but also a correlation with the micro-architecture of the osteochondral interface is found.

Chapter 8: A multi-zone biphasic-solute platform is developed to quantify the diffusion of neutral solutes across the osteochondral interface based on contrast-enhanced micro-computed tomographic data. This computational platform allows the simultaneous determination of diffusion coefficient in various zones of cartilage and the subchondral bone plate at tissue level.

Chapter 9: The first aim of this chapter is to uncover the details of pore structure at the interface of non-calcified cartilage and calcified cartilage, as

well as of calcified cartilage and the subchondral bone plate, using focused-ion-beam scanning electron microscopy (FIB-SEM). Using the FIB-SEM tomography data, the diffusion coefficient and hydraulic permeability of the pericellular matrix of calcified cartilage and the subchondral bone plate are for the first time obtained using a pore-network modeling platform.

Chapter 10: The role of mechanical factors on advanced glycation end products is investigated in articular cartilage under different osmotic swelling conditions using mechanical tests, contrast-enhanced micro-computed tomography, biochemical assays and cartilage surface colorimetry. The extent of collagen fibril deformation is found to markedly affect the non-enzymatic glycation process, which precedes the ageing process.

Chapter 11: The main concepts of the aforementioned chapters are recapped and discussed concisely and suggestions for future further research are provided in this chapter.

Last but not least, an experimental and computation protocol to perform transport tests using neutral and charged solutes in cartilage is presented in Appendix A.

1.3. **REFRENCES**

1. Malekipour, F., et al., *Shock absorbing ability of articular cartilage and subchondral bone under impact compression.* J Mech Behav Biomed Mater, 2013. **26**: p. 127-35.
2. Sophia Fox, A.J., A. Bedi, and S.A. Rodeo, *The Basic Science of Articular Cartilage: Structure, Composition, and Function.* Sports Health, 2009. **1**(6): p. 461-8.
3. Goldring, M.B., *Articular cartilage degradation in osteoarthritis.* HSS J, 2012. **8**(1): p. 7-9.
4. Intema, F., et al., *In early OA, thinning of the subchondral plate is directly related to cartilage damage: results from a canine ACLT-meniscectomy model.* Osteoarthritis Cartilage, 2010. **18**(5): p. 691-8.
5. Weinans, H., *Periarticular bone changes in osteoarthritis.* HSS J, 2012. **8**(1): p. 10-2.
6. Stolz, M., et al., *Early detection of aging cartilage and osteoarthritis in mice and patient samples using atomic force microscopy.* Nat Nanotechnol, 2009. **4**(3): p. 186-92.
7. Setton, L.A., D.M. Elliott, and V.C. Mow, *Altered mechanics of cartilage with osteoarthritis: human osteoarthritis and an experimental model of joint degeneration.* Osteoarthritis Cartilage, 1999. **7**(1): p. 2-14.
8. Hwang, J., et al., *Increased hydraulic conductance of human articular cartilage and subchondral bone plate with progression of osteoarthritis.* Arthritis Rheum, 2008. **58**(12): p. 3831-42.
9. Bajpayee, A.G. and A.J. Grodzinsky, *Cartilage-targeting drug delivery: can electrostatic interactions help?* Nat Rev Rheumatol, 2017. **13**(3): p. 183-193.
10. Yuan, X.L., et al., *Bone-cartilage interface crosstalk in osteoarthritis: potential pathways and future therapeutic strategies.* Osteoarthritis Cartilage, 2014. **22**(8): p. 1077-89.
11. Verzijl, N., et al., *Age-related accumulation of the advanced glycation endproduct pentosidine in human articular cartilage aggrecan: the use of pentosidine levels as a quantitative measure of protein turnover.* Matrix Biol, 2001. **20**(7): p. 409-17.
12. Verzijl, N., et al., *Crosslinking by advanced glycation end products increases the stiffness of the collagen network in human articular cartilage: a possible mechanism through which age is a risk factor for osteoarthritis.* Arthritis Rheum, 2002. **46**(1): p. 114-23.
13. Verzijl, N., et al., *Age-related accumulation of Maillard reaction products in human articular cartilage collagen.* Biochem J, 2000. **350 Pt 2**: p. 381-7.

CHAPTER 2

MULTI-SCALE IMAGING TECHNIQUES TO STUDY MOLECULAR TRANSPORT ACROSS ARTICULAR CARTILAGE

This chapter is prepared for submission as a review paper:

Pouran B., Arbabi V., Bajpayee A. G., van Tiel J., Töyras J., Jurvelin J., Malda J., Zadpoor A. A., Weinans H.

Chapter 2

ABSTRACT

As articular cartilage is an avascular tissue, the transport of nutrients and cytokines through the tissue is essential for the health of cells, i.e. chondrocytes. Transport of specific contrast agents through cartilage has been investigated to elucidate cartilage quality. In laboratory, pre-clinical and clinical studies, imaging techniques such as magnetic imaging resonance (MRI), computed tomography (CT) and fluorescent microscopy have been widely employed to visualize and quantify solute transport in cartilage. Many parameters related to the physico-chemical properties of the solute, such as molecular weight, net charge and chemical structure, have a profound effect on the transport characteristics. Information on the interplay of the solute parameters with the imaging-dependent parameters (e.g. resolution, scan and acquisition time) could assist in selecting the most optimal imaging systems and data analysis tools in a specific experimental set up. Here, we provide a comprehensive review of various imaging systems to investigate solute transport properties in articular cartilage, by discussing their potentials and limitations. The presented information can serve as a guideline for applications in cartilage imaging and therapeutics delivery and improve understanding of the set-up of solute transport experiments in articular cartilage.

Chapter 2

2.1. INTRODUCTION

Articular cartilage is an avascular tissue mainly comprising large macromolecular assemblies of collagen II and aggrecans. The aggrecans contain highly negatively charged glycosaminoglycan groups (GAGs) chains, which receive their negative charges from the carboxyl and sulfate groups present in the repeating disaccharide unit of GAGs [7, 8] (Figure 2.1). Solute transport in cartilage occurs through passive (Brownian) or active (Convective interstitial fluid flow) diffusion [9] mechanisms. These mechanisms determine solute's uptake and retention within the tissue extracellular matrix and their interactions with extracellular and intracellular receptors [9-11]. Several previous studies have investigated the effects of solute size and charge on their ability to penetrate and reside within the articular cartilage [9, 10, 12-15]. Cartilage tissue has a heterogeneous structure. For example, density of negatively charged aggrecans and the spacing between collagen fibrils increase with depth, thereby resulting in depth-dependent solute diffusivities [4, 9, 12, 16]. The densely packed structure of the tissue restricts the transport of most solutes due to steric hindrance, which is particularly important for larger and branched molecules [10, 14, 17]. The negative tissue charge could further slowdown the transport of negatively charged solutes and prevent them from penetrating into the deeper GAG-rich regions of the tissue. This can make intra-cartilage delivery of imaging dyes and also therapeutics challenging [12, 13, 15, 18]. Other parameters such as the relative volumes of solute bath and tissue, presence of stagnant solute layers at the solute bath-cartilage interface, and the diffusivity ratio of the bath to that of the cartilage were considered in experimental and numerical studies [16]. Despite previous efforts to improve understanding the solute-tissue interactions, comprehensive guidelines to help in applying the above-mentioned findings and principles *ex-vivo*, pre-clinical, and even clinical settings are still lacking. Therefore, this review article will first introduce the transport principles essential to molecular diffusion in hydrated tissues, followed by an analysis of various imaging modalities and their applicability in studying intra-cartilage solute diffusion *ex-vivo* and *in-vivo,* as well as for clinical purposes. We will also discuss some critical considerations for

setting up a transport experiment, such as the importance of tissue thickness, tissue deformation, pericellular and extracellular matrix properties, interactions with synovial fluid, external solute bath attributes, solute's charge, acquisition time, and resolution and data analysis. This review concludes by providing directions towards more efficient design of *ex-vivo* and *in-vivo* experiments and translating these considerations into clinical applications of tissue imaging and therapeutics to yield more effective results.

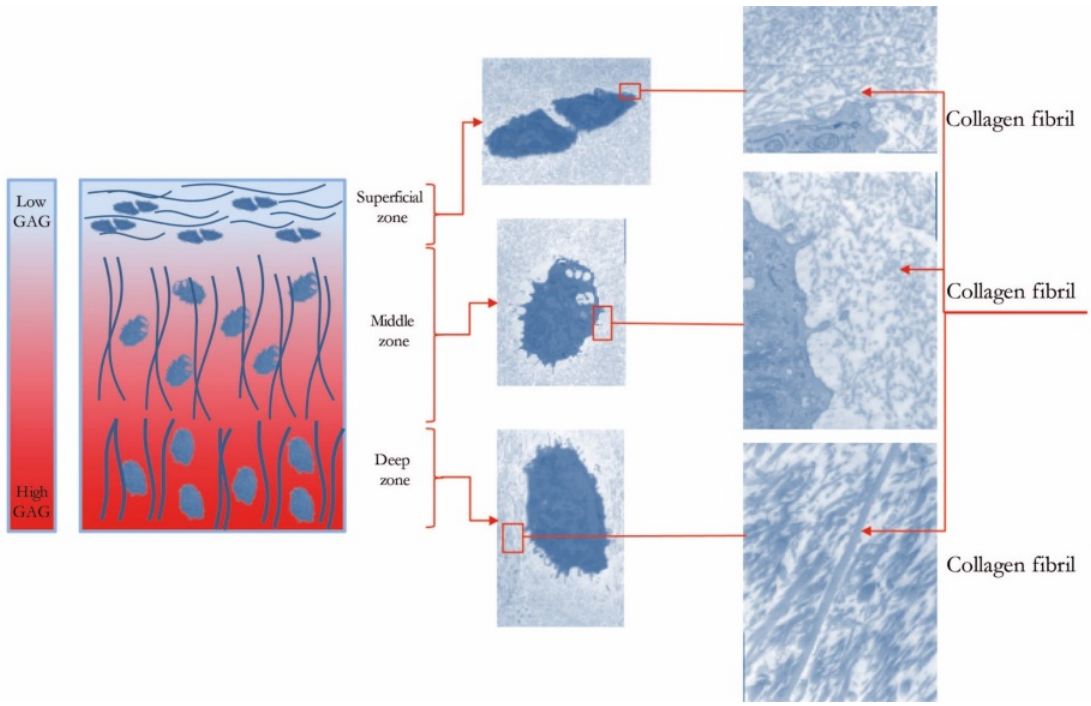

Figure 2.1. Cellular information and constituents of articular cartilage obtained using scanning electron microscopy: implications for solute transport. Collagen fibrils, glycosaminoglycans (GAGs) and chondrocytes are displayed.

2.2. MOLECULAR TRANSPORT

2.2.1. PRINCIPLES

Depending on the mechanical state of the tissue, both passive and active transport mechanisms take place in articular cartilage. In absence of joint motion, e.g., when the subject is relaxing or sleeping, the interstitial fluid flow does not significantly affect solute transport. However, physical activities, such as jumping and climbing enhance the interstitial fluid flow [7], thereby increasing the transport rate of larger solutes by a factor of two [19]. The effect of convective fluid flow is less pronounced on the transport of smaller molecules [19, 20]. In practice, experimental approaches investigating the transport properties of healthy and diseased cartilage are often based on passive diffusion. We will therefore focus on passive diffusion processes while also considering fluid flow effects, whenever appropriate. For the sake of simplicity, we will call passive diffusion simply diffusion in further text.

2.2.2. EXPERIMENTAL BOUNDARY CONDITIONS

Application of boundary conditions precedes the design of the diffusion experiments. The boundary conditions depend on the characteristics of the external solute bath in contact with the cartilage tissue, solute charge, and the direction of solute diffusion. The concentration of the external bath may or may not change depending on whether it has finite or infinite volume as compared to the cartilage volume. Furthermore, the external bath may be well-stirred or not well-stirred, which will influence the presence and the extent of stagnant solute layers on the tissue surface (i.e. at the solute bath-tissue interface). The external bath may contain either electrically neutral or charged solutes, which create additional interactions between the bath and the ECM. The last boundary condition is determined by the direction of solute diffusion that may occur in axial, radial, or angular direction (or a combination of them).

In the finite-bath condition, solute concentration in the bath continuously changes with time, complicating the analysis and interpretation of the results. This setup, however, may more closely mimic the relative cartilage

tissue-synovial fluid volume and the actual diffusion process in the diarthrodial joints [4, 15]. Thereby, it is relevant for studying intra-joint transport kinetics of therapeutics and imaging dyes following their intra-articular administration. The infinite volume condition, on the other hand, maintains constant bath solute concentration over time. In both cases, constant mechanical stirring of the external bath helps to prevent the formation of stagnant solute layers at the interface of the solute bath and cartilage. Mechanical stirring could, however, cause additional fluid flow effects and result in experimental conditions that deviate from a pure diffusion model. The finite bath volume model also creates additional complexities associated with stirring limitations and the potential formation of a stagnant layer at the cartilage-bath interface. The resulting equations cannot often be solved using analytical techniques and may require advanced computational approaches.

External baths containing neutral or charged solutes behave differently, because self-repulsion within the bath and electrostatic interactions between the charged solute and proteoglycans of the ECM complicate the situation as compared to the baths that only contain neutral solutes where steric hindrance predominates.

In the human body, articular cartilage is heterogeneously organized in direction perpendicular to its surface. As diffusion from synovial fluid to cartilage primarily occurs through the articular surface, most ex-vivo studies have designed their setups such that diffusion could only occur perpendicular to its surface. Consequently, there is limited number of studies focusing on radial and/or angular diffusive properties.

2.3. IMAGING TECHNIQUES

The development of imaging tools has enabled characterization of the diffusive behavior of solutes within articular cartilage. In fact, characterization of diffusion requires application of advanced imaging tools, such as fluorescent microscopy (Figure 2.2), clinical or micro-CTs (Figure 2.2), and magnetic resonance imaging (MRI) (Figure 2.2). Therefore, accurate characterization of the tissue requires broad knowledge of imaging techniques. In this section, we

introduce and describe the principles and potentials of these imaging techniques used for cartilage imaging in particular with respect to the diffusive properties of the tissue.

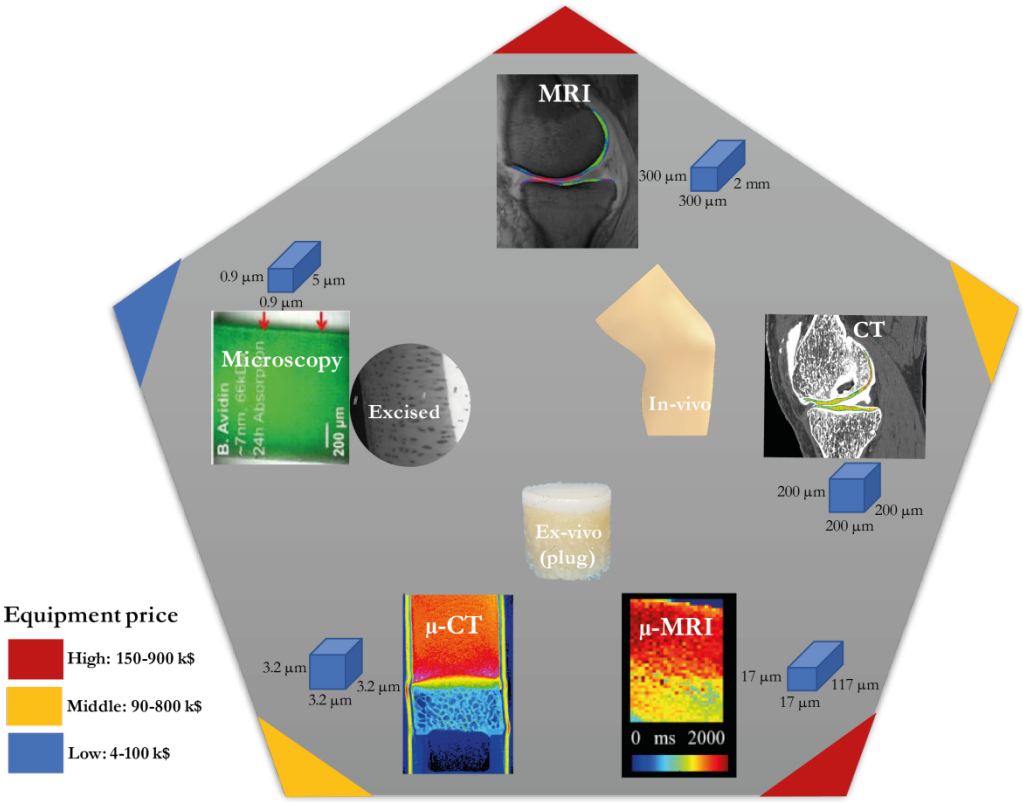

FIGURE 2.2. Info-graph of multi-scale cartilage imaging using CT, MRI and microscopy to study solute transport across articular cartilage: Resolution and cost [1, 21]. Microscopy as a cost-efficient tool can be extremely beneficial for imaging the diffusion in excised tissue (Mainly 2D). CT provides high spatial resolution of the diffusion process in 3D. Clinical MRI as a costly technique suffers from poor out-of-plane resolution while in experimental setups can achieve high spatial resolution using high magnetic fields.

2.3.1. FLUORESCENT MICROSCOPY

Primarily, two fluorescence microscopy techniques have been used to study intra-cartilage solute diffusion: scanning microphytolysis (SCAMP) and fluorescence recovery after photobleaching (FRAP). The application of SCAMP in diffusion through the pericellular matrix of articular cartilage was introduced in 2008 [22]. SCAMP works based on changes in the fluorescent signal change, which is a function of two independent variables: the rate of photobleaching and the rate of diffusion of fluorescent molecule. Molecules with fast motion traverse the laser path faster and therefore are exposed to laser path for a shorter time period, whereas slow-moving molecules are more likely to remain within the laser path and bleached. The diffusivities and bleaching constants are then obtained by fitting a 3D diffusion-reaction model to the intensity vs. time data. FRAP has been extensively used to study the diffusion of fluorescent molecules in articular cartilage slices [9, 10]. A photobleached region is first created by intense laser illumination causing the fluorescence to fade away and then fluorescent molecules diffusing from the nearby region would result in gradual fluorescent recovery until complete recovery. Analytical models are then used to derive the diffusivity from the dynamic fluorescent intensity. The planar resolution of the FRAP and SCAMP has been as high as 0.9 μm^2 [9]. Using confocal microscopy, these techniques can be applied to thin cartilage slices (<100 μm) allowing a z-resolution of up to a few microns [9].

In normal cartilage, diffusion in the pericellular matrix is slower than in the extracellular matrix [22]. In osteoarthritic cartilage, diffusivity of the pericellular matrix increases and becomes similar to that of the ECM [22]. As most of the SCAMP and FRAP setups have used 37 μm^2 large region of interest (ROI), the distance of the boundaries of the ROI from the chondrocytes (~ 10 μm), determines whether the measurement is performed in pericellular or extracellular matrix. SCAMP has the advantage of imaging in mili-seconds range, whereas FRAP requires several minutes. SCAMP, however, requires solving the relatively complex diffusion-reaction equations numerically, while the analytical solutions to FRAP are easily accessible in most

cases. Fluorescent microscopy has also been employed to assess the effects of surface cracks on solute diffusion and adsorption properties using different sized florescent molecules in 200 μm thick cartilage slices [23-25]. Desorption experiments [26, 27] were used as an indirect way to study the diffusion in cartilage where diffusion was studied from the cartilage specimen to the bath. In those experiments, the dynamic diffusion behavior in the bath in contact with cartilage containing fluorescently labeled solutes was studied.

2.3.2. **X-RAY COMPUTED TOMOGRAPHY (CT)**

X-ray attenuation is a function of elemental atomic number and bulk density of the materials. Mass attenuation of cartilaginous tissues is extremely close to that of water [28], which complicates visualization of such hydrated tissues bathed in synovial fluid inside the joint. X-ray contrast agent molecules attenuate the X-ray signal and assist in visualizing the soft cartilaginous tissues. Computed tomography (CT) allows acquisition of three-dimensional information on the diffusion of contrast agent molecules. Iodine (I) and Gadolinium (Gd) are well known for their X-ray attenuation characteristics and therefore vastly used to study the diffusion processes [28]. They are used as contrast agents to visualize articular cartilage post-equilibration- the time after which no further diffusion from the source (bath) to reservoir (cartilage) takes place. Negatively charged contrast agents, e.g., ioxaglate (iodine-based) and gadopentetic acid (Gadolinium-based) [15, 18, 29], have been applied as their interactions with proteoglycans provide quantitative essential information about the cartilage health. Positively charged iodinated contrast agents (ammonium ion. $–NH_3+$) with different charge densities were recently introduced [30-32] and used to enhance the retention and diffusion within articular cartilage. Nearly all above-mentioned molecules (both iodine-based and Gd-based) represent relatively small molecular weight (below 2 kDa). To study the effects of solute's charge on the diffusion characteristics, Pouran et al. [15] compared the transport of similarly sized molecules with varying net charges including iodinated molecules of ioxaglate (electrical charge= -1) and iodixanol (charge=0) and found 2.5-fold lower ioxaglate flux in the superficial

zone. Another study, showed that at equilibrium, micro-CT signal for iodinated molecules with +4 charge correlated strongly with the intra-tissue proteoglycan content [31] resulting in high-quality images of cartilage in *in vivo* rabbit models [33] and *ex-vivo* mouse models [32] even with low iodine concentration. *In-vivo* research conducted on healthy and osteoarthritic knee joints of patients using clinical CT (voxel size = 0.21×0.21×0.40 mm^3) proved effective for OA identification and determination of contrast agent lifetime [34]. *In vivo* delayed cone-beam CT after ioxaglate injection into the knee joint (voxel size = 0.20×0.20×0.20 mm^3) showed promise in low-dose radiation imaging, yet capable of detecting knee cartilage lesions accurately [35, 36]. When using peripheral quantitative CT (voxel size = 0.2 mm×0.2 mm×2.3 mm), immersion of bovine osteochondral blocks in ioxaglate solution allowed simultaneous morphological scoring of cartilage and subchondral bone [37]. Clinically applicable CT arthrography (voxel size = 0.265×0.265×0.750 mm^3) was proposed based on the equilibrium penetration of ioxaglate by comparing the results with contrast-enhanced micro-CT (voxel size = 35×35×35 μm^3) [38]. Similarly, ioxaglate partitioning experiments in 3D on *ex-vivo* rabbit specimens were in agreement with the 2D histological sGAG distribution for both articular cartilage and meniscus [39, 40]. Detection of surface injuries of *ex-vivo* articular cartilage specimens was recently accomplished by assessing the transport kinetics of sodium iodide using high-resolution micro-CT (voxel size = 8.6×8.6×8.6 μm^3) [18]. Similar strategies employing micro-CT technique were applied to calculate the diffusion and near-equilibrium distribution of contrast agents in healthy and non-enzymatically cross-linked *ex-vivo* cartilage specimens (voxel size = 30.2×30.2×30.2 μm^3) [17, 41]. Collagen distribution in *ex-vivo* non-calcified cartilage was successfully determined using micro-CT (voxel size = 3.2×3.2×3.2 μm^3 [42] and 17.4×17.4×17.4 μm^3 [43]) after equilibration with phosphotungstic acid and phosphomolybdic acid). Most recently, contrast-enhanced micro-CT with high spatial resolution (voxel size = 3.0×3.0×3.0 μm^3) has proven advantageous for assessing GAG content of murine articular cartilage but was not accurate enough to measure cartilage thickness [44]. The studies on diffusion involving CT techniques have used a wide range of voxel sizes ranging between approximately 0.2 mm×0.2 mm×2.3

mm and 3.0 μm ×3.0 μm ×3.0 μm, indicating the feasibility of CT contrast agent imaging in laboratory, pre-clinical and clinical studies.

The thickness of articular cartilage varies between different species, anatomical locations, and cartilage health conditions. Cartilage can be as thin as 100 μm in mice, up to 2.5 mm in humans and 3 mm in African elephant [45]. This wide variation implies that studying the solute diffusion in different zones of cartilage particularly for thin specimens requires the highest possible resolutions. Moreover, the scan time of a particular micro-CT setup could be an issue for diffusion studies especially when scans have to be repeated multiple times. For *ex-vivo* experiments, bath volume, bath concentration, and presence of stagnant layers at the cartilage-bath interface are other contributing factors. These factors influence the choice of the best imaging tool and are discussed in more detail below.

2.3.3. MAGNETIC RESONANCE IMAGING (MRI)

Hydrogen ions (protons) residing e.g. in water molecules and proteins are major constituents of soft tissues like articular cartilage. As MRI-images are based on the variations in relaxation times due to differences in response of hydrogen atoms in an externally applied magnetic field, it is possible to acquire depth-dependent information on the composition and structure of extracellular matrix in articular cartilage. Three major relaxation times, namely T_1 (spin-lattice relaxation time), T_2 (spin-spin relaxation time) and T_1 (spin-lattice relaxation time in the rotating frame) have been used in both clinical and experimental studies. T_2 relaxation anisotropy, due to proton-collagen interactions, varies depth-wise and relates to depth-dependent organization of collagen network. On the contrary, T_1 relaxation is much more isotropic in articular cartilage and is known to be isotropic to the magnetic field direction. T_1 becomes important when imaging articular cartilage with paramagnetic Gd-DTPA^{2-} that shortens the T_1 relaxation [46-48]. This protocol is often referred to as the delayed gadolinium-enhanced or dGEMRIC. T_1 is dependent on the strength of spin-lock field. When the field approaches zero, it approaches T_2 relaxation and when the field increases, it becomes less anisotropic. As the

main focus of the present paper is the diffusion in articular cartilage, we focus on the MRI techniques useful for diffusion studies, namely dGEMRIC, Sodium (^{23}Na), and diffusion weighted imaging (DWI).

The equilibrium partitioning of Gd-DTPA^{2-} results from its interactions with negatively charged GAGs. Thereby, degeneration of cartilage, characterized by the decreased GAG content, increases the Gd-DTPA^{2-} partitioning. This leads to low T_1 values [49]. Gd-DTPA^{2-} could be administered either intravenously or intraarticularly, which generates two different mechanisms for diffusion. To a large extent, the former contributes to diffusion by both direct diffusion from the synovial fluid (SF) and perfusion from the subchondral bone, whereas the latter takes place by the direct diffusion from SF to the cartilage. However, it should be noted that diffusion across the subchondral bone plate for small molecules has been recently confirmed [50] and therefore it can also take place post-intravenous injections, which would depend on the micro-architecture of the subchondral bone plate, i.e. porosity and thickness [50, 51]. In MRI, the highest achievable resolution, particularly in the z-direction (direction of main magnetic field), is limited due to relatively low magnetic fields (1.5 and 3 T), which tremendously reduces the SNR [52, 53]. In clinical settings, voxel sizes up to 0.40 mm×0.40 mm×3 mm have typically been used. Dynamic *ex-vivo* dGEMRIC MRI (cartilage thickness of up to 2.1 mm, infinite bath, 9.4 T) was performed over 18 h to measure the diffusivity and depth-wise distribution of Gd-DTPA^{2-} in healthy and enzymatically degraded bovine articular cartilage (voxel size = 78 μm×78 μm×1 mm) [54]. Application of three negatively charged and one neutral MR contrast agents with both T_1 and T_2 sequences (1.5 T, voxel size = 300 μm×300 μm×2mm) highlighted that charge of the contrast agent only controls the amount of contrast agent and not the spatial distribution of contrast agent. The authors also found that the rate of relaxation (ΔR_1 and ΔR_2) for both sequences were of the same magnitude for all tested contrast agents [55]. Sweeping imaging with Fourier's transformation (SWIFT, scan time=185.5 min, isotropic voxel size=117 μm^3, 9.4T) was developed to generate T_1-relaxation time maps of enzymatically treated and non-treated osteochondral

plugs [56]. A comparative study confirmed the superiority of Gd-DTPA^{2-} over single negatively charged contrast agents for evaluation of GAG content, however Gd-BOPTA^{2-} did provide higher contrast, suggesting an alternative for the conventional dGEMRIC [57]. Cationic Gd-based contrast agent (net charge = +4) was synthesized and its diffusion was monitored in bovine cartilage and human finger cartilage using a 8.5 T scanner (0.2 mm×0.2 mm×1 mm, scan time=16.5 min) , which provided sufficient T_1 signal at one-tenth the effective dosage of gadopentetic acid [58]. Consistently, determination of fixed charge density (FCD) of cartilage using T_1 relaxation post-contrast ex-vivo has been successful [46, 54]. Another strategy to determine FCD in articular cartilage is sodium MRI, which functions based on interactions between positively charged sodium and FCD of cartilage. Although non-invasive, this method was shown to suffer from intrinsically insufficient SNR in the clinical imaging, chiefly due to low concentration of ^{23}Na in articular cartilage [59]. Using experimental μMRI (7T, 17.6 μm×17.6 μm×1 mm), the authors found important synergistic effects of mechanical loading and Gd-DTPA^{2-} concentration on quantification of GAGs in healthy and degraded articular cartilage [60].

Diffusion weighted imaging (DWI) uses the variability of diffusive motion of water within cartilage. DWI provides promising non-invasive information about tissue composition and structure, particularly collagens and GAGs [61]. Previous studies using DWI indicate that in- resolutions up to 78 μm^2 and slice thicknesses of 2 mm are feasible [62].

2.4. IMAGING CONSIDERATIONS

Depending on the type of the instrument and the goal of the experiments, one may encounter challenges when using any of the above-mentioned imaging tools. Therefore, a general set of considerations from the authors' perspective could be insightful to facilitate proper selection of the imaging tools in diffusion studies: tissue thickness, tissue deformation, pericellular matrix and extracellular matrix, synovial fluid, bath characteristics, scan time, equipment costs and availabilities.

2.4.1. TISSUE THICKNESS

The thickness of articular cartilage not only depends on the type of the joint and anatomical location but also on the species of interest. Cartilage thickness spans a wide range from a few hundred microns, for instance in mice ~ 100 μm, to a few millimeters in species such as human and horse ~ 2 mm and elephant ~ 3 mm. Thickness can be an important factor when choosing the imaging facility particularly when investigating zone-dependent transport properties. For example, even 9.4 T MRI provides relatively low resolutions in out-of-plane orientation (Figure 2.1) [63], which hampers the 3D characterizations, particularly in very thin cartilage of small animals. Therefore, for mice and rat cartilage, the preferred modalities would be either micro-CT (voxel size ~ a few microns) or fluorescent microscopy techniques (planar resolution <1 μm). Prior to the scans, the dimensions of the *ex-vivo* samples should sometimes be chosen optimally, particularly for the micro-CTs with resolutions that depend on the field of view (FOV). To study the diffusion across different zones of mice and rat cartilage, one might adopt voxel sizes less than 10 μm as this accommodates at least one voxel for the superficial zone of mice cartilage (~20 μm thickness).

Diffusion investigations often require estimating the equilibration time before start of the experiments. Some studies have reported that 18-24 hr is sufficient to reach equilibrium [17, 18, 41, 64] when applying small solutes (less than 2 kDa), whereas equilibrium time was not reached even after around 48 hr for other studies [15, 16, 50]. The key elements that play a role are the thickness of the tissue as well as integrity and density of the matrix, which exhaust solute transport through frictional loss, i.e., steric hindrance.

2.4.2. TISSUE DEFORMATION

As cartilage contains high negative charge, it can easily undergo osmotic-induced deformations, which depend on the osmolality of the external bath. Some diffusion experiments, similar to [15], leads to deformations that must be accounted for before proceeding to image processing. The above-mentioned

work and similar studies [15, 65] have reported deformations of about 5 to 8 %, which for a 2.7 mm thick cartilage means 200 μm. A minimum spatial resolution of 200 μm is therefore recommended. As this resolution should be applied out-of-plane, application of MRI techniques would be limited. Visualization of the tissue deformation during the diffusion process is also challenging using fluorescent-based techniques. Then, the only robust technique for this particular case would be micro-CT.

2.4.3. EXTRACELLULAR MATRIX AND PERICELLULAR MATRIX

Due to higher charge and density of PCM in healthy cartilage, the diffusive properties of PCM could be distinctly different from those of ECM. Proper understanding of PCM diffusive properties requires imaging tools with resolutions in the order of a few microns, thereby necessitating application of ultra-high resolution micro-CTs (~ 10 μm^3 voxel size) and fluorescent techniques. Fluorescent techniques boast the advantage that diffusion of larger molecules (> 2 kDa) and perhaps more clinically relevant molecules could more conveniently be studied. Obviously, MRI techniques could not be used to study diffusion in PCM.

2.4.4. SYNOVIAL FLUID

The volume, viscosity, and composition of the synovial fluid could potentially influence solute transport. The required amount of diffusing molecule for either visualization or therapeutic purposes, or in other words, solute concentration in the joint could influence the solute distribution within the cartilage, especially if the diffusing molecule is charged [12, 16]. This is even more important if the diffusing molecule is negatively charged and therefore charge-driven transport plays a role [12]. Moreover, injected solute concentration and synovial fluid osmolality are inter-related and therefore tissue swelling/shrinkage is expected, which requires attention to be paid prior to the scans. If the injection volume is too low, solute transport could be adversely affected because of lack of sufficient transport to deeper zones. On the contrary, if the injection volume is too high, the osmolality may rise,

causing tissue deformation, which complicates the post-processing. Viscosity and composition of the synovial fluid are two major factors that change during the disease progression and could alter the solute transport features, e.g., by formation of undesirable stagnant layers near the cartilage surface.

2.4.5. EXTERNAL BATH ATTRIBUTES

Some of important factors that control solute penetration are the solute molecular size, stirring conditions, and concentration of the bath. In CT-based experiments, large and particularly concentrated baths could cause considerable beam hardening (X-ray spectrum shape changes), which creates artefacts in the resulting images. The orientation of the bath with respect to the cartilage specimen is crucial in MRI experiments. The stirring of the bath has been suggested to minimize the unfavorable effects of stagnant layer at the cartilage-bath interface. Although gentle stirring, particularly when the mechanical stirrer is kept far enough from the cartilage surface, inhibits the formation of the stagnant layer [66], it could also influence solute transport through eddy formation, i.e., a convective flow near the cartilage surface. The concept of finite bath was introduced to reduce the consumption of contrast agent and associated beam hardening [4, 15]. Moreover, the minimum bath size to sufficiently feed the deep zones of cartilage could be determined using advanced computational techniques [16]. The ratio of solute diffusivity in the bath to that of the cartilage has been also shown to be critical [16]. Using confined volumes of external bath enables studying the actual diffusive behavior of cartilage in the confined joint space. The concentration of the applied bath affects the diffusion in two ways: (1) possible deviations from the Fick's assumption particularly in baths containing charged particles (charge repulsion-assisted transport) and (2) increased osmolality that affects the compaction of the matrix components which may affect the transport [15]. The associated complexities involved in some baths, such as those discussed, could be overcome through application of computational methods.

2.4.6. IMAGE ACQUISITION

The scan time is of utmost importance in CT- and MRI-, and fluorescent-based diffusion experiments. Recording the solute diffusion during the first few minutes after exposing the cartilage to the bath may be critical to determine the solute diffusivity and/or solute flux in the superficial zone (i.e. the first ~20% of the entire cartilage thickness). Then, the short scan times that have become available through sophisticated CT and MRI machines are beneficial, particularly when the solute of interest is small. The required scanning time of 10 minutes to few tens of minutes required by most micro-CTs and μMRIs may limit the imaging in such cases. Preparatory steps, such as active motion of the joints, are crucial in the clinics to allow sufficient distribution of the contrast agents into the cartilage. Although long waiting times allow for sufficient penetration of the solute, they cause faster clearance from the joint [67, 68]. Optimal waiting time, e.g., imaging at 120 min after injection of dGEMRIC, has been therefore applied [68].

For the CTs with spatial resolution defined by the FOV, proper selection of the dimensions of sample is needed to ensure sufficient volume coverage. Moreover, *in-vivo* scans of relatively large rabbits and rats, two important animal models, could be challenging as well as proper positioning of the animal to allow sufficient view of the region of interest. Therefore, scanning of injected larger joints, for instance in rabbits, may be associated with relatively lower spatial resolutions, which may impair the investigation of diffusion in different cartilage zones. Application of fluorescent microscopy obviously is limited to studying diffusion across thin *ex-vivo* slices and therefore monitoring temporal diffusion behavior in 3D becomes literally infeasible.

2.4.7. EQUIPMENT COST

Selection criteria for the appropriate imaging tool should take instrument cost into account as well. Although the high cost of MRI systems may be seen as a disadvantage, it is counterbalanced by capability of determining the diffusion attributes of water molecules in a minimally invasive manner. On the

other hand, clinical CT and micro-CT systems with lower costs allow for high-resolution 3D imaging of diffusion process. Involvement of ionizing radiation, however, could be a concern when designing animal experiments and clinical studies. Among the systems reviewed so far, the fluorescent microscopy techniques are the most accessible and cost-efficient, which also allow for studying the diffusion of a wide range of molecules.

The pros and cons as well as the selection criteria for the imaging systems discussed earlier are summarized in Table 2.1 and Figure 2.2. Figure 2.3 illustrates the different scales of imaging tools ranging from clinical to ex-vivo applications.

Table 2.1. Specifications of Fluorescent Microscopy, CT and MRI used in solute transport studies

Imaging Tool	*Tissue Form*	*Cartilage Zones*	*Maximum Resolution*	*Imaging Time Interval*	*Live Species*	*Solute Size*	*Bath Concentration Limitation*	**PCM/ECM*	*Cost*
Fluorescent microscopy	Excised	Zonal	Few hundred nanometers	Tens of seconds	None	Large	No limitation	PCM and ECM	Low
Clinical CT	In-vivo, in-vitro and clinical	Thickness dependent	Few hundred microns	Tens of seconds	Except mouse and rat (cartilage thickness < spatial resolution)	Mostly small	Low to medium concentrations	ECM	Middle
Experimental CT	In-vivo and in-vitro	Zonal	Few microns	Tens of seconds	Up to rabbit size (Chamber size limitation)	Mostly small	Low to medium concentrations	PCM and ECM	Middle
Clinical MRI	In-vivo, in-vitro and clinical	Thickness dependent	Few hundred microns (2D), few millimeters thick slice	Tens of minutes	Except mouse, rat and rabbit (cartilage thickness < spatial resolution)	Mostly small	Low	ECM	High
Experimental MRI	In-vivo, in-vitro	Thickness dependent	Few microns (2D), few millimeters thick slice	Few hours	Up to rabbit size (Chamber size limitation)	Mostly small	Low	ECM	High

* PCM: Pericellular Matrix
* ECM: Extracellular Matrix

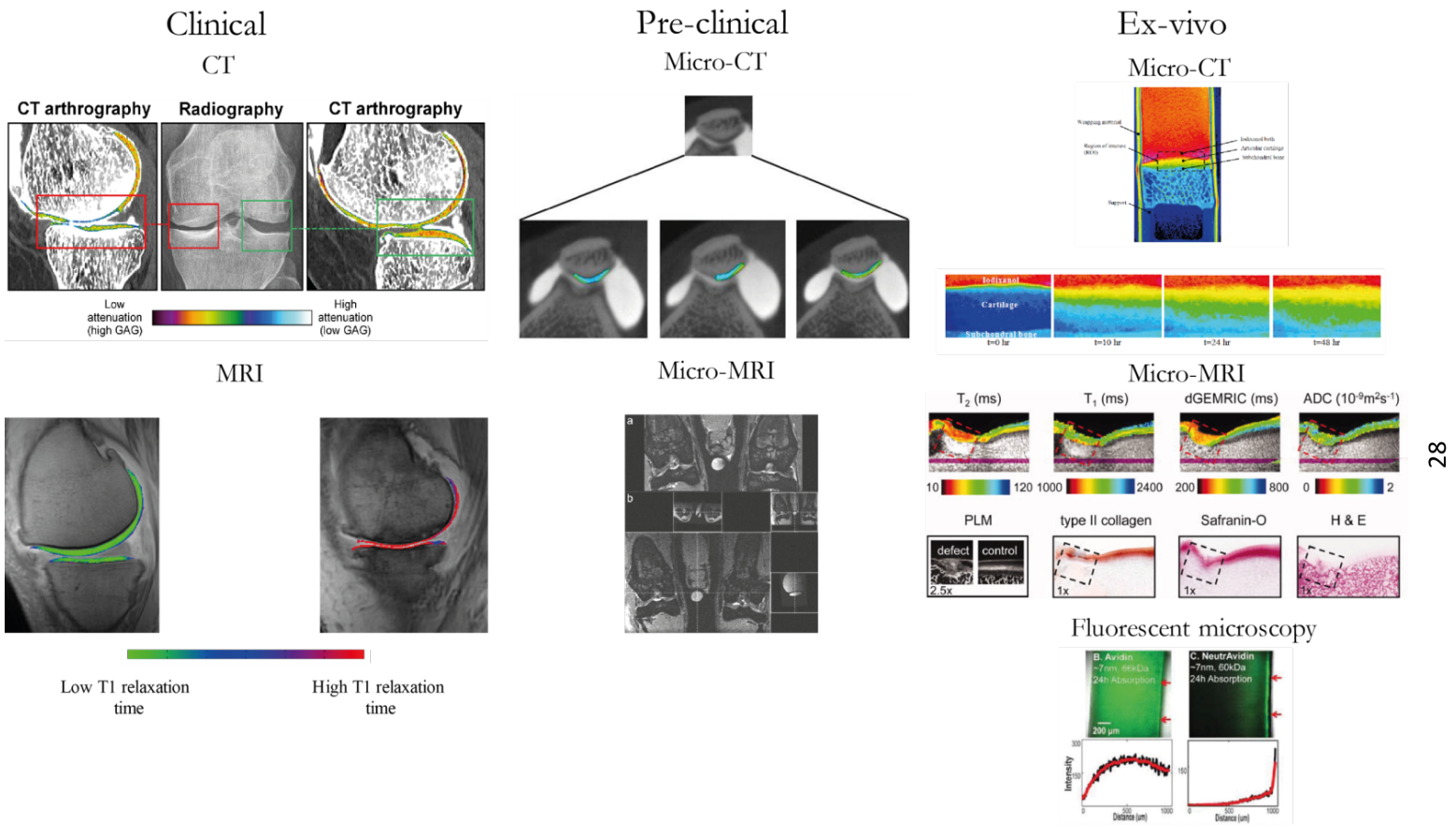

Figure 2.3. Examples of predominant imaging tools

at different imaging scales [1-6] (Reprint with permission from Elsevier, ASME and Wiley).

2.5. TRANSPORT AUGMENTATION

Enhancing solute transport could revolutionize drug delivery strategies as well as image acquisition technologies. The ECM of articular cartilage presents a densely-packed structure and is highly negatively charged, which hinders the transport of polymer-based therapeutics and negatively-charged solutes [69]. One way to enhance the retention of the drugs is to modify them with ligands, e.g. WYRGRL (a peptide sequence of collagen II binding domain), which binds to collagen II and allows matrix binding. On the other hand, the size of the particles governs their ability to penetrate through the matrix. Sufficiently small nanoparticles (<38 nm) were initially believed to diffuse across various zones of cartilage [70]. However, synthesized nanoparticles often present a Gaussian size distribution, which is remarkable as a later study suggested that even 15 nm quantum dots only penetrate into a small fraction of the superficial zone after 24 hr [1]. The same study concluded that the transport is size- and shape-dependent. Traumatic damage of cartilage was shown to facilitate the transport of fragments of anti-inflammation therapeutics (anti-IL-6 antigen binding fragments, ~ 48 kDa) unlike the full-sized antibodies [71]. As already mentioned, molecules larger than 15 nm experience difficulty penetrating into ECM, although positively charged gene delivery agents (i.e. self-complementary recombinant adeno-associated virus vectors) even with 20 nm size could be successfully delivered across equine articular cartilage [72]. Harnessing electrostatic features enabled more efficient delivery of some therapeutics, e.g. Dexamethasone to the cells and matrix targets. Avidin (7 nm, 66 kDa, net charge = +20), unlike NeutroAvidin (7 nm, 60 kDa, net charge=0) dramatically increased the retention (minimum 15 days) and uptake (400 times larger than that of NeutrAvidin) inside bovine cartilage explants owing to electrostatic partitioning and binding to ECM. Consequently, positively charged Avidin was shown to deliver dexamethasone inside the cartilage, thereby controlling the cytokine induced GAG loss over a period of three weeks with only a single low dose of the drug [13].

2.6. CONCLUSIONS

This review provides an overview of the practical aspects of solute transport through articular cartilage, particularly in light of imaging perspectives in clinic and experimental setups. First, the transport mechanisms and their underlying background were reviewed and the effects of bath attributes on diffusion, which are often overlooked, were discussed. In short, fluorescent microscopy enables high-resolution diffusion of large molecules in relatively short amount of time and in different zones, as well as in pericellular matrix, although out-of-plane study is limited to few hundred microns. Instead, several thin tissue sections can be prepared and the diffusion can be monitored. Unfortunately, this inflicts disruption of tissue integrity. MRI has been extensively applied to measure the diffusion of typically small molecules, e.g., Gd-DTPA and water, and high-resolution MRI substantially ameliorates the accuracy when measuring the diffusivity in 3D. However, relatively long scan times associated with this technique and low out-of-plane resolution limit its application, particularly if different zones of cartilage are studied. Even though CT-based techniques have been widely used mainly for measuring the 3D diffusivity of small iodinated molecules and offer high resolutions and short scan times, their immediate application is somewhat challenged for measuring the diffusion of larger therapeutic molecules which are often radiolucent. In the end, as delivering and retention of therapeutics have long been to high extent associated with critical challenges, guidelines with respect to namely, drug incorporation in positively charged carriers, considerations of cartilage thickness and charged bath-cartilage interactions were provided. The review, by providing sufficient tools and guidelines, can assist future research efforts on diffusion-aided cartilage imaging and quantitative characterization of solute diffusion using imaging techniques.

2.7. ACKNOWLEDGEMENTS

The authors would like to express their gratitude for the support of Dutch Arthritis Foundation (Grant No. 13-3-406) and Academy of Finland (Grant No. 269315).

2.8. **References**

1. Bajpayee, A.G., et al., *Avidin as a model for charge driven transport into cartilage and drug delivery for treating early stage post-traumatic osteoarthritis.* Biomaterials, 2014. **35**(1): p. 538-49.
2. Oei, E.H., et al., *Quantitative radiologic imaging techniques for articular cartilage composition: toward early diagnosis and development of disease-modifying therapeutics for osteoarthritis.* Arthritis Care Res (Hoboken), 2014. **66**(8): p. 1129-41.
3. de Visser, H.M., et al., *Groove model of tibia-femoral osteoarthritis in the rat.* J Orthop Res, 2017. **35**(3): p. 496-505.
4. Arbabi, V., et al., *Transport of neutral solute across articular cartilage: the role of zonal diffusivities.* J Biomech Eng, 2015. **137**(7).
5. Wachsmuth, L., et al., *In vivo contrast-enhanced micro MR-imaging of experimental osteoarthritis in the rabbit knee joint at 7.1T1.* Osteoarthritis Cartilage, 2003. **11**(12): p. 891-902.
6. Nieminen, M.T., et al., *Evaluation of chondral repair using quantitative MRI.* J Magn Reson Imaging, 2012. **36**(6): p. 1287-99.
7. Nia, H.T., et al., *Aggrecan nanoscale solid-fluid interactions are a primary determinant of cartilage dynamic mechanical properties.* ACS Nano, 2015. **9**(3): p. 2614-25.
8. Nia, H.T., C. Ortiz, and A. Grodzinsky, *Aggrecan: approaches to study biophysical and biomechanical properties.* Methods Mol Biol, 2015. **1229**: p. 221-37.
9. Leddy, H.A. and F. Guilak, *Site-specific molecular diffusion in articular cartilage measured using fluorescence recovery after photobleaching.* Ann Biomed Eng, 2003. **31**(7): p. 753-60.
10. Leddy, H.A. and F. Guilak, *Site-specific effects of compression on macromolecular diffusion in articular cartilage.* Biophys J, 2008. **95**(10): p. 4890-5.
11. Evans, C.H., V.B. Kraus, and L.A. Setton, *Progress in intra-articular therapy.* Nat Rev Rheumatol, 2014. **10**(1): p. 11-22.
12. Arbabi, V., et al., *Multiphasic modeling of charged solute transport across articular cartilage: Application of multi-zone finite-bath model.* J Biomech, 2016. **49**(9): p. 1510-7.
13. Bajpayee, A.G., et al., *Charge based intra-cartilage delivery of single dose dexamethasone using Avidin nano-carriers suppresses cytokine-induced catabolism long term.* Osteoarthritis Cartilage, 2016. **24**(1): p. 71-81.
14. Bajpayee, A.G., et al., *A rabbit model demonstrates the influence of cartilage thickness on intra-articular drug delivery and retention within cartilage.* J Orthop Res, 2015. **33**(5): p. 660-7.
15. Pouran, B., et al., *Isolated effects of external bath osmolality, solute concentration, and electrical charge on solute transport across articular cartilage.* Med Eng Phys, 2016. **38**(12): p. 1399-1407.
16. Pouran, B., et al., *Application of multiphysics models to efficient design of experiments of solute transport across articular cartilage.* Comput Biol Med, 2016. **78**: p. 91-96.

17. Kokkonen, H.T., et al., *Computed tomography detects changes in contrast agent diffusion after collagen cross-linking typical to natural aging of articular cartilage.* Osteoarthritis Cartilage, 2011. **19**(10): p. 1190-8.
18. Kokkonen, H.T., et al., *Solute Transport of Negatively Charged Contrast Agents Across Articular Surface of Injured Cartilage.* Ann Biomed Eng, 2016.
19. Evans, R.C. and T.M. Quinn, *Dynamic compression augments interstitial transport of a glucose-like solute in articular cartilage.* Biophys J, 2006. **91**(4): p. 1541-7.
20. Huang, C.Y. and W.Y. Gu, *Effects of tension-compression nonlinearity on solute transport in charged hydrated fibrous tissues under dynamic unconfined compression.* J Biomech Eng, 2007. **129**(3): p. 423-9.
21. Rautiainen, J., et al., *Multiparametric MRI assessment of human articular cartilage degeneration: Correlation with quantitative histology and mechanical properties.* Magn Reson Med, 2014.
22. Leddy, H.A., S.E. Christensen, and F. Guilak, *Microscale diffusion properties of the cartilage pericellular matrix measured using 3D scanning microphotolysis.* J Biomech Eng, 2008. **130**(6): p. 061002.
23. Chin, H.C., M. Moeini, and T.M. Quinn, *Solute transport across the articular surface of injured cartilage.* Arch Biochem Biophys, 2013. **535**(2): p. 241-7.
24. Decker, S.G., et al., *Adsorption and distribution of fluorescent solutes near the articular surface of mechanically injured cartilage.* Biophys J, 2013. **105**(10): p. 2427-36.
25. Moeini, M., et al., *Decreased solute adsorption onto cracked surfaces of mechanically injured articular cartilage: towards the design of cartilage-specific functional contrast agents.* Biochim Biophys Acta, 2014. **1840**(1): p. 605-14.
26. Quinn, T.M., et al., *Preservation and analysis of nonequilibrium solute concentration distributions within mechanically compressed cartilage explants.* J Biochem Biophys Methods, 2002. **52**(2): p. 83-95.
27. Shafieyan, Y., et al., *Diffusion of MRI and CT contrast agents in articular cartilage under static compression.* Biophys J, 2014. **107**(2): p. 485-92.
28. Lusic, H. and M.W. Grinstaff, *X-ray-computed tomography contrast agents.* Chem Rev, 2013. **113**(3): p. 1641-66.
29. Kulmala, K.A., et al., *Diffusion coefficients of articular cartilage for different CT and MRI contrast agents.* Med Eng Phys, 2010. **32**(8): p. 878-82.
30. Lakin, B.A., et al., *Cationic agent contrast-enhanced computed tomography imaging of cartilage correlates with the compressive modulus and coefficient of friction.* Osteoarthritis Cartilage, 2013. **21**(1): p. 60-8.
31. Lakin, B.A., et al., *Contrast enhanced CT attenuation correlates with the GAG content of bovine meniscus.* J Orthop Res, 2013. **31**(11): p. 1765-71.
32. Lakin, B.A., et al., *Contrast-enhanced CT using a cationic contrast agent enables non-destructive assessment of the biochemical and biomechanical properties of mouse tibial plateau cartilage.* J Orthop Res, 2016. **34**(7): p. 1130-8.
33. Stewart, R.C., et al., *Contrast-enhanced CT with a high-affinity cationic contrast agent for imaging ex vivo bovine, intact ex vivo rabbit, and in vivo rabbit cartilage.* Radiology, 2013. **266**(1): p. 141-50.

34. Kokkonen, H.T., et al., *Delayed Computed Tomography Arthrography of Human Knee Cartilage In Vivo.* Cartilage, 2012. **3**(4): p. 334-41.
35. Kokkonen, H.T., et al., *In vivo diagnostics of human knee cartilage lesions using delayed CBCT arthrography.* J Orthop Res, 2014. **32**(3): p. 403-12.
36. Myller, K.A., et al., *In Vivo Contrast-Enhanced Cone Beam CT Provides Quantitative Information on Articular Cartilage and Subchondral Bone.* Ann Biomed Eng, 2017. **45**(3): p. 811-818.
37. Aula, A.S., J.S. Jurvelin, and J. Toyras, *Simultaneous computed tomography of articular cartilage and subchondral bone.* Osteoarthritis Cartilage, 2009. **17**(12): p. 1583-8.
38. Siebelt, M., et al., *Clinically applied CT arthrography to measure the sulphated glycosaminoglycan content of cartilage.* Osteoarthritis Cartilage, 2011. **19**(10): p. 1183-9.
39. Honkanen, J.T., et al., *Cationic Contrast Agent Diffusion Differs Between Cartilage and Meniscus.* Ann Biomed Eng, 2016. **44**(10): p. 2913-21.
40. Palmer, A.W., R.E. Guldberg, and M.E. Levenston, *Analysis of cartilage matrix fixed charge density and three-dimensional morphology via contrast-enhanced microcomputed tomography.* Proc Natl Acad Sci U S A, 2006. **103**(51): p. 19255-60.
41. Kulmala, K.A., et al., *Diffusion of ionic and non-ionic contrast agents in articular cartilage with increased cross-linking--contribution of steric and electrostatic effects.* Med Eng Phys, 2013. **35**(10): p. 1415-20.
42. Nieminen, H.J., et al., *Determining collagen distribution in articular cartilage using contrast-enhanced micro-computed tomography.* Osteoarthritis Cartilage, 2015. **23**(9): p. 1613-21.
43. Karhula, S.S., et al., *Effects of Articular Cartilage Constituents on Phosphotungstic Acid Enhanced Micro-Computed Tomography.* PLoS One, 2017. **12**(1): p. e0171075.
44. Mashiatulla, M., et al., *Murine articular cartilage morphology and compositional quantification with high resolution cationic contrast-enhanced muCT.* J Orthop Res, 2017.
45. Malda, J., et al., *Of mice, men and elephants: the relation between articular cartilage thickness and body mass.* PLoS One, 2013. **8**(2): p. e57683.
46. Bashir, A., M.L. Gray, and D. Burstein, *Gd-DTPA2- as a measure of cartilage degradation.* Magn Reson Med, 1996. **36**(5): p. 665-73.
47. Donahue, K.M., et al., *Studies of Gd-DTPA relaxivity and proton exchange rates in tissue.* Magn Reson Med, 1994. **32**(1): p. 66-76.
48. Allen, R.G., D. Burstein, and M.L. Gray, *Monitoring glycosaminoglycan replenishment in cartilage explants with gadolinium-enhanced magnetic resonance imaging.* J Orthop Res, 1999. **17**(3): p. 430-6.
49. Ronga, M., et al., *Imaging of articular cartilage: current concepts.* Joints, 2014. **2**(3): p. 137-40.
50. Pouran, B., et al., *Solute transport at the interface of cartilage and subchondral bone plate: Effect of micro-architecture.* J Biomech, 2016.
51. Arbabi, V., et al., *Neutral solute transport across osteochondral interface: A finite element approach.* J Biomech, 2016. **49**(16): p. 3833-3839.

52. Hawezi, Z.K., et al., *Regional dGEMRIC analysis in patients at risk of osteoarthritis provides additional information about activity related changes in cartilage structure.* Acta Radiol, 2016. **57**(4): p. 468-74.
53. Lattanzi, R., et al., *Detection of cartilage damage in femoroacetabular impingement with standardized dGEMRIC at 3 T.* Osteoarthritis Cartilage, 2014. **22**(3): p. 447-56.
54. Salo, E.N., et al., *Diffusion of Gd-DTPA(2)(-) into articular cartilage.* Osteoarthritis Cartilage, 2012. **20**(2): p. 117-26.
55. Wiener, E., et al., *Contrast enhanced cartilage imaging: Comparison of ionic and non-ionic contrast agents.* Eur J Radiol, 2007. **63**(1): p. 110-9.
56. Nissi, M.J., et al., *Measurement of T1 relaxation time of osteochondral specimens using VFA-SWIFT.* Magn Reson Med, 2014.
57. Kang, Y., et al., *Delayed Gadolinium-enhanced MR Imaging of Cartilage: A Comparative Analysis of Different Gadolinium-based Contrast Agents in an ex Vivo Porcine Model.* Radiology, 2017. **282**(3): p. 734-742.
58. Freedman, J.D., et al., *A cationic gadolinium contrast agent for magnetic resonance imaging of cartilage.* Chem Commun (Camb), 2015. **51**(56): p. 11166-9.
59. Trattnig, S., et al., *23Na MR imaging at 7 T after knee matrix-associated autologous chondrocyte transplantation preliminary results.* Radiology, 2010. **257**(1): p. 175-84.
60. Wang, N., E. Chopin, and Y. Xia, *The effects of mechanical loading and gadolinium concentration on the change of T1 and quantification of glycosaminoglycans in articular cartilage by microscopic MRI.* Phys Med Biol, 2013. **58**(13): p. 4535-47.
61. Meder, R., et al., *Diffusion tensor imaging of articular cartilage as a measure of tissue microstructure.* Osteoarthritis Cartilage, 2006. **14**(9): p. 875-81.
62. Bajd, F., et al., *Diffusion tensor MR microscopy of tissues with low diffusional anisotropy.* Radiol Oncol, 2016. **50**(2): p. 175-87.
63. Rautiainen, J., et al., *Effect of collagen cross-linking on quantitative MRI parameters of articular cartilage.* Osteoarthritis Cartilage, 2016. **24**(9): p. 1656-64.
64. Kokkonen, H.T., et al., *Detection of mechanical injury of articular cartilage using contrast enhanced computed tomography.* Osteoarthritis Cartilage, 2011. **19**(3): p. 295-301.
65. Silvast, T.S., et al., *Bath Concentration of Anionic Contrast Agents Does Not Affect Their Diffusion and Distribution in Articular Cartilage In Vitro.* Cartilage, 2013. **4**(1): p. 42-51.
66. Garcia, A.M., et al., *Contributions of fluid convection and electrical migration to transport in cartilage: relevance to loading.* Arch Biochem Biophys, 1996. **333**(2): p. 317-25.
67. Sigurdsson, U., et al., *In vivo transport of Gd-DTPA2- into human meniscus and cartilage assessed with delayed gadolinium-enhanced MRI of cartilage (dGEMRIC).* BMC Musculoskelet Disord, 2014. **15**: p. 226.
68. Sigurdsson, U., et al., *Delayed gadolinium-enhanced MRI of meniscus (dGEMRIM) and cartilage (dGEMRIC) in healthy knees and in knees with*

different stages of meniscus pathology. BMC Musculoskelet Disord, 2016. **17**(1): p. 406.
69. Bajpayee, A.G. and A.J. Grodzinsky, *Cartilage-targeting drug delivery: can electrostatic interactions help?* Nat Rev Rheumatol, 2017. **13**(3): p. 183-193.
70. Rothenfluh, D.A., et al., *Biofunctional polymer nanoparticles for intra-articular targeting and retention in cartilage*. Nat Mater, 2008. **7**(3): p. 248-54.
71. Byun, S., et al., *Transport of anti-IL-6 antigen binding fragments into cartilage and the effects of injury*. Arch Biochem Biophys, 2013. **532**(1): p. 15-22.
72. Watson, R.S., et al., *scAAV-mediated gene transfer of interleukin-1-receptor antagonist to synovium and articular cartilage in large mammalian joints*. Gene Ther, 2013. **20**(6): p. 670-7.

CHAPTER 3

ISOLATED EFFECTS OF EXTERNAL BATH OSMOLALITY, SOLUTE CONCENTRATION, AND ELECTRICAL CHARGE ON SOLUTE TRANSPORT ACROSS ARTICULAR CARTILAGE

This chapter is published as a scientific paper:

Pouran B., Arbabi V., Zadpoor A.A., Weinans H. *Isolated effects of external bath osmolality, solute concentration, and electrical charge on solute transport across articular cartilage. Medical Engineering and Physics*, 2016. Medical Engineering and Physics 38 (2016) 1399–1407.

Chapter 3

ABSTRACT

The metabolic function of cartilage primarily depends on transport of solutes through diffusion mechanism. In the current study, we use contrast enhanced micro-computed tomography to determine equilibrium concentration of solutes through different cartilage zones and solute flux in the cartilage, using osteochondral plugs from equine femoral condyles. Diffusion experiments were performed with two solutes of different charge and approximately equal molecular weight, namely iodixanol (neutral) and ioxaglate (charge = -1) in order to isolate the effects of solute charge on diffusion. Furthermore, solute concentrations as well as bath osmolality were changed to isolate the effects of steric hindrance on diffusion. Bath concentration and bath osmolality only had minor effects on the diffusion of the neutral solute through cartilage at the surface, middle and deep zones, indicating that the diffusion of the neutral solute was mainly Fickian. The charged solute diffused considerably slower through cartilage than the neutral solute, indicating a large non-Fickian contribution in the diffusion of charged molecules. The numerical models determined maximum solute flux in the superficial zone up to a factor of 2.5 lower for the negatively charged solutes (charge= -1) as compared to the neutral solutes confirming the importance of charge-matrix interaction in diffusion of molecules across cartilage.

Chapter 3

3.1. INTRODUCTION

Articular cartilage is an avascular tissue with highly inhomogeneous organization that lines the end of long bones and enables low-friction joint mobility [1, 2]. The avascular nature of articular cartilage means that it has to rely mainly on diffusion for transport of vital signaling molecules, nutrients and oxygen. Cyclic loading and the associated fluid flow augment the transport of large molecules through an additional transport mechanism, namely convection [3-5]. Transport of small solutes such as ions, however, cannot be significantly amplified via convection [5]. Extracellular matrix (ECM) of cartilage consists mostly of collagen type II, proteoglycans (PGs) and water. Fragments of PG and collagen type II are continuously transported within ECM as a result of enzymatic digestion and remodeling. Collagen type II and PGs account for the major components of cartilage that provide the ECM with its shear and tensile properties as well as with resilience [2, 6]. Articular cartilage is characterized by a zonal architecture where water content, as the major parameter influencing solute diffusion, varies from 80% in the superficial layer to 60% in the deep layer [7-10]. The orientation, thickness, and concentration of collagen type II fibrils together with uneven distribution of PGs in various zones of articular cartilage play significant roles in the solute diffusion across the tissue [1, 11]. Solute diffusion depends predominantly on the nature of the interaction that can vary as a consequence of different density and morphology of the tissue at the molecular level (steric hindrance) and ion-ion interactions. The latter is believed to take place when the solute is charged and thereby repulsion/attraction interaction with the negatively fixed charges of the glycosaminoglycans chains (GAGs) is dominant [12-14]. The combined effects of electric phenomena with the steric hindrance make the diffusion process across the articular cartilage extremely complicated.

To better understand the above-mentioned complexities in the transport of solutes across cartilage, the current study aims to separate the various physical mechanisms as much as possible by using a carefully designed set of diffusion experiments and associated finite element modeling.

First, we address the question whether the solute transport in cartilage has a Fickian nature. This would be the case if the concentration-time curves remain unchanged for different levels of osmolality and different levels of solute concentration in case the solute molecules are non-charged. Osmolality difference between bath and cartilage deforms the cartilage and consequently alters the molecular morphology and thus the interaction between the solute and the extracellular matrix that causes deviation from Fickian diffusion. For instance, it has been shown that Fickian models could poorly predict the diffusion of cryoprotective agent (CPA) through articular cartilage primarily due to local osmolality variation within the extracellular matrix [15].

Second, we address the contribution of electrical charges to the transport of solutes across cartilage. In the majority of previous studies, the charged solute's diffusion attributes have been obtained by adopting Fickian-based models [16-18]. Answering the second research question allows us to quantify the effect of this simplification on the accuracy of determined solute fluxes and the described diffusion behavior. We therefore not only isolate the effects of external bath osmolality, concentration and charge from each other but also quantify those effects using equilibrium curves and zonal concentration curves as well as solute fluxes. The present study features a unique experimental approach through which the aforementioned effects could be separated. Moreover, biphasic-solute and multiphasic models [9, 19] that we had previously developed have been used to determine solute fluxes.

3.2. MATERIALS AND METHODS

3.2.1. SAMPLE HARVEST AND CONDITIONING

Equine knees for this study were obtained from the Equine Clinic in Utrecht University (approved by Animal Experiments Committee in Utrecht University). Using a custom-made hollow drill bit, four osteochondral plugs (8.5 mm diameter, cartilage thickness = 2.57±0.27 mm) were harvested from the medial femoral condyle of two 6-year old equine femurs (samples 1 and 2 from one donor and samples 3 and 4 from the other). To prevent sample overheating and to keep the drilling site moist during drilling, we continuously sprayed

phosphate buffer saline (PBS, 290 mOsmol/kg H2O, pH=7.4, Life technologies) on the drilling site. We stored the osteochondral plugs in a large bath of a solution comprising PBS, protease inhibitors (cOmplete tablets, EDTA free, Roche, Netherlands) and 5 mM Ethylenediaminetetraacetic acid (EDTA) at -20 °C before the diffusion experiments. Upon thawing, the samples were tightly wrapped laterally using heat-shrinking sleeves to prevent lateral contrast agent leakage (Figure 3.1). The sample was protected from heat during heat-shrinking process by optimizing the heat source distance from the sample, constantly spraying cold PBS on the sample surface, and mounting small wet cotton pieces on the boundaries.

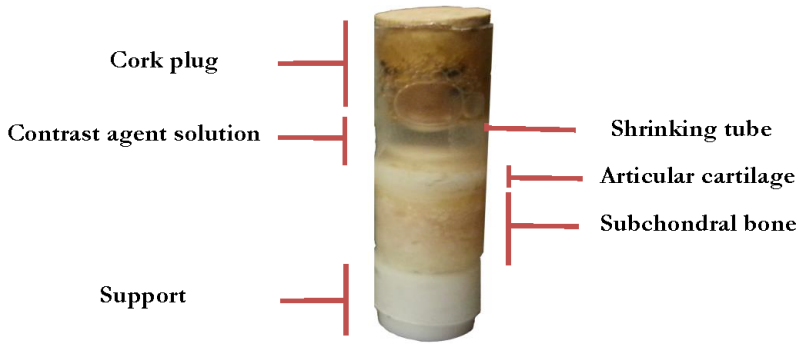

Figure 3.1. The sample consists of an osteochondtal plug, a cork plug, a shrinking tube, contrast agent solution and a support.

3.2.2. CONTRAST AGENT SOLUTIONS

The transport of two clinical contrast agents with similar molecular weights was investigated: iodixanol (Visipaque, 1550 g/mol, charge=0, GE Healthcare, Netherlands) and ioxaglate (Hexabrix, 1269 g/mol, charge=-1, GE Healthcare, Netherlands). In order to study the effects of bath concentration, osmolality, and electrical charge on solute transport, we prepared four different contrast agent baths (Table 3.1). We adjusted the osmolality of each solution at the required level by adding sodium chloride. Enzymatic digestion was prevented during the diffusion experiments through the addition of

protease inhibitors (cOmplete, Roche, Netherlands) and EDTA to the baths. A freezing point osmometer (Advanced® Model 3320 Micro-Osmometer, Netherlands) was used to measure osmolalities.

3.2.3. **CECT IMAGING**

We placed the wrapped samples on a custom-made holder and fixed the holder inside micro-CT (Quantum FX, Perkin Elmer, USA). In each condition, we loaded approximately 650 μL from the baths onto the cartilage surface. A cork plug and proper micro-CT chamber humidification were used to minimize solution evaporation during micro-CT scans (Figure 3.1). We scanned the samples at room temperature using micro-CT under a tube current of 180 μA and a tube voltage of 90 kV, resulting in a scan time of 2 min and a voxel size of 40×40×40 μm3. The resolution was chosen such that the field of view included the cartilage specimen, the contrast agent bath, and the subchondral bone. We acquired images during diffusion process at time points t-1 (before adding the bath), t_0 (bath injection), t= 5, 10, 30 min and t= 1, 2, 3, 4, 5, 7, 10, 12, 24 and 48 hours. When the experiment on every specimen was finished using one bath and before starting a new experiment with another bath (Figure 3.2), we washed the osteochondral plugs in series of large desorption baths [20] (PBS+protease inhibitor+EDTA (5mM) for 48 hours (4 °C) which proved to be effective (less than 5% difference between the gray values). The average grey values for each sample and each condition were recorded at t_0 to make sure of the efficacy of the contrast agent washout process. The equilibrium concentration of ioxaglate (inversely related to GAG content [21]) did not vary after performing the aforementioned experiments during our pilot studies suggesting no cartilage degeneration (data not shown). Furthermore, the remaining of each bath was tested after each experiment to search for any clues of GAG leakage using Dimethylmethylene Blue assay (DMMB), which proved no visual sign of GAG loss.

Table 3.1. Specification of the baths used in the diffusion experiments: Four different bath conditions were used to investigate the effects of concentration (*Iodix 320,290* vs. *Iodix 160,290*), external bath osmolality (*Iodix 320,290* vs. *Iodix 320,600*) and solute's charge (*Iodix 320,600* vs. *Ioxag 320,600*) on the diffusion in cartilage.

Bath	Solute	Charge	Concentration (mgI/ml)	Osmolality ($mOsm/kg\ H_2O$)
*Iodix 320,290**	Iodixanol	0	320	290
*Iodix 320,600**	Iodixanol	0	320	600
*Iodix 160,290**	Iodixanol	0	160	290
*Ioxag 320,600**	Ioxaglate	-1	320	600

* The conditions are described by their abbreviated solute name (iodixanol (*Iodix*) and ioxaglate (*Ioxag*)), solute concentration in the bath and bath's osmolality.

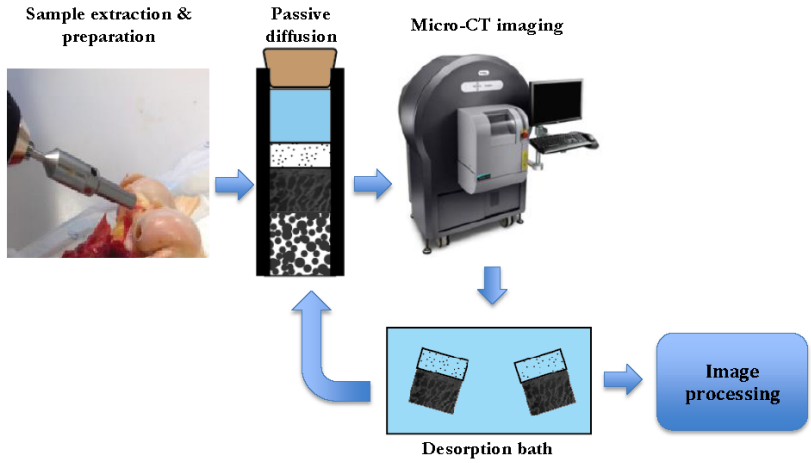

Figure 3.2. Flowchart of the experimental setup: Osteochondral plugs from the fresh equine femoral condyles were extracted. The osteochondral plugs were mounted on a support while being wrapped using a shrinking tube. Passive diffusion experiments were conducted in a micro-CT chamber. Immediately after each experiment the samples underwent serial desorption process within large baths before start of the next experiment.

3.2.4. IMAGE ACQUISITION AND PRE-PROCESSING

Image acquisition included 3D image reconstruction that was undertaken automatically using the built-in micro-CT software. The 3D files were transferred to Anlayze 11.0 (Perkin elmer, USA) to convert them to a sequence of 2D images (TIFF format). The images underwent noise removal using 3D Gaussian filter (ImageJ, 1.47v).

3.2.5. EQUILIBRIUM CURVES

We then exported the 2D image sequences to ImageJ (ImageJ, 1.47v) to process the images. The mid-sagittal slice that included cartilage, contrast agent, and subchondral bone was chosen as the representative image to study the transport of contrast agent molecules across cartilage. Our earlier calculations suggest that mid-sagittal slice can act as a representative slice and therefore we restricted our analyses to a single mid-sagittal slice. We applied a rectangular region of interest (ROI) (width = 5.6 mm) to all mid-sagittal images at every time point. The cartilage was segmented from the contrast agent bath and subchondral bone by global thresholding. This allowed for generation of cartilage masks that could be used to create another ROI that precisely outlined the cartilage. We overlaid this ROI onto the corresponding original images to evaluate the average grey values (Q). The average grey values were then calculated using the following formula:

$$Q = \frac{\sum P_i X_i}{\sum X_i} \quad (1)$$

where P_i and X_i are the pixel intensity and frequency, respectively.

We used an experimentally confirmed linear relationship between the grey value of the cartilage at t = 0 and that of the contrast agent bath and their corresponding concentrations to obtain the actual solute concentration within cartilage:

$$C = \alpha Q + \beta \quad (2)$$

where C is the solute concentration, Q is the average grey value and α and β are constants.

3.2.6. IMAGE REGISTRATION

To obtain the zonal diffusion curves, we performed elastic (i.e. deformable) image registration, which accounted for small elastic deformations in the cartilage as observed in our experiments (8±2.55 % of the total cartilage thickness) and spatial movements during the diffusion process. We registered the images using the Elastix package (University Medical Center Utrecht, Netherlands) [22, 23]. Two images were required to perform the registration process, a moving image and a fixed image. Images at t = 0 minutes for each bath condition (Table 3.1) were selected as the fixed images while images at t = 1, 6, 12, 24, 30 and 48 hours were selected as the moving images to which the ROIs for the zonal equilibrium curves will be assigned. Registration is mathematically formulated as an optimization problem where the cost function has to be minimized with respect to T to achieve the optimal transformation [22]. T is the image transformation matrix which is given as:

$$T(x) = x + u(x) \quad (3)$$

where $u(x)$ is the translation vector.

Elastix software limits the amount of possible transformations by introducing a parameterization of the transformation. Eventually, we examined the accuracy of the registration process through checking the location of a few fixed points on the cartilage-bath and cartilage-subchondral bone interfaces using MeVisLab (MeVis Medical Solutions AG, Bremen, Germany) (Figure 3.3).

(A)

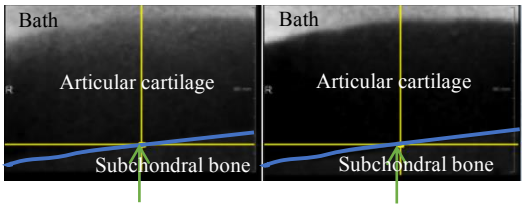

Matched points on the cartilage-subchondral plate interface

Matched points on the cartilage-bath interface

(B)

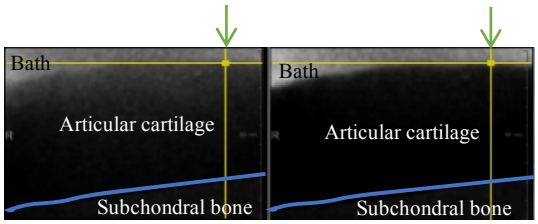

Figure 3.3. Visual inspection of the registration outcome using *MeVisLab*. Random points on the (A) cartilage-subchondral bone interface (blue line) and (B) cartilage-bath interface were selected to visually inspect whether the points in the fixed and the registered image matched.

3.2.7. ZONAL DIFFUSION CURVES

Articular cartilage can be considered to comprise three major zones, i.e. superficial, middle, and deep zones [7, 24-26]. Zonal diffusion curves can therefore be obtained to provide a more detailed description of diffusion and equilibrium concentration in each individual zone. Zonal diffusion curves were generated based on the previously registered images at 0, 1, 6, 12, 24 and 48 hours. The first step was to determine the thickness of cartilage at t = 0 for each sample using BoneJ (plugin of imageJ). Then, for each image, cartilage was divided into three different zones: superficial (20% of cartilage thickness), middle (50% of cartilage thickness), and deep zone (30% of cartilage thickness)

[7]. Thereafter, ImageJ was used to cover the superficial, middle, and deep zones separately, thereby generating three new ROIs corresponding to each zone. Those ROIs were applied to the registered images at 0, 1, 6, 12, 24 and 48 hours to obtain the average grey values. The average grey values were converted to concentration values using a similar approach as described in equilibrium curves. The normalized concentrations were then obtained by dividing the concentration values by the initial bath concentration.

Since solute flux is the rate of solute transport per unit area, we used multi-zone biphasic-solute and multiphasic models to curve-fit the concentration-time data followed by plotting the solute flux versus time in the middle of the superficial zone (20% of cartilage thickness) in each sample to compare the transport of neutral (Iodix 320,600) and charged (Ioxag 320,600) solutes in cartilage. The models [9, 27, 28] included the solid phase, the fluid phase, and the solutes and could describe the interactions of the solid matrix and the fluid and solute phases. Physical phenomena such as water exodus and return, cartilage swelling, electric interactions (ioxaglate) and the deformations of the solid phase caused by osmolality shocks and water transport were therefore taken into account [9, 27]. The model consisted of a finite bath (≈14 mm) and a cartilage that resembled the experimental setup. The diffusion was restricted to occur only through the surface of the cartilage (axial diffusion) while the cartilage-subchondral bone interface was prescribed as a no-flux boundary condition. The initial concentration of the solute in the cartilage was set to zero. The model was fitted to the equilibrium curves and the solute flux curves were subsequently plotted.

3.2.8. **STATISTICAL ANALYSIS**

Two-factor ANOVA statistical analysis was used to determine the statistical significance of the normalized concentrations at 48 hours in the equilibrium curves as well as in the zonal diffusion curves. A significance threshold of $p < 0.05$ was used. It should be noted though that the aim of this chapter is to address the effects of external bath osmolality, solute

concentration as well as solute's charge on the transport within each sample, thereby those effects should be studied in each sample separately.

3.3. RESULTS

Changes in bath concentration and osmolality may cause local deformation in cartilage matrix and mass transfer resistance at the bath-cartilage interface, which consequently alter solute-matrix interactions through steric hindrance mechanism. On the other hand, strong solute charge-matrix charge interactions affect the diffusion and make it deviate from Fickian behavior. Here we study these interactions with the aid of equilibrium curves, zonal diffusion curves and solute flux curves.

3.3.1. EQUILIBRIUM CURVES

The near-equilibrium state was reached approximately 24 hours after the start of the experiments (Figure 3.4). The effect of bath solute concentration on diffusion was assessed by comparing the equilibrium curves of bath Iodix 320,290 and Iodix 160,290 that represent the diffusion of iodixanol at different solute concentrations but with the same osmolality. The normalized concentrations (% initial bath concentration) for both baths Iodix 320,290 and Iodix 160,290 were very close to each other (Table 3.2A). For the early time points, Iodix 160,290 showed a steeper slope compared to Iodix 320,290 indicating a faster diffusion rate (Figure 3.4).

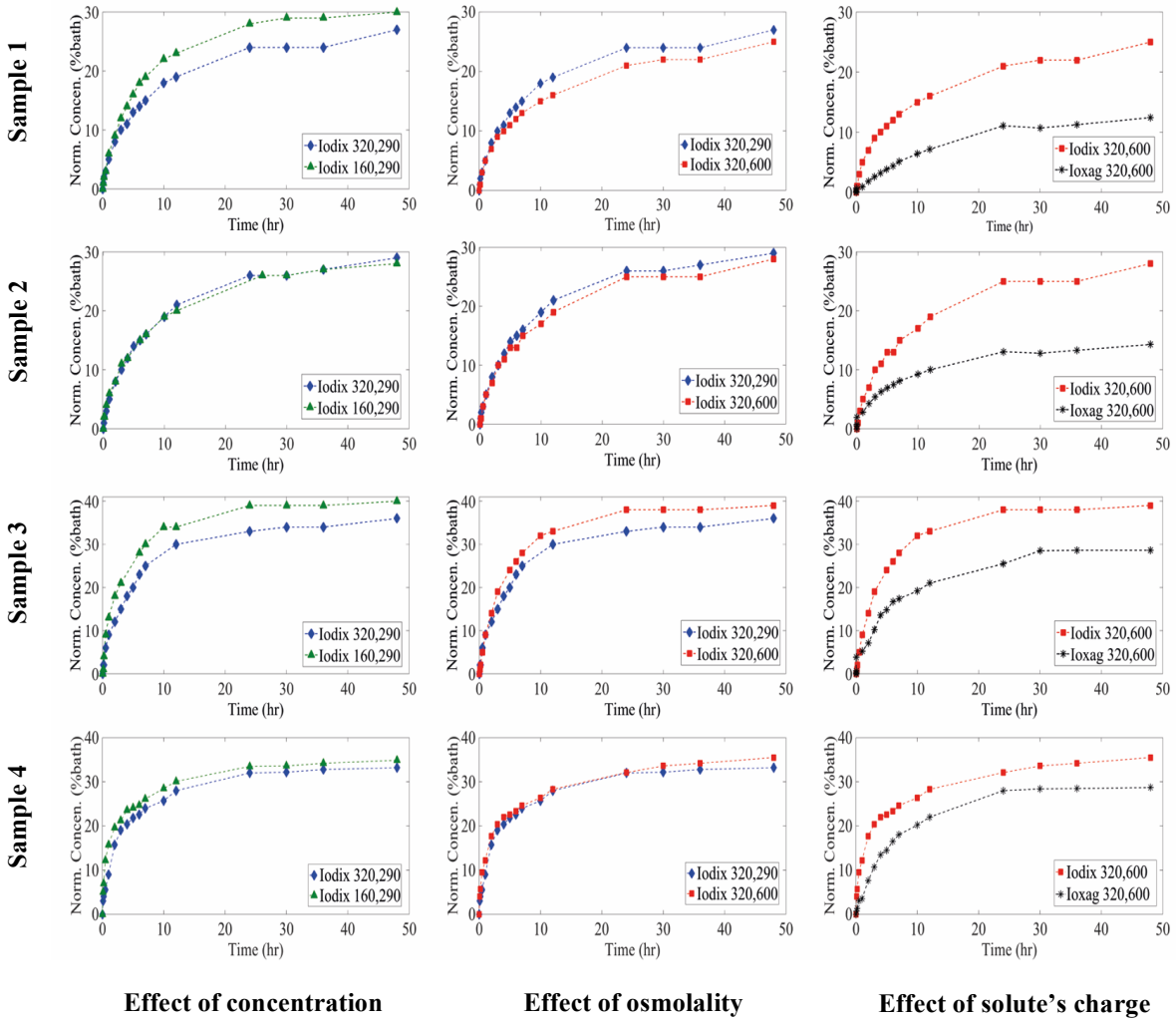

Figure 3.4. Plot of normalized concentration (% initial bath concentration) vs. time for the full thickness of the cartilage for samples 1-4. Slight difference for the effect of bath concentration (*Iodix 320,290 vs. Iodix 160,290*) and bath osmolality (*Iodix 320,290 vs. Iodix 320,600*) can be observed whereas effect of solute's charge is more pronounced (*Iodix 320,600 vs. Ioxag 320, 600*).

Table 3.2. Solute's equilibrium concentrations. Effect of bath concentration on the solute transport was investigated by comparing normalized final concentration value in finite baths *Iodix 320,290* and *Iodix 160,290*. Effect of bath osmolality on the solute transport was investigated by comparing normalized final concentration value in finite baths *Iodix 320,290* and *Iodix 320,600*. Effect of solute's charge on the solute transport was investigated by comparing normalized final concentration value in finite baths *Iodix 320,600* and *Ioxag 320,600* (A). Final normalized concentrations in the superficial, middle and deep zones (B).

(A)

Condition	*Iodix 320,290**	*Iodix 160,290**	*p-value*	*Iodix 320,290**	*Iodix 320,600**	*p-value*	*Iodix 320,600**	*Ioxag 320,600**	*p-value*
Concentration (*mgI/ml*)	33.7±5.9	33±6.1	0.082	33.7±5.9	30.7±7.4	0.133	30.7±7.4	18.3±9.3	0.006

(B)

	Condition		*p*-value	Condition		*p*-value	Condition		*p*-value
	*Iodix 320,290**	*Iodix 160,290**		*Iodix 320,290**	*Iodix 320,600**		*Iodix 320,600**	*Ioxag 320,600**	
Superficial concen. (*mgI/ml*)	57.58±1.37	54.25±4.98	0.374	57.58±1.37	61.4±6.98	0.422	61.4±6.98	52.18±6.75	0.00008
Middle concen. (*mgI/ml*)	30.55±5.31	32.44±5.21	0.435	30.55±5.31	31.57±5.99	0.987	31.57±5.99	25.37±4.61	0.00838
Deep concen. (*mgI/ml*)	16.62±2.78	19.48±3.20	0.051	16.62±2.78	17.17±5.25	0.099	17.17±5.25	11.80±3.42	0.02731

*The conditions are described by their abbreviated solute name (iodixanol (*Iodix*) and ioxaglate (*Ioxag*)), solute's concentration in the bath and bath's osmolality

The effect of osmolality on diffusion was assessed by comparing the equilibrium curves of Iodix 320,290 and Iodix 320,600 that represent the diffusion of iodixanol at different osmolalities but with the same concentration. In this experiment, the different osmolalities (hypo- and hyper-osmolal) will lead to differences in expansion and as a consequence the diffusion can deviate from Fickian through potential effects of steric hindrance. Fickian diffusion would require identical diffusion curves for the two conditions. For both conditions, the near-equilibrium state was reached at 24 hours (Figure 3.4). On average, the difference between these two conditions was very small.

We further investigated the effects of charge and consequently non-Fickian solute diffusion across articular cartilage by comparing the normalized concentration curves between Iodix 320,600 and Ioxag 320,600. These conditions represented the same contrast agent concentration and osmolality, but different solute charges. Similar to the previous situations, for both conditions, the near-equilibrium state was reached at 24 hours (Figure 3.4). The diffusion rate in Iodix 320,600 was considerably higher than that of Ioxag 320,600 particularly in the very early time points (Figure 3.4). Moreover, the equilibrium normalized concentrations in Iodix 320,600 were markedly higher than those in Ioxag 320,600 (p-value=0.006, Table 3.2A), which indicate a fairly large non-Fickian aspect in the diffusion.

3.3.2. ZONAL DIFFUSION CURVES

The superficial zone represents the highest values of normalized concentrations (Figure 3.5A). Solute transport rate was found to be the highest in the superficial layer for all conditions. However, it approached the near-equilibrium state shortly after the onset of the experiments (Figure 3.5A).

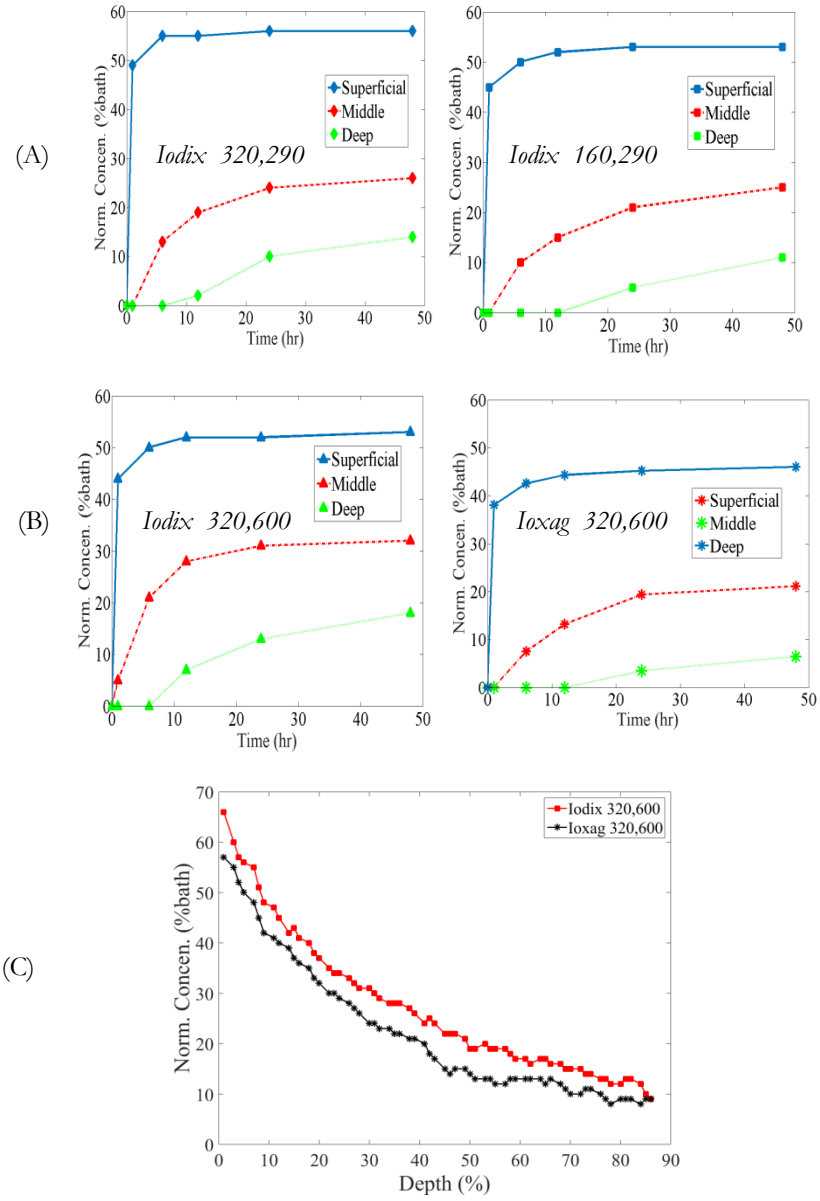

Figure 3.5. (A) Plot of normalized concentration vs. time in the superficial, middle and deep zones (example, sample 1). For all different conditions the concentration values are lower in the deep zones. In all zones effect of charge on the transport is tangible. (B) Plot of concentration vs. cartilage depth for *Iodix 320,600* and *Ioxag 320,600* to highlight the effect of charge on solute transfer (example, sample 1).

To address the effect of concentration on diffusion, resulting curves for Iodix 320,290 and Iodix 160,290 were compared. The diffusion rate was similar between Iodix 320,290 and Iodix 160,290 but the deep layer showed a larger difference (Figure 3.5A). In the superficial zone, the near-equilibrium state is reached for Iodix 320,290 and Iodix 160,290 after 6 hours (Figure 3.5A). Regardless of bath conditions, the equilibrium state is not reached for the middle or deep zones since the diffusion curves keep rising (Figure 3.5A). The equilibrium concentration was not significantly higher in Iodix 160,290 within the deep zone compared to that in Iodix 320,290 (p-value>0.05, Table 3.2B).

Effect of osmolality on diffusion was addressed by comparing resulting curves for Iodix 320,290 and Iodix 320,600. Both Iodix 320,290 and Iodix 320,600 reached the near-equilibrium concentrations at 12 hours in the superficial zone (Figure 3.5A). The equilibrium concentrations in the superficial, middle and deep zones between Iodix 320,290 and Iodix 320,600 were not significantly different (p-value>0.05, Table 5.2B).

The effect of solute's charge on diffusion was studied by comparing Iodix 320,600 and Ioxag 320,600. In all zones, the normalized concentration curve for Ioxag 320,600 depicts significantly lower concentrations compared to those of Iodix 320,600 (Figure 3.5, $p < 0.05$, Table 3.2B). However, the time point where each condition reaches near-equilibrium state was almost similar and was 12 hours (Figure 3.5A). The typical concentration versus cartilage depth curves at 48 hours showed also higher concentration of iodixanol (Iodix 320,600) compared to ioxaglate (Ioxag 320,600) (Figure 3.5B).

The solute flux for Iodix 320,600 showed higher peak than that of Ioxag 320,600 and the peak occurred in the early time points (Figure 3.6). The maximum flux of iodixanol was 0.0084 ± 0.0061 mmol/m2.s, while that of ioxaglate was 0.0047 ± 0.0031 mmol/m2.s (p-value=0.185).

(A)

(B)

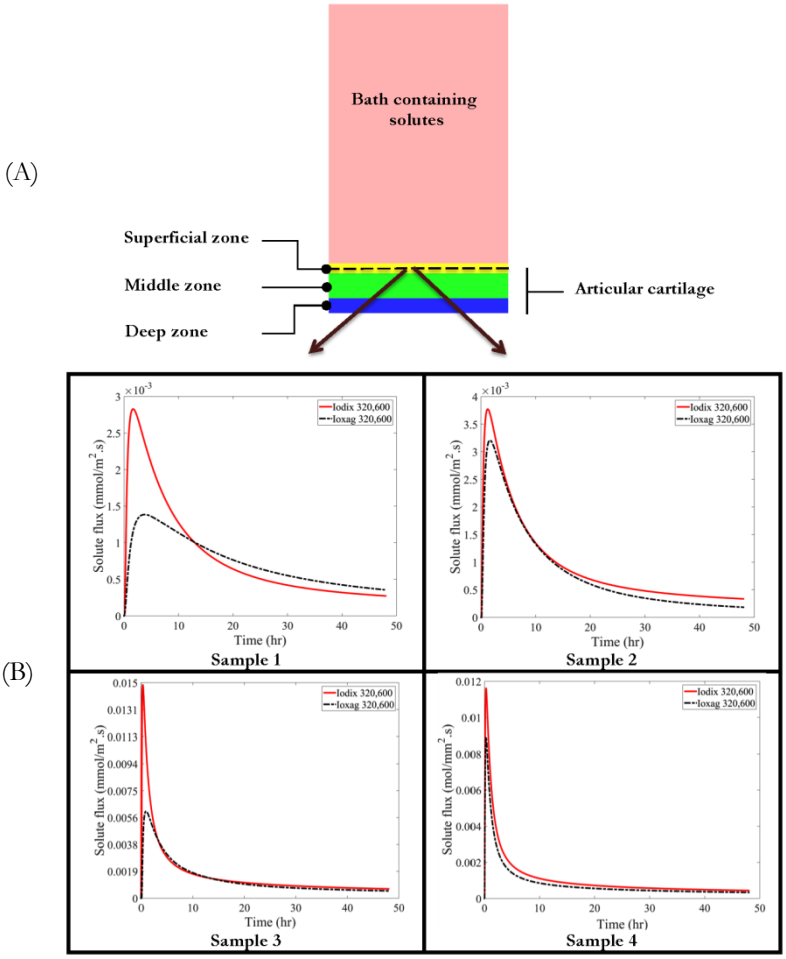

Figure 3.6. (A) Computational model representing bath containing either iodixanol or ioxaglate and articular cartilage comprising of superficial, middle and deep zones. (B) Plot of solute flux vs. time in the middle of superficial zone for both Iodixanol (*Iodix 320,600*) and Ioxaglate (*Ioxag 320,600*) for samples 1-4 to investigate the effect of charge on solute transport.

3.4. DISCUSSION

Multiple factors contribute simultaneously to the diffusion of solutes across cartilage. In this study, we strived to use a carefully designed set of experiments to separate the effects of three of those factors, namely bath concentration, bath osmolality and solute's charge, from each other. Exact Fickian diffusion should lead to exactly the same diffusion patterns for all experiments and deviation from this can be observed by comparing the various experiments. We used equilibrium and zonal diffusion curves as well as finite element models to study the effects of those factors.

3.4.1. EFFECT OF CONCENTRATION

Normalized concentration values as well as diffusion rates at early time points within cartilage were slightly higher in the bath with lower concentration (Iodix 160,290) compared to the more concentrated bath (Iodix 320,290) (Figure 3.4). Nevertheless, the final normalized values were largely similar regardless of concentration (Table 3.2A). Previous study showed insignificant effect of concentration on the diffusion mechanism using charged, i.e. anionic solutes [18].

Somewhat different behaviors in Iodix 320,290 and Iodix 160,290 are observed when the superficial, middle and deep zones are concerned (Figure 3.5A). That is associated with some mild differences between the final normalized concentration values of Iodix 320,290 and Iodix 160,290 in those zones (Table 3.2B). However, the final normalized concentration in all zones is not significantly different between Iodix 160,290 and Iodix 320,290 (Table 3.2B). It can be therefore concluded that while the main diffusion mechanism for neutral solutes is Fickian, some zonal deviations from the Fickian assumption can be pinpointed. The final normalized concentration values for the superficial zone were observed to be higher compared to middle and deep zones for both Iodix 320,290 and Iodix 160,290 that refers to highly inhomogeneous nature of the articular cartilage. The major reason that leads to enhancement of diffusion rate in the superficial zone might be the sparse

distribution of GAGs, high water content, and fine collagen fibers [1, 14, 29, 30]. A previous study, however, showed that collagen does not considerably affect the transport of small solutes because collagen fibrils are widely spaced in comparison to proteoglycans [31]. Relevant research also addressed the importance of various cartilage zones when determining the diffusion coefficient of cartilage. Indeed, up to 100 times higher diffusion coefficients were found in the superficial zone as compared to the deep cartilage zone [9, 24, 32]. The effects of concentration can also be viewed from the standpoint of more facilitated transport in low concentrated solutions due to lower mass transfer resistance in the cartilage-bath interface [33]. Furthermore, lower concentration might lead to lower solution viscosity that in turn enhances the transport rate within the bath and also in the cartilage-bath interface [34]. This underscores the fact that the solute diffusivity within the bath may need to be considered as a separate parameter to improve on the accuracy of previously conducted research [14, 16-18].

3.4.2. **EFFECT OF OSMOLALITY**

Equilibrium curves showed a subtle difference between Iodix 320,290 and Iodix 320,600 indicating that the effect of osmolality on the transport of neutral solutes is insignificant (Figure 3.4, Table 3.2A) and the diffusion therefore can be considered Fickian. The zonal differences between Iodix 320,290 and Iodix 320,600 were present but generally small (Figure 3.5 and Table 3.2B). Since we used a hyper-osmolal bath, cartilage shrank 8±2.55 % of its total thickness in the early time points due to water loss. Thereafter, cartilage recovered to its original thickness, since increased ionic concentration in cartilage after initial water loss caused reversal of the water exodus. This could lead to a more compact structure of the ECM giving rise to increased solute-ECM friction and therefore hindered diffusion. However, water exodus stopped after a few hours and water gain started to maintain the equilibrium between the cartilage and the bath. This counteracts the previous hindrance phenomenon and can potentially nullify the reduced diffusion rate within the ECM. In spite of little effect of osmolality on diffusion of small molecules

observed in this study, larger tissue deformation and its consequent local re-orientation of collagen fibrils as well as alterations of proteoglycans concentration is anticipated to change the cartilage diffusive attributes [1].

3.4.3. **EFFECT OF CHARGE**

Negatively charged fixed macromolecules, i.e. keratin sulfate and chondroitin sulfate, are the major components that give cartilage its excellent physical and mechanical features [35]. These highly charged molecules interact with the diffusing charged solutes, thereby introducing an additional mechanism that, together with steric hindrance, cause the diffusion process to deviate from the Fickian model. The last aim of this work was to study the effects of solute charge on the diffusion of solutes across articular cartilage. Equilibrium curves for Iodix 320,600 showed considerably higher diffusion rate as well as higher final normalized concentration values as compared to Ioxag 320,600 (Figure 3.4, Table 3.2A). Zonal diffusion curves also confirm the trends seen in the equilibrium curves (Figure 3.5A, Table 3.2B). Ioxaglate, as a negatively charged contrast agent, had the highest final normalized concentration in the superficial zone as compared to two other zones chiefly due to higher water content, less concentrated GAGs, and less interaction with the ECM in the superficial zone. Moreover, the concentration versus cartilage depth at equilibrium for ioxaglate lied below that of iodixanol (Figure 3.5B) underscoring the effect of repulsion between two negatively charged molecules (PGs and ioxaglate) on the diffusion. The effect of proteoglycans on the diffusion of solutes even neutral ones rather than collagen has been confirmed due to their compact structure [36]. It is worth mentioning that the negatively charged ioxaglate solute has considerably slower diffusion rate and lower final normalized concentration, as compared to the neutral iodixanol solute (Figure 3.6 and Table 3.2). The two contrast agents used in this study had very similar molecular weights i.e. hydrodynamic radii and therefore it allowed studying the effect of charge while neglecting the effect of solute size on diffusion across cartilage.

Based on the prescribed experimental boundary conditions solute diffusion occurred primarily along the vertical axis of the cylindrical specimens and therefore the radial component of diffusion equations has been neglected in our models. Lower ioxaglate flux peak compared to that of iodixanol (Figure 3.6) indicates the restrictive effect of electric interactions between the negatively charged solute (ioxaglate) and negative fixed charges of articular cartilage. Furthermore, samples 3 and 4, which demonstrated lower GAG content compared to samples 1 and 2 (higher ioxaglate equilibrium penetration) showed higher maximum solute flux (Figure 3.4 and Figure 3.6). The findings of this study highlight the importance of electrical charge and show that the effects of electrical charge by far exceed those of other factors considered in the current study including solute concentration and external bath osmolality.

3.4.4. LIMITATIONS

This study introduces a few limitations associated with the experiments. Since the aim of this study was to investigate the isolated effects of physical parameters on the diffusive transport in articular cartilage, four samples were randomly extracted from two different same-age equine femoral condyles, which enables drawing general conclusion regardless of the donor's joint. The sample size could be increased to enhance the power of the study; nevertheless, the aim was to create an experimental setup by which conclusions could be made while comparing conditions within each individual sample without further need to increase sample size. The time frame of the experiments was chosen to be 48 hours to ensure reaching the equilibrium state although this might slightly affect the GAG concentration within the tissue. To support that, our previous experiments using DMMB assay of the bath confirmed minimal GAG loss. The study of the effects of ionic strength and concentration of charged solutes in the bath on the diffusion process are proposed for the future studies. In this study, we used osteochondral plugs to ensure minimal damage to the cartilage constituents particularly collagen fibrils and proteoglycans. This allowed maintaining physiologic diffusion condition as faithfully as possible. In our computational model, we used a no-flux boundary

condition at the cartilage-bone interface, which stayed valid within the timeframe of the experiments.

3.5. CONCLUSIONS

We investigated the isolated effects of solute concentration, external bath osmolality, and solute charge on the diffusion of solutes across articular cartilage. The main novelties of the study are in using the experiments that separate the effects of different factors from each other to the maximum possible extent and using zonal diffusion curves and computational models to study the diffusion behavior of the various cartilage zone, namely superficial, middle, and deep zones. It was observed that the concentration and external bath osmolality do not significantly change the diffusion behavior of cartilage as a whole and the various cartilage zones. The diffusion mechanism of neutral solutes was therefore found to be Fickian in general with some zonal deviations from the Fickian model, thereby justifying the use of terms such as near-Fickian for describing the diffusion mechanism of neutral solutes across cartilage. Comparing the solute fluxes and the diffusion behavior of solutes with similar sizes but different charges (neutral versus negatively charged) showed that the maximum solute fluxes are significantly smaller for negatively charged solutes, indicating the profound effect of electrical charge on the diffusion behavior. The effects of electrical charge on the diffusion behavior were the same regardless of the cartilage zone under consideration.

3.6. ACKNOWLEDGMENT

This work was supported by a grant from Dutch Arthritis Foundation (13-3-406).

3.7. **REFERENCES**

1. Leddy, H.A. and F. Guilak, *Site-Specific Molecular Diffusion in Articular Cartilage Measured using Fluorescence Recovery after Photobleaching.* Annals of Biomedical Engineering, 2003. **31**(7): p. 753-760.
2. Decker, Sarah G.A., et al., *Adsorption and Distribution of Fluorescent Solutes near the Articular Surface of Mechanically Injured Cartilage.* Biophysical Journal, 2013. **105**(10): p. 2427-2436.
3. Ohara, B.P., J.P.G. Urban, and A. Maroudas, *Influence of Cyclic Loading on the Nutrition of Articular-Cartilage.* Annals of the Rheumatic Diseases, 1990. **49**(7): p. 536-539.
4. Evans, R.C. and T.M. Quinn, *Dynamic compression augments interstitial transport of a glucose-like solute in articular cartilage.* Biophys J, 2006. **91**(4): p. 1541-7.
5. Jackson, A. and W. Gu, *Transport Properties of Cartilaginous Tissues.* Curr Rheumatol Rev, 2009. **5**(1): p. 40.
6. Allhands, R.V., P.A. Torzilli, and F.A. Kallfelz, *Measurement of diffusion of uncharged molecules in articular cartilage.* Cornell Vet, 1984. **74**(2): p. 111-23.
7. Sophia Fox, A.J., A. Bedi, and S.A. Rodeo, *The Basic Science of Articular Cartilage: Structure, Composition, and Function.* Sports Health, 2009. **1**(6): p. 461-468.
8. Arkill, K.P. and C.P. Winlove, *Solute transport in the deep and calcified zones of articular cartilage.* Osteoarthritis Cartilage, 2008. **16**(6): p. 708-14.
9. Arbabi, V., et al., *Transport of Neutral Solute Across Articular Cartilage: The Role of Zonal Diffusivities.* Journal of Biomechanical Engineering, 2015. **137**(7): p. 071001-071001.
10. Kock, L., C. van Donkelaar, and K. Ito, *Tissue engineering of functional articular cartilage: the current status.* Cell and Tissue Research, 2012. **347**(3): p. 613-627.
11. Leddy, H.A., H.A. Awad, and F. Guilak, *Molecular diffusion in tissue-engineered cartilage constructs: effects of scaffold material, time, and culture conditions.* J Biomed Mater Res B Appl Biomater, 2004. **70**(2): p. 397-406.
12. Bansal, P.N., et al., *Cationic contrast agents improve quantification of glycosaminoglycan (GAG) content by contrast enhanced CT imaging of cartilage.* Journal of Orthopaedic Research, 2011. **29**(5): p. 704-709.
13. Stewart, R.C., et al., *Contrast-enhanced CT with a high-affinity cationic contrast agent for imaging ex vivo bovine, intact ex vivo rabbit, and in vivo rabbit cartilage.* Radiology, 2013. **266**(1): p. 141-50.
14. Kokkonen, H.T., et al., *Computed tomography detects changes in contrast agent diffusion after collagen cross-linking typical to natural aging of articular cartilage.* Osteoarthritis and Cartilage, 2011. **19**(10): p. 1190-1198.
15. Abazari, A., et al., *Transport phenomena in articular cartilage cryopreservation as predicted by the modified triphasic model and the effect of natural inhomogeneities.* Biophys J, 2012. **102**(6): p. 1284-93.

16. Kokkonen, H.T., et al., *Detection of mechanical injury of articular cartilage using contrast enhanced computed tomography.* Osteoarthritis Cartilage, 2011. **19**(3): p. 295-301.
17. Kulmala, K.A.M., et al., *Diffusion coefficients of articular cartilage for different CT and MRI contrast agents.* Medical Engineering & Physics, 2010. **32**(8): p. 878-882.
18. Tuomo S. Silvast, J.S.J., Virpi Tiitu, Thomas M. Quinn and Juha Töyräs, *Bath Concentration of Anionic Contrast Agents Does Not Affect Their Diffusion and Distribution in Articular cartilage In Vitro.* Cartilage, 2013. **4**(1): p. 42-51.
19. Arbabi, V., et al., *Multiphasic modeling of charged solute transport across articular cartilage: Application of multi-zone finite-bath model.* J Biomech, 2016. **49**(9): p. 1510-7.
20. Entezari, V., et al., *Effect of mechanical convection on the partitioning of an anionic iodinated contrast agent in intact patellar cartilage.* J Orthop Res, 2014. **32**(10): p. 1333-40.
21. van Tiel, J., et al., *CT arthrography of the human knee to measure cartilage quality with low radiation dose.* Osteoarthritis Cartilage, 2012. **20**(7): p. 678-85.
22. Klein, S., et al., *elastix: a toolbox for intensity-based medical image registration.* IEEE Trans Med Imaging, 2010. **29**(1): p. 196-205.
23. Bron, E.E., et al., *Image registration improves human knee cartilage T1 mapping with delayed gadolinium-enhanced MRI of cartilage (dGEMRIC).* Eur Radiol, 2013. **23**(1): p. 246-52.
24. Huttunen, J.M.J., et al., *Estimation of fixed charge density and diffusivity profiles in cartilage using contrast enhanced computer tomography.* International Journal for Numerical Methods in Engineering, 2014. **98**(5): p. 371-390.
25. Pouran, B., et al., *Zone-dependent diffusion of contrast agent molecules in healthy articular cartilage.* Osteoarthritis and Cartilage, 2014. **22**: p. S105-S106.
26. Pouran, B., et al., *Contrast Agent's Transport Across Healthy Articular Cartilage Under Various Bath Conditions.* ORS 2015 Annual Meeting, Las Vegas, Nevada, 2015.
27. Arbabi, V., B. Pouran, H. Weinans and A. A. Zadpoor, *Multiphasic modeling of charged solute transport across articular cartilage: application of finite-bath model.* Journal of Biomechanics (under review), 2015.
28. Ateshian, G.A., S. Maas, and J.A. Weiss, *Multiphasic Finite Element Framework for Modeling Hydrated Mixtures With Multiple Neutral and Charged Solutes.* Journal of Biomechanical Engineering, 2013. **135**(11): p. 111001-111001.
29. Han, J. and J. Herzfeld, *Macromolecular diffusion in crowded solutions.* Biophys J, 1993. **65**(3): p. 1155-61.
30. Pluen, A., et al., *Diffusion of Macromolecules in Agarose Gels: Comparison of Linear and Globular Configurations.* Biophysical Journal, 1999. **77**(1): p. 542-552.
31. Maroudas, A., *Biophysical chemistry of cartilaginous tissues with special reference to solute and fluid transport.* Biorheology, 1975. **12**(3-4): p. 233-48.

32. Pan, J., et al., *In situ measurement of transport between subchondral bone and articular cartilage.* J Orthop Res, 2009. **27**(10): p. 1347-52.
33. Maroudas A, B.P., Swanson SA, Freeman MA, *The permeability of articular cartilage.* J Bone Joint Surg [Br], 1968. **50**: p. 166–177.
34. Pyun, C.W. and M. Fixman, *Frictional Coefficient of Polymer Molecules in Solution.* Journal of Chemical Physics, 1964. **41**(4): p. 937-&.
35. Mow, V.C., et al., *Effects of fixed charges on the stress–relaxation behavior of hydrated soft tissues in a confined compression problem.* International Journal of Solids and Structures, 1998. **35**(34–35): p. 4945-4962.
36. Leddy, H.A. and F. Guilak, *Site-specific effects of compression on macromolecular diffusion in articular cartilage.* Biophys J, 2008. **95**(10): p. 4890-5.

CHAPTER 4

TRANSPORT OF NEUTRAL SOLUTE ACROSS ARTICULAR CARTILAGE: THE ROLE OF ZONAL DIFFUSIVITIES

This chapter is published as a scientific paper:

Arbabi V., **Pouran B**., Weinans H., Zadpoor A.A. *Transport of Neutral Solute Across Articular Cartilage: The Role of Zonal Diffusivities*. Journal of Biomechanical Engineering, 2015. 137(7): p. 071001-071001.

Chapter 4

ABSTRACT

Transport of solutes through diffusion is an important metabolic mechanism for the avascular cartilage tissue. Three types of inter-connected physical phenomena, namely mechanical, electrical, and chemical, are all involved in the physics of transport in cartilage. In this study, we use a carefully designed experimental-computational setup to separate the effects of mechanical and chemical factors from those of electrical charges. Axial diffusion of a neutral solute (iodixanol) into cartilage was monitored using calibrated micro-CT images for up to 48 hours. A biphasic-solute computational model was fitted to the experimental data to determine the diffusion coefficients of cartilage. Cartilage was modeled either using one single diffusion coefficient (single-zone model) or using three diffusion coefficients corresponding to superficial, middle, and deep cartilage zones (multi-zone model). It was observed that the single-zone model cannot capture the entire concentration-time curve and under-predicts the near-equilibrium concentration values, whereas the multi-zone model could very well match the experimental data. The diffusion coefficient of the superficial zone was found to be at least one order of magnitude larger than that of the middle zone. Since neutral solutes were used, GAG content cannot be the primary reason behind such large differences between the diffusion coefficients of the different cartilage zones. It is therefore concluded that other features of the different cartilage zones such as water content and the organization (orientation) of collagen fibers may be enough to cause large differences in diffusion coefficients through the cartilage thickness.

Chapter 4

4.1. INTRODUCTION

Articular cartilage is a multiphasic, porous, and avascular tissue that primarily relies on diffusion for transport of crucial signaling molecules, oxygen, and nutrients that help maintain its proper metabolic function [1-5]. Osteoarthritis is recognized as a debilitating disease that mainly affects articular cartilage and subchondral bone, and is characterized by abnormal loss of glycosaminoglycans (GAGs) molecules, subsequent collagen damage, and increased subchondral bone remodeling [6-11]. Reduced GAG concentration and disrupted collagen fibers can directly affect the interactions between the solutes and the cartilage's matrix. Solute-matrix interaction plays an integral role in the diffusion of various molecules ranging from therapeutics and fragments of GAGs and collagen II to the contrast agents [12, 13]. Effective early diagnosis of cartilage degeneration most importantly using computed tomography (CT) and magnetic resonance imaging (MRI) therefore requires in-depth knowledge of solute diffusion and partitioning within articular cartilage [11, 14-17]. That is why several previous studies have used imaging modalities such as CT, MRI, and fluorescent-based diagnostic techniques to study the diffusion of contrast agents and fluorescent labeled molecules across articular cartilage and to obtain the diffusion coefficient of articular cartilage, e.g. [1, 3, 18-22].

The above-mentioned studies contributed towards better understanding of diffusion across articular cartilage. However, there are certain limitations associated with their methodology. In particular, large baths of contrast agent are often used in diffusion experiments to I) facilitate the use of analytical relationships or computational models that have been developed for infinite bath conditions and II) simultaneously perform diffusion experiments for several specimens [6, 7, 23, 24]. This type of experimental setup introduces certain inaccuracies in the measurements. Most importantly, large baths of concentrated solutions of contrast agents could cause substantial beam hardening artifacts in CT measurements as a result of preferential absorption of low-energy photons [25, 26]. Moreover, excessive amount of solutions has to be used to establish a successful diffusion setup. Finally, testing multiple

specimens at the same time requires the use of a larger field of view in CT scanners [7], thereby reducing the maximum achievable resolution [27, 28].

As previously mentioned, the infinite bath assumption was applied to keep a relatively easy mathematical operation [24]. However, the use of those simplified analytical or computational models may be associated with some limitations of their own. Firstly, these models often overlook the effects of limited solute diffusivity within the bath itself [6, 7, 24, 27-29]. Those effects are particularly important for non-stirred viscous baths, because a thin layer forms at the interface of bath and cartilage that has high solute concentration values and results in additional transport resistance that is not captured by simple analytical and computational models. Ultimately, in the vast majority of previous studies, only one diffusion coefficient is used for the entire cartilage [6, 7, 22, 24, 28, 29]. That assumption neglects the potentially large differences between the diffusion coefficients of the superficial, middle, and deep cartilage zones [1, 30], in particular since the collagen orientation and likely the preferred diffusion direction as well, varies considerably in the different zones.

This research aims to study the transport of neutral solutes across articular cartilage using a combination of an experimental setup and a computational model that represents the involved physics as faithfully as possible. Regarding the experimental setup, finite baths were used to minimize beam hardening. Different concentrations of contrast agent and osmolality of the solution were used to study the effects of those on diffusion. On the computational front, we used a finite-bath biphasic-solute computational model that properly captures the transport of neutral solutes across articular cartilage in the experimental setup. In addition, the computational model takes the diffusion of solute in the bath into account. We then determine the diffusion coefficient of cartilage by directly fitting the computational model to experimental readings. The diffusion of solute is studied both using single-zone and multi-zone computational models to see how zonal difference in diffusion coefficient could influence the transport of neutral solutes across articular cartilage.

4.2. METHODOLOGY
4.2.1. EXPERIMENTS
4.2.1.1. BATH AND SAMPLE PREPARATION

Visipaque solutions that contained iodixanol solutes (1550.191 g/mol, charge=0) were prepared in different concentrations and osmolalities (Table 4.1).

Table 4.1. Experimental conditions (A-C) for diffusion from a finite bath of iodixanol with different concentrations and osmolalities.

Condition	Concentration [mM]	Osmolality [mOsm/kg H_2O]
A	420	290
B	420	600
C	210	290

Solution A was directly taken from the original vial of Visipaque (GE Healthcare, The Netherlands) resulting in an osmolality of 290 mOsm/kg H2O and a concentration of 420 mM (Table 4.1). In order to assess the effect of bath osmolality on the transport of iodixanol, we elevated the osmolality of solution A using NaCl to make condition B (600 mOsm/kg H2O and 420 mM) (Table 4.1). Finally, condition C was prepared by two-fold dilution of solution A, while maintaining the final osmolality the same as in condition A (Table 4.1). A freezing point osmometer (Advanced® Model 3320 Micro-Osmometer, The Netherlands) was used to measure osmolalities.

Osteochondral plugs (n=3, cartilage thickness= 2.8 mm, and diameter= 8.5 mm) were drilled out of two fresh equine femora using custom-made drill tips. During drilling, phosphate buffer serum (PBS) was constantly sprayed on the site of sample extraction to prevent thermal damage to the cartilage. The samples were kept in PBS solution enriched with protease inhibitor and ethylenediaminetetraacetic acid (EDTA) at -20 ^{o}C before proceeding to

diffusion experiments. Upon thawing, samples were wrapped laterally using impermeable shrinking tube (CTFC Series, pro-POWER, UK) to prevent leakage and to ensure axial diffusion through the cartilage surface. During our pilot studies, we measured the grey values of the shrinking tube and found no evidence of the diffusion of iodixanol into the material. Moreover, the osteochondral plugs were placed firmly on a plastic support. A schematic drawing of the sample is presented in Figure 4.1.

4.2.1.2. **IMAGE ACQUISITION**

We used a micro-CT scanner (Quantum FX, Perkin Elmer, USA) to measure the transport of iodixanol across cartilage. The samples were placed on a holder during scans to minimize possible movement artifacts. The fluid baths contained 650 μL (equal to 14 mm bath height) of solutions A, B & C and were positioned on top of the cartilage specimens. Images were acquired before adding the solution and up to 48 hours after adding the solution (17 times points). The scanning parameters were: 180 μA tube current, 90 kV tube voltage, 2 min scan time, 40×40×40 μm^3 voxel size and 3600 projections. After completion of each experiment, the diffused molecules within each sample were fully washed out using serial desorption baths (PBS+ protease inhibitor + EDTA at 4 ^{o}C, 48 hours) before performing diffusion experiments using the next solution.

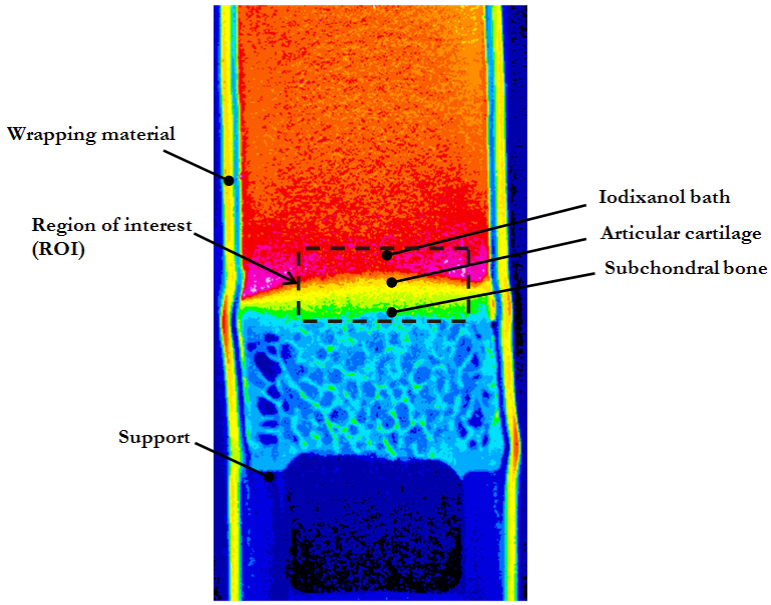

Figure 4.1. The specimen used in the diffusion experiments.

4.2.1.3. IMAGE PROCESSING

The 3D reconstructed images were converted to 2D slices (TIFF format) using in-built software of the micro-CT machine (Analyze 11.0). We used a Gaussian filter to enhance the signal to noise ratio. Thereafter, we used ImageJ 1.47v to select the mid sagittal slice of each stack and assigned a rectangular region of interest (ROI) that contained the cartilage, the subchondral bone, and a small part of the bath (Figure 4.1). The images within the prescribed ROI were then thresholded globally for each experimental time point to isolate cartilage from subchondral bone and the contrast agent solution. The outline of the cartilage mask at different time points (Figure 4.2) was then laid over the original cartilage image to calculate the average grey value.

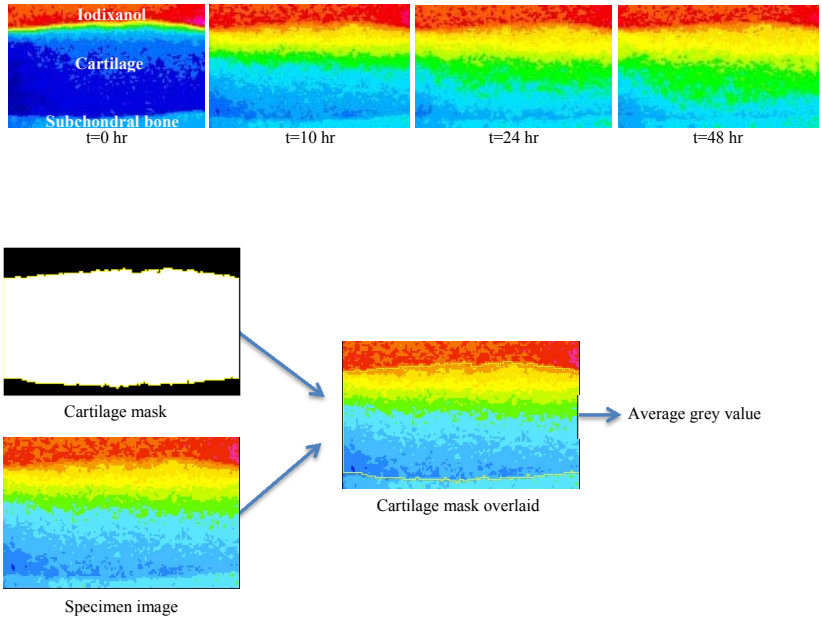

Figure 4.2. The sequence of images for one sample specimen and the different image processing steps used for calculating the average gray values.

No diffusion at t and known concentration of the contrast agent solution at t were then used to establish a linear relationship that could convert the average grey values to iodixanol concentration. The average grey values were calculated using ImageJ 1.47v based on the following equation:

$$\text{Average gray value} = \frac{\sum P_i X_i}{\sum X_i} \tag{4.1}$$

where P_i and X_i are pixel intensity and pixel frequency, respectively.

4.2.2. COMPUTATIONAL MODEL

Biphasic-solute mixture models are capable of capturing the diffusion of neutral solutes across cartilage [31]. Three governing equations need to be solved for such mixture models including the conservation of linear momentum for the mixture, conservation of mass for the mixture, and the

conservation of mass for the solute [31-33]. Conservation of linear momentum for the mixture can be expressed as:

$$\mathrm{div}\,\mathbf{T}=0 \tag{4.2}$$

where $\mathbf{T}$ is the Cauchy stress for the mixture. Conservation of mass for the mixture is given as:

$$\mathrm{div}\,(\mathbf{v}^s + \mathbf{w}) = 0 \tag{4.3}$$

where $\mathbf{v}^s$ is the solid matrix velocity and $\mathbf{w}$ is the volume flux of solvent relative to the solid. Finally, the overall amount of solute in the bath and tissue remains constant:

$$\frac{1}{J}\frac{D^s}{Dt}(J\varphi^w\tilde{\kappa}\tilde{c}) + \mathrm{div}\mathbf{j} = 0 \tag{4.4}$$

where $J = \det \boldsymbol{F}$, $\boldsymbol{F}$ is the deformation gradient of the solid matrix, $D^s(\cdot)/Dt$ is the material time derivative in the spatial frame, and $\mathbf{j}$ is the molar flux of solute relative to the solid. In Equation (4.4), φ^w is volume fraction of the solvent, $\tilde{\kappa}$ is the effective solubility, and c is the solute concentration. Since effective solute concentration $\tilde{c} = c/\tilde{\kappa}$ is continuous across boundaries and contact surfaces, it has been used in the computational model instead of c [32, 34, 35]. The volume flux of solvent relative to the solid, $\mathbf{w}$, and the relative molar solute flux, $\mathbf{j}$, are given as [32, 36, 37]:

$$\mathbf{w} = \mathbf{-k}.\mathrm{grad}p \tag{4.5}$$

$$\mathbf{j} = \tilde{\kappa}\mathbf{d}.\left(-\varphi^w \mathrm{grad}\tilde{c} + \frac{\tilde{c}}{d_0}\mathbf{w}\right) \tag{4.6}$$

where

$$\tilde{\mathbf{k}} = \left[\mathbf{k}^{-1} + \frac{R\theta}{\varphi^w} \frac{\tilde{\kappa}\tilde{c}}{d_0} \left(\mathbf{I} - \frac{\mathbf{d}}{d_0} \right) \right]^{-1} \tag{4.7}$$

with

$$\varphi^w = 1 - \frac{\varphi_r^s}{J} \tag{4.8}$$

where p is the fluid pressure, $\tilde{\mathbf{k}}$ is the hydraulic permeability tensor for the flow of the solution, i.e., solvent plus solute through the solid matrix, $\mathbf{k}$ is the hydraulic permeability tensor for the flow of pure solvent, through the solid matrix, $\mathbf{d}$ is the solute diffusivity tensor in the mixture, d_0 is the solute diffusivity in absence of the solid phase, R is the universal gas constant, θ is the absolute temperature, and φ_r^s is the volume fraction of the solid phase in the reference configuration [32, 36, 37].

The virtual work principle was used to solve the conservation equations according to the previous studies [33, 38]. The dedicated open-source finite element modeling platform FEBio 2.0.1 was used for solving the governing equations of the biphasic-solute model.

4.2.2.1. GEOMETRY

The diffusion of solutes was assumed to happen primarily in the axial direction [6, 7]. The computational model consisted of cartilage and an overlaying bath. Two types of computational models were used to analyze the diffusion of neutral solutes across cartilage, namely single-zone and multi-zone models. In the single zone approach, we considered the cartilage specimen as a single phase with spatially homogenized properties in the axial direction (Figure 4.3A) including one single diffusion coefficient. A mesh was generated using an 8-node trilinear hexahedral element, which was more refined close to

the cartilage-bath interface to ensure high computational accuracy (Figure 4.3A).

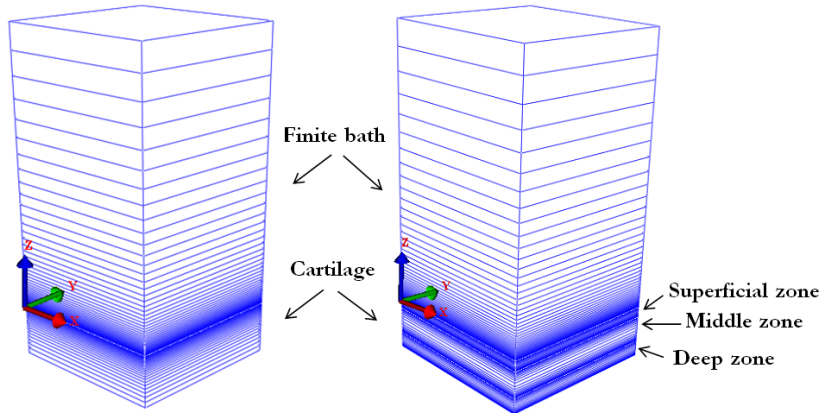

Figure 4.3. Schematic drawings of the single-zone (A) and multi-zone (B) for computational models.

In the multi-zone approach, cartilage was assumed to be composed of three zones with three different sets of properties including three different diffusivities. The multi-zone approach may better capture the inhomogeneous structure of cartilage caused by uneven distribution of glycoaminoglycans (GAGs) and different density and orientation of collagen (type II) fibers. This results in location-dependency of mechanical and physical properties of cartilage. The first zone considered in the model was the superficial zone that formed 20% of the cartilage thickness, while the second and third zones were the middle and deep zones respectively representing 50% and 30% of the cartilage thickness [39]. In this approach, the mesh is refined also at the boundary of the different zones (Figure 4.3B).

4.2.2.2. MECHANICAL AND PHYSICAL PROPERTIES OF CARTILAGE AND BATH

Similar to previous studies [32, 33], cartilage was modeled as a neo-Hookean material with a Young's modulus (E) of 10 MPa and a Poisson's ratio (ν) of 0. The hydraulic permeability of the cartilage to the solvent ($\mathbf{k}$) and the effective solubility ($\tilde{\kappa}$) were set to 10^{-3} mm^4/Ns and 1, respectively [33, 36]. The diffusivity tensor was considered isotropic. The iodixanol diffusivity within the bath was set according to a previous study [40]. In the cases where the well-stirred condition in the bath was to be simulated, the solute diffusivity in the bath was set much higher than the diffusivity of the solute in cartilage. The cartilage water content was assumed to be 0.8 in the single-zone approach [32, 33].

In the multi-zone approach, we introduced three different values of water content for each cartilage zone: 0.8 for the superficial zone, 0.7 for the middle zone, and 0.6 for the deep zone [1, 14, 39].

4.2.2.3. INITIAL AND BOUNDARY CONDITIONS

Solute concentration in the bath (c) was prescribed as an initial condition for the bath. The concentrations presented in Table 4.1 were used to simulate the diffusion of the solutes under conditions A, B, and C. Continuity of effective pressure ($p_{effective}$) across boundaries is ensured [32, 33] through:

$$p_{effective} = p - R\theta\Phi c \tag{4.9}$$

where $R = 8.314\times10^{-6}$ mJ/nmol·K and Φ is the osmotic coefficient that was assumed to be 1 for all simulations. The ambient fluid pressure and absolute temperature were considered $p = 101$ kPa and $\theta = 298$ K, respectively.

A prescribed displacement equal to 0.001 mm was applied to maintain a stable contact between the finite bath and cartilage [33]. All faces except for

the cartilage-bath interface (Figure 4A-B) were assigned the no-flux boundary condition.

4.2.2.4. **FITTING METHOD**

In the single-zone approach, the diffusivity value in cartilage was determined by minimizing the difference between the computationally predicted curve and experimental data points based on the root mean squared error (RMSE) value of their difference. A similar approach was used in the multi-zone approach to determine the diffusion coefficients of the superficial $D_{Superficial}$, middle D_{Middle}, and deep D_{Deep} zones. Direct scanning of the parameter space was used for minimizing the RMSE values. This approach ensures all possible solutions are found within the tolerance of the scanning resolution.

4.2.3. **ANALYTICAL MODEL**

To verify the computational model for a finite bath, we used an analytical model. The analytical solution for axial diffusion from a well-stirred finite bath to cartilage can be obtained by solving the Fick's 2nd law using the Laplace transformation [41]:

$$\frac{C(z,t)}{C_\infty} = \left\{ 1 + \sum_{n=1}^{\infty} \frac{2(1+\alpha)\exp(-\gamma^2 t)}{(1+\alpha+\alpha^2 q_n^2)} \frac{\cos(\frac{q_n z}{l})}{\cos q_n} \right\} \tag{4.10}$$

where $\gamma = \frac{\sqrt{D} q_n}{l}$ and $q_n s$ are the none-zero roots of $\tan(q_n) = -\alpha q_n$ with $\alpha = \frac{a}{l}.D$ is the solute diffusivity across cartilage, $C(z,t)$ is the solute concentration profile within the cartilage as a function of time (t) and spatial dimension (z), C_∞ is the equilibrium solute concentrations in the cartilage and a and l are the length of the solution and length of the cartilage specimen, respectively.

Assuming a final solute uptake equal to 30% within cartilage, we calculated the bath height as 2.33 mm with a given cartilage thickness of 1 mm using the following mass conservation equation (k =1) [41]:

$$\frac{aC_\infty}{k} + lC_\infty = aC_0 \tag{4.11}$$

where k is the partition coefficient equal to the ratio of the equilibrium solute concentration in cartilage and in the bath and C_0 is the initial solute concentration in the bath, respectively [41]. We set the operating conditions and mechanical properties of cartilage according to a previous study by Ateshian et. al [33]. The cartilage is modeled as a neo-Hookean material with E =10 MPa, ν=0 and fluid volume fraction of 0.8. The other parameters were assumed to be: k=10^{-3} mm^4/Ns, C =1 mM, θ =298 K, p =0 kPa, θ =1, $\tilde{\kappa} = 1$ and D = 5×10^{-4} mm^2/s. Equation (4.10) was used to validate the results of the computational model in different locations across cartilage, i.e. z=-0.15, -0.29, -0.5, and -0.94 mm for the well-stirred condition. We also simulated the same diffusion process in FEBio and plotted the solute concentration vs. $\eta = \frac{\sqrt{Dt}}{l}$

4.3. **RESULTS**

4.3.1. **VERIFICATION OF THE COMPUTATIONAL MODEL**

To assess the robustness of the computational model for predicting diffusion from a well-stirred finite bath, we plotted the ratio of normalized concentration ($\frac{C}{C_\infty}$) at several locations versus time (Figure 4.4). The computational results perfectly matched the analytical solution for all considered cases (Figure 4.4). The concentration rate decreased by both time lapse and distance from the surface of the cartilage specimen (Figure 4.4). The larger the distance from the cartilage surface, the more time was required for equilibrium (Figure 4.4). All layers of cartilage could finally reach the equilibrium concentration (C_∞) (Figure 4.4). Moreover, the finite element

model could predict the transient solute diffusion for a well-stirred finite bath model for all η values (Figure 4.4).

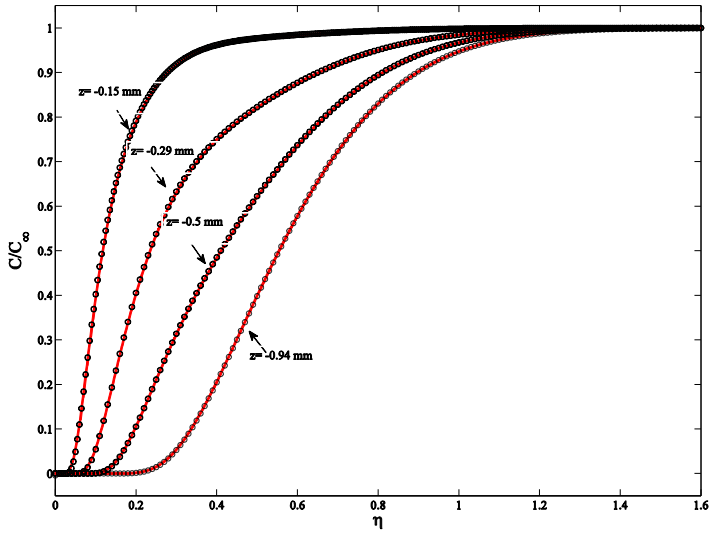

Figure 4.4. Analytical (symbols) and finite element model (solid lines) solutions for finite well-stirred bath: normalized concentration ($\frac{C}{C_\infty}$) is plotted versus $\eta = \frac{\sqrt{Dt}}{l}$ for different locations within cartilage.

4.3.2. EXPERIMENTS

For all conditions (A-C), the highest diffusion rate was observed for the early-time points (Figure 4.5). The near equilibrium state could be observed 24 hours after the start of the experiments (Figure 4.5). The normalized near-equilibrium iodixanol concentrations (%initial bath concentration) were 27.8±4.6% (mean ± SD) for condition A, 28.8±8.8% for condition B, and 30.9±7.1% for condition C.

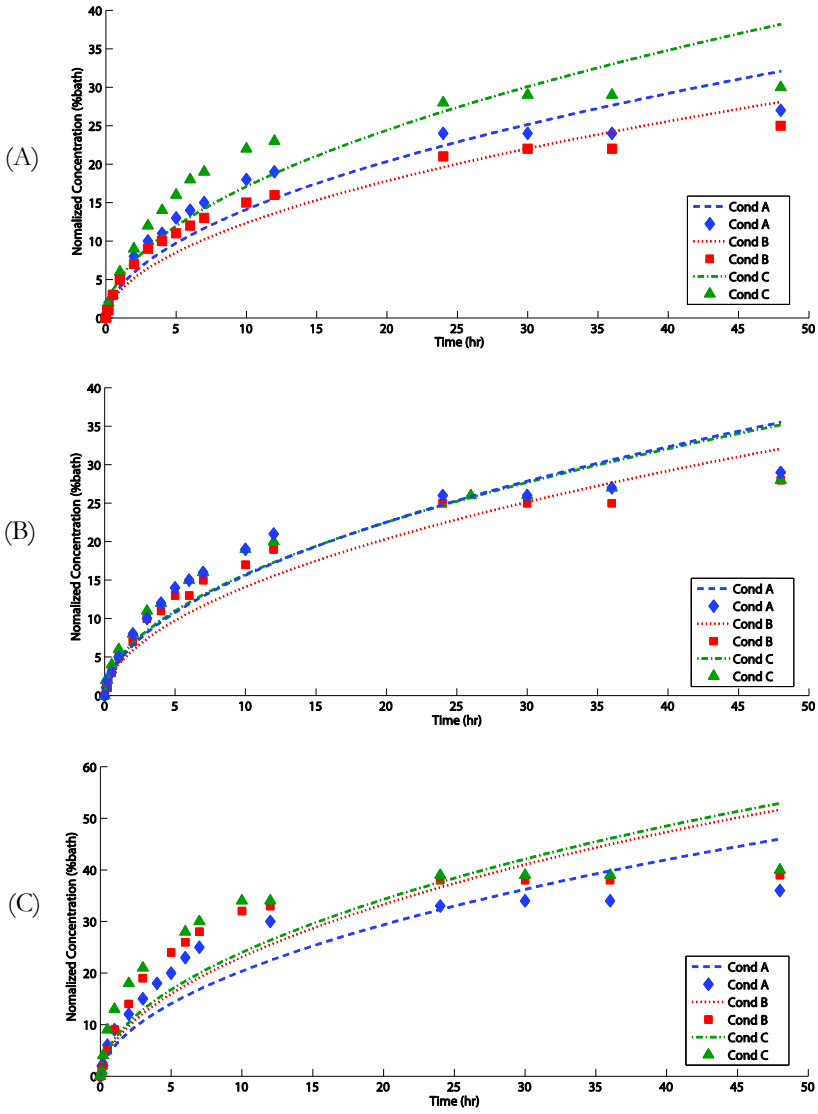

Figure 4.5. Experimental (symbols) and simulated (dashed-lines) concentration vs. time for conditions A-C and samples 1(A) to 3 (C). Computational models (single-zone) were fitted to all experimental data points.

4.3.3. COMPUTATIONAL MODEL

4.3.3.1. SINGLE-ZONE MODEL

When the single-zone model was fitted to all experimental data points of the concentration-time curves, the coefficient of determination (R2) was ranging between 0.85 and 0.96 for conditions A-C (Table 4.2). Moreover, the computational model did not follow the experimental data points and substantially over-predicted the near-equilibrium concentration values for all conditions (A-C) (Figure 4.5). Once the single-zone computational model was only fitted to the early-time points, the coefficient of determination increased to values ranging between 0.97 and 1.00 (Table 4.2) for conditions A-C, indicating that the computational model could very well capture the early-time diffusion behavior of cartilage (Figure 4.6). As expected, when the computational model was fitted only to early-time diffusion data, there was a poor agreement between the near-equilibrium concentration values predicted by the model and the measured concentrations (Figure 4.6).

Table 4.2. RMSE and R^2 to compare the experimental and simulation solute concentration vs. time for the single-zone computational model.

	Condition	A		B		C	
	Fitting data	Total	Early-time	Total	Early-time	Total	Early-time
Sample 1	R^2	0.94	1	0.96	0.99	0.91	0.99
	RMSE	0.0266	0.0040	0.0201	0.0056	0.0355	0.0082
Sample 2	R^2	0.95	0.99	0.95	0.99	0.94	1
	RMSE	0.0286	0.0052	0.0234	0.0054	0.0259	0.0046
Sample 3	R^2	0.88	0.99	0.86	0.99	0.85	0.97
	RMSE	0.0518	0.0085	0.0634	0.0144	0.0710	0.0232

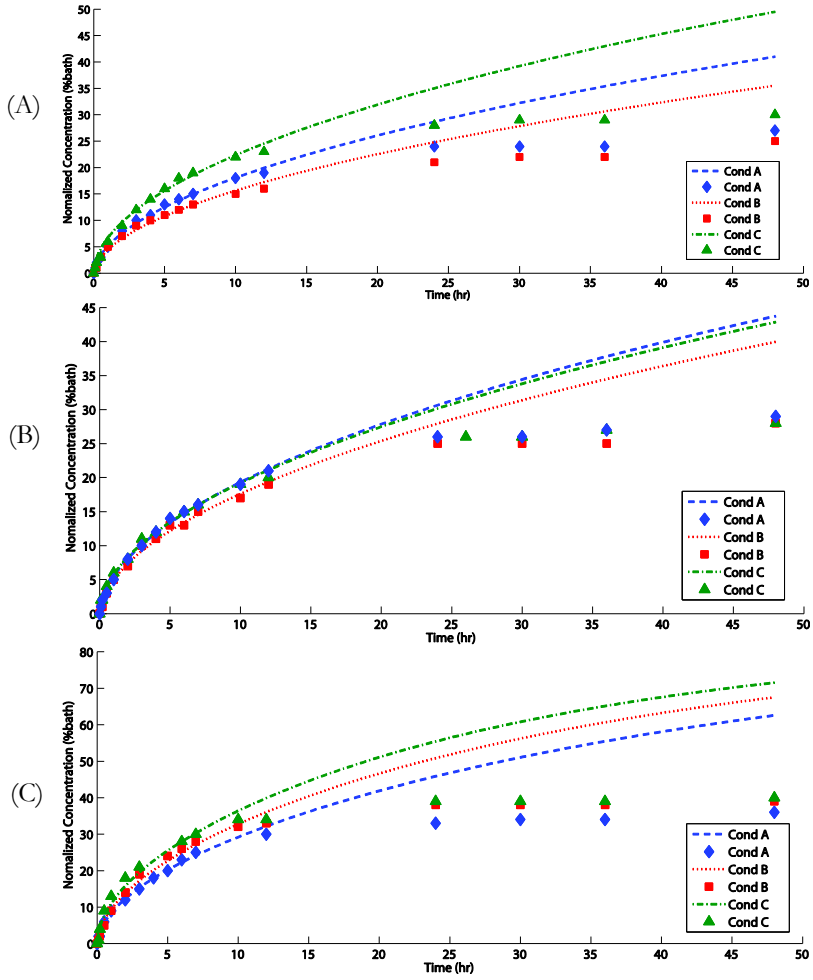

Figure 4.6. Experimental (symbols) and simulated (dashed-lines) concentration vs. time for conditions A-C and samples 1(A) to 3 (C). Computational models (single-zone) were fitted only to early-time experimental data points.

In all conditions and for all specimens, the diffusion coefficients determined using the early-time diffusion data were larger than the ones determined using all data points (Table 4.3). The diffusivities determined for sample 3 were larger than those of both other samples (Table 4.3).

Table 4.3. Diffusion coefficients obtained from the single-zone computational model based on fitting of the model to both early-time data points and all data points.

	Fitting data	Condition A	Condition B	Condition C
Sample 1	Total	4	3	6
	Early-time	6.9	5	11
Sample 2	Total	5	4	5
	Early-time	8	6.5	7.8
Sample 3	Total	9	12	13
	Early-time	20.8	27.5	36

4.3.3.2 **MULTI-ZONE MODEL**

The multi-zone computational model could very well capture the diffusion behavior of neutral solutes in articular cartilage both for the early and late time points (Figure 4.7). The coefficients of determination were between 0.99 and 1.00 for samples 1 and 2 (Table 4.4) regardless of condition (A-C). The coefficients of determination were slightly lower for sample 3, i.e. between 0.94 and 0.97 (Table 4.4). For this last sample, the multi-zone model could not fully capture the concentration curve. In agreement with the above-mentioned coefficients of determination, the computational model could follow the experimental data points very well and could predict not only the early-time concentration values but also the near-equilibrium concentration values particularly for samples 1 and 2 (Figure 4.7).

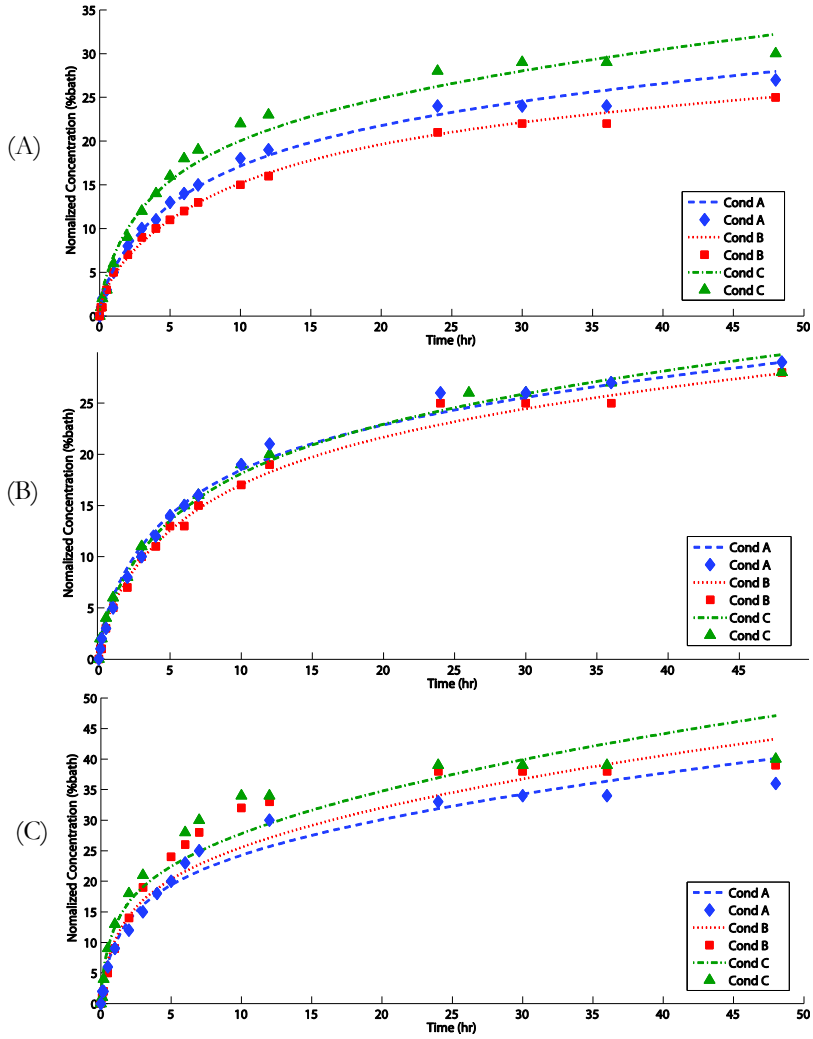

Figure 4.7. Experimental (symbols) and simulated (dashed-lines) concentration vs. time for conditions A-C and samples 1(A) to 3 (C). Computational models (multi-zone) were fitted to all experimental data points.

Table 4.4. RMSE and R^2 to compare the experimental and simulation solute concentration vs. time for the multi-zone computational model.

	Condition	A	B	C
Sample 1	R^2	0.99	1	0.99
	RMSE	0.0068	0.0044	0.0122
Sample 2	R^2	1	0.99	0.99
	RMSE	0.0058	0.0074	0.0079
Sample 3	R^2	0.97	0.95	0.94
	RMSE	0.0207	0.0348	0.0349

A parametric study indicated that the diffusivities of the superficial and middle zones played key roles in contrast to that of the deep zone, which had minimal impact on the predicted diffusion behavior of cartilage. Therefore, only the diffusivities of the superficial and middle zones are reported (Table 4.5). Similar to the single-zone model, the diffusion coefficients determined for sample 3 were larger than those of samples 1 and 2 (Table 4.5). However, the ratio of the diffusion coefficient of the superficial zone to that of the middle zone ($D_{Superficial}/D_{Middle}$) was consistent between all samples and for all conditions (Table 4.6): 14.53±1.88 for condition A, 14.23±3.1 for condition B, and 13.25±1.64 for condition C.

Table 4.5. Diffusion coefficients obtained from the multi-zone computational model based on fitting of the model to all experimental data points.

	Diffusion coefficient ($\mu m^2/s$)								
	Condition A			Condition B			Condition C		
	$D_{Superficial}$	D_{Middle}	D_{Deep}	$D_{Superficial}$	D_{Middle}	D_{Deep}	$D_{Superficial}$	D_{Middle}	D_{Deep}
Sample 1	7.5	0.55	*Insensitive**	5.5	0.3	*Insensitive*	13	1	*Insensitive*
Sample 2	10	0.6	*Insensitive*	7.3	0.55	*Insensitive*	8.8	0.74	*Insensitive*
Sample 3	30	2.25	*Insensitive*	35	3	*Insensitive*	60	4	*Insensitive*

*The average concentration values were not sensitive enough to the diffusion coefficient of the deep cartilage zone to enable us determine the diffusion coefficient of the deep cartilage zone.

Table 4.6. The ratio of diffusion coefficient of superficial zone to middle zone ($D_{Superficial}/D_{Middle}$).

Condition	A	B	C
Diffusion coefficient ratio	$D_{Superficial}/D_{Middle}$	$D_{Superficial}/D_{Middle}$	$D_{Superficial}/D_{Middle}$
Sample 1	13.6	17.7	13
Sample 2	16.7	13.3	11.7
Sample 3	13.3	11.7	15

4.4. **DISCUSSION**

Due to the importance of diffusion for nutrition and oxygenation of cells in the avascular cartilage tissue, transport of solutes in cartilage has been studied in several previous studies. There are three main categories of inter-connected physical phenomena, namely mechanical, chemical, and electrical that occur simultaneously and complicate understanding the diffusion of solutes across cartilage. Those physical complexities particularly the role of fixed electrical charges and mechanical stresses/strain were not respected in many previous studies where purely Fickean diffusion models were used to describe the transport of charged particles across cartilage. In this study, we used neutral solutes to separate the effects of electrical charges from those of mechanics, i.e. stresses and deformations, and concentration gradients as much as possible. To make sure the role of both mechanical forces and concentration gradients are taken into account, a biphasic-solute model was used to describe the transport of neutral solutes across articular cartilage. Moreover, the effects of variation in the diffusion coefficients of the various cartilage zones, i.e. superficial, middle, and deep zones, on the transport of neutral solutes were studied using both single-zone and multi-zone

computational models. The fact that the presented computational model perfectly matches the analytical solution in the case of finite well-stirred bath (one of the closest cases for which an analytical solution is available) increases our confidence in the accuracy of the presented computational model.

4.4.1. EFFECTS OF CARTILAGE ZONES ON DIFFUSION

Perhaps the most important conclusion of the current study is that a single diffusion coefficient is not sufficient to describe the transport of solutes across articular cartilage. The biphasic-solute model is incapable of following the experimental concentration-time curve when the entire cartilage is considered to be one tissue with one single diffusion coefficient. It is well known that the different cartilage layers are different both in terms of GAG content and the arrangement of collagen fibers. The use of neutral solutes means that electrical charges are not playing a major role in this observation, suggesting that variation in the organization of collagen fibers may be sufficient to cause large variations in the diffusion coefficients of the different cartilage zones.

One needs to note that only the averaged concentration values were used in the current study to describe the diffusion of neutral solutes. Two diffusion coefficients may be sufficient to describe these averaged concentration values because the concentration values of the deep cartilage zone do not significantly influence the average concentration value that is calculated for the entire cartilage. The concentration values of the deep cartilage zone are expected to play more important roles when the spatial distribution of concentration is taken into account. However, two diffusion coefficients may not be enough for capturing the spatial variation of solute concentration values through the cartilage thickness. We therefore need detailed experimental data regarding the spatial distribution of concentration values throughout cartilage in order to be able to determine the diffusion coefficient of the deep cartilage zone.

Throughout the course of diffusion experiments under large osmolality differences, cartilage is likely to experience large thickness variations due to

swelling/shrinkage. This causes serious complexities when trying to determine the concentration values through the cartilage thickness. Major improvements in experimental and image processing techniques are therefore needed before one could determine the number of zones required for accurately capturing the spatial distribution of concentration values through the cartilage thickness. The mechanical property gradient across the cartilage's zones due to altered collagen fiber orientation, concentration and thickness as well as water content might also play a role in the diffusion. However, we observed only a negligible shift in the diffusion curves when the hydraulic permeability and Poisson's ratio were varied within the expected range of the cartilage mechanical properties. Young's modulus was chosen so that it was always significantly greater than the effective pressure generated within the cartilage to prevent large deformations, which was in accordance with the experimental observations. On the contrary, water content gradient presents a strong effect on the diffusion behavior. The near-equilibrium condition was reached after 24 hr in experiments. However, even after 48 hr the concentration curve still had the tendency to slightly rise. As for computational results, the single-zone model highly overestimated the increase of the concentration after 24 hr. It is much less so for the multi-zone computational model. The concentration curves obtained by both multi-zone computational model and experiments show slight increase after 24 hr. For the first two samples, the level of the increase in the concentration curves is similar in the multi-zone computational model and experiments. For sample 3, however, there is increased discrepancy between the concentration curve of the multi-zone computational model and the experimentally determined concentration curve.

4.4.2. **DIFFUSION COEFFICIENTS**

The diffusion coefficients are comparable in conditions A-C, despite large differences in the concentration values. This shows the Fickian nature of diffusion in the case of neutral solutes: there is a more or less linear relationship between the concentration gradient and diffusion flux.

As for the different zones, the diffusion coefficient of the middle zone is at least one order of magnitude lower than that of the superficial zone. This is consistently observed within the three samples used in the current study and implies that the structure of the superficial zone is specialized for facilitating the diffusion of solutes into cartilage. As previously mentioned, this observation may not be primarily attributed to the fixed charge density of the superficial zone (i.e. its GAG content), as the solutes used in the current study are not electrically charged. The arrangement of collagen fibers including their orientation, density, and the steric hindrance may, however, play important roles in this regard. Since nutrition and oxygenation of cells inside cartilage should occur through diffusion and given that the superficial zone is responsible for most of that diffusion, it is natural to expect the superficial zone to be specialized in facilitating the process of solute transport across cartilage.

Interestingly, the diffusion coefficients calculated for sample 3 are much higher than those of both other samples. A relatively wide range of diffusion coefficients is therefore observed in the current study. This is consistent with the previous studies that report wide ranges of diffusion coefficients [30, 42]. Despite these relatively large differences in the absolute values of the diffusion coefficients, the ratio of the diffusion coefficients of different zones is very consistent between samples, highlighting the observation that the diffusion coefficient of the superficial zone is much higher than of the middle zone regardless of the absolute values of the diffusion coefficients.

4.4.3. LIMITATIONS AND RECOMMENDATIONS FOR FUTURE RESEARCH

As mentioned several times so far, we tried to minimize the effects of fixed charge density on our study through the use of neutral solutes and a biphasic-solute computational model. It should be, however, noted that the assumed water content could significantly influence the diffusion of neutral solutes across cartilage. In this study, we used realistic water contents decreasing from 80% at the superficial zone to 60% for the deep layer [1, 14,

39]. This assumption helps us obtain realistic results in terms of diffusion, but also indirectly introduces the effects of fixed charge density (i.e. GAG content). That is because water content is, among other factors, a function of the fixed charge density [12]. It is therefore not possible to entirely exclude the indirect effects of GAG content on diffusion, even in this carefully designed set of experiments and computational models.

Similar to many recent studies [6, 7, 24], only through-the-thickness (i.e. axial) diffusion of contrast agent was considered in the current study. The diffusion tensor is, however, known to be anisotropic [13] and this could cause specific patterns of radial diffusion that cannot be captured using axial models. The specific patterns of radial diffusion are, however, outside the scope of the current study.

Finally, the biphasic-solute model presented here could be replaced by a multi-phasic model to study the diffusion of charged molecules into cartilage. The experiments need to be performed using both neutral and charged molecules to enable separation of the effects of electrical charges from those of other effects. These topics will be addressed in a future study.

In this study, we tried to take advantage of a clinically used radiopaque molecule, i.e. iodixanol, to facilitating the use of CT technology for monitoring the diffusion process. In reality, wide ranges of molecules with significantly different sizes are transported in and out of cartilage through diffusion. Some of the molecules important for cartilage metabolism such as collagen fragments generated during enzymatic activity and some therapeutics are small enough to be comparable to our solute [43, 44]. But many other relevant molecules are much larger than iodixanol. Since the size of relevant molecules could be very different and given that diffusion coefficients change with molecule size, no single molecule could represent the entire range of all relevant molecules. However, this study shows the difference between the diffusion coefficients of the different zones within cartilage. Even though the absolute diffusivity values might be different for different molecules, the main conclusion of the current

study, i.e. significantly different diffusion coefficients through the cartilage thickness, is expected to hold regardless of the molecule size.

4.5. **CONCLUSIONS**

The diffusion of neutral solutes across cartilage was studied using both experiments and computational models. It was found that one single diffusion coefficient is not sufficient to describe the diffusion of solutes across cartilage even when the solutes are uncharged and, thus, not influenced by GAG content. Computational models with three separate zones corresponding to superficial, middle, and deep cartilage zones could very well describe the diffusion of neutral solutes. The diffusion coefficient of the superficial zone was in all three tested samples at least one order of magnitude larger than that of the middle zone.

4.6. **REFERENCES**

1. Leddy H.A., Guilak F., *Site-Specific Molecular Diffusion in Articular Cartilage Measured using Fluorescence Recovery after Photobleaching.* Annals of Biomedical Engineering, 2003. **31**(7): p. 753-760.
2. Torzilli P.A., Adams T.C., Mis R.J., *Transient solute diffusion in articular cartilage.* Journal of Biomechanics, 1987. **20**(2): p. 203-214.
3. Williams R.M., Zipfel W.R., Tinsley M.L., Farnum C.E., *Solute transport in growth plate cartilage: in vitro and in vivo.* Biophys J, 2007. **93**(3): p. 1039-50.
4. Abazari A., Elliott J.A.W., McGann L.E., Thompson R.B., *MR spectroscopy measurement of the diffusion of dimethyl sulfoxide in articular cartilage and comparison to theoretical predictions.* Osteoarthritis and Cartilage, 2012. **20**(9): p. 1004-1010.
5. Abazari A., Thompson R.B., Elliott J.A., McGann L.E., *Transport phenomena in articular cartilage cryopreservation as predicted by the modified triphasic model and the effect of natural inhomogeneities.* Biophys J, 2012. **102**(6): p. 1284-93.
6. Kokkonen H.T., Mäkelä J., Kulmala K.A.M., Rieppo L., Jurvelin J.S., Tiitu V., Karjalainen H.M., Korhonen R.K., Kovanen V., Töyräs J., *Computed tomography detects changes in contrast agent diffusion after collagen cross-linking typical to natural aging of articular cartilage.* Osteoarthritis and Cartilage, 2011. **19**(10): p. 1190-1198.
7. Kulmala K.A.M., Korhonen R.K., Julkunen P., Jurvelin J.S., Quinn T.M., Kröger H., Töyräs J., *Diffusion coefficients of articular cartilage for different CT and MRI contrast agents.* Medical Engineering & Physics, 2010. **32**(8): p. 878-882.
8. Siebelt M., Groen H.C., Koelewijn S.J., de Blois E., Sandker M., Waarsing J.H., Muller C., van Osch G.J., de Jong M., Weinans H., *Increased physical activity severely induces osteoarthritic changes in knee joints with papain induced sulphate-glycosaminoglycan depleted cartilage.* Arthritis Res Ther, 2014. **16**(1): p. R32.
9. Siebelt M., van der Windt A.E., Groen H.C., Sandker M., Waarsing J.H., Müller C., de Jong M., Jahr H., Weinans H., *FK506 protects against articular cartilage collagenous extra-cellular matrix degradation.* Osteoarthritis and Cartilage, 2014. **22**(4): p. 591-600.
10. Piscaer T.M., Sandker M., van der Jagt O.P., Verhaar J.A., de Jong M., Weinans H., *Real-time assessment of bone metabolism in small animal models for osteoarthritis using multi pinhole-SPECT/CT.* Osteoarthritis Cartilage, 2013. **21**(6): p. 882-8.
11. Weinans H., Siebelt M., Agricola R., Botter S.M., Piscaer T.M., Waarsing J.H., *Pathophysiology of peri-articular bone changes in osteoarthritis.* Bone, 2012. **51**(2): p. 190-6.
12. Ko Lok S., Quinn Thomas M., *Matrix Fixed Charge Density Modulates Exudate Concentration during Cartilage Compression.* Biophysical Journal, 2013. **104**(4): p. 943-950.

13. Leddy H.A., Guilak F., *Site-Specific Effects of Compression on Macromolecular Diffusion in Articular Cartilage.* Biophysical Journal, 2008. **95**(10): p. 4890-4895.
14. Salo E.N., Nissi M.J., Kulmala K.A.M., Tiitu V., Töyräs J., Nieminen M.T., *Diffusion of Gd-DTPA2− into articular cartilage.* Osteoarthritis and Cartilage, 2012. **20**(2): p. 117-126.
15. van Tiel J., Siebelt M., Waarsing J.H., Piscaer T.M., van Straten M., Booij R., Dijkshoorn M.L., Kleinrensink G.J., Verhaar J.A., Krestin G.P., Weinans H., Oei E.H., *CT arthrography of the human knee to measure cartilage quality with low radiation dose.* Osteoarthritis Cartilage, 2012. **20**(7): p. 678-85.
16. Siebelt M., Waarsing J.H., Kops N., Piscaer T.M., Verhaar J.A., Oei E.H., Weinans H., *Quantifying osteoarthritic cartilage changes accurately using in vivo microCT arthrography in three etiologically distinct rat models.* J Orthop Res, 2011. **29**(11): p. 1788-94.
17. Siebelt M., Waarsing J.H., Groen H.C., Muller C., Koelewijn S.J., de Blois E., Verhaar J.A., de Jong M., Weinans H., *Inhibited osteoclastic bone resorption through alendronate treatment in rats reduces severe osteoarthritis progression.* Bone, 2014. **66**: p. 163-70.
18. Leddy H.A., Awad H.A., Guilak F., *Molecular diffusion in tissue-engineered cartilage constructs: effects of scaffold material, time, and culture conditions.* J Biomed Mater Res B Appl Biomater, 2004. **70**(2): p. 397-406.
19. Greene G.W., Zappone B., Zhao B., Söderman O., Topgaard D., Rata G., Israelachvili J.N., *Changes in pore morphology and fluid transport in compressed articular cartilage and the implications for joint lubrication.* Biomaterials, 2008. **29**(33): p. 4455-4462.
20. Bansal P.N., Joshi N.S., Entezari V., Grinstaff M.W., Snyder B.D., *Contrast Enhanced Computed Tomography can predict the glycosaminoglycan content and biomechanical properties of articular cartilage.* Osteoarthritis and Cartilage, 2010. **18**(2): p. 184-191.
21. Chin H.C., Moeini M., Quinn T.M., *Solute transport across the articular surface of injured cartilage.* Arch Biochem Biophys, 2013. **535**(2): p. 241-7.
22. Decker Sarah G.A., Moeini M., Chin Hooi C., Rosenzweig Derek H., Quinn Thomas M., *Adsorption and Distribution of Fluorescent Solutes near the Articular Surface of Mechanically Injured Cartilage.* Biophysical Journal, 2013. **105**(10): p. 2427-2436.
23. Huttunen J.M.J., Kokkonen H.T., Jurvelin J.S., Töyräs J., Kaipio J.P., *Estimation of fixed charge density and diffusivity profiles in cartilage using contrast enhanced computer tomography.* International Journal for Numerical Methods in Engineering, 2014. **98**(5): p. 371-390.
24. Kokkonen H.T., Jurvelin J.S., Tiitu V., Toyras J., *Detection of mechanical injury of articular cartilage using contrast enhanced computed tomography.* Osteoarthritis Cartilage, 2011. **19**(3): p. 295-301.
25. Meganck J.A., Kozloff K.M., Thornton M.M., Broski S.M., Goldstein S.A., *Beam hardening artifacts in micro-computed tomography scanning can be reduced by X-ray beam filtration and the resulting images can be used to accurately measure BMD.* Bone, 2009. **45**(6): p. 1104-16.

26. Bansal P.N., Stewart R.C., Entezari V., Snyder B.D., Grinstaff M.W., *Contrast agent electrostatic attraction rather than repulsion to glycosaminoglycans affords a greater contrast uptake ratio and improved quantitative CT imaging in cartilage.* Osteoarthritis Cartilage, 2011. **19**(8): p. 970-6.
27. Aula A.S., Jurvelin J.S., Töyräs J., *Simultaneous computed tomography of articular cartilage and subchondral bone.* Osteoarthritis and Cartilage, 2009. **17**(12): p. 1583-1588.
28. Tuomo S. Silvast J.S.J., Virpi Tiitu, Thomas M. Quinn and Juha Töyräs, *Bath Concentration of Anionic Contrast Agents Does Not Affect Their Diffusion and Distribution in Articular cartilage In Vitro.* Cartilage, 2013. **4**(1): p. 42-51.
29. Silvast T.S., Jurvelin J.S., Lammi M.J., Töyräs J., *pQCT study on diffusion and equilibrium distribution of iodinated anionic contrast agent in human articular cartilage – associations to matrix composition and integrity.* Osteoarthritis and Cartilage, 2009. **17**(1): p. 26-32.
30. Pan J., Zhou X., Li W., Novotny J.E., Doty S.B., Wang L., *In situ measurement of transport between subchondral bone and articular cartilage.* J Orthop Res, 2009. **27**(10): p. 1347-52.
31. Mauck R.L., Hung C.T., Ateshian G.A., *Modeling of Neutral Solute Transport in a Dynamically Loaded Porous Permeable Gel: Implications for Articular Cartilage Biosynthesis and Tissue Engineering.* Journal of biomechanical engineering, 2003. **125**(5): p. 602-614.
32. Ateshian G.A., Albro M.B., Maas S., Weiss J.A., *Finite element implementation of mechanochemical phenomena in neutral deformable porous media under finite deformation.* J Biomech Eng, 2011. **133**(8): p. 081005.
33. Ateshian G.A., Maas S., Weiss J.A., *Solute transport across a contact interface in deformable porous media.* Journal of Biomechanics, 2012. **45**(6): p. 1023-1027.
34. Ateshian G.A., *On the Theory of Reactive Mixtures for Modeling Biological Growth.* Biomechanics and modeling in mechanobiology, 2007. **6**(6): p. 10.1007/s10237-006-0070-x.
35. Sun D.N., Gu W.Y., Guo X.E., Lai W.M., Mow V.C., *A mixed finite element formulation of triphasic mechano-electrochemical theory for charged, hydrated biological soft tissues.* International Journal for Numerical Methods in Engineering, 1999. **45**(10): p. 1375-1402.
36. Ateshian G.A., Weiss J.A., *Finite Element Modeling of Solutes in Hydrated Deformable Biological Tissues.* 2013: p. 231-249.
37. Ateshian G.A., Maas S., Weiss J.A., *Finite element algorithm for frictionless contact of porous permeable media under finite deformation and sliding.* J Biomech Eng, 2010. **132**(6): p. 061006.
38. Bonet J., Wood, R.D., *Nonlinear Continuum Mechanics for Finite Element Analysis.* Cambridge University Press, Cambridge, NewYork, NY, 1997.
39. Sophia Fox A.J., Bedi A., Rodeo S.A., *The Basic Science of Articular Cartilage: Structure, Composition, and Function.* Sports Health, 2009. **1**(6): p. 461-468.

40. Nair N., Kim W.J., Braatz R.D., Strano M.S., *Dynamics of surfactant-suspended single-walled carbon nanotubes in a centrifugal field.* Langmuir, 2008. **24**(5): p. 1790-5.
41. Crank J., *The mathematics of diffusion.* Clarendon Press:, Oxford, Eng:, 1979.
42. Jackson A., Gu W., *Transport Properties of Cartilaginous Tissues.* Curr Rheumatol Rev, 2009. **5**(1): p. 40.
43. Schadow S., Siebert H.C., Lochnit G., Kordelle J., Rickert M., Steinmeyer J., *Collagen metabolism of human osteoarthritic articular cartilage as modulated by bovine collagen hydrolysates.* PLoS One, 2013. **8**(1): p. e53955.
44. Ameye L.G., Chee W.S., *Osteoarthritis and nutrition. From nutraceuticals to functional foods: a systematic review of the scientific evidence.* Arthritis Res Ther, 2006. **8**(4): p. R127.

CHAPTER 5

MULTIPHASIC MODELING OF CHARGED SOLUTE TRANSPORT ACROSS ARTICULAR CARTILAGE: APPLICATION OF MULTI-ZONE FINITE-BATH MODEL

This chapter is published as a scientific paper:

Arbabi V., **Pouran B.**, Weinans H., Zadpoor A.A. *Multiphasic modeling of charged solute transport across articular cartilage: application of finite-bath model.* Journal of Biomechanics, 0021-9290, 2016.

ABSTRACT

Charged and uncharged solutes penetrate through cartilage to maintain the metabolic function of chondrocytes and to possibly restore or further breakdown the cartilage tissue in different stages of osteoarthritis. In this study, the transport of charged solutes across the various zones of cartilage was quantified, taken into account the physicochemical interactions between the solute and the cartilage constituents. A multiphasic finite-bath finite element (FE) model was developed to simulate equine cartilage diffusion experiments that used a negatively charged contrast agent (ioxaglate) in combination with serial micro-computed tomography (micro-CT) to measure the diffusion. By comparing the FE model with the experimental data both the diffusion coefficient of ioxaglate and the fixed charge density (FCD) were obtained. In the multiphasic model, cartilage was divided into multiple (three) zones to help understand how diffusion coefficient and FCD vary across cartilage thickness. The direct effects of charged solute-FCD interaction on diffusion were investigated by comparing the diffusion coefficients derived from the multiphasic and biphasic-solute models. We found a relationship between the FCD obtained by the multiphasic model and ioxaglate partitioning obtained from micro-CT experiments. Using our multi-zone multiphasic model, diffusion coefficient of the superficial zone was up to ten-fold higher than that of the middle zone, while the FCD of the middle zone was up to almost two-fold higher than that of the superficial zone. In conclusion, the developed finite-bath multiphasic model provides us with a non-destructive method by which we could obtain both diffusion coefficient and FCD of different cartilage zones. The outcomes of the current work will also help understand how charge of the bath affects the diffusion of a charged molecule and also predict the diffusion behavior of a charged solute across articular cartilage.

Chapter 5

5.1. INTRODUCTION

Extracellular matrix of articular cartilage (AC) is a heterogeneous material that mainly consists of collagen fibrils, self-assembled aggrecan molecules that contain negatively charged glycosaminoglycans chains (GAGs), mobile counter-ions, and interstitial water [1, 2]. Understanding the interactions of external diffusing solutes with the cartilage matrix particularly charged solutes can help us better understand the role of GAG loss, damaged collagen (type II) fiber organization, and alterations of water content as hallmarks of osteoarthritis (OA) [3]. Two distinct mechanisms contribute to the diffusion of solutes in cartilage: I) steric hindrance imparted by GAG chains and collagen fibers and II) electrostatic interactions between FCD of GAG chains and solute's charge [1, 4]. Numerous studies have been investigating the transport of neutral and charged solutes such as drug carriers, computed tomography (CT) and magnetic resonance imaging (MRI) contrast agents across normal and osteoarthritic articular cartilage [5-13]. However, the vast majority of previous works have applied Fickean models to obtain the diffusion coefficient of cartilage. As described before [14], the use of purely Fickian models might result in inaccurate diffusion coefficients. In a recent study, we introduced a biphasic-solute finite-bath finite element model to establish a platform by which the diffusion coefficients of neutral solutes in different cartilage zones could be accurately determined (chapter 3) [14]. The finite-bath model enables us to I) minimize the effect of beam-hardening artifacts while employing micro-computed tomography technique (micro-CT) to study the diffusion of CT contrast agents [15, 16] II) minimize the required volume of bath solution III) maximize the spatial resolution of CT/MRI [17, 18], and IV) more realistically mimic the physiology of the diarthrodial joints given the fact that the volume of synovial fluid within the joints is finite.

Different methods were proposed to obtain the FCD of cartilage such as delayed gadolinium-enhanced MRI (dGEMRIC), nuclear magnetic resonance (NMR), indentation, conductivity and dimethylmethylene blue (DMMB) binding assay (destructive) [19-25], although many of them are based on the ideal Donnan theory that might cause inaccuracies when calculating FCD.

Recently, a more advanced approach using combination of dGEMRIC and Monte Carlo simulations was developed to more precisely take the electrostatic interactions into account [26]. Moreover, accurate FCD calculation using known GAG content by DMMB binding assay requires accounting for ratio of Keratin sulfate (KS) to Chondroitin sulfate (CS) in the tissue [25]. Recently, multiphasic computational models in Abaqus using subroutines have emerged to study swelling behavior of healthy and OA cartilage [27-29]. Other related work applied user-developed codes based on multiphasic models to calculate diffusion coefficient and fixed charge density across cartilage [30].

We aim to introduce a multiphasic finite element model based on finite-bath model to account for the electrostatic interaction between a charged solute and the constituents of articular cartilage particularly FCD of GAGs. We fit the computational data to the contrast-enhanced micro-CT data to obtain the FCD and diffusion coefficients simultaneously in different zones within articular cartilage. The outcome of this work enables determination of FCD and diffusion coefficients non-destructive. Our findings based on the multiphasic multi-zone model will be compared with those obtained using biphasic-solute model to thoroughly investigate the effects of solute's charge and FCD i.e. electrostatic interactions on the molecular diffusion in cartilage.

5.2. METHODOLOGY

5.2.1. EXPERIMENTS

The design of experiments was described thoroughly in our previous works [14, 31]. A brief description of the experimental steps is provided in this study. Ioxaglate solutions (1268.9 g/mol, charge=-1, 420 mM, 600 mOsm/kg H2O, GE Healthcare, The Netherlands) were prepared. Osteochondral plugs (n=3, cartilage thickness= 2.8 mm, and diameter= 8.5 mm) were extracted out of two fresh equine femora using a custom-made drill bit. The schematic of the sample comprising of cartilage, subchondral bone, cork plug, contrast agent solution, wrapping sleeve is illustrated (Figure 5.1A).

We used a micro-CT scanner (Quantum FX, Perkin Elmer, USA) to monitor the transport of ioxaglate across cartilage (ambient temperature ≈ 25 °C). The samples were placed on a holder during scans to minimize possible movement artifacts. The volume of ioxaglate bath was 650 μL (equal to 14 mm bath height) and it was injected on the articular surface of the cartilage specimens. We acquired images at 17 time points within 48 hours using the following scan parameters: 180 μA tube current, 90 kV tube voltage, 2 min scan time, 40×40×40 μm^3 voxel size, and 3600 projections.

The 3D reconstructed images were converted to 2D slices (TIFF format) using in-built software of the micro-CT machine (Analyze 11.0). We used imageJ v 1.47 to select the mid sagittal slice and create regions of interest (ROI) containing the cartilage according to the previous study (chapters 3) [14, 31]. The average grey values of cartilage at different time points were then calculated and converted to ioxaglate concentration.

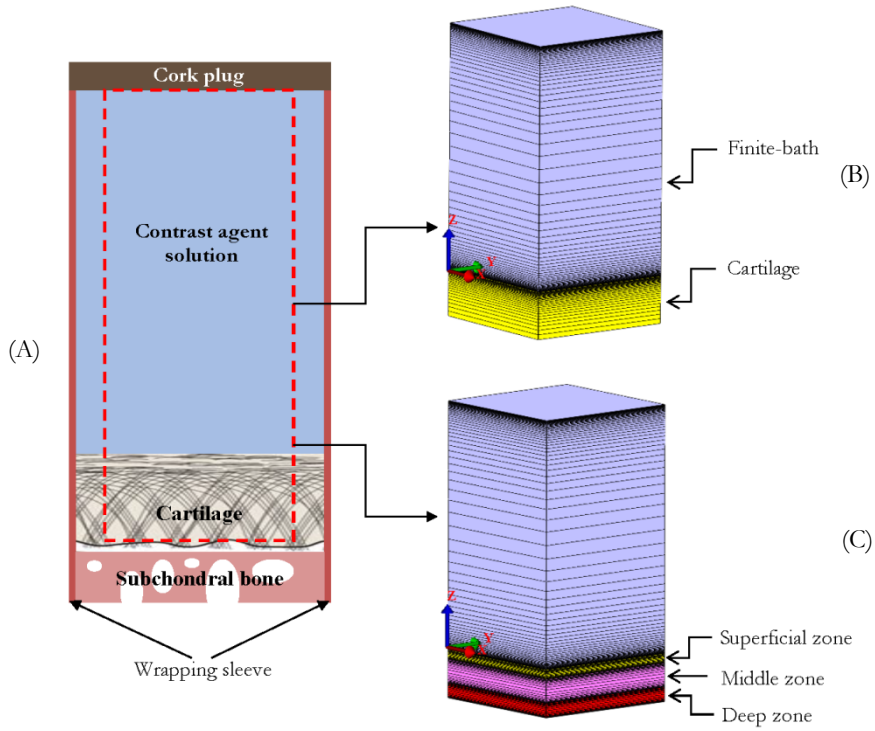

Figure 5.1. Schematic of experimental setup (A), the single-zone (B) and multi-zone models (C). Single-zone model consists of a finite-bath and a uniform cartilage and multi-zone model consists of a finite-bath and a cartilage with superficial, middle and deep zones. Mesh is finer near the interfaces.

5.2.2. COMPUTATIONAL MODEL

Diffusion of charge molecules across cartilage could be described computationally using multiphasic finite element models [32-36]. The formulas used below are adopted from the previous work of Gerard Ateshian [34].

Conservation of momentum for the mixture in the absence of external body forces and in the quasi-static condition is given as:

$$\mathrm{div}\,\mathbf{T}=0 \tag{5.1}$$

where $\mathbf{T}$ is the Cauchy stress for the mixture. Conservation of mass for the mixture and for the solute when solid volume fraction is negligible compared to the solute and solvent content can be given as:

$$\operatorname{div}(\mathbf{v}^s + \mathbf{w}) = 0 \tag{5.2}$$

$$\frac{1}{J}\frac{D^s}{Dt}(J\varphi^w \tilde{\kappa}^\alpha \tilde{c}^\alpha) + \operatorname{div}\mathbf{j}^\alpha = 0 \tag{5.3}$$

where $\mathbf{v}^s$ is the solid velocity and $\mathbf{w}$ is the volume flux of solvent relative to the solid. $J = \det \boldsymbol{F}$, $\boldsymbol{F}$ is the deformation gradient of the solid matrix, $D^s(\cdot)/Dt$ is the material time derivative in spatial frame following the solid, $\mathbf{j}^\alpha$ is the molar flux of the solute α relative to the solid and φ^w the volume fraction of the solvent. The effective solute concentration ($\tilde{c}^\alpha$) is given by:

$$\tilde{c}^\alpha = c^\alpha / \tilde{\kappa}^\alpha \tag{5.4}$$

where c^α is molar concentration of solute α and $\tilde{\kappa}^\alpha$ is the partition coefficient of solute α relative to an ideal solution:

$$\tilde{\kappa}^\alpha = \frac{\kappa^\alpha}{\gamma^\alpha}\exp(-\frac{z^\alpha F_c \psi}{R\theta}) \tag{5.5}$$

where κ^α is the solubility of solute α in the mixture, γ^α is the activity coefficient of solute α, z^α is the charge number of solute α, F_c is Faraday's constant, ψ is electric potential, R is universal gas constant and θ is absolute temperature.

The volume flux of solvent relative to the solid, $\mathbf{w}$, and the relative molar flux of solute α , $\mathbf{j}^\alpha$, are expressed as:

$$\mathbf{w} = -\tilde{\mathbf{k}}.\left(\text{grad}\tilde{p} + R\theta\sum_{\beta}\frac{\tilde{\kappa}^{\beta}}{d_0^{\beta}}\mathbf{d}^{\beta}.\text{grad}\tilde{c}^{\beta}\right) \tag{5.6}$$

$$\mathbf{j}^{\alpha} = \tilde{\kappa}^{\alpha}\mathbf{d}^{\alpha}.\left(-\varphi^{w}\text{grad}\tilde{c}^{\alpha} + \frac{\tilde{c}^{\alpha}}{d_0^{\alpha}}\mathbf{w}\right) \tag{5.7}$$

where

$$\tilde{\mathbf{k}} = \left[\mathbf{k}^{-1} + \frac{R\theta}{\varphi^{w}}\sum_{\alpha}\frac{\tilde{\kappa}^{\alpha}\tilde{c}^{\alpha}}{d_0^{\alpha}}\left(\mathbf{I} - \frac{\mathbf{d}^{\alpha}}{d_0^{\alpha}}\right)\right]^{-1} \tag{5.8}$$

where $\tilde{p}$ is the effective fluid pressure which is the mechanical contribution of the total mechanochemical pressure (p) and $R\theta\Phi\sum_{\alpha}c^{\alpha}$ is the osmotic contribution of p:

$$\tilde{p} = p - R\theta\Phi\sum_{\alpha}c^{\alpha} \tag{5.9}$$

where $\mathbf{d}^{\alpha}$ is the diffusivity tensor of solute α in the mixture (solid + fluid), d_0^{α} is the isotropic diffusivity of solute in free solution (fluid), $\tilde{\mathbf{k}}$ is the hydraulic permeability tensor of the porous solid to the interstitial fluid (solvent + solutes), $\mathbf{k}$ is the hydraulic permeability tensor of the porous solid to the interstitial solvent and Φ is the osmotic coefficient.

Electroneutrality requires the following relationship to hold:

$$\sum_{\alpha}z^{\alpha}c^{\alpha} = 0 \tag{5.10}$$

Multiplying equation 5.3 by z^{α} and using electroneutrality constraint yields:

$$\operatorname{div}\sum_{\alpha} z^{\alpha}\mathbf{j}^{\alpha} = 0 \tag{5.11}$$

In cartilage, due to presence of fixed charges of proteoglycans, fixed charge density $c^F \equiv z^s c^s$ is defined. Conservation of fixed charge in the solid matrix can be expressed as:

$$c^F = \frac{1-\varphi_r^s}{J-\varphi_r^s} c_r^F \tag{5.12}$$

where c_r^F is the fixed charge density in the reference configuration. In the presence of fixed charge density, the electroneutrality can be expressed as follows:

$$c^F + \sum_{\alpha} z^{\alpha} c^{\alpha} = 0 \tag{5.13}$$

Finite element method was used to discretize and solve the aforementioned equations simultaneously.

5.2.2.1. **GEOMETRY**

We assumed the diffusion to take place only from the cartilage surface in the axial direction (chapter 3) [14]. Similar to our previous study, we used both single-zone and multi-zone models to investigate the axial diffusion from the finite-bath through cartilage (chapter 3) [14]. Single-zone model assumes that cartilage is homogeneous across its thickness. Therefore, only one diffusion coefficient and fixed charge density can be defined (Figure 5.1B). The multi-zone model (Figure 5.1C) assumes that cartilage properties remain constant within individual zones but different in each zone. Those differences may originate from inhomogeneous distribution of glycosaminoglycans, orientation of collagen (type II) fibers, and water content. The first zone in this model represents the superficial zone (20% of cartilage thickness), while the second (50% of cartilage thickness) and third zones (30% of cartilage thickness)

represent middle and deep zones [37]. Both single- and multi-zone models used eight-node trilinear hexahedral elements for mesh generation, which was refined near the boundaries (Figure 5.1B and C).

5.2.2.2. MECHANICAL AND PHYSICAL PROPERTIES OF CARTILAGE AND BATH

We modeled the cartilage as a neo-Hookean material with a Young's modulus of 10 MPa, Poisson's ratio of 0, hydraulic permeability of 10^{-3} mm^4/Ns, and effective solute solubility of 1 (chapter 3) [14]. We examined the effect of hydraulic permeability and Poisson's ratio on the concentration-time curves and found negligible impact when they were changed within their expected ranges. The Young's modulus was chosen high enough to resist the osmotic pressure which in agreement with the experiments, large deformations could be prevented. We used a viscosity-dependent relationship to estimate the diffusion coefficient of ioxaglate in the bath considering actual diffusion coefficient of iodixanol [38]. Cartilage water content was assumed to be 0.8 throughout the cartilage thickness in the single-zone model [14, 31, 39, 40]. In the multi-zone model, however, it was assumed to gradually decrease from 0.8 in the superficial zone to 0.7 in the middle zone and finally to 0.6 in the deep zone [37, 41, 42]. We considered a wide range of possible FCD (0-350 mEq/l) across cartilage [11, 43, 44].

5.2.2.3. INITIAL AND BOUNDARY CONDITIONS

The following steps were prescribed to define FCD, initial, and boundary conditions:

Step 1, Steady-state: we used the same effective fluid pressures and concentrations inside and outside cartilage while rising FCD to the desired value. This allowed equilibrium free swelling of the cartilage and bath.

Step 2, Transient: to set the concentration in the bath, we linearly increased the solute concentrations and effective fluid pressures at the bath boundaries to the desired level. The diffusion coefficient of the solute in the

bath was chosen to be high enough to maintain the bath well-stirred to enable assigning a single concentration throughout the bath. Time at which the solute was added and diffusion coefficient of the solute in the bath were considered as two factors with which we minimized solute diffusion in the cartilage. This would help to converge the problem.

Step 3, Transient: we removed the prescribed solute concentrations and effective fluid pressures at the bath boundary and reverted the diffusion coefficient of the solute in the bath to its actual value.

There is one more level of complexity that needs to be addressed: In the step 3, once we remove all the boundary conditions for the solute concentrations, there will no longer be any electrical grounding of the mixture. This means that the electric potential can float and the analysis will either converge very slowly or fail to converge. To resolve this problem, we needed to add two other monovalent counter-ions to the bath and tissue. Since the concentration of monovalent counter-ions does not interfere with the diffusion of other solutes, we set their concentrations to some arbitrary values (e.g. 1 mM) both as initial conditions and as boundary conditions at the bath boundary. The precise value of the monovalent concentrations does not matter as long as it does not significantly affect the osmotic pressure of the analysis. To maintain realistic deformation one needs to choose sufficiently high Young's modulus to overcome the effect of generated osmotic pressure in the bath. Ambient fluid pressure and temperature were considered $p = 101\ \mathrm{kPa}$ and $\theta = 298\ \mathrm{K}$, respectively.

5.2.2.4. FITTING METHOD

We developed a MATLAB (2013b, TU Delft, Delft, The Netherlands) code to automatically perform simulations in FEBio in wide range of FCDs and diffusion coefficients for all cartilage zones, to plot the concentration-time curves and find the minimum root mean square error (RMSE) between experimental and computational values of concentration at all time points.

5.3. RESULTS

5.3.1. EXPERIMENTS

Diffusion rate was highest in the early time points followed by a gradual decrease until the near-equilibrium ioxaglate concentration (Figure 5.2A). The near-equilibrium ioxaglate concentration for these samples was reached after 24 hours and was 23.31±4.66 % of the initial average bath concentration (Figure 5.2A).

5.3.2. COMPUTATIONAL MODEL

5.3.2.1. SINGLE-ZONE MODEL

To account for the effects of charged solute in the bath and FCD of cartilage and their interactions we have compared the results obtained by biphasic-solute (solid/fluid) and multiphasic model (solid/fluid/charge). We obtained the diffusion coefficients using both a biphasic-solute model and a multiphasic model while also calculating the FCDs in the latter case (Figure 5.2A and 5.3A).

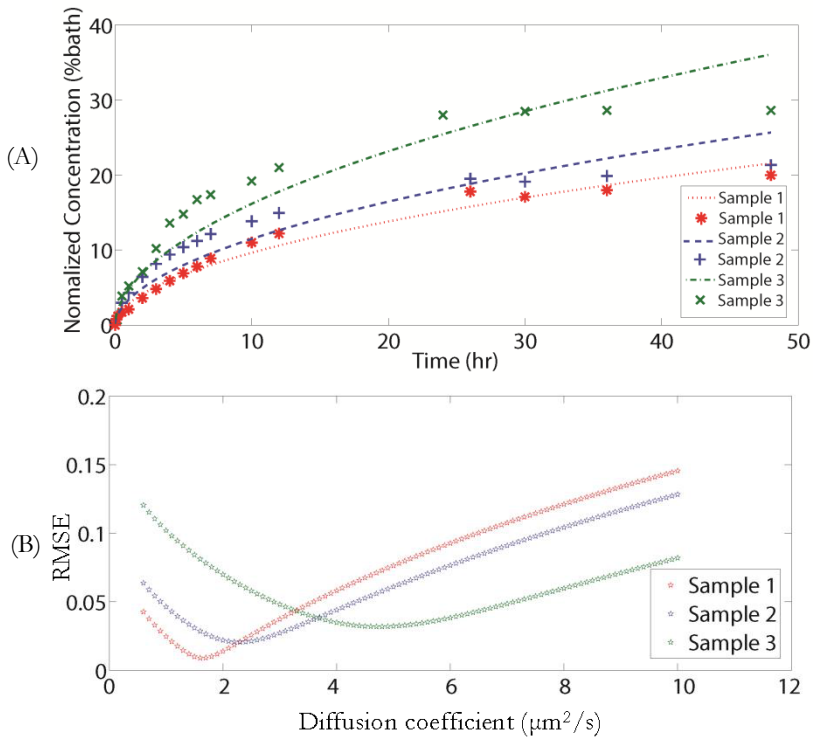

Figure 5.2. Plots of normalized ioxaglate concentration (% initial bath concentration) measured from the micro-CT data versus time (experiment: symbol, FE model: dotted line) (A) and root mean square error (RMSE) versus diffusion coefficient (B) in samples 1-3 using single-zone biphasic-solute model.

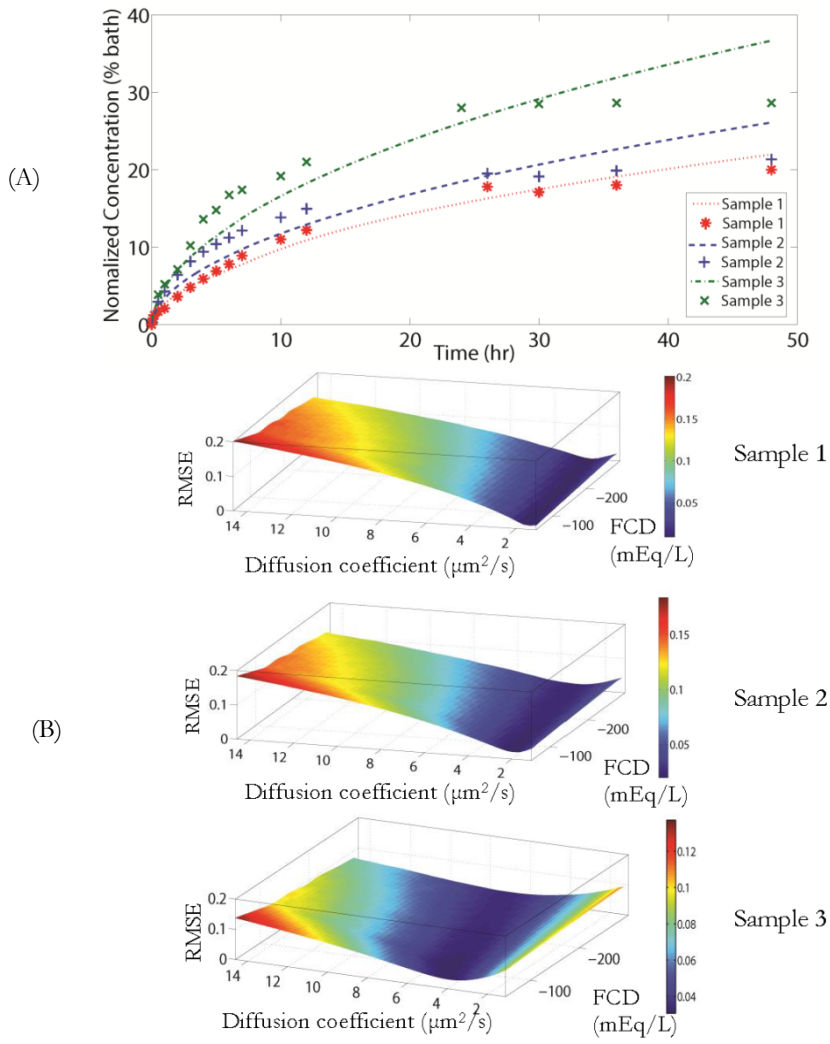

Figure 5.3. Plots of normalized ioxaglate concentration based on the initial bath concentration versus time (experiment: symbol, FE model: dotted line) (A) and root mean square error (RMSE) versus diffusion coefficient and FCD (B) in samples 1-3 using single-zone multiphasic model.

RMSE was used to ensure the models fit to the experimental data (Figure 5.2B and 5.3B). The entire solution process is provided as a flowchart (Figure 5.4). The diffusion coefficients and R^2 obtained for both biphasic-solute and multiphasic models were quite similar while the results of multiphasic model were slightly more accurate than those of biphasic-solute model (Table 5.1A).

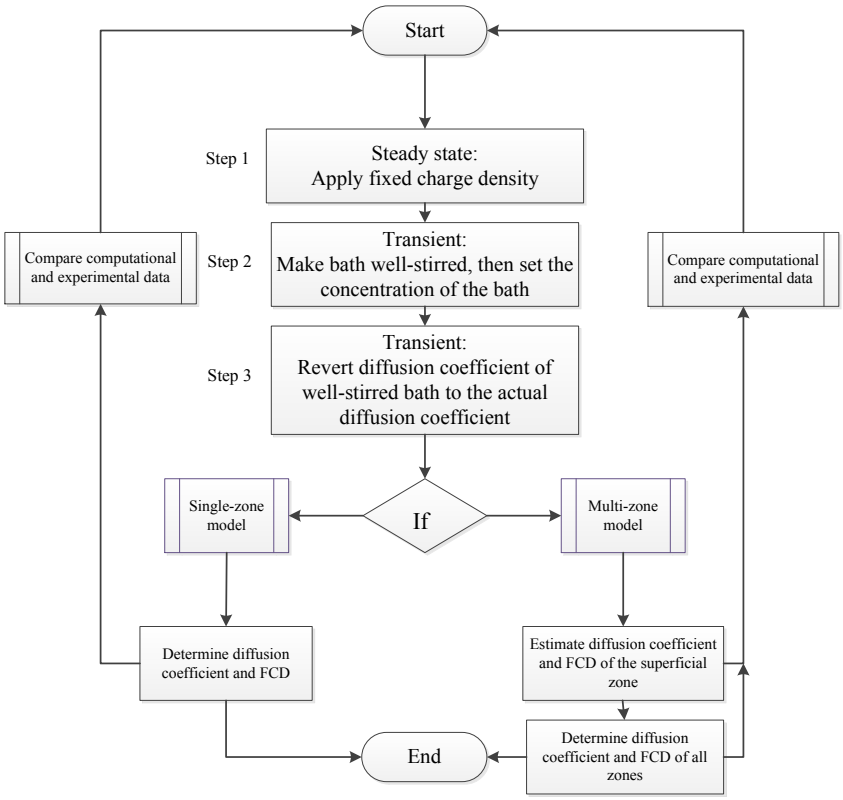

Figure 5.4. Matlab-FEBio interface to solve the multiphasic finite element model of a finite-bath.

Table 5.1. Root mean square error (RMSE) and R^2 for single-zone biphasic-solute and multiphasic models (A). Diffusion coefficients for single-zone biphasic-solute and multiphasic models and FCD for single-zone multiphasic model are presented (B).

(A)

	Fitting data	Biphasic-solute model	Multiphasic model
Sample 1	R^2	0.98	0.98
	RMSE	0.0091	0.0089
Sample 2	R^2	0.94	0.95
	RMSE	0.0207	0.0203
Sample 3	R^2	0.92	0.93
	RMSE	0.032	0.0308

(B)	Fitting data	Diffusion coefficient ($\mu m^2/s$)	Fixed charged density (mEq/L)
Sample 1	Biphasic solute model	1.6	-
	Multiphasic model	1.6	-125
Sample 2	Biphasic solute model	2.3	-
	Multiphasic model	2.1	-65
Sample 3	Biphasic solute model	4.7	-
	Multiphasic model	4.6	-80

5.3.2.2. MULTI-ZONE MODEL

The multi-zone biphasic model was capable of capturing the trends of experimental data for all samples (Figure 5.5).

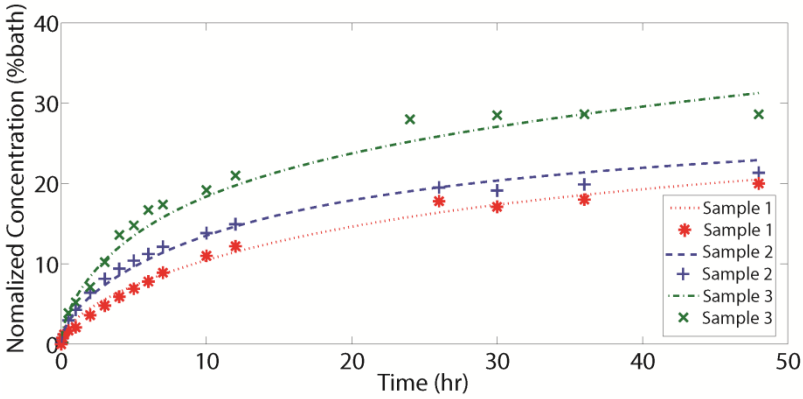

Figure 5.5. Plots of normalized ioxaglate concentration based on the initial bath concentration versus time using multi-zone biphasic-solute model (experiment: symbol, FE model: dotted line).

The optimization algorithm of the multiphasic model requires to consider several parameters i.e. diffusion coefficients and FCDs of the superficial, middle and deep zones which makes the entire process computationally expensive. Therefore, we first estimated the diffusion coefficient and FCD of the superficial zone by minimizing RMSE (Figure 5.6A). This was done in such a way that changing diffusion coefficient and FCD of the middle and deep zones did not affect the curve trend before ~3 h (Figure 5.6A). Using the estimated diffusion coefficient and FCD in the superficial zone, we continued the simulation until we reached the minimum RMSE to obtain the diffusion coefficients and FCDs for the cartilage zones (Figure 5.6B). RMSE and R2 for both biphasic-solute and multiphasic models confirmed robust results (Table 5.2A). Larger differences between the

diffusion coefficients obtained from biphasic-solute and multiphasic models were observed in the middle zone than in the superficial zone (Table 5.2B).

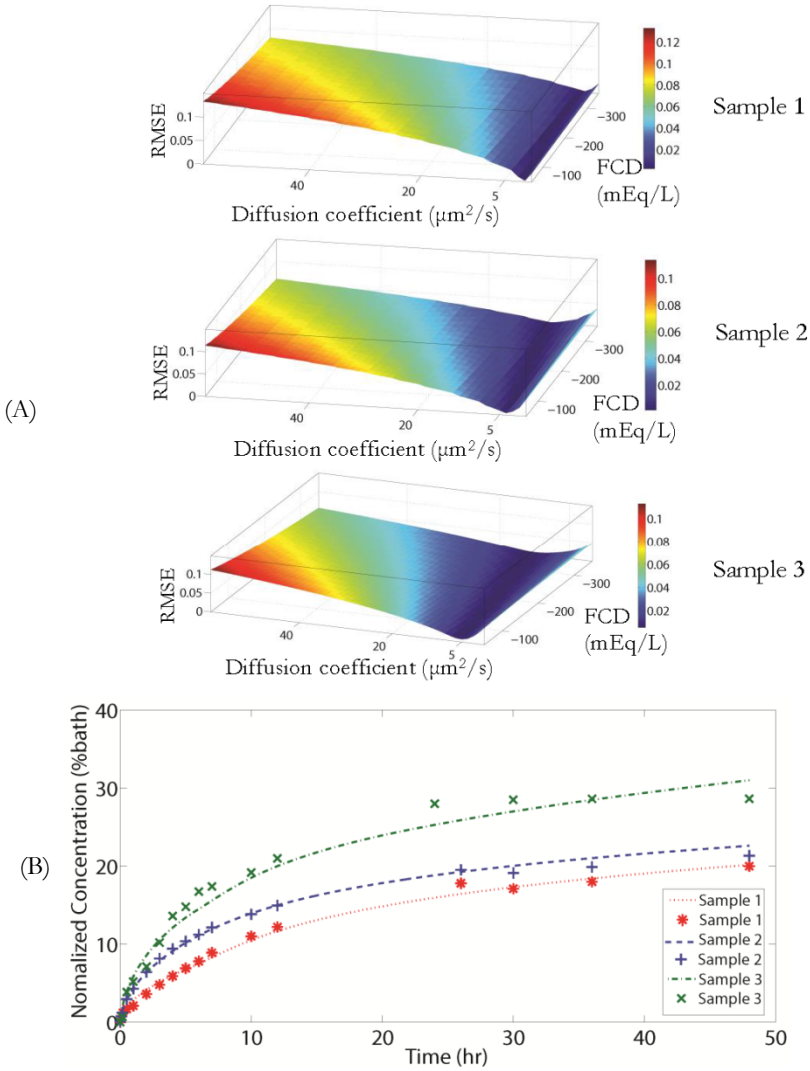

Figure 5.6. Plot of root mean square error (RMSE) against the diffusion coefficient and FCD until ~3 hrs (A) and curve-fitting using multi-zone multiphasic model (experiment: symbol, FE model: dotted line) (B).

Table 5.2. Root mean square error (RMSE) and R^2 for multi-zone biphasic-solute and multiphasic models (A). Diffusion coefficients for multi-zone biphasic-solute and multiphasic models for each zone and FCD of each zone for multi-zone multiphasic model are presented (B).

(A)

	Fitting data	Biphasic solute model	Multiphasic model
Sample 1	R^2	0.99	0.99
	RMSE	0.0064	0.0049
Sample 2	R^2	0.99	1
	RMSE	0.0079	0.0021
Sample 3	R^2	0.98	0.98
	RMSE	0.0150	0.0140

(B)

Condition		Diffusion coefficient (μm²/s)			Fixed charged density (mEq/L)		
		$D_{Superficial}$	D_{Middle}	D_{Deep}	$FCD_{Superficial}$	FCD_{Middle}	FCD_{Deep}
Sample 1	Biphasic-solute model	1.9	0.15	*Insensitive**	-	-	-
	Multiphasic model	1.75	0.22	*Insensitive*	-130	-250	*Insensitive*
Sample 2	Biphasic-solute model	3.4	0.15	*Insensitive*	-	-	-
	Multiphasic model	4.1	0.4	*Insensitive*	-115	-210	*Insensitive*
Sample 3	Biphasic-solute model	7.1	0.95	*Insensitive*	-	-	-
	Multiphasic model	7.1	1.1	*Insensitive*	-80	-160	*Insensitive*

* The average concentration values were not sensitive enough to the diffusion coefficient and fixed charged density of the deep cartilage zone to enable us determine the diffusion coefficient and fixed charged density of the deep cartilage zone.

The ratios of the diffusion coefficient in the superficial to that of the middle zone were more consistent using multiphasic model i.e. 8.25±1.89 as compared to those obtained using the biphasic-solute model, i.e. 14.39± 7.90 (Table 5.3). Furthermore, the ratio of FCDs of the middle zone to the FCDs of the superficial zone was 1.9±0.09 (Table 5.3).

Table 5.3. The ratio of diffusion coefficient of superficial zone to middle zone ($D_{Superficial}/D_{Middle}$) and the ratio of FCD of middle zone to the superficial zone ($FCD_{Middle}/FCD_{Superficial}$).

		$D_{Superficial}/D_{Middle}$	$FCD_{Middle}/FCD_{Superficial}$
Sample 1	Biphasic-solute model	12.7	-
	Multiphasic model	8	1.9
Sample 2	Biphasic-solute model	23	-
	Multiphasic model	10.25	1.82
Sample 3	Biphasic-solute model	7.47	-
	Multiphasic model	6.5	2

Equilibrium partitioning of ioxaglate clearly illustrated the FCD difference between three samples (Figure 5.7A). There was an inverse relationship between the concentration of ioxaglate and FCD in the superficial zone and in the middle zone (Figure 5.7B).

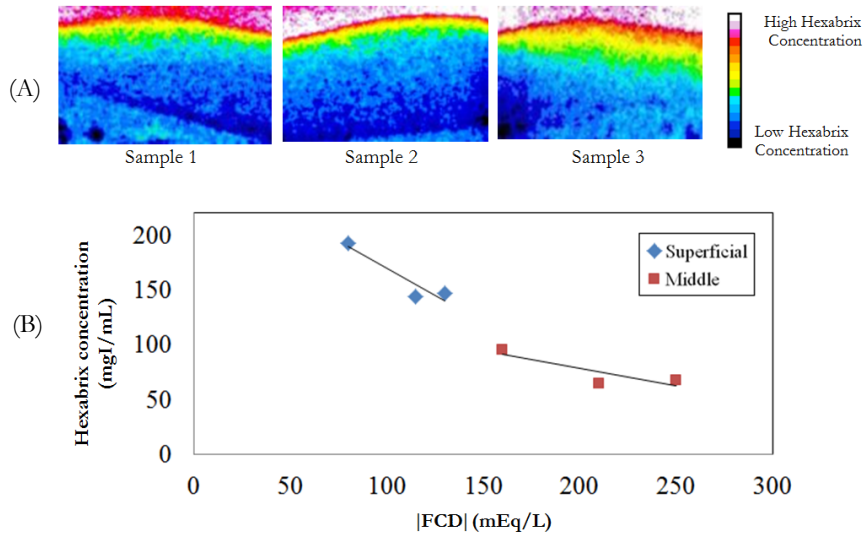

Figure 5.7. Near-equilibrium partitioning of ioxaglate in samples 1-3 where the color bar represents the ioxaglate partitioning across cartilage samples (A) and strong relationship between near-equilibrium ioxaglate concentration in the superficial and middle zones and FCD calculated using multi-zone multiphasic model.

5.3.2.3. PARAMETRIC STUDY

We investigated the direct effects of FCD on the concentration-time curve by comparing the outputs of the multiphasic model that did or did not consider FCD, i.e. FCD=0 (Figure 5.8A-C). In all samples, concentration-time curves obtained from the multiphasic model that considered FCD were below those obtained from the multiphasic model that did not consider FCD. We investigated the direct effect of bath ionic strength on the concentration-time curve by comparing concentration-time curves obtained from the biphasic-solute model and multiphasic model that did not consider FCD (Figure 5.8A-C). The curves obtained using the biphasic-solute model were below those obtained from multiphasic model that did not consider FCD. The synergistic effect of bath ionic strength and FCD in cartilage can be observed by comparing the concentration-time curves of the biphasic-solute model with that of the multiphasic model that considered FCD (Figure 5.8A-C).

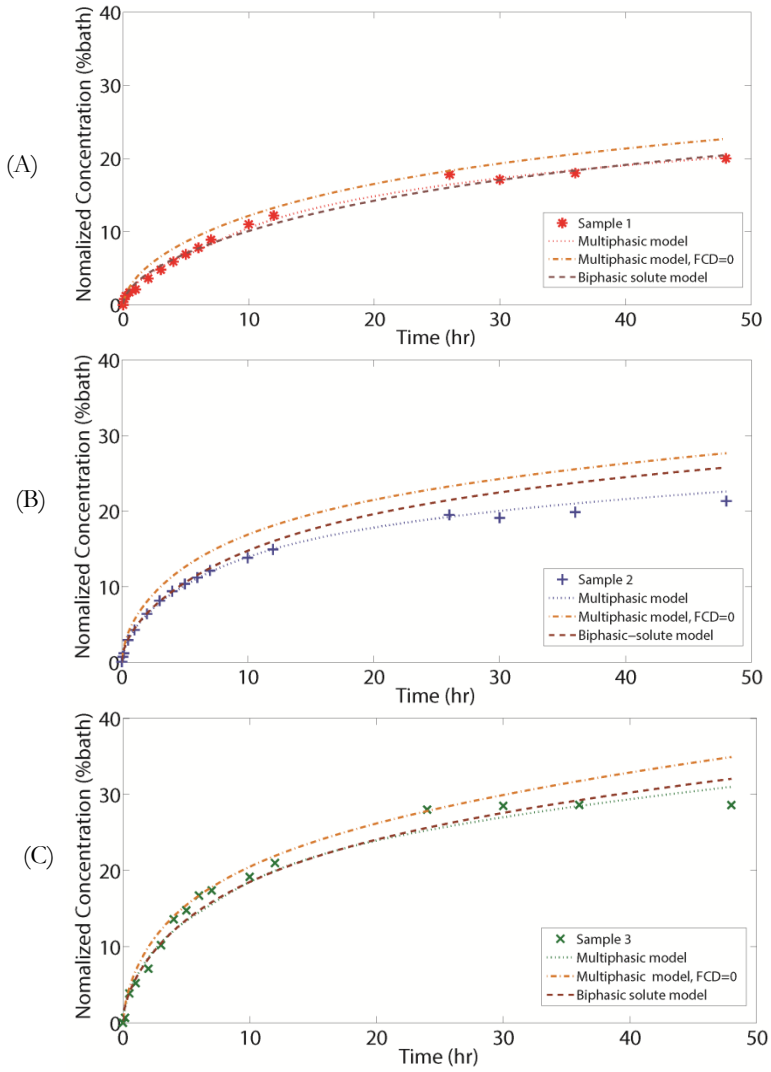

Figure 5.8. Comparing fit obtained using multi-zone multiphasic model, multi-zone multiphasic model without considering FCD (FCD=0) and multi-zone biphasic-solute model for samples 1-3 to elucidate the effects of FCD and bath ionic strength (experiment: symbol, FE model: dotted line).

5.4. **Discussion**

Both single-zone biphasic-solute and multiphasic models could capture the experimental curves (Figure 5.2A and 5.3A; Table 5.1A). However, curve

trends could not be fully predicted by both single-zone models (Figure 5.2A and 5.3A). The multi-zone biphasic and multiphasic models produced excellent fit over the experimental curves (Figure 5.5 and 5.6B; Table 5.2A). The rationale behind can be sought through variation in cartilage properties such as water content, FCD and orientation of collagen fibers across its thickness [14, 31].

In the single-zone model, quite similar diffusion coefficients between biphasic and multiphasic models were observed (Table 5.1B). Multi-zone model resulted in more distinct diffusion coefficients between biphasic-solute and multiphasic models in the middle zone (Table 5.2B). Small differences between the diffusion coefficients of the superficial zone calculated with biphasic-solute and multiphasic models may be due to the fact that movement of negatively charged solutes from the bath to the cartilage (self-repulsion) counterbalances the repulsion force between the negatively charged solute and negative fixed charges of cartilage in this zone. Nevertheless, in the biphasic-solute model, likely due to neglecting the interaction between charged bath and fixed charges in the middle zone, the difference between the diffusion coefficients of multiphasic and biphasic-solute model are more pronounced. These messages imply that efficient delivery of charged therapeutics relies on both sufficient charge density as well as taking the role of higher FCD in the middle and deep zones into account e.g. intra-articular injection systems. This corroborates the strategy that was previously suggested to enhance penetration depth and retention of pharmaceutics by using a positively charged carrier (Avidin) across cartilage [12, 13]. Although determination of diffusion coefficient and FCD in the deep zone for these samples (Figure 5.7A) is infeasible due to little diffusion in this zone, previous data shows that the FCD of the deep zone of equine cartilage remains similar to that of the middle zone [44]. Consistent diffusion coefficient ratios ($D_{Superficial}/D_{Middle}$) may be linked to the more realistic diffusion coefficients predicted by the multiphasic model as compared to the biphasic-solute model. Our findings show that the ratio of FCD of the middle to that of the superficial zone was found to be almost 1.9 (Table 5.3). This is consistent with the reported ratio of FCD (correlated with

GAG) in the middle zone to that of the superficial zone [44]. Partition of a negatively charged solute such as ioxaglate is inversely related to FCD [8]. ioxaglate partitioning in sample 3 implicitly indicates that FCD in this sample should be lower than the other two samples (Figure 5.7A). This is in agreement with FCD values reported (Table 5.2B). Due to proximity of equilibrium partitioning of ioxaglate in samples 1 and 2 it is difficult to draw a conclusion in terms of their FCDs (Figure 5.7A and Table 5.2B), yet, a linear relationship between ioxaglate equilibrium concentration and FCD (Figure 5.7B) exists in the superficial and middle zones of all samples.

According to Figure 5.8A-C, diffusion curve of biphasic-solute model always stayed below the diffusion curve of the multiphasic model that did not consider FCD. This comparison shows that the diffusion of negatively charged solutes can be amplified via downward repulsion forces within the overlaying baths that direct the solutes toward bath-cartilage interface. Comparing the diffusion curves between the multiphasic models that did and did not consider FCD suggests that FCD can significantly hinder the penetration of negatively charged ioxaglate through cartilage. These conclusions might help design efficient OA treatment strategies by considering e.g. therapeutics' charge and injection volume as well as GAG content of cartilage. In addition, our findings might open windows toward better understanding of OA (e.g. GAG loss) through interactions between charged solute and cartilage matrix.

The multi-zone multiphasic model could very well capture the diffusion of a relatively small charged molecule through articular cartilage. However, steric hindrance due to uneven distribution of collagen fibers and their interaction especially with larger solutes such as therapeutically relevant solutes cannot be yet described using the existing model and therefore requires further research. In order to determine the diffusion coefficient and FCD of deep zone of cartilage using the developed multiphasic model we offer some solutions: thinner samples, prolonged experimental time as well as using positively charged solute in the bath such as CA4+ [16]. Moreover, diffusion is an anisotropic tensor. Performing experiments involving radial diffusion might therefore add further information in terms of spatial distribution of cartilage

components. The solution containing ioxaglate used in our experiment was a hyper-osmolal solution (600 mOsm/kg H2O) and its effect was not assessed in the current work, however, this will be addressed in our future studies.

In summary, multiphasic model enabled obtaining both FCD and diffusion coefficients in the different zones of equine cartilage in a finite-bath model of diffusion in a non-destructive way while considering the negative charges imparted by both keratin sulfate and chondroitin sulfate. The equilibrium partitioning of ioxaglate was shown to correlate with the FCD obtained using our multiphasic model. The findings of this work suggest that diffusion coefficient of the superficial zone can be up to 10 times higher than that of the middle zone and that FCD can be up to two times higher in the middle zone as compared to the superficial zone.

5.5. **ACKNOWLEDGEMENT**

We would like to kindly express our acknowledgements for all the scientific supports of Professor Gerard Ateshian (Columbia University). This work was supported by a grant from Dutch Arthritis Foundation (13-3-406).

5.6. **REFERENCES**

1. Tavakoli Nia, H., et al., *Aggrecan Nanoscale Solid–Fluid Interactions Are a Primary Determinant of Cartilage Dynamic Mechanical Properties.* ACS Nano, 2015. **9**(3): p. 2614-2625.
2. Nia, Hadi T., et al., *Poroelasticity of Cartilage at the Nanoscale.* Biophysical Journal, 2011. **101**(9): p. 2304-2313.
3. Weinans, H., et al., *Pathophysiology of peri-articular bone changes in osteoarthritis.* Bone, 2012. **51**(2): p. 190-6.
4. Kulmala, K.A., et al., *Diffusion of ionic and non-ionic contrast agents in articular cartilage with increased cross-linking--contribution of steric and electrostatic effects.* Med Eng Phys, 2013. **35**(10): p. 1415-20.
5. Kokkonen, H.T., et al., *Detection of mechanical injury of articular cartilage using contrast enhanced computed tomography.* Osteoarthritis Cartilage, 2011. **19**(3): p. 295-301.
6. Kokkonen, H.T., et al., *Computed tomography detects changes in contrast agent diffusion after collagen cross-linking typical to natural aging of articular cartilage.* Osteoarthritis and Cartilage, 2011. **19**(10): p. 1190-1198.
7. Ding, C., F. Cicuttini, and G. Jones, *How important is MRI for detecting early osteoarthritis?* Nat Clin Pract Rheum, 2008. **4**(1): p. 4-5.
8. Kulmala, K.A.M., et al., *Diffusion coefficients of articular cartilage for different CT and MRI contrast agents.* Medical Engineering & Physics, 2010. **32**(8): p. 878-882.
9. Bajpayee, A.G., et al., *Charge based intra-cartilage delivery of single dose dexamethasone using Avidin nano-carriers suppresses cytokine-induced catabolism long term.* Osteoarthritis and Cartilage.
10. Abazari, A., et al., *Transport phenomena in articular cartilage cryopreservation as predicted by the modified triphasic model and the effect of natural inhomogeneities.* Biophys J, 2012. **102**(6): p. 1284-93.
11. Abazari, A., et al., *MR spectroscopy measurement of the diffusion of dimethyl sulfoxide in articular cartilage and comparison to theoretical predictions.* Osteoarthritis and Cartilage, 2012. **20**(9): p. 1004-1010.
12. Bajpayee, A.G., et al., *Avidin as a model for charge driven transport into cartilage and drug delivery for treating early stage post-traumatic osteoarthritis.* Biomaterials, 2014. **35**(1): p. 538-549.
13. Bajpayee, A.G., et al., *Electrostatic interactions enable rapid penetration, enhanced uptake and retention of intra-articular injected avidin in rat knee joints.* Journal of Orthopaedic Research, 2014. **32**(8): p. 1044-1051.
14. Arbabi, V., et al., *Transport of Neutral Solute Across Articular Cartilage: The Role of Zonal Diffusivities.* Journal of Biomechanical Engineering, 2015. **137**(7): p. 071001-071001.
15. Meganck, J.A., et al., *Beam hardening artifacts in micro-computed tomography scanning can be reduced by X-ray beam filtration and the resulting images can be used to accurately measure BMD.* Bone, 2009. **45**(6): p. 1104-16.
16. Bansal, P.N., et al., *Contrast agent electrostatic attraction rather than repulsion to glycosaminoglycans affords a greater contrast uptake ratio and improved*

quantitative CT imaging in cartilage. Osteoarthritis Cartilage, 2011. **19**(8): p. 970-6.

17. Aula, A.S., J.S. Jurvelin, and J. Töyräs, *Simultaneous computed tomography of articular cartilage and subchondral bone.* Osteoarthritis and Cartilage, 2009. **17**(12): p. 1583-1588.
18. Tuomo S. Silvast, J.S.J., Virpi Tiitu, Thomas M. Quinn and Juha Töyräs, *Bath Concentration of Anionic Contrast Agents Does Not Affect Their Diffusion and Distribution in Articular cartilage In Vitro.* Cartilage, 2013. **4**(1): p. 42-51.
19. Le, N.-A.T. and B.C. Fleming, *Measuring fixed charge density of goat articular cartilage using indentation methods and biochemical analysis.* Journal of Biomechanics, 2008. **41**(3): p. 715-720.
20. Shapiro, E.M., et al., *23Na MRI accurately measures fixed charge density in articular cartilage.* Magn Reson Med, 2002. **47**(2): p. 284-91.
21. Bashir, A., et al., *Nondestructive imaging of human cartilage glycosaminoglycan concentration by MRI.* Magn Reson Med, 1999. **41**(5): p. 857-65.
22. Lu, X.L., et al., *Indentation Determined Mechanoelectrochemical Properties and Fixed Charge Density of Articular Cartilage.* Annals of Biomedical Engineering, 2004. **32**(3): p. 370-379.
23. Lesperance, L.M., M.L. Gray, and D. Burstein, *Determination of fixed charge density in cartilage using nuclear magnetic resonance.* Journal of Orthopaedic Research, 1992. **10**(1): p. 1-13.
24. Dai, H., K. Potter, and E.W. McFarland, *Determination of Ion Activity Coefficients and Fixed Charge Density in Cartilage with 23Na Magnetic Resonance Microscopy.* Journal of Chemical & Engineering Data, 1996. **41**(5): p. 970-976.
25. Jackson, A.R., et al., *A conductivity approach to measuring fixed charge density in intervertebral disc tissue.* Ann Biomed Eng, 2009. **37**(12): p. 2566-73.
26. Algotsson, J., et al., *Electrostatic interactions are important for the distribution of Gd(DTPA) in articular cartilage.* Magn Reson Med, 2015.
27. Manzano, S., M. Doblare, and M.H. Doweidar, *Parameter-dependent behavior of articular cartilage: 3D mechano-electrochemical computational model.* Comput Methods Programs Biomed, 2015. **122**(3): p. 491-502.
28. Manzano, S., et al., *Cartilage dysfunction in ALS patients as side effect of motion loss: 3D mechano-electrochemical computational model.* Biomed Res Int, 2014. **2014**: p. 179070.
29. Manzano, S., et al., *Altered swelling and ion fluxes in articular cartilage as a biomarker in osteoarthritis and joint immobilization: a computational analysis.* J R Soc Interface, 2015. **12**(102): p. 20141090.
30. Huttunen, J.M.J., et al., *Estimation of fixed charge density and diffusivity profiles in cartilage using contrast enhanced computer tomography.* International Journal for Numerical Methods in Engineering, 2014. **98**(5): p. 371-390.
31. Pouran, B., et al., *Isolated effects of external bath osmolality, solute concentration, and electrical charge on solute transport across articular cartilage.* Journal of Biomechanical Engineering (Under review), 2015.

32. Gu, W.Y., W.M. Lai, and V.C. Mow, *A mixture theory for charged-hydrated soft tissues containing multi-electrolytes: passive transport and swelling behaviors.* J Biomech Eng, 1998. **120**(2): p. 169-80.
33. Ateshian, G. and J. Weiss, *Finite Element Modeling of Solutes in Hydrated Deformable Biological Tissues*, in *Computer Models in Biomechanics*, G.A. Holzapfel and E. Kuhl, Editors. 2013, Springer Netherlands. p. 231-249.
34. Ateshian, G.A., S. Maas, and J.A. Weiss, *Multiphasic Finite Element Framework for Modeling Hydrated Mixtures With Multiple Neutral and Charged Solutes.* Journal of Biomechanical Engineering, 2013. **135**(11): p. 111001-111001.
35. Sun, D.N., et al., *A mixed finite element formulation of triphasic mechano-electrochemical theory for charged, hydrated biological soft tissues.* International Journal for Numerical Methods in Engineering, 1999. **45**(10): p. 1375-1402.
36. Lai, W.M., J.S. Hou, and V.C. Mow, *A triphasic theory for the swelling and deformation behaviors of articular cartilage.* J Biomech Eng, 1991. **113**(3): p. 245-58.
37. Sophia Fox, A.J., A. Bedi, and S.A. Rodeo, *The Basic Science of Articular Cartilage: Structure, Composition, and Function.* Sports Health, 2009. **1**(6): p. 461-468.
38. Brillo, J., A.I. Pommrich, and A. Meyer, *Relation between self-diffusion and viscosity in dense liquids: new experimental results from electrostatic levitation.* Phys Rev Lett, 2011. **107**(16): p. 165902.
39. Ateshian, G.A., et al., *Finite element implementation of mechanochemical phenomena in neutral deformable porous media under finite deformation.* J Biomech Eng, 2011. **133**(8): p. 081005.
40. Ateshian, G.A., S. Maas, and J.A. Weiss, *Solute transport across a contact interface in deformable porous media.* Journal of Biomechanics, 2012. **45**(6): p. 1023-1027.
41. Leddy, H.A. and F. Guilak, *Site-Specific Molecular Diffusion in Articular Cartilage Measured using Fluorescence Recovery after Photobleaching.* Annals of Biomedical Engineering, 2003. **31**(7): p. 753-760.
42. Salo, E.N., et al., *Diffusion of Gd-DTPA2− into articular cartilage.* Osteoarthritis and Cartilage, 2012. **20**(2): p. 117-126.
43. Wheaton, A.J., et al., *Correlation of T1rho with fixed charge density in cartilage.* J Magn Reson Imaging, 2004. **20**(3): p. 519-25.
44. Malda, J., et al., *Comparative study of depth-dependent characteristics of equine and human osteochondral tissue from the medial and lateral femoral condyles.* Osteoarthritis Cartilage, 2012. **20**(10): p. 1147-51.

CHAPTER 6

APPLICATION OF MULTIPHYSICS MODELS TO EFFICIENT DESIGN OF EXPERIMENTS OF SOLUTE TRANSPORT ACROSS ARTICULAR CARTILAGE

This chapter is published as a scientific paper (Honored):

Pouran B., Arbabi V., Weinans H., Zadpoor A.A. *Application of multiphysics models to efficient design of experiments of solute transport across articular cartilage*. Comput. Biol. Med., 78 (2016) 91-96.

ABSTRACT

Transport of solutes helps to regulate normal physiology and proper function of cartilage in diarthrodial joints. Multiple studies have shown the effects of characteristic parameters such as concentration of proteoglycans and collagens and the orientation of collagen fibrils on the diffusion process. However, not much quantitative information and accurate models are available to help understand how the characteristics of the fluid surrounding articular cartilage influence the diffusion process. In this study, we used a combination of micro-computed tomography experiments and biphasic-solute finite element models to study the effects of three parameters of the overlying bath on the diffusion of neutral solutes across cartilage zones. Those parameters include bath size, degree of stirring of the bath, and the size and concentration of the stagnant layer that forms at the interface of cartilage and bath. Parametric studies determined the minimum of the finite bath size for which the diffusion behavior reduces to that of an infinite bath. Stirring of the bath proved to remarkably influence neutral solute transport across cartilage zones. The well-stirred condition was achieved only when the ratio of the diffusivity of bath to that of cartilage was greater than ≈1000. While the thickness of the stagnant layer at the cartilage-bath interface did not significantly influence the diffusion behavior, increase in its concentration substantially elevated solute concentration in cartilage. Sufficient stirring attenuated the effects of the stagnant layer. Our findings could be used for efficient design of experimental protocols aimed at understanding the transport of molecules across articular cartilage.

Chapter 6

6.1. INTRODUCTION

Synovial joints provide an excellent enclosed environment where exchange of macromolecules, small ions and solutes as well as oxygen between articular cartilage, synovium and subchondral bone can efficiently take place [1-3]. Delivery of therapeutic agents and solutes to articular cartilage and understanding of pathophysiology of the diseased synovial joints rely on various parameters including volume, viscosity and movement of the synovial fluid as well as the status of healthiness of articular cartilage [4-7]. Active mechanical loading of joints increases the transport of molecules by providing well-mixed synovial fluid and convection [8, 9]. Recently, efficient design of large cartilage constructs was accomplished by providing sufficient nutrient supply as well as enhancement of mechanical stirring in the medium [10, 11]. The micro-structure of articular cartilage including orientation and concentration of essential macromolecules namely collagen type II and proteoglycans across its thickness affects solute transport remarkably [7, 12-14]. Therefore, past experimental and computational efforts focusing on the diffusion across cartilage have acknowledged the inhomogeneity of cartilage and implemented it [12, 13]. However, the diffusion phenomena are not only linked with the conditions of articular cartilage but also with the characteristics of the overlying bath, which continuously supplies solutes to articular cartilage [15].

Several studies have tried to use well-stirred infinite baths of solutes for experiments aimed at understanding the diffusion behavior of cartilage [16, 17]. That is because application of the well-stirred finite bath boundary conditions simplifies the theoretical models that are needed for interpretation of the obtained data. However, creating infinite baths for the diffusion experiments involving contrast enhanced micro-computed tomography (micro-CT) may require large volumes of contrast agent solution that the x-ray beam has to penetrate through. That adversely affects the accuracy of the micro-CT readings due to the beam hardening effect particularly when using concentrated contrast agent solutions. Therefore, the concept of finite baths of contrast agents have been recently

introduced and computationally implemented to study the diffusion of neutral and charged solutes across articular cartilage [7, 12, 13]. The boundary between finite and infinite bath is, however, not clear and the errors introduced by assuming infinite bath conditions when the bath is finite have not been quantified before.

The assumption of a well-stirred bath is also difficult to realize in actual experiments, because that requires continuous stirring of the contrast agent solution inside the micro-CT chamber, which is not performed in the vast majority of the experiments performed to date. It is therefore important to understand how deviations from this assumption could influence interpretation of the experimental data. Finally, a stagnant layer forms at the interface of solid-liquid systems including the bath-cartilage interface in diffusion experiments. This stagnant layer has been studied analytically and is shown to change the diffusion characteristics [15, 18]. Nevertheless, most studies ignore the stagnant layer when interpreting the results of diffusion experiments.

In this study, we consider the three above-mentioned bath attributes, namely size of the bath, the stirring condition of the bath, and the proprieties of the stagnant layer, and quantify their effect on the computational results of models describing solute transport across articular cartilage. Towards that end, we use a combination of micro-CT experimental data and multi-zone computational biphasic-solute models. Our findings are expected to enhance the understanding of solute transport across cartilage under various boundary conditions and provide a platform to more robustly design diffusion experiments.

6.2. METHODOLOGY

6.2.1. EXPERIMENTS

The experimental setup has been described in our previous study (chapter 5) [7]. Briefly, cylindrical osteochondral plugs (n=3, diameter=8.5 mm) were extracted from fresh femora's of 6-10 year-old horses post euthanasia. Finite volumes (650 μL) of a neutral contrast agent (iodixanol, MW=1560 g/mol, 420 mM) with osmolalities of 290 mOsm/kg water and 600 mOsm/kg water were injected on top of the cartilage surface, while iodixanol diffusion from lateral direction was restricted by wrapping the sample using heat-shrinking plastic sleeve. Temporal diffusion of iodixanol (up to 48 hours) was then monitored using a micro-CT machine (Quantum FX, Perkin elmer, USA, 40×40×40 μm^3 voxel size, scan time of 2 min, tube voltage of 90 kV and tube current of 180 μA) in a field of view consisting of bath, cartilage and subchondral bone. The grey values in the bath and cartilage were then converted to iodixanol concentration using a linear function presented previously [7, 13]. Post-injection of iodixanol on cartilage surface, thickness and concentration of stagnant layer forming at the cartilage-bath boundary as well as overlying homogeneous layer of the bath were measured (imageJ v1.47) and fed to the computational model (Figure 6.1A).

6.2.2. FINITE ELEMENT MODELING

Biphasic-solute models can accurately describe the transport of neutral solutes across articular cartilage [19] and can describe complex boundary conditions such as non-well stirred bath as well as solute transport across inhomogeneous tissues. The constitutive equations of biphasic-solute model implemented in FEBio 2.4.1 have been presented extensively [19].

6.2.2.1. GEOMETRY AND BOUNDARY CONDITIONS

The entire height of the bath was 14 mm and the thickness of cartilage was 2.7 mm (Figure 6.1B) where the cartilage layer was, split into three different homogeneous zones i.e. superficial (20% of cartilage thickness), middle (50% of cartilage thickness) and deep (30% of cartilage thickness) [14] zones to account for the inhomogeneity of cartilage across its thickness [13]. We used a mesh consisting of eight-node trilinear hexahedral elements, that was further refined near the interfaces.

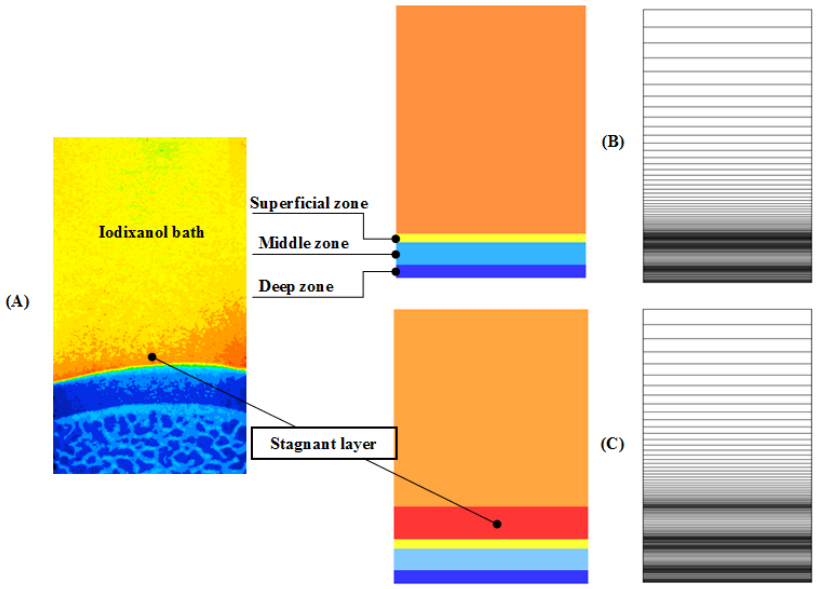

Figure 6.1. (A) Iodixanol finite bath including the stagnant layer, articular cartilage and subchondral bone are shown (B) Finite element model consisting of finite bath, superficial, middle and deep zones of articular cartilage (C) Finite element model including the stagnant layer.

We applied the no-flux boundary condition at the cartilage-bone interface and insulated the other faces of cartilage and bath to enable studying axial solute diffusion.

6.2.2.2. PHYSICAL AND MECHANICAL PROPERTIES

Both bath and cartilage were modeled as neo-Hookean materials with a Young's modulus of 10 MPa, hydraulic permeability of 10^{-3} mm^4/Ns and effective solute solubility of 1 according to our previous studies [12, 13]. The water content of each cartilage zone varied from 80% in the superficial zone and 70% in the middle zone to 60% in the deep zone [14]. The stagnant layer was tied to the overlying bath while it maintained contact with the underlying cartilage (Figure 6.1C). A prescribed displacement of 0.001 mm was used to ensure the stability of contact between boundaries.

6.2.2.3. PARAMETRIC STUDY

In our previous study, we fitted biphasic-solute model to experimental concentration versus time data to obtain the diffusivity of cartilage zones [13]. Based on those results, we performed parametric studies to investigate the effects of bath size, bath stirring and stagnant layer on the diffusion behavior. To study the effect of bath size with identical solute concentrations on diffusion, different length ratios of bath to cartilage were used which spanned from 1 to 100 while cartilage thickness was maintained constant at 2.7 mm, reflecting the actual experiment design. Effect of bath stirring was investigated by step-wise increase of solute diffusivity in the bath relative to superficial zone of cartilage (diffusivity ratio varying from 10 to 10000) until fully well-stirred condition is satisfied. Increase in diffusivity ratio is equivalent to higher bath stirring while decrease in it could make the bath deviate from the conventional well-stirred assumption. To assess the effects of thickness and concentration of possible stagnant layer formed at the cartilage-bath interface, computational models with different thicknesses and concentrations of the stagnant layer were built to perform a parametric study whose parameter ranges were based on the actual initial concentration and thickness of the stagnant layer observed during our experiments in six different conditions [7, 13].

6.3. RESULTS

6.3.1. EFFECT OF BATH SIZE (PARAMETER α)

Based on the previous studies [7, 13] experimental concentration versus time for one sample is illustrated (Figure 6.2A) to provide a better understanding of the influence of bath size on diffusion behavior across articular cartilage. Concentrations versus time curves were plotted in different length ratios of bath to cartilage (α) ranging from 1 to 100, which covers a wide spectrum from a small finite bath to an infinite bath. Increase in bath size showed increase in the predicted concentrations up to 48 hours (Figure 6.2A). Ratios greater than 5.18 (previous experimental setup) resulted in root mean square error (RMSE) of 2e-6 and R^2 of 1 compared to length ratio of 10, yet, the solutions for length ratios above 10 converged to diffusion behavior corresponding to infinite baths (RMSE=2e-7 and R^2=1). RMSE values between solution at each length ratio and length ratio of 10 (infinite bath) indicate that length ratio of 5.18 (previous experimental setup) behaves the same as infinite bath (Table 6.1). To examine the effect of bath size on diffusion in different cartilage layers, we plotted the concentration versus time curves at a distance of 0.4 mm, 0.74 mm and 1.46 mm from the cartilage surface in an extended time period of 96 hours for length ratios 1 and 5.18 (equivalent to infinite bath). We observed lower concentration values in different cartilage zones corresponding to length ratio 1 compared to those corresponding to length ratio 5.18 at different time points including final time point (Figure 6.2B).

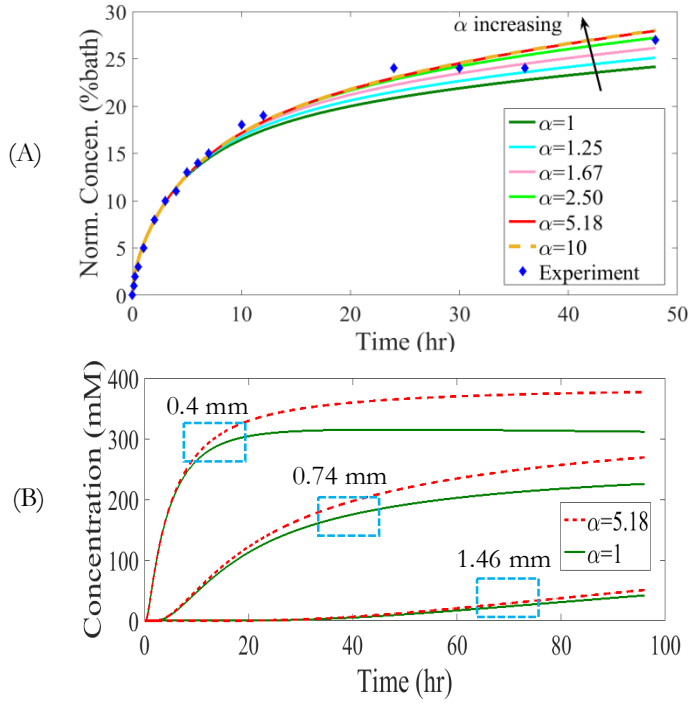

Figure 6.2. (A) Effect of length ratio of bath to cartilage (α) on concentration vs. time curves (B) Effect of length ratio of bath to cartilage (α) on zonal concentration vs. time curves at 0.4, 0.74 and 1.46 mm distance from the cartilage surface.

Table 6.1. RMSE to compare the concentration vs. time curves of different bath sizes with concentration vs. time curve of an infinite bath (α =10).

Length ratio of bath to cartilage (α)	RMSE
1.00	0.022192
1.25	0.011623
1.67	0.004247
2.50	0.000592
5.18	0.000002

6.3.2 EFFECT OF STIRRING (PARAMETER β)

A wide range of diffusivity ratios of bath to cartilage (β) from 10 to 10000 including the actual experimental setup $(\beta = 33.33)$ were used. RMSE and R2 between concentration versus time curves of diffusivity ratio of 1000 and 10000 were 0.00018 and 1. Greater than 1000-fold diffusivity ratio resulted in fully stirred bath condition (Figure 6.3A) and the degree of stirring strongly influenced the concentration versus time curves (Table 6.2).

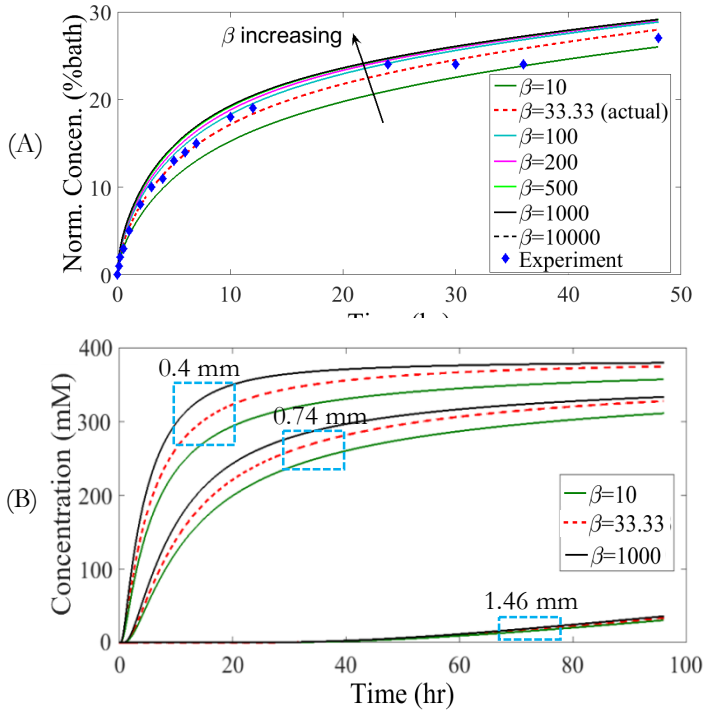

Figure 6.3. (A) Effect of bath stirring (β) on concentration vs. time curves. Note that the curves of β=1000 and β=10000 are almost overlapping (B) Effect of bath stirring (β) on zonal concentration vs. time curves at 0.4, 0.74 and 1.46 mm distance from the cartilage surface.

Concentration versus time curves for different cartilage layers at 0.4, 0.74 and 1.46 mm distance from cartilage surface explicitly demonstrate that more stirred bath generates higher concentration values in different time points across cartilage (Figure 6.3B).

Table 6.2. RMSE to compare the concentration vs. time of different degrees of stirring with curve-fitted concentration vs. time (actual bath diffusivity).

Stirring degree (β)	RMSE
10	0.0228
100	0.0078
200	0.0152
500	0.0229
1000	0.0265
10000	0.0304

6.3.3 EFFECT OF STAGNANT LAYER (PARAMETER γ)

The micro-CT observations on diffusion of iodixanol within the bath in six cases (chapter 3 and 5) [7, 13] showed that the thickness of stagnant layer varied from 1.6 to 2 mm and the concentration ratio of stagnant layer to overlying bath (γ) varied from 1.1 to 1.15 (iodixanol injection). To perform the parametric study, the maximum thickness of 2 mm and maximum concentration ratio of 1.15 were used and compared with the cases where stagnant layer was not considered (curve-fitting situation). Considering γ values of 1.5 and 2 completed the parametric study. As γ increased, the level of the concentration versus time curves increased (Figure 6.4A), while no considerable changes were observed when comparing curve fitted data without considering stagnant layer and the concentration versus time data with maximum realistic concentration ratio of γ=1.15 and stagnant layer thickness of 2 mm (Table 6.3).

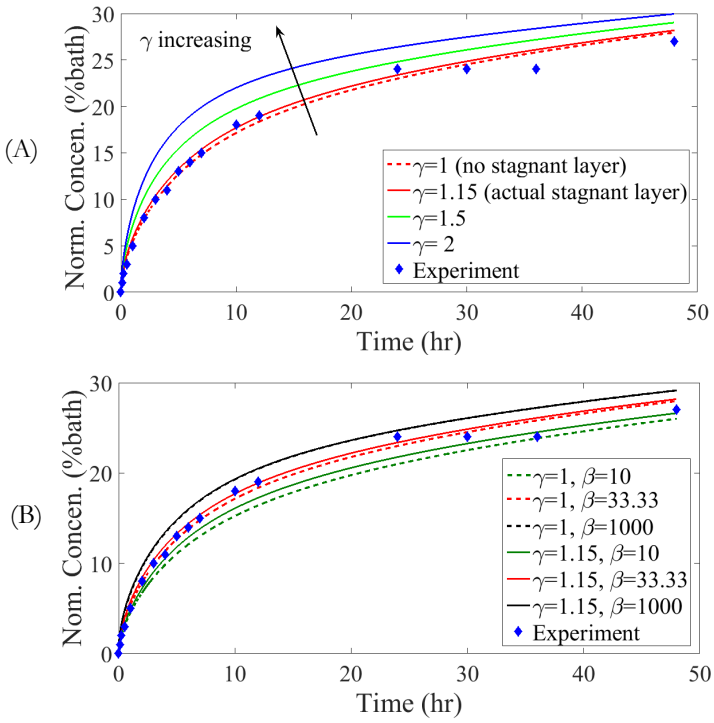

Figure 6.4. (A) Effect of concentration ratio of stagnant layer to overlying bath (γ) on concentration vs. time curves where γ=1.15 corresponds to maximum realistic concentration ratio of stagnant layer to overlying bath. (B) Effect of stirring (β) with or without stagnant layer on concentration vs. time curves.

Table 6.3. RMSE to compare the concentration vs. time of different concentration ratios of stagnant layer to overlying bath with the concentration vs. time of the case with no stagnant layer.

Concentration ratio of stagnant layer to overlying bath (γ)	RMSE
1.15	0.0018
1.50	0.0250
2.00	0.0300

Given the stagnant layer with a thickness of 2 mm and γ=1.15, stirring strongly affected its stability and diminished the effect of

formation of the stagnant layer on the diffusion behavior (Figure 6.4B and Table 6.4). Changing the thickness of stagnant layer from 2 mm to 3 mm while keeping β and γ at 5.18 and 1.15 respectively did not affect the total concentration versus time curves (Figure 6.5A) nor the zonal ones (Figure 6.5B).

Table 6.4. RMSE to compare the concentration vs. time of different degrees of stirring (if γ =1.15) with the case with no stagnant layer.

Stirring effect on stagnant layer (β) (if γ =1.15)	RMSE
10	0.003818
33.33	0.001835
1000	0.000063

(A)

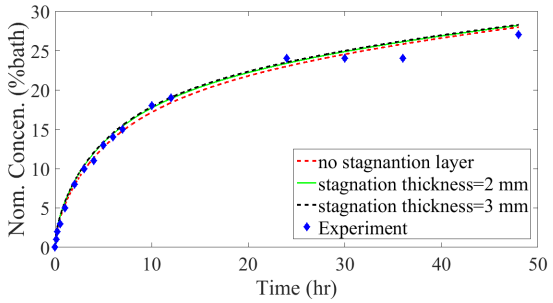

(B)

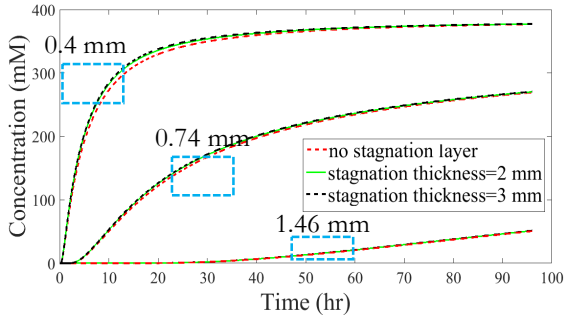

Figure 6.5. (A) Effect of stagnation thickness on concentration vs. time curves (if $\gamma = 1.15$) (B) Effect of stagnation thickness on zonal concentration vs. time curves (if $\gamma = 1.15$) at 0.4, 0.74 and 1.46 mm distance from the cartilage surface.

6.4. **DISCUSSION**

The primary objective of this research was to develop a parametric computational study based on experimental micro-CT observations to investigate the effects of bath size, bath stirring and stagnant layer formation on the diffusion of neutral solutes across articular cartilage. Our results of bath size effect revealed that too low length ratio of bath to cartilage may lead to insufficient penetration of solutes and thereby reduced equilibrium concentration. Furthermore, increase of bath size up to a convergence value seems to be necessary to ensure of sufficient supply of solute into the cartilage. Comparing the computational fit to the experimental concentration versus time curves (ratio of 5.18) with the curves corresponding to higher ratios showed that minimum approximate ratio of 5 can ensure of infinite diffusion behavior (Figure 6.2A and Table 6.1). This highlights the importance of considering the minimum solute required to reach equilibrium prior to designing the experiments. Appropriate selection of bath size, therefore, guarantees optimal required amount of solute as well as volume of the bath, which in case of micro-CT experiments can be of paramount significance chiefly due to possible effects of beam hardening [20] in large baths of contrast agent. The optimal ratio presented here may vary slightly depending on the concentration (compactness) of collagen and GAG, orientation of collagen fibrils and water content, which affect the solute partitioning [21].

The degree of stirring as well as formation of stagnant layer at bath-cartilage interface play roles in determining the maximum rate at which solute can be transported to the tissue, thereby became the second and third factors considered in this research.

In our study, we investigated the stirring effect by changing the diffusivity ratio of bath to the curve fitted diffusivity of the cartilage superficial layer. Increasing the diffusivity of the bath relative to cartilage simulates different degrees of stirring without including the additional convection effects (vortex generation) commonly generated by mechanical stirrers. We observed that, as expected, stirring could substantially facilitate

the transport of neutral solute across cartilage. Above 1000-factor higher diffusivity in the bath than in cartilage potentially makes the assumption of well-stirred condition legitimate (Figure 6.3A). The zonal influence of stirring on diffusion decreased from the surface to the bottom of cartilage suggesting that solute transfer can be more effectively augmented in the superficial and middle zones (Figure 6.3B). Increasing the stirring lowers the mass transfer resistance in the bath, therefore allowing more solutes to penetrate into the superficial zone, although lower diffusivity of deeper layers dampens lowered mass transfer resistance in the bath side. Therefore, one may apply other approaches e.g. using positively charged solutes to target the deeper cartilage zones rather than inducing stirring mechanically, although surface of cartilage may be more easily accessible to the solutes post-stirring.

Based on the experimental observations, the typical concentration and thickness of stagnant layer on the cartilage-bath interface were obtained and applied to conduct parametric study. We showed that failure to consider the exact concentration of stagnant layer only causes small errors in tracking the concentration versus time curves as compared to the actual experimental situation (our experimental observations) (Figure 6.4A). However, care should be taken when the stagnant layer concentration lies highly above that of the overlying bath (Figure 6.4A), which might be the case in other experiments and may cause large deviations in e.g. estimation of equilibrium concentration. We also showed that when realistic concentration ratio of stagnant layer to the overlying bath is used, at high stirring rates, the role of the stagnant layer becomes minimal (Figure 6.4B). This can be explained in the way that high stirring power more easily dissipates the formed boundary layer at the cartilage-bath interface and therefore homogenizes the bath and minimizes the effect of stagnant layer. Finally, our findings support that the thickness of the stagnant layer has little effect on the concentration versus time curves with lowest effect on the equilibrium concentration (Figure 6.5). This infers that formation of stagnant layer as long as it does not cause large concentration gradients within the bath, does not affect the diffusion attributes of neutral solutes although this may be different for charged

solutes [12] due to their repulsive-driven diffusion that may even facilitate the transport into cartilage. Surface chemistry of articular cartilage, as the substrate changes the solute-substrate interactions which affects the rate of solute adsorption and possibly the stability and formation of stagnant layers [22]. Moreover, the size of the solutes and the viscosity of the solution influence the diffusivity within the bath that can affect the size of unstirred layer at the interfaces [18].

This study is associated with some limitations with respect to experiments and computations. The presented study strived to provide a realistic approach on diffusion problems. However, minor assumptions such as considering uniform stagnant layer in the biphasic-solute model were made. The findings of the study may be extended in the future works to investigating the effects of bath size, stirring and stagnant layer formation on charged solutes.

6.5. **CONCLUSIONS**

The presented study provided an opportunity to study the effects of bath size, degree of bath stirring and stagnant layer on the diffusion of a neutral solute with the aid of multi-zone finite element modeling. Degree of stirring and size of the bath as well as concentration of the stagnant layer relative to overlying bath concentration were identified as the dominant factors affecting neutral solute transport across articular cartilage. The findings of this study may be used in robust design of diffusion experiments particularly when cartilage as the tissue type is used.

6.6. **REFERENCES**

1. Wang, Y., et al., *Nutrition and degeneration of articular cartilage.* Knee Surg Sports Traumatol Arthrosc, 2013. **21**(8): p. 1751-62.
2. Maroudas, A., *Distribution and diffusion of solutes in articular cartilage.* Biophys J, 1970. **10**(5): p. 365-79.
3. Zhang, L., et al., *The effect of cyclic deformation and solute binding on solute transport in cartilage.* Arch Biochem Biophys, 2007. **457**(1): p. 47-56.
4. Bajpayee, A.G., et al., *Charge based intra-cartilage delivery of single dose dexamethasone using Avidin nano-carriers suppresses cytokine-induced catabolism long term.* Osteoarthritis Cartilage, 2016. **24**(1): p. 71-81.
5. Abazari, A., et al., *Transport phenomena in articular cartilage cryopreservation as predicted by the modified triphasic model and the effect of natural inhomogeneities.* Biophys J, 2012. **102**(6): p. 1284-93.
6. Wang, P., et al., *Cryoprotective effects of low-density lipoproteins, trehalose and soybean lecithin on murine spermatogonial stem cells - CORRIGENDUM.* Zygote, 2013: p. 1.
7. Pouran, B., et al., *Isolated effects of external bath osmolality, solute concentration, and electrical charge on solute transport across articular cartilage.* (Under review), 2016.
8. Garcia, A.M., et al., *Contributions of Fluid Convection and Electrical Migration to Transport in Cartilage: Relevance to Loading.* Archives of Biochemistry and Biophysics, 1996. **333**(2): p. 317-325.
9. Entezari, V., et al., *Effect of mechanical convection on the partitioning of an anionic iodinated contrast agent in intact patellar cartilage.* J Orthop Res, 2014. **32**(10): p. 1333-40.
10. Cigan, A.D., et al., *Nutrient channels and stirring enhanced the composition and stiffness of large cartilage constructs.* J Biomech, 2014. **47**(16): p. 3847-54.
11. Nims, R.J., et al., *Matrix Production in Large Engineered Cartilage Constructs Is Enhanced by Nutrient Channels and Excess Media Supply.* Tissue Eng Part C Methods, 2015. **21**(7): p. 747-57.
12. Arbabi, V., et al., *Multiphasic modeling of charged solute transport across articular cartilage: application of finite-bath model.* Journal of Biomechanics, 2016.
13. Arbabi, V., et al., *Transport of Neutral Solute Across Articular Cartilage: The Role of Zonal Diffusivities.* Journal of Biomechanical Engineering, 2015. **137**(7): p. 071001-071001.
14. Sophia Fox, A.J., A. Bedi, and S.A. Rodeo, *The Basic Science of Articular Cartilage: Structure, Composition, and Function.* Sports Health, 2009. **1**(6): p. 461-468.
15. Torzilli, P.A., E. Askari, and J.T. Jenkins, *Water Content and Solute Diffusion Properties in Articular Cartilage*, in *Biomechanics of Diarthrodial Joints*, A. Ratcliffe, S.-Y. Woo, and V. Mow, Editors. 1990, Springer New York. p. 363-390.
16. Tuomo, S.S., et al., *Diffusion and near-equilibrium distribution of MRI and CT contrast agents in articular cartilage.* Physics in Medicine and Biology, 2009. **54**(22): p. 6823.

17. Kokkonen, H.T., et al., *Detection of mechanical injury of articular cartilage using contrast enhanced computed tomography*. Osteoarthritis Cartilage, 2011. **19**(3): p. 295-301.
18. Pohl, P., S.M. Saparov, and Y.N. Antonenko, *The size of the unstirred layer as a function of the solute diffusion coefficient*. Biophys J, 1998. **75**(3): p. 1403-9.
19. Mauck, R.L., C.T. Hung, and G.A. Ateshian, *Modeling of Neutral Solute Transport in a Dynamically Loaded Porous Permeable Gel: Implications for Articular Cartilage Biosynthesis and Tissue Engineering*. Journal of biomechanical engineering, 2003. **125**(5): p. 602-614.
20. Meganck, J.A., et al., *Beam hardening artifacts in micro-computed tomography scanning can be reduced by X-ray beam filtration and the resulting images can be used to accurately measure BMD*. Bone, 2009. **45**(6): p. 1104-16.
21. Nimer, E., R. Schneiderman, and A. Maroudas, *Diffusion and partition of solutes in cartilage under static load*. Biophys Chem, 2003. **106**(2): p. 125-46.
22. Decker, S.G., et al., *Adsorption and distribution of fluorescent solutes near the articular surface of mechanically injured cartilage*. Biophys J, 2013. **105**(10): p. 2427-36.

CHAPTER 7

SOLUTE TRANSPORT AT THE INTERFACE OF CARTILAGE AND SUBCHONDRAL BONE PLATE: EFFECT OF MICRO-ARCHITECTURE

This chapter is published as a scientific paper (Featured):

Pouran B., Arbabi V., Bleys R.L., van Weeren P.R., Zadpoor A.A., Weinans H. *Solute transport at the interface of cartilage and subchondral bone plate: effect of micro-architecture*. Journal of Biomechanics., 52 (2017) 148-154.

ABSTRACT

Cross-talk of subchondral bone and articular cartilage could be an important aspect in the etiology of osteoarthritis. Previous research has provided some evidence of transport of small molecules (~370 Da) through the calcified cartilage and subchondral bone plate in murine osteoarthritis models. The current study, for the first time, uses a neutral diffusing computed tomography (CT) contrast agent (iodixanol, ~1550 Da) to study the permeability of the osteochondral interface in equine and human samples. Sequential CT monitoring of diffusion after injecting a finite amount of contrast agent solution onto the cartilage surface using a micro-CT showed penetration of the contrast molecules across the cartilage-bone interface. Moreover, diffusion through the cartilage-bone interface was affected by thickness and porosity of the subchondral bone as well as the cartilage thickness in both human and equine samples. Our results revealed that porosity of the subchondral plate contributed more strongly to the diffusion across osteochondral interface compared to other morphological parameters in healthy equine samples. However, thickness of the subchondral plate contributed more strongly to the diffusion in slightly osteoarthritic human samples.

Chapter 7

7.1. INTRODUCTION

Etiology of osteoarthritis (OA) implies deterioration of subchondral bone plate quality such as early thinning, sclerosis and porosity alterations beside the damage of articular cartilage [1, 2]. The severity and type of those changes depend primarily on the OA stage [3-6]. According to some theories that go against conventional theories [7, 8], OA initiates from the subchondral bone, over-time progressing to the overlying articular cartilage [9, 10]. Regardless of whether one subscribes to the conventional or alternative theories associated with the etiology of OA, it is clear that morphological changes in the subchondral bone and articular cartilage create a driving force for transfer of putative harmful molecules [1]. Enhanced activity of osteoclasts and subsequent increased subchondral bone perforations and thinning augment the diffusion of cytokines and enzymes as well as cross-talk between cartilage and subchondral bone [2, 5, 11, 12]. These mechanisms highlight the fact that diffusion likely plays a key role in molecular signaling across the osteochondral interface. Some earlier studies on OA models of rabbits and rats reported the diffusion at the osteochondral interface [1]. The diffusion of small molecules (<400 Da) was confirmed between the uncalcified and calcified cartilage in the metacarpophalangeal joints of healthy mature horses [13]. Diffusion of small molecules across the osteochondral interface in a murine model using sodium fluorescein (376 Da) was correlated with OA progression and diffusion of Gd-DTPA2- (MRI contrast agent, 547 Da) in the clinic was observed [2, 11, 14]. The presence of non-mineralized patches (~100 nm) within the calcified cartilage as well as invasion of uncalcified cartilage through the calcified cartilage might explain the molecular transport [11, 15]. Unlike articular cartilage, consensus exists regarding the diffusion of molecules between the intervertebral disk (IVD) and the vertebral body through the endplate. Diffusion is known to dramatically influence the health of the spine, because insufficient

nutrition of the IVD is suggested to accelerate its degeneration [16]. However, it was shown that load-dependent convection facilitates the transport in the IVD as well as across the endplate-IVD interface in both healthy and degenerated disks [17, 18]. A previous study using advanced micro-computed tomography (micro-CT) showed increased perforations in the subchondral endplate when the IVD degenerates [19]. All the previous evidence therefore supports the theory that direct diffusion between cartilaginous tissues and underlying bone plays a key role in the normal physiology of articulating joints as well as the spine.

In the present study, we aim to investigate solute transport between articular cartilage and subchondral bone of equine and human samples using multi-resolution micro-CT by applying a neutral solute. Using the neutral solute enables to exclude the mechano-electrical phenomena arising when an external charged solute is transferred through the highly charged articular cartilage. The effects of the micro-architecture (i.e. porosity and thickness) of the calcified cartilage/subchondral bone plate complex and thickness of uncalcified cartilage on diffusion will be determined.

7.2. METHODOLOGY

7.2.1. EXPERIMENTS

7.2.1.1. BATH AND SAMPLE PREPARATION

The criterion for OA detection was based on visual observations performed by two surgeons and one engineer: regions where the cartilage has completely disappeared were considered as advanced OA, whereas, regions with existing cartilage but having relatively rough surface were considered as slight OA. Cylindrical osteochondral plugs from four cadaveric fresh-frozen human medial femoral condyles with slight OA (approved by university medical center Utrecht, age=67-85, n=4, cartilage thickness=2.53±0.31, diameter=8.5 mm) and three healthy cadaveric equine medial femoral condyles (approved by

Utrecht university, age=7, n1=6, n2=5, n3=6, cartilage thickness=1.48±0.53 mm, diameter=8.5 mm) were drilled using custom-made drill bits (Figure 7.1). For the human samples, care was taken to extract them from a location that was visually intact. The site of drilling was constantly sprayed using phosphate buffer serum (PBS) to ensure minimal dehydration and damage to the cartilage.

We prepared iodixanol solutions (molecular weight (MW)=1.55 kDa, concentration=420 mM, charge=0, osmolality=300 mOsm/kgH2O, volume=600 μL, GE Healthcare, Netherlands) enriched with protease inhibitors (5mM) to study the axial diffusion through cartilage and the cartilage-bone interface. Since iodixanol is a neutral contrast agent, the effect of cartilage charge on molecular transport was eliminated. Immediately post-harvest, the osteochondral plugs were wrapped using plastic shrinking sleeves to prevent lateral diffusion (Figure 7.1).

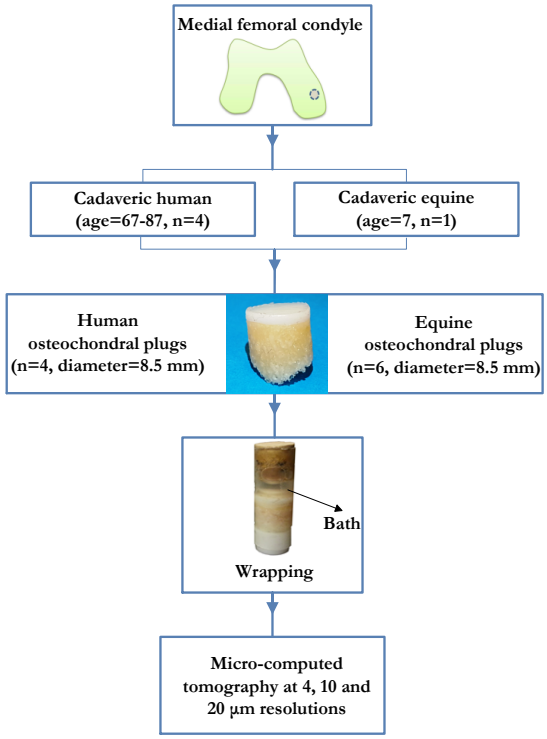

Figure 7.1. Preparing samples for the micro-CT scanning: osteochondral plugs were extracted from four cadaveric human medial femoral condyles and one cadaveric equine medial femoral condyle. A shrinking sleeve was used to wrap the samples before injecting the contrast agent onto the cartilage surface. Then the samples underwent multi-resolution micro-computed tomography.

7.2.1.2. QUANTITATIVE MICRO-CT

To study the transport of iodixanol across cartilage and the cartilage-bone interface, we used a micro-CT scanner (Quantum FX, Perkin Elmer, USA, spatial resolution of 20 µm3 voxel size, scan time= 2 min, tube voltage= 90 kV and tube current=180 µA, number of projections=3600) and captured images at t-1 (before injection of iodixanol solution), t0 (point of injection of iodixanol solution), t= 12, 24, 48 and 72 hours within the field of views consisting of bath, cartilage, and subchondral bone (Figure 7.2A).

The projected images were transformed automatically to 3D reconstructed files using in-built software of the micro-CT machine (Quantum FX). After rigid image registration based on the t0 images, the 3D reconstructed files were converted to a series of 2D images for further analyses (Analyze 11.0). We used Gaussian blurring 3D filter (radius=3) to minimize the noise and then selected 20 middle slices of the 2D stack and created rectangular regions of interest (ROI) in FIJI (free software for image analyses), which comprised the bath, cartilage, and subchondral plate. The t-1 images were locally thresholded (Bernsen) using BoneJ (plugin of FIJI) to calculate the thickness and porosity of the subchondral plate/calcified cartilage as well as the thickness of uncalcified cartilage (Figure 7.2B and Table 7.1). The subchondral plate/calcified cartilage zone was defined as the region lying above the region where the trabecular structure could be easily pinpointed. The mean of the average grey values of the subchondral plate/calcified cartilage at t0 in 20 selected slices was subtracted from the mean average grey values at the later time points to measure the diffusion. The relationship between the diffusion at 72 hours with the micro-architecture of subchondral plate/calcified cartilage, i.e. porosity and thickness, was also investigated.

7.2.1.3. QUALITATIVE MICRO-CT

To qualitatively visualize the diffusion at the cartilage-bone interface we also performed micro-CT scan using the previously mentioned micro-CT parameters but with higher spatial resolution of 10 μm3. To visualize the cartilage-bone interface with ultra-high resolution phoenix nanotom micro-CT was used (GE, USA, tube voltage= 70 kV tube current=110 μA, 4 μm^3 voxel size, scan time= 2 hours, field of view: 4 mm).

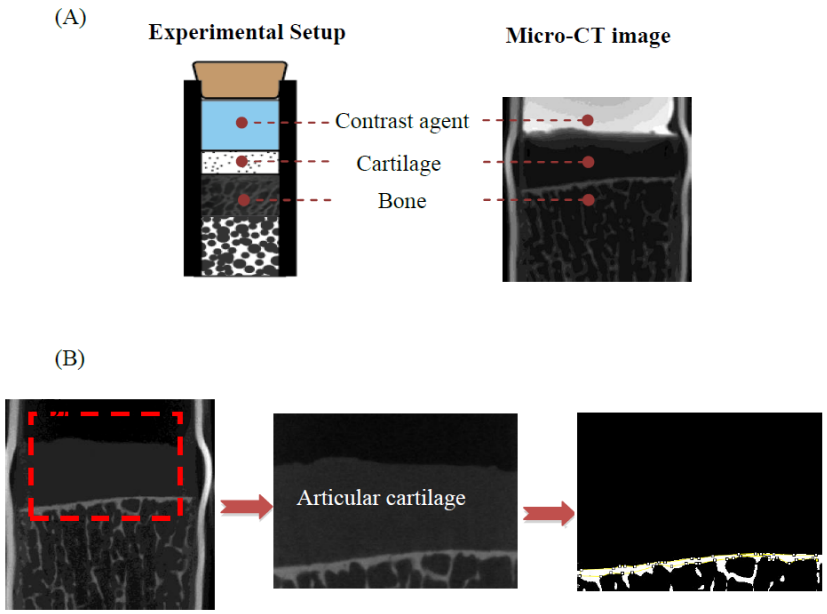

Figure 7.2. Micro-computed tomography image with spatial resolution of 20 μm^3 (A). Local thresholding was employed before injection of contrast agent to calculate the thickness and porosity of the subchondral bone plate/calcified cartilage (B).

Table 7.1. Cartilage thickness, subchondral plate/calcified cartilage thickness and porosity for human samples and for equine samples.

	Sample	Cartilage thickness (μm)	Subchondral plate/calcified cartilage thickness (μm)	Subchondral plate/calcified cartilage porosity (%)
Human	1	2500	175	4.8
	2	2700	115	6.4
	3	2100	186	4.0
	4	2800	147	8.1
Equine (donor 1)	1	700	178	12.1
	2	1100	468	7.6
	3	830	117	17.2
	4	1320	193	5.1
	5	1190	175	3.5
	6	2100	332	1.5
Equine (donor 2)	1	1800	115	6
	2	1300	153	10
	3	1108	112	6.1
	4	1228	427	2.8
	5	2560	738	3
Equine (donor 3)	1	900	235	2
	2	1611	350	7.5
	3	1800	545	3.2
	4	1240	525	4.9
	5	2246	850	1.5
	6	2070	900	1

7.3. RESULTS

The thickness of cartilage for human and equine samples was 2525±310 μm and 1476±537 μm, respectively. For human samples the thickness and porosity of the subchondral plate were 155.7±31.3 μm and 5.8±1.8 % and for equine samples the thickness and porosity of the subchondral plate were 377.2±260.1 μm and 5.6±4.3 % (Table 7.1).

Diffusion of iodixanol from uncalcified cartilage to the subchondral bone via the calcified cartilage layer for both the human and equine samples was confirmed (Figure 7.3 and 7.4). Low cartilage thickness, high subchondral plate/calcified cartilage porosity and low subchondral plate/calcified cartilage thickness are factors contributing to diffusion (Table 7.1, Figure 7.5A and 7.5B). In the human samples, we observed the steepest rise in the diffusion within the subchondral plate/calcified cartilage until t=24 h (Figure 7.5A). After 24 hours, the diffusion curves tended to reach near-equilibrium, achieving the highest average grey value at 72 hours. For all time points, the average grey values were the highest in sample 2 (human), which has the lowest thickness of the subchondral plate/calcified cartilage (Figure 7.5A and Table 7.1). Samples 1 and 3 (human) showed diffusion patterns that were very similar to each other (Figure 7.5A), as well as similar morphological characteristics (Table 7.1). Like the observations regarding human samples, the diffusion curves in the equine samples reach near-equilibrium at 72 hours (Figure 7.5B).

Plots of near-equilibrium diffusion values versus morphological features (porosity and thickness) of the subchondral plate/calcified cartilage for both equine and human samples suggested a link between diffusion behavior of the neutral solute and the micro-architecture of the subchondral plate/calcified cartilage (Figure 7.6). To investigate the relationship of cartilage thickness and subchondral plate/calcified thickness and porosity on diffusion we performed multi-regression

analysis. This analysis was not possible to perform on human samples due to relatively low sample number. Multi-regression on equine samples showed strong correlation (multiple R=0.97) with significance of porosity (p-value<5e-7) and thickness (p-value<0.05) of subchondral plate/calcified cartilage on diffusion. Diffusion in human samples did not correlate with porosity as compared to equine samples (Figure 7.6A, R^2= 0.24 vs. R^2= 0.90). Nevertheless, diffusion in the human samples had a stronger correlation with the thickness of subchondral plate/calcified cartilage compared to equine samples (Figure 7.6B, R^2 = 0.92 vs. R^2= 0.50).

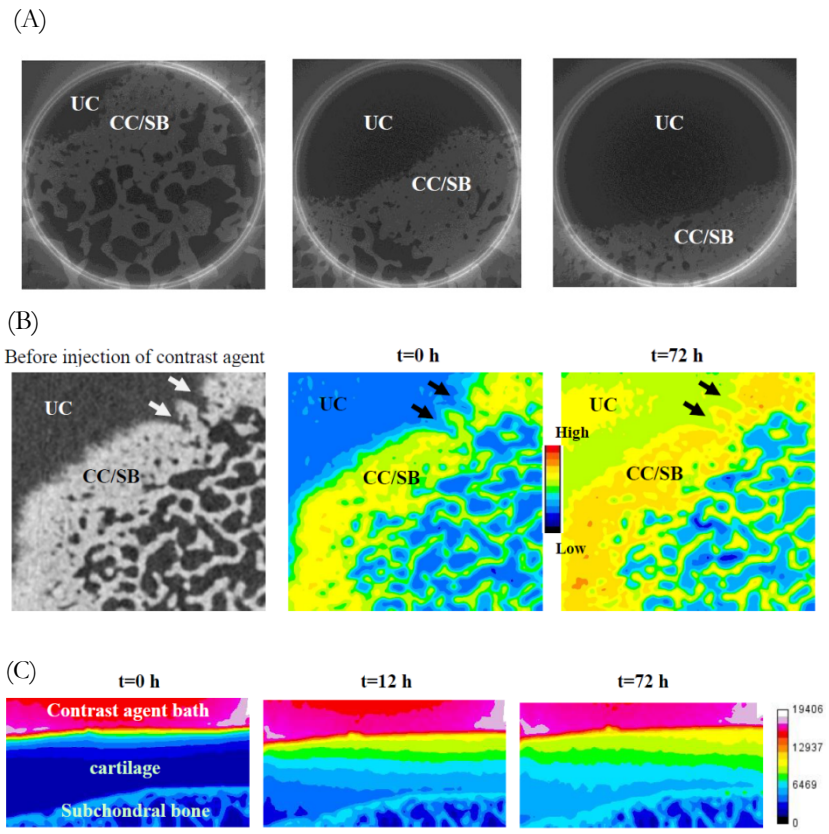

Figure 7.3. Ultra-high micro-CT (4 μm^3 spatial resolution) was used to highlight the interface of cartilage and subchondral bone plate in three representative slices in a human osteochondral plug. The diffusion at the interface of uncalcified cartilage (UC) and subchondral bone plate (SB)/calcified cartilage (CC) is depicted (A). The protrusion of uncalcified cartilage into the calcified cartilage and mineralized region (arrows) facilitates the diffusion (10 μm^3 spatial resolution) (B). The progress of the diffusion front wave is shown at different time points (20 μm^3 spatial resolution) (C).

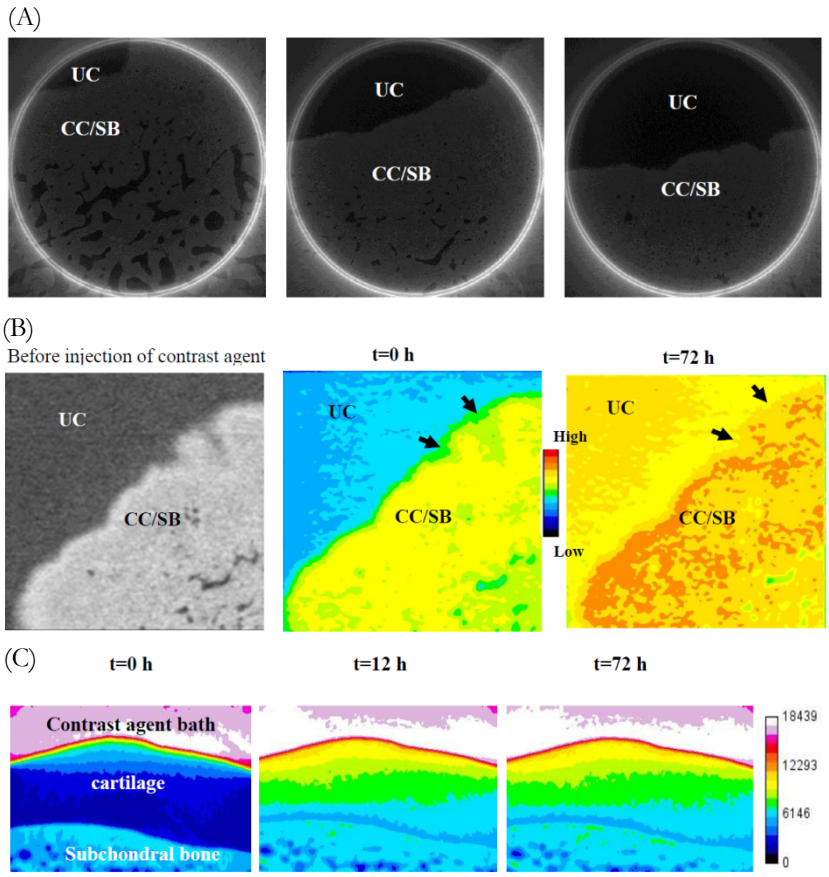

Figure 7.4. Ultra-high micro-CT (4 μm³ spatial resolution) was used to highlight the interface of cartilage and subchondral bone plate in three representative slices in an equine osteochondral plug. The diffusion at the interface of uncalcified cartilage (UC) and subchondral bone plate (SB)/calcified cartilage (CC) is depicted (A). The protrusion of uncalcified cartilage into the calcified cartilage and mineralized region (arrows) facilitates the diffusion (10 μm³ spatial resolution) (B). The progress of the diffusion front wave is shown at different time points (20 μm³ spatial resolution) (C).

(A)

(B)

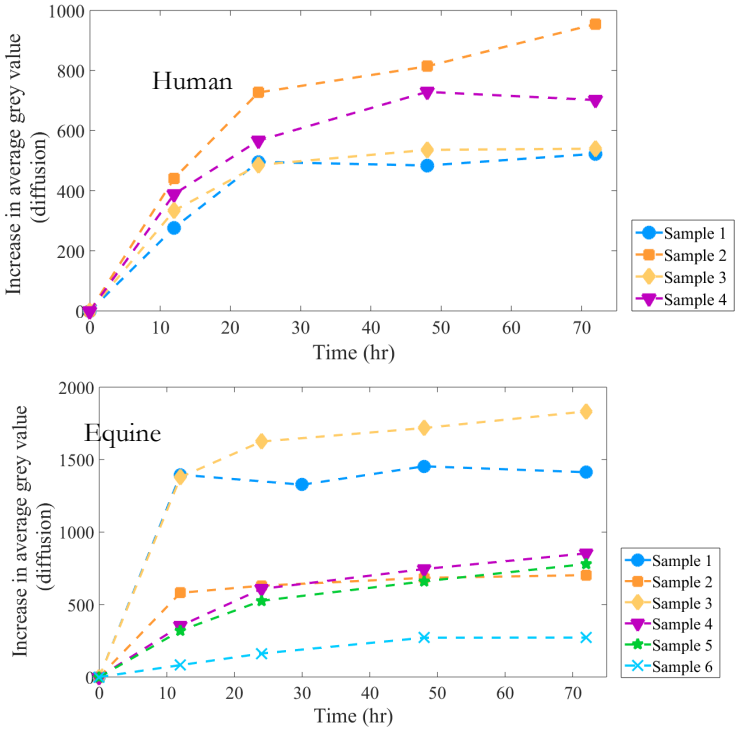

Figure 7.5. Average grey values (diffusion) in the subchondral plate/calcified cartilage over time for human (A) and equine samples (B).

(A)

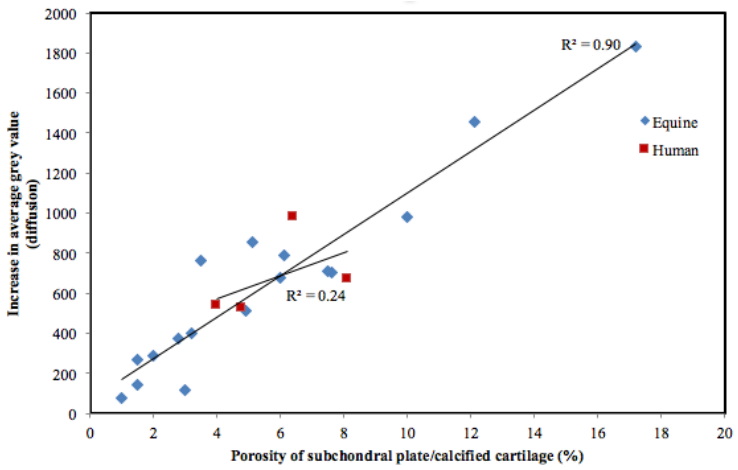

(B)

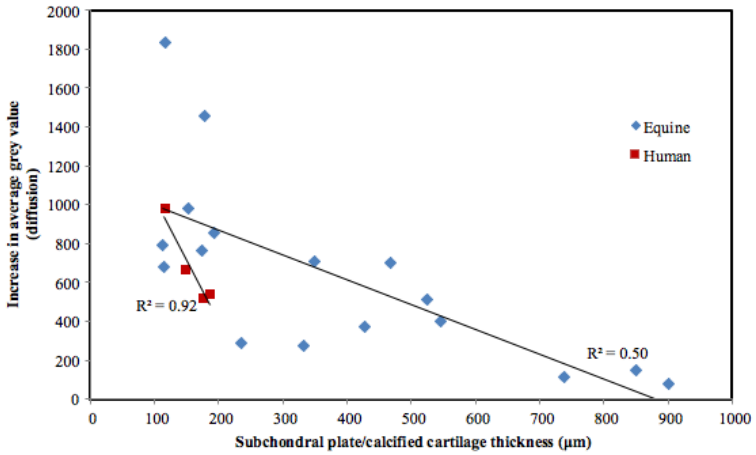

Figure 7.6. Plot of average grey values (diffusion) at 72 hours in the subchondral plate/calcified cartilage versus subchondral plate/calcified cartilage porosity (A) and subchondral plate/calcified cartilage thickness (B).

7.4. DISCUSSION

In this study, we have observed the direct diffusion between articular cartilage and subchondral bone plate/calcified cartilage in human as well as equine osteochondral plugs when a finite volume of bath containing a neutral solute was inserted at the cartilage surface. Furthermore, we confirmed that the molecular transport to the subchondral bone plate depends on the morphological parameters of both uncalcified cartilage and subchondral bone plate. We identified cartilage thickness and porosity and thickness of subchondral bone plate as the factors influencing the transport. Porosity and thickness of the subchondral plate in horse samples were found to have more effect on the diffusion across osteochondral interface compared to cartilage thickness. Although in human samples small variation in subchondral plate porosity was observed, the effect of subchondral plate on diffusion was more tangible.

The electrically neutral molecules (MW=1.55 kDa) used in our study allowed excluding the effects of fixed charges entrapped in the articular cartilage and the resulting electro-mechanically induced transport. Therefore, in the current study molecular friction between the diffusing solute and the extracellular matrix of the cartilage, i.e. water content, collagen fibrils and proteoglycans as well as the morphology of subchondral plate (porosity and thickness) are the only limiting factors for neutral molecular transport between cartilage and underlying bone. This implies that the diffusion mechanism in our study can be described as a Fickean diffusion process. In human samples with similar thickness of the articular cartilage, we observed higher near-equilibrium increase in average grey value (diffusion, 72 hours) (Figure 7.5A), which is likely due to the thinner subchondral plate/calcified cartilage (28% difference, Table 7.1). Similar diffusion behavior in human samples before 12 hours (Figure 7.5A) may be linked to the fact that similar cartilage thicknesses could lead to similar

frictional loss in driving force eventually causing similar diffusion behavior in the subchondral plate/calcified cartilage (Table 7.1).

The structural changes such as thinning of the subchondral plate in early OA [3, 5] and subchondral bone sclerosis observed in advanced OA may alter the transport rate causing interruptions in trans-signaling between cartilage and subchondral bone plate. Our study also emphasizes the importance of structure of the subchondral bone on the transport across osteochondral interface. Human samples that represent similar thickness and porosity of the subchondral plate/calcified cartilage showed very similar diffusion behavior in all time points (Figure 7.5A and Table 7.1). Enhanced porosity creates more access for the solutes to diffuse across the subchondral plate since the pores filled with soft tissue with high water content are more permeable than the mineralized regions of subchondral plate. A previous study on murine model of OA also suggested that the transport between cartilage and subchondral plate increases due to thinning of cartilage and subchondral plate [2], which is in agreement with our observations. It should be borne in mind that the inter-connectivity and tortuosity of the pores has not been investigated in this study, but could itself play an integral role in solutes distribution and partitioning. Since both young (equine) and old and perhaps slightly OA joints (human) were used in this study we can draw the conclusion that the interface of cartilage and subchondral bone plate is permeable to at least relatively small solutes (less than 2 kDa) in both healthy and slightly degenerated joints. To our best of knowledge, we were the first who investigated the transport of relatively larger solutes across osteochondral interface compared to other previous studies [13, 14] in both human and horse knees taking the morphology of the cartilage and bone into account.

Whereas the current study strived to be as thorough as possible, it is inevitably associated with some limitations. First, the calcified cartilage and subchondral plate could not be differentiated clearly

from each other using micro-CT images, especially when the contrast agent (iodixanol) diffused through it which limited the capability of studying the diffusion separately in these two zones. Second, although our study used largest solute among the similar studies and applied in large animal model and human, the diffusion of vital signaling macromolecules may be studied by labeling them with contrast agent. Furthermore, the effect of solute charge on diffusion in the subchondral plate/calcified cartilage could be investigated in future studies to enable studying charged signaling molecule transfer across the osteochondral interface.

The present study sheds light on the transport of a neutral solute across the interface of articular cartilage and subchondral plate. Our findings confirm the direct cross-talk between cartilage and subchondral bone/calcified cartilage in both human samples (slightly osteoarthritic) and equine samples (healthy) when applying a neutral contrast agent to nullify the mechano-electrical-affected diffusion in the articular cartilage. Besides, we highlighted that diffusion in the subchondral plate/calcified cartilage could be estimated when micro-architecture data concerning porosity and thickness of the subchondral plate/calcified cartilage and cartilage thickness are available.

7.5. ACKNOWLEDGEMENTS

This work was supported by a grant from Dutch Arthritis Foundation (LRP-22). The authors are grateful to Mr. Michael Afanasyev and Mr. Wim Verwaal for their assistance during high-resolution micro-CT scans.

7.6. **REFERENCES**

1. Weinans H., Siebelt M., Agricola R., Botter S.M., Piscaer T.M., Waarsing J.H., *Pathophysiology of peri-articular bone changes in osteoarthritis.* Bone, 2012. **51**(2): p. 190-6.
2. Pan J., Wang B., Li W., Zhou X., Scherr T., Yang Y., Price C., Wang L., *Elevated cross-talk between subchondral bone and cartilage in osteoarthritic joints.* Bone, 2012. **51**(2): p. 212-7.
3. Intema F., Hazewinkel H.A., Gouwens D., Bijlsma J.W., Weinans H., Lafeber F.P., Mastbergen S.C., *In early OA, thinning of the subchondral plate is directly related to cartilage damage: results from a canine ACLT-meniscectomy model.* Osteoarthritis Cartilage, 2010. **18**(5): p. 691-8.
4. Li B., Aspden R.M., *Mechanical and material properties of the subchondral bone plate from the femoral head of patients with osteoarthritis or osteoporosis.* Ann Rheum Dis, 1997. **56**(4): p. 247-54.
5. Botter S.M., van Osch G.J., Clockaerts S., Waarsing J.H., Weinans H., van Leeuwen J.P., *Osteoarthritis induction leads to early and temporal subchondral plate porosity in the tibial plateau of mice: an in vivo microfocal computed tomography study.* Arthritis Rheum, 2011. **63**(9): p. 2690-9.
6. Botter S.M., *Dynamic Subchondral Bone Changes in Murine Models of Osteoarthritis.* PhD thesis, 2010.
7. Sniekers Y.H., Intema F., Lafeber F.P., van Osch G.J., van Leeuwen J.P., Weinans H., Mastbergen S.C., *A role for subchondral bone changes in the process of osteoarthritis; a micro-CT study of two canine models.* BMC Musculoskelet Disord, 2008. **9**: p. 20.
8. Intema F., Sniekers Y.H., Weinans H., Vianen M.E., Yocum S.A., Zuurmond A.M., DeGroot J., Lafeber F.P., Mastbergen S.C., *Similarities and discrepancies in subchondral bone structure in two differently induced canine models of osteoarthritis.* J Bone Miner Res, 2010. **25**(7): p. 1650-7.
9. Westacott C., *Interactions between subchondral bone and cartilage in OA. Cells from osteoarthritic bone can alter cartilage metabolism.* J Musculoskelet Neuronal Interact, 2002. **2**(6): p. 507-9.
10. Radin E.L., Rose R.M., *Role of subchondral bone in the initiation and progression of cartilage damage.* Clin Orthop Relat Res, 1986(213): p. 34-40.
11. Pan J., Zhou X., Li W., Novotny J.E., Doty S.B., Wang L., *In Situ measurement of transport between subchondral bone and articular cartilage.* Journal of orthopaedic research : official publication of the Orthopaedic Research Society, 2009. **27**(10): p. 1347-1352.
12. Siebelt M., Waarsing J.H., Groen H.C., Muller C., Koelewijn S.J., de Blois E., Verhaar J.A., de Jong M., Weinans H., *Inhibited osteoclastic bone resorption through alendronate treatment in rats reduces severe osteoarthritis progression.* Bone, 2014. **66**: p. 163-70.
13. Arkill K.P., Winlove C.P., *Solute transport in the deep and calcified zones of articular cartilage.* Osteoarthritis Cartilage, 2008. **16**(6): p. 708-14.
14. Burstein D., Velyvis J., Scott K.T., Stock K.W., Kim Y.-J., Jaramillo D., Boutin R.D., Gray M.L., *Protocol issues for delayed Gd(DTPA)2--enhanced*

MRI (dGEMRIC) for clinical evaluation of articular cartilage. Magnetic Resonance in Medicine, 2001. **45**(1): p. 36-41.

15. Lyons T.J., McClure S.F., Stoddart R.W., McClure J., *The normal human chondro-osseous junctional region: evidence for contact of uncalcified cartilage with subchondral bone and marrow spaces.* BMC Musculoskelet Disord, 2006. **7**: p. 52.
16. Galbusera F., Brayda-Bruno M., Wilke H.-J., *Is post-contrast MRI a valuable method for the study of the nutrition of the intervertebral disc?* Journal of Biomechanics, 2014. **47**(12): p. 3028-3034.
17. Gullbrand S.E., Peterson J., Mastropolo R., Roberts T.T., Lawrence J.P., Glennon J.C., DiRisio D.J., Ledet E.H., *Low rate loading-induced convection enhances net transport into the intervertebral disc in vivo.* Spine J, 2015. **15**(5): p. 1028-33.
18. Gullbrand S.E., Peterson J., Ahlborn J., Mastropolo R., Fricker A., Roberts T.T., Abousayed M., Lawrence J.P., Glennon J.C., Ledet E.H., *ISSLS Prize Winner: Dynamic Loading-Induced Convective Transport Enhances Intervertebral Disc Nutrition.* Spine (Phila Pa 1976), 2015. **40**(15): p. 1158-64.
19. Rutges J.P.H.J., Jagt van der O.P., Oner F.C., Verbout A.J., Castelein R.J.M., Kummer J.A., Weinans H., Creemers L.B., Dhert W.J.A., *Micro-CT quantification of subchondral endplate changes in intervertebral disc degeneration.* Osteoarthritis and Cartilage, 2011. **19**(1): p. 89-95.

CHAPTER 8

NEUTRAL SOLUTE TRANSPORT ACROSS OSTEOCHONDRAL INTERFACE: A FINITE ELEMENT APPROACH

This chapter is published as a scientific paper:

Arbabi V., **Pouran B**., Weinans H., Zadpoor A.A. *Neutral solute transport across osteochondral interface: a finite element approach*. Journal of Biomechanics, 2016. 49, 3833-3839.

Chapter 8

ABSTRACT

Investigation of the solute transfer across articular cartilage and subchondral bone plate could nurture the understanding of the mechanisms of osteoarthritis (OA) progression. In the current study, we approached the transport of neutral solutes in human (slight OA) and equine (healthy) samples using both computed tomography and biphasic-solute finite element modeling. We developed a multi-zone biphasic-solute finite element model (FEM) accounting for the inhomogeneity of articular cartilage (superficial, middle and deep zones) and subchondral bone plate. Fitting the FEM model to the concentration-time curves of the cartilage and the equilibrium concentration of the subchondral plate/calcified cartilage enabled determination of the diffusion coefficients in the superficial, middle and deep zones of cartilage and subchondral plate. We found slightly higher diffusion coefficients for all zones in the human samples as compared to the equine samples. Generally, the diffusion coefficient in the superficial zone of human samples was about 3-fold higher than the middle zone, the diffusion coefficient of the middle zone was 1.5-fold higher than that of the deep zone, and the diffusion coefficient of the deep zone was 1.5-fold higher than that of the subchondral plate/calcified cartilage. Those ratios for equine samples were 9, 2 and 1.5, respectively. Regardless of the species considered, there is a gradual decrease of the diffusion coefficient as one approaches the subchondral plate, whereas the rate of decrease is dependent on the type of species.

Chapter 8

8.1. INTRODUCTION

Molecular exchange (diffusion) between articular cartilage and the underlying bone has been identified as one of the parameters that changes during osteoarthritis (OA) progression [1, 2]. The pathways for the molecular transport in diarthrodial joints span from direct cross-talk between articular cartilage and underlying subchondral bone plate to transport via synovial fluid [3, 4]. Few studies addressed the direct cross-talk between uncalcified cartilage and calcified cartilage [5] and between calcified cartilage and subchondral plate [3, 4], whereas vast majority of the studies dealing with molecular transport were mostly centered upon morphology-driven transport between intervertebral disk (IVD) and endplates [6, 7]. Two consecutive studies have shown the direct diffusion between calcified and non-calcified cartilage and subchondral plate in a murine model and have highlighted how remarkable reduction in subchondral plate and cartilage thickness post-OA enhanced the transport rate [3, 4]. Assessment of the Fickean molecular transport in OA and healthy joints of mice [3, 4] and uncalcified cartilage and calcified cartilage of horses [5] was achieved by fitting a simplified analytical formula to the fluorescent intensity versus time curves based on fluorescence loss induced by photobleaching (FLIP) technique and fluorescent intensity tracing technique to obtain the diffusion coefficient of sodium fluorescein (376 Da, charge=0). Molecular transport at osteochondral interface (OI) depends not only on the concentration and distribution of the exctracellular matrix (ECM) components but also on the morphological features, e.g. porosity and thickness of the calcified cartilage and subchondral plate, which determine the mass transfer resistance at the cartilage-bone interface [1, 3, 8, 9].

Previously, we developed biphasic-solute and multiphasic finite element models to study the diffusion of neutral and charged solutes across different zones of articular cartilage (chapters 3 and 9) [10, 11]. Those models allowed obtaining the diffusion coefficients and fixed charge density in various cartilage layers, i.e. superficial, middle and deep zones, and also shed light on the effect of inhomogeneity of articular cartilage across its thickness on the solute

diffusion behavior. Besides, the application of the models capable of predicting the diffusive properties of cartilage in different zones, the models could potentially be extended to the cartilage-bone interface.

The current work, for the first time, introduces a combination of experimental set-up and computational models to enable studying the diffusion of neutral solutes across cartilage and osteochondral interface. The experimental setup includes monitoring the diffusion of a neutral solute from a finite bath inserted on the cartilage surface of cadaveric human and equine osteochondral plugs using serial micro-computed tomography (micro-CT) images. The computational models were established using a multi-zone biphasic-solute mixture approach. Determination of diffusion coefficients in various cartilage layers and subchondral bone was performed by simultaneously fitting the computational model to the experimental findings.

8.2. METHODOLOGY

8.2.1. EXPERIMENTS

The descriptive details of the experiments consisting of sample preparation, image acquisition, and image processing are presented elsewhere (chapter 6) [8]. Osteochondral plugs were obtained (diameter = 8.5 mm) from four cadaveric human (68-90 years old) femoral condyles (one sample from each) and one equine femoral condyle (six samples) (Figure 8.1A). Upon harvest, the osteochondral plugs were wrapped with shrinking plastic sleeve to enable axial diffusion

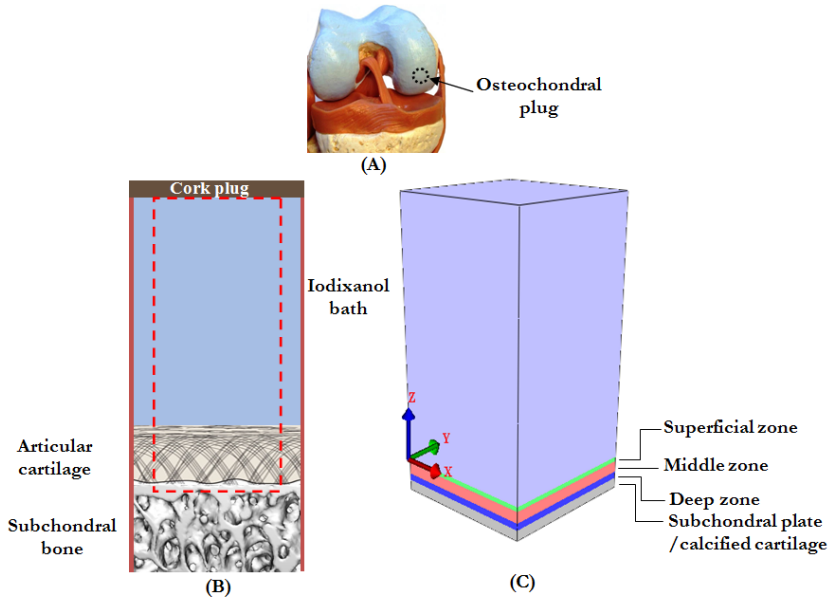

Figure 8.1. Schematics of A) femoral condyle and osteochondral sample location B) sample consisting of finite bath of iodixanol, articular cartilage and subchondral plate C) multi-zone biphasic-solute model**.**

of a neutral computed tomography (CT) contrast agent (iodixanol, 1551 Da, 290 mOsm/kg H2o, charge=0, 420 mM). Finite volumes of the iodixanol solution was placed on the cartilage surface and its diffusion across the cartilage and subchondral bone was monitored up to 72 hours using micro-CT (Qauntum FX, USA) (Figure 8.1B).

The 3D reconstructed images (until 72 hours) were registered and after applying Gaussian filter (radius=2) 20 stacks of TIFF images in the middle were selected. Average grey values within the cartilage and subchondral bone were converted to the actual iodixanol concentration using a linear calibration function. The morphological parameters, i.e. porosity and thickness of the subchondral plate/calcified cartilage, were calculated by locally thresholding the micro-CT image before injecting the contrast agent (Table 8.1).

Table 8.1. Morphological specifications i.e. of cartilage and subchondral plate/calcified cartilage in A) human samples and B) equine samples [8].

(A)

Sample	Cartilage thickness (mm)	Subchondral plate /calcified cartilage thickness (mm)	Subchondral plate /calcified cartilage porosity (%)
1	2.5	0.175	4.8
2	2.7	0.115	6.4
3	2.1	0.186	4.0
4	2.8	0.147	8.1

(B)

Sample	Cartilage thickness (mm)	Subchondral plate /calcified cartilage thickness (mm)	Subchondral plate /calcified cartilage porosity (%)
1	0.7	0.178	12.1
2	1.1	0.468	7.6
3	0.83	0.117	17.2
4	1.32	0.193	5.1
5	1.19	0.175	3.5
6	2.1	0.332	1.5

8.2.2. COMPUTATIONAL MODEL

Finite element models based on biphasic-solute mixture models can describe the transport of neutral solutes across biphasic tissues [12, 13]. Considering $\mathbf{T}$ as the Cauchy stress tensor for the mixture, $\mathbf{v}^s$ as the velocity of the solid matrix and $\mathbf{w}$ as the volume flux of the solvent (water) relative to the solid (tissue matrix), the conservation of linear momentum and mass for the mixture (tissue) can be described as:

$$\mathrm{div}\,\mathbf{T}=0 \tag{7.1}$$

$$\text{div}\,(\mathbf{v}^s + \mathbf{w}) = 0 \tag{7.2}$$

and the balance of mass for the solute can be given as:

$$\frac{1}{J}\frac{D^s}{Dt}(J\varphi^w\tilde{\kappa}\tilde{c}) + \text{div}\mathbf{j} = 0 \tag{7.3}$$

where $J = \det \boldsymbol{F}$, $\boldsymbol{F}$ is the deformation gradient of the solid matrix, $D^s(\cdot)/Dt$ is the material time derivative in the spatial frame, $\mathbf{j}$ is the molar flux of solute relative to the solid, φ^w is volume fraction of the solvent, $\tilde{\kappa}$ is the effective solubility, c is the solute concentration and ($\tilde{c} = c/\tilde{\kappa}$) is the effective solute concentration, which is continuous across boundaries and contact surfaces [13, 14]. The relative molar solute flux, $\mathbf{j}$, is given as:

$$\mathbf{j} = \tilde{\kappa}\mathbf{d}.\left(-\varphi^w \text{grad}\tilde{c} + \frac{\tilde{c}}{d_0}\mathbf{w}\right) \tag{7.4}$$

while

$$\tilde{\mathbf{k}} = \left[\mathbf{k}^{-1} + \frac{R\theta}{\varphi^w}\frac{\tilde{\kappa}\tilde{c}}{d_0}\left(\mathbf{I} - \frac{\mathbf{d}}{d_0}\right)\right]^{-1} \tag{7.5}$$

where p is the fluid pressure, $\tilde{\mathbf{k}}$ is the hydraulic permeability tensor for the flow of the solution, i.e. solvent plus solute through the solid matrix, $\mathbf{k}$ is the hydraulic permeability tensor for the flow of pure solvent through the solid matrix, $\mathbf{d}$ is the diffusion coefficient tensor of the solute in the mixture, d_0 is the diffusion coefficient tensor in absence of the solid phase, R is the universal gas constant, θ is the absolute temperature, and φ_r^s is the volume fraction of the solid phase in the reference configuration [13, 15, 16].

Using the principle of virtual work, the above-mentioned equations could be solved simultaneously in an open-source finite element modeling platform FEBio 2.2.6 to describe the transport of a neutral solute through a mixture.

8.2.2.1. **GEOMETRY**

Osteochondral plugs contain two distinct phases namely uncalcified cartilage and subchondral plate/calcified cartilage. Previously, we have shown that a multi-zone biphasic-solute model could track the axial diffusion behavior of a neutral solute across articular cartilage (chapter 3) [10]. Therefore, we introduced a multi-zone model consisting of four different zones of superficial (20% of the cartilage thickness), middle (50% of the cartilage thickness), deep (30% of the cartilage thickness) [17] and subchondral plate/calcified cartilage (thickness obtained based on micro-CT [8]) to account for the inhomogeneity of osteochondral plugs (Figure 8.1C and Table 8.1). The overlaying iodixnol bath was 12 mm in height for all samples corresponding to the actual experiments. We used an 8-node trilinear hexahedral element, which was refined in the vicinity of the interfaces. For each cartilage zone and subchondral plate/calcified cartilage, individual diffusion coefficients were calculated.

8.2.2.2. **MECHANICAL AND PHYSICAL PROPERTIES**

Cartilage and subchondral plate/calcified cartilage were modeled as neo-Hookean materials with effective solubility ($\tilde{\kappa}$) of 1 while the Young's modulus was chosen to be high enough to correspond to the realistic experimental deformations resulting from the osmotic pressure of the external bath. The diffusion coefficient tensor for bath, cartilage and bone was considered isotropic. The actual diffusion coefficient of iodixanol within the bath was 250 $\mu m^2/s$ according to the previous studies [10, 18]. Four different values of water content for each cartilage zone as well as for subchondral plate/calcified cartilage were used: 0.8 for the superficial zone, 0.7 for the

middle zone, 0.6 for the deep zone [17] and 0.2 for the subchondral plate/calcified cartilage [19] .

8.2.2.3. **INITIAL AND BOUNDARY CONDITIONS**

Actual experimental solute concentration in the bath (420 mM) was prescribed as the initial condition. Effective pressure ($p_{effective}$) is continuous across boundaries [13, 20] and is expressed as:

$$p_{effective} = p - R\theta\Phi c \tag{7.6}$$

where $R = 8.314 \times 10\text{-}6$ mJ/nmol·K and Φ is the osmotic coefficient that was set to 1. The ambient fluid pressure and absolute temperature were p =101 kPa and θ =298 K.

8.2.2.4. **FITTING METHOD**

To obtain the diffusion coefficients of different zones of uncalcified cartilage and subchondral plate/calcified cartilage regarded as two distinct phases, we fitted the computational data to the experimental concentration-time curves for the cartilage and to the equilibrium concentration point at 72 hours for subchondral plate/calcified cartilage. The latter is done since distinguishing the calcified cartilage from subchondral plate is infeasible using micro-CT (two mineralized materials) and that they are different materials in terms of diffusive properties [4]. Direct scanning of the parameter space was used to minimize the root mean square error (RMSE) values between computational and experimental concentration-time data (uncalcified cartilage) and between computational and experimental equilibrium concentration (subchondral plate/calcified cartilage) to obtain the diffusion coefficients of all uncalcifed cartilage zones as well as subchondral plate/calcified cartilage. This guarantees that all possible solutions can be found within the scanning resolution.

8.3. **RESULTS**

The near-equilibrium concentration (72 hours) in the cartilage and subchondral plate/calcified cartilage was 32.73±7.36 % (mean ± SD) and 5.16±1.84 % (mean ± SD) for the human samples and 41.4 ±7.05% (mean ± SD) and 8.08±4.50 % (mean ± SD) for the equine samples (Figure 8.2 and 8.3).

The computational model for the human and equine samples provided satisfactory fits over the experimental data (Figure 8.4 and 8.5). In general, our multi-zone biphasic model provided more robust fits in human samples as compared to equine samples (Table 8.2A-B). The average diffusion coefficients for the superficial, middle, deep zones and subchondral plate/calcified cartilage of the human samples were 5.63±2.05, 2.07±0.78, 1.53±0.30 and 1.22±0.35 $\mu m^2/s$ (Table 8.3A). The average diffusion coefficients for the superficial, middle, deep zones and subchondral plate/calcified cartilage of the equine samples were 4.47±1.4, 0.60±0.34, 0.44±0.29 and 0.36±0.30 $\mu m^2/s$ (Table 8.3B). The ratio of the diffusion coefficients in human samples were as follows: superficial to middle ($D_{Superficial}/ D_{Middle}$): 2.73±0.54, middle to deep (D_{Middle}/ D_{Deep}): 1.35±0.47 and deep to subchondral plate/calcified cartilage (D_{Deep}/ D_{SPCC}):1.28±0.15 (Table 8.4A). The ratio of the diffusion coefficients in equine samples were as follows: superficial to middle ($D_{Superficial}/ D_{Middle}$): 8.70±2.42, middle to deep (D_{Middle}/ D_{Deep}):1.61±0.60 and deep to subchondral plate/calcified cartilage (D_{Deep}/ D_{SPCC}):1.50±0.33 (Table 8.4B).

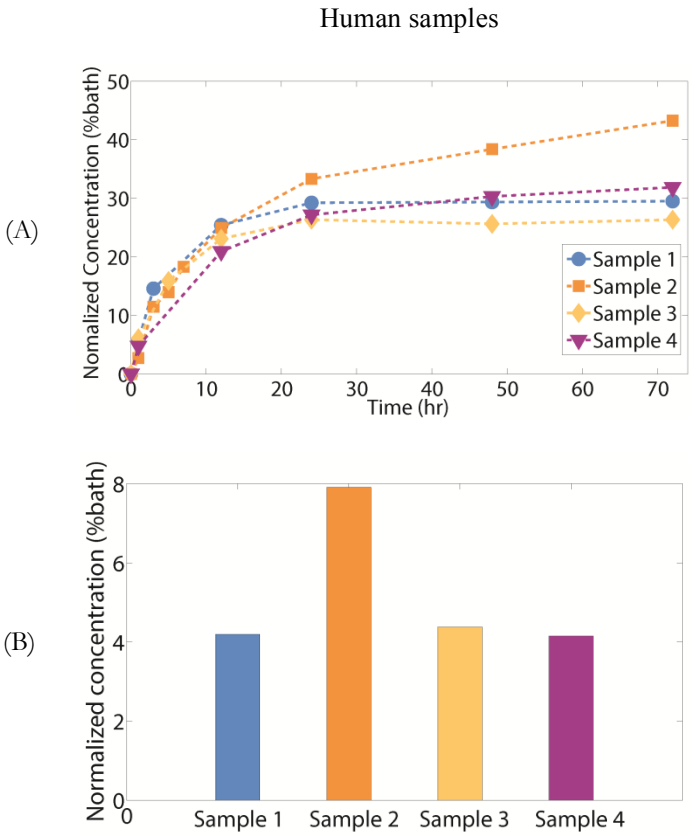

Figure 8.2. Plot of A) normalized concentration versus time of iodixanol in human cartilage and B) normalized equilibrium concentration in human subchondral plate/calcified cartilage.

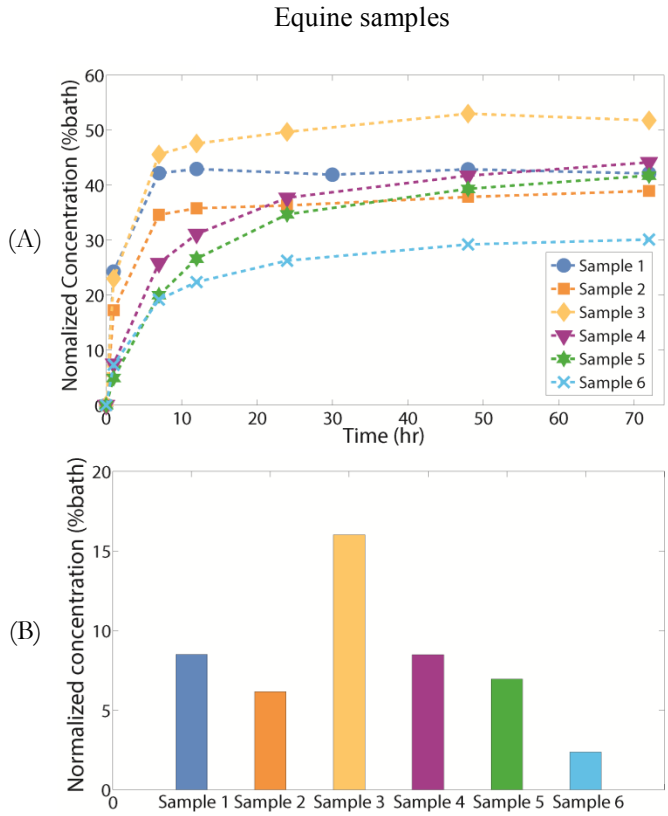

Figure 8.3. Plot of A) normalized concentration versus time of iodixanol in equine cartilage and B) normalized equilibrium concentration in equine subchondral plate/calcified cartilage.

Human samples

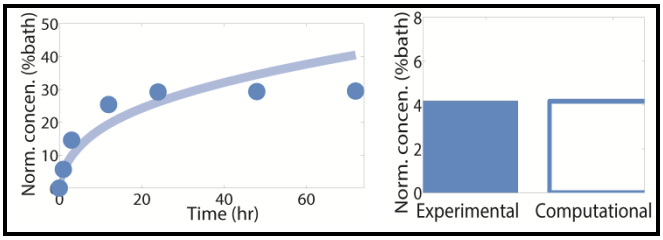

Sample 1

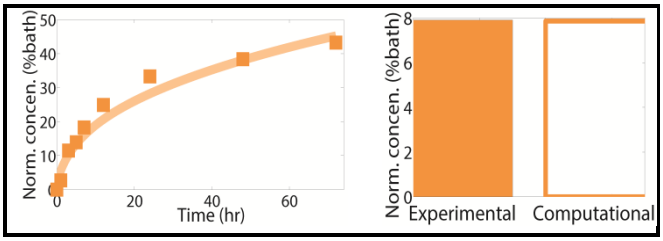

Sample 2

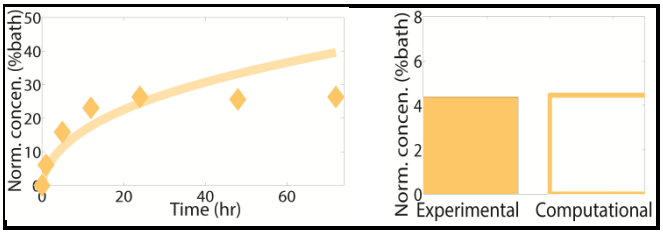

Sample 3

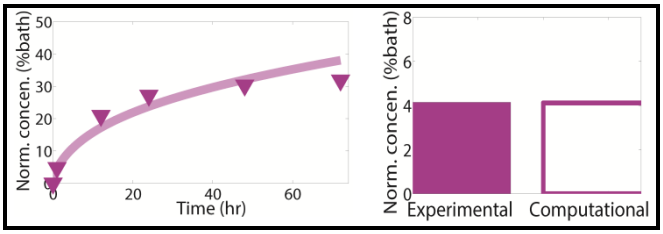

Sample 4

Figure 8.4. Experimental (symbols) and simulated (lines) normalized concentration versus time for human cartilage samples and normalized computational and experimental equilibrium concentration for human subchondral plate/calcified cartilage.

Equine samples

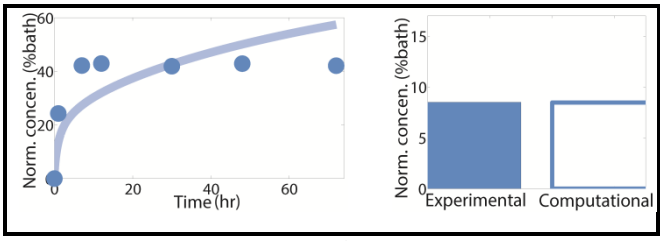

Sample 1

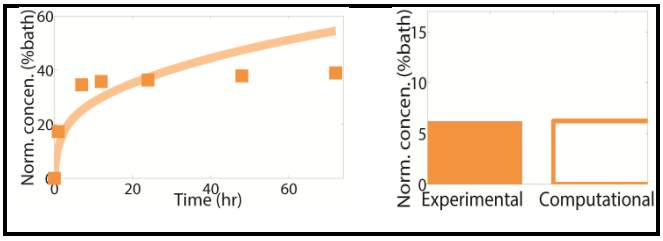

Sample 2

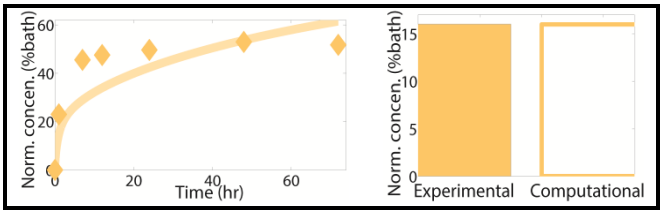

Sample 3

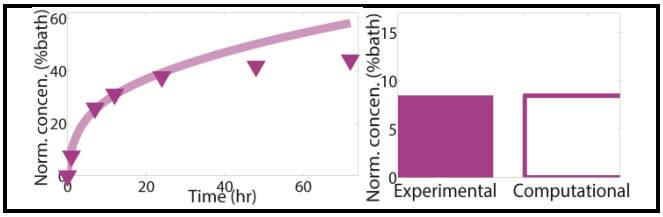

Sample 4

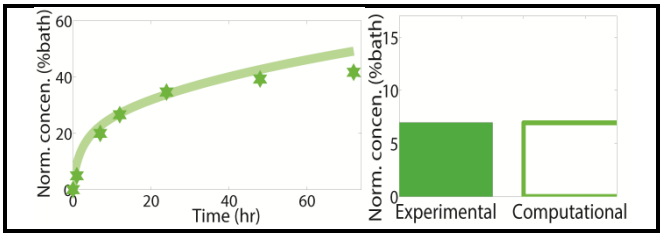

Sample 5

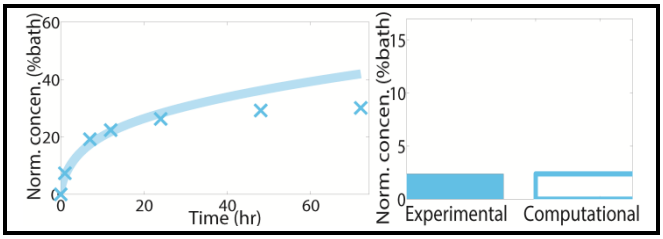

Sample 6

Figure 8.5. Experimental (symbols) and simulated (lines) normalized concentration versus time for equine cartilage samples and normalized computational and experimental equilibrium concentration for equine subchondral plate/calcified cartilage.

Table 8.2. A) RMSE and R^2 to compare the experimental and simulation solute concentration versus time in cartilage and RMSE to compare the experimental and simulation normalized equilibrium concentration in subchondral plate for A) human samples and B) equine samples.

(A)

		Human samples			
		Sample 1	Sample 2	Sample 3	Sample 4
Cartilage	R^2	0.86	0.98	0.85	0.95
	RMSE	0.0599	0.0281	0.0694	0.0377
Subchondral plate /calcified cartilage	RMSE	0.0002	0.0005	0.0007	0.0003

(B)

		Equine samples					
		Sample 1	Sample 2	Sample 3	Sample 4	Sample 5	Sample 6
Cartilage	R^2	0.73	0.80	0.83	0.96	0.97	0.95
	RMSE	0.1114	0.0906	0.1061	0.0680	0.0398	0.0574
Subchondral plate /calcified cartilage	RMSE	0.0003	0.0005	0.0004	0.0001	0.0003	0.0001

Table 8.3. Diffusion coefficients obtained from the multi-zone computational model for superficial, middle, deep and subchondral plate/calcified cartilage zones A) human samples B) equine samples.

	Diffusion coefficient ($\mu m^2/s$), human samples			
	Sample 1	Sample 2	Sample 3	Sample 4
$D_{Superficial}$	6.00	8.00	3.00	5.54
D_{Middle}	1.70	3.10	1.30	2.20
D_{Deep}	1.50	1.50	1.20	1.94
D_{SPCC}	1.20	1.00	0.95	1.72

	Diffusion coefficient ($\mu m^2/s$), equine samples					
	Sample 1	Sample 2	Sample 3	Sample 4	Sample 5	Sample 6
$D_{Superficial}$	4.35	4.25	4.80	3.40	3.00	7.00
D_{Middle}	0.4	0.50	0.44	0.60	0.40	1.30
D_{Deep}	0.18	0.43	0.18	0.55	0.35	0.95
D_{SPCC}	0.12	0.30	0.09	0.48	0.25	0.90

Table 8.4. The ratio of diffusion coefficients of superficial zone to middle zone ($D_{Superficial}/D_{Middle}$), middle zone to deep zone (D_{Middle}/D_{Deep}) and deep zone to subchondral plate/calcified cartilage (D_{Deep}/D_{SPCC}) for A) human samples and B) equine samples.

(A)	Human samples			
	Sample 1	Sample 2	Sample 3	Sample 4
$D_{Superficial}/D_{Middle}$	3.53	2.58	2.31	2.52
D_{Middle}/D_{Deep}	1.13	2.07	1.08	1.13
D_{Deep}/D_{SPCC}	1.25	1.50	1.27	1.13

(B)	Equine samples					
	Sample 1	Sample 2	Sample 3	Sample 4	Sample 5	Sample 6
$D_{Superficial}/D_{Middle}$	10.75	8.5	10.90	5.66	7.50	5.38
D_{Middle}/D_{Deep}	2.22	1.16	2.44	1.09	1.14	1.37
D_{Deep}/D_{SPCC}	1.50	1.43	2.00	1.14	1.40	1.05

8.4. **DISCUSSION**

In the present study, we provided a quantitative approach to study neutral solute transport across cartilage and the subchondral bone plate based on a multi-zone biphasic-solute finite element model. We have previously shown the capability of the multi-zone biphasic-solute models in obtaining the diffusion coefficients in different equine cartilage zones when a finite bath of neutral solute is placed on the cartilage surface (chapter 3) [10]. In this study, we showed that for human samples (maximum thickness of 2.8 mm) and equine samples (maximum thickness of 2.1 mm) 72 hours of the diffusion experiments not only enabled determining the diffusion coefficient of the deep zone as well as that of the subchondral plate/calcified cartilage. The diffusion coefficients obtained in this study were the first reported for both human and equine osteochondral plugs using finite-bath multi-zone biphasic-solute models. Since the thickness of the cartilage used in the previous study was relatively high (~2.8 mm), the diffusion coefficient of the deep zone of cartilage could not be exclusively calculated using concentration-time curves (up to 48 hours). The rationale behind it is likely due to the insufficient time of the contrast to penetrate through the entire cartilage and bon layer (48 hours), which caused the diffusive resistance of the deep zone to overcome the required driving force.

In this study, diffusion coefficients found in different zones of uncalcified cartilage and subchondral plate/calcified cartilage in human samples were generally higher than those in equine samples (Table 8.3). However, the ratios of diffusion coefficients (D_{Middle}/ D_{Deep} and D_{Deep}/ D_{SPCC}) between human and equine samples were highly comparable (Table 8.4). The diffusion coefficients obtained for equine calcified cartilage/subchondral plate (femoral condyle) in the current study were in the same order of magnitude compared to diffusion coefficient of equine calcified cartilage (metacarpophalangeal joint) in another study (using fluorescent trace distribution), although the molecular size of the molecule in our study (1550 Da) was four times larger (~ 400 Da) [5]. It should be noted that micro-CT

experiments in our study did not allow differentiation between calcified cartilage and subchondral plate. Therefore, the values that we reported as the diffusion coefficients of the subchondral plate/calcified cartilage are in fact representative for the entire unit of calcified cartilage and subchondral bone plate. In spite of this mismatch, the values we obtained for the subchondral plate/calcified cartilage and the previously reported values fall within the same order of magnitude although the applied methods and the sample sources were different [4, 5]. The diffusion coefficient of the calcified cartilage is expected to be lower than that of subchondral plate in healthy joints since porosity of the calcified cartilage is lower (according to our high resolution micro-CT data (chapter 6) [8]) and therefore restricts the solute transport more considerably. However, upon transport across calcified cartilage, the thickness of the subchondral plate could also affect the transport due to mass transfer resistance imposed by the materials in the subchondral plate. In our previous study (chapter 3) [10] where equine cartilage (2.8 mm in thickness) was split into three distinct zones with their recommended water content similar to the current study we obtained extremely accurate fits (nine tests, average R^2=0.98) over the experimental data using multi-zone biphasic-solute model. In the current study, we observed a correlation between accuracy of the fit and cartilage thickness (Table 8.1 and 8.2). This indicates that thin samples may represent different zonal features i.e. water content and zonal percentages which contributed to larger errors associated with the computational fits (Table 8.2 and Figure 8.4 and 8.5). As a result, determination of exact properties of cartilage zones particularly for thin samples is recommended for future diffusion-related works. Furthermore, we believe that accurate determination of diffusion coefficients of the cartilage zones requires knowledge of flux at the cartilage-subchondral bone interface as considered in this study. Therefore, failure in consideration of the flux boundary condition at the cartilage-subchondral plate/calcified cartilage might cause the obtained diffusion coefficients of cartilage to be error-prone. Although the loaded volume of the finite-bath was slightly less in the current study compared to the previous study (chapter 3) [10], the diffusion coefficients for the equine cartilage fell under a similar range as expected. The design of the current study implies that two

different samples were used: human samples (slightly osteoarthritic) and equine samples (healthy), thereby the obtained diffusion coefficients for the healthy human samples may be slightly different, and perhaps higher than healthy human samples likely due to elevated permeability and disorientation and damage of collagen fibrils and proteoglycans. The solute used in this study although larger in size than in the previously used studies, still does not lie within the range of most signaling molecules, therefore, more research needs to emerge to account for the effect of size on the transport across articular cartilage and subchondral bone. The effect of solute's charge, particular positive, may be addressed in the future work to amplify agent delivery through the cartilage down to the subchondral plate.

In conclusion, the developed multi-zone biphasic-solute computational model enabled determining the diffusion coefficients of neutral solutes across cartilage and osteochondral interface. The findings of the current work deepen our understanding of how each layer within the cartilage and subchondral bone plate communicates when a neutral solute is administered on the articulating surface of cartilage.

8.5. **REFERENCES**

1. Botter, S.M., et al., *Osteoarthritis induction leads to early and temporal subchondral plate porosity in the tibial plateau of mice: an in vivo microfocal computed tomography study.* Arthritis Rheum, 2011. **63**(9): p. 2690-9.
2. Westacott, C., *Interactions between subchondral bone and cartilage in OA. Cells from osteoarthritic bone can alter cartilage metabolism.* J Musculoskelet Neuronal Interact, 2002. **2**(6): p. 507-9.
3. Pan, J., et al., *Elevated cross-talk between subchondral bone and cartilage in osteoarthritic joints.* Bone, 2012. **51**(2): p. 212-7.
4. Pan, J., et al., *In Situ measurement of transport between subchondral bone and articular cartilage.* Journal of orthopaedic research : official publication of the Orthopaedic Research Society, 2009. **27**(10): p. 1347-1352.
5. Arkill, K.P. and C.P. Winlove, *Solute transport in the deep and calcified zones of articular cartilage.* Osteoarthritis Cartilage, 2008. **16**(6): p. 708-14.
6. Galbusera, F., M. Brayda-Bruno, and H.-J. Wilke, *Is post-contrast MRI a valuable method for the study of the nutrition of the intervertebral disc?* Journal of Biomechanics, 2014. **47**(12): p. 3028-3034.
7. Sélard, É., A. Shirazi-Adl, and J.P.G. Urban, *Finite Element Study of Nutrient Diffusion in the Human Intervertebral Disc.* Spine, 2003. **28**(17): p. 1945-1953.
8. Pouran, B., Arbabi, V., Weinans, H., Zadpoor, A.A, *Solute transport at the interface of cartilage and subchondral bone plate: effect of micro-architecture.* (under review), 2016.
9. Botter, S.M., *Dynamic Subchondral Bone Changes in Murine Models of Osteoarthritis.* PhD thesis, 2010.
10. Arbabi, V., et al., *Transport of Neutral Solute Across Articular Cartilage: The Role of Zonal Diffusivities.* Journal of Biomechanical Engineering, 2015. **137**(7): p. 071001-071001.
11. Arbabi, V., et al., *Multiphasic modeling of charged solute transport across articular cartilage: Application of multi-zone finite-bath model.* Journal of Biomechanics, 2016.
12. Mauck, R.L., C.T. Hung, and G.A. Ateshian, *Modeling of Neutral Solute Transport in a Dynamically Loaded Porous Permeable Gel: Implications for Articular Cartilage Biosynthesis and Tissue Engineering.* Journal of biomechanical engineering, 2003. **125**(5): p. 602-614.
13. Ateshian, G.A., et al., *Finite element implementation of mechanochemical phenomena in neutral deformable porous media under finite deformation.* J Biomech Eng, 2011. **133**(8): p. 081005.
14. Ateshian, G.A., *On the Theory of Reactive Mixtures for Modeling Biological Growth.* Biomechanics and modeling in mechanobiology, 2007. **6**(6): p. 10.1007/s10237-006-0070-x.
15. Ateshian, G.A., S. Maas, and J.A. Weiss, *Finite element algorithm for frictionless contact of porous permeable media under finite deformation and sliding.* J Biomech Eng, 2010. **132**(6): p. 061006.
16. Ateshian, G. and J. Weiss, *Finite Element Modeling of Solutes in Hydrated Deformable Biological Tissues*, in *Computer Models in Biomechanics*, G.A.

Holzapfel and E. Kuhl, Editors. 2013, Springer Netherlands. p. 231-249.
17. Sophia Fox, A.J., A. Bedi, and S.A. Rodeo, *The Basic Science of Articular Cartilage: Structure, Composition, and Function.* Sports Health, 2009. **1**(6): p. 461-468.
18. Nair, N., et al., *Dynamics of surfactant-suspended single-walled carbon nanotubes in a centrifugal field.* Langmuir, 2008. **24**(5): p. 1790-5.
19. Li, B. and R.M. Aspden, *Mechanical and material properties of the subchondral bone plate from the femoral head of patients with osteoarthritis or osteoporosis.* Ann Rheum Dis, 1997. **56**(4): p. 247-54.
20. Ateshian, G.A., S. Maas, and J.A. Weiss, *Solute transport across a contact interface in deformable porous media.* Journal of Biomechanics, 2012. **45**(6): p. 1023-1027.

CHAPTER 9

TOPOGRAPHIC FEATURES OF NANO-PORES WITHIN THE OSTEOCHONDRAL INTERFACE AND THEIR EFFECTS ON TRANSPORT PROPERTIES –A 3D IMAGING AND MODELING STUDY

This chapter is prepared for submission as a research paper:

Pouran B., Raoof R., de Winter D.A.M., Arbabi V., Bleys R.L.A.W., Beekman F.J., Malda J., Zadpoor A. A., Weinans H.

ABSTRACT

Recent insights suggest that the osteochondral interface plays a pivotal role in maintaining the metabolic health state of articulating joints by enabling the transport of solutes. Uncovering the underlying transport mechanisms is therefore important for understanding the cross-talk between articular cartilage and subchondral bone. Here we describe previously unknown mechanisms that derive molecular transport at the osteochondral interface. In particular, Using scanning electron microscopy (SEM), we found a continuous transition of mineralization architecture from the non-calcified cartilage region towards the calcified cartilage, revoking the textbook picture of the so-called tidemark; a well-defined discontinuity at the osteochondral interface zone. Moreover, applying focused-ion-beam SEM (FIB-SEM) tomography on samples of human cadaveric knee tissue, we clarified the pore structure varying gradually while traversing from calcified cartilage towards the subchondral bone plate. Using FIB-SEM tomographic data, we here show how the presence of an interconnected network of nano-pores determines the solute diffusivity as well as hydraulic permeability using solute and fluid flow modeling platforms. Using this proposed approach, one can appreciate that the connectivity of nano-pores in calcified cartilage is to a large extent compromised compared to that of subchondral bone plate, affecting both the permeability and diffusivity. Furthermore, four times larger connected pores found in bone compared to calcified cartilage elevates the permeability and diffusivity by a factor of 2000 and 1.5 in the bone. Taken together, the inter-connected network of nano-pores and complex mineralization pattern draw a new mechanistic picture of how molecules transport between cartilage and bone, crucial to our understanding of the etiology of joint diseases as well as the transport of potential therapeutic molecules.

The osteochondral interface bridges the articular cartilage to the subchondral bone plate and balances the un-matching mechanical properties of non-calcified soft cartilage and stiff subchondral bone plate. Our previous experimental observations in conjunction with other studies confirmed possibility for solute transport across the osteochondral interface [1-4]; a crucial property that explains homeostasis, the viability of chondrocytes and osteocytes and mutual signal transduction in articulating joints, all involved in development and recovery processes of cartilage and related diseases such as osteoarthritis [3, 5]. Means for the solute and fluid transport in the cortical bone have been attributed to an interconnected network within the lacunar-canalicular region [6, 7]. The existence and the exact role of porosity inside the deep cartilage layers, the extracellular matrix of calcified cartilage and subchondral bone plate have not been clarified.

Therefore, in this study, we evaluated the topographic features of nano-pores within the osteochondral interface both in relatively healthy and more degenerated tissue. For this, we selected two samples, after micro-computed tomography (micro-CT)-based inspection of human osteochondral plugs from three donors, with different cartilage and bone health status. Ultramicrotome-cut sections of 10 μm thick were used either for histology or FIB-SEM. The FIB-SEM observations of the sections were correlated to the histology staining to verify the location of the calcified cartilage and the subchondral bone.

A FIB cross-section was milled over a length of 500 μm, perpendicular to the osteochondral interface and imaged by the SEM (Figure 9.1A).

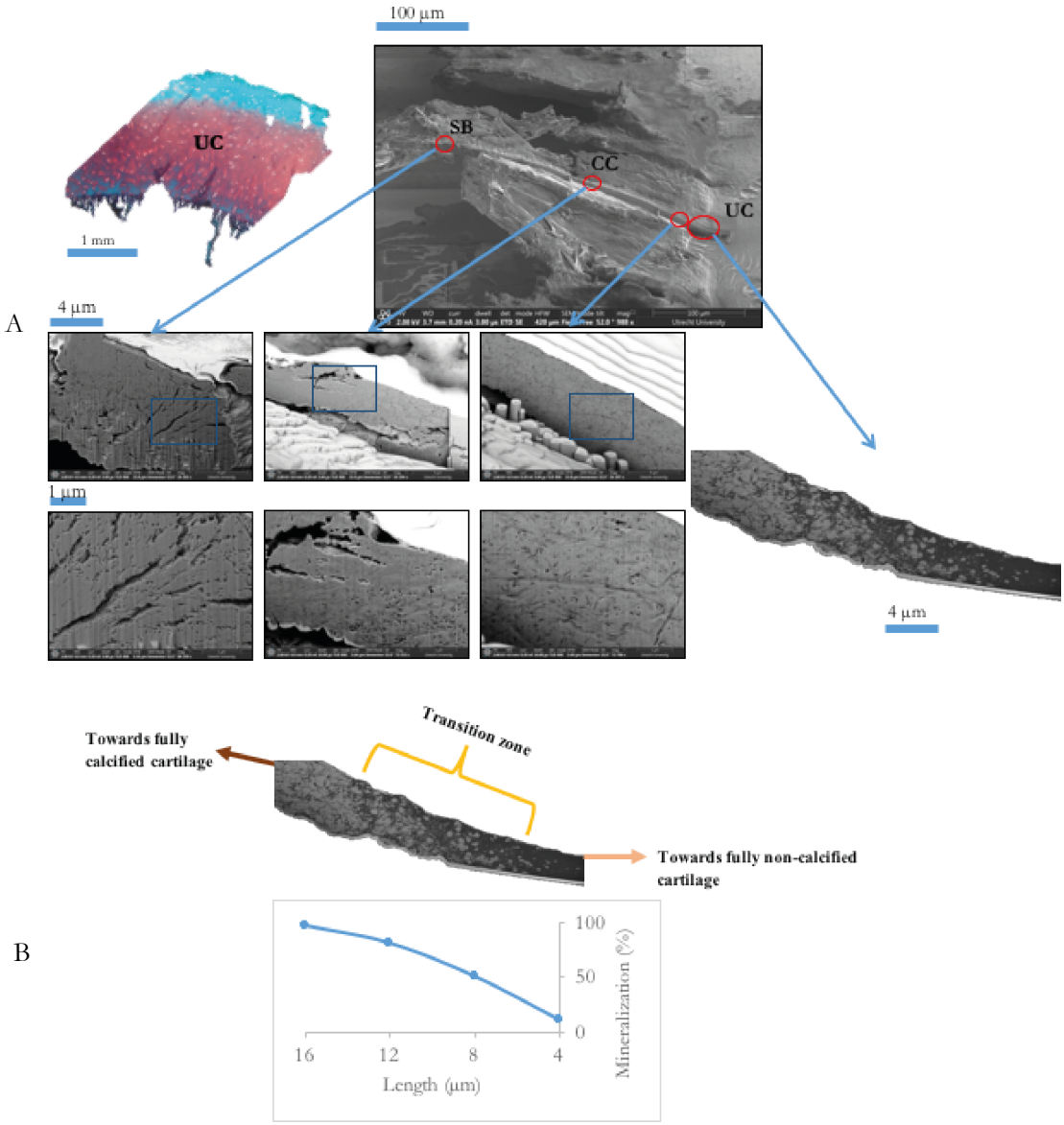

Figure 9.1. (A) Nano-topographic features of cartilage-bone interface (relatively healthy): UC: non-calcified cartilage, CC: Calcified cartilage and SB: Subchondral bone plate, highlighting the continuous transition from non-calcified cartilage to the subchondral bone plate while traversing the calcified cartilage region. B) Continuous increase in mineralization while proceeding from non-calcified cartilage to the calcified cartilage.

The cross section revealed presence of nano-porosity across the entire interface. Directly noticeable is the gradual transition in the extent of mineralization between the non-calcified cartilage (~11% mineral) and the deeper zones of calcified cartilage close to the subchondral bone (~97% mineral) (Figure 9.1B). This observation denies the classical cartilage model [8], which describes a sharp finite-size interface. The fact that mineralization increases rapidly in once transiting from non-calcified cartilage to calcified cartilage has been reflected using Fourier transform infrared imaging [9], however, the maximum resolution of few microns did not allow nano-sized objects to be detected at the interfaces which were found successfully in our current study using FIB-SEM. The calcified cartilage contains segregated non-mineralized regions near the non-calcified cartilage which enhances transport of solutes due to presence of gel-like material comprising of water, collagen and glycosaminoglycans (Figure 9.1B) [8]. Solute arriving at the calcified cartilage could reach to the bone more conveniently in the regions where non-calcified cartilage meets the subchondral bone plate [10]. Moreover, the transition between calcified cartilage and subchondral bone is gradual (Figure 9.1B).

The cross-section of calcified cartilage reveals numerous fishbone patterns, showing collagen-apatite create the pore spaces (Figure 9.1A, first magnified image at the right-hand-side). The calcified cartilage in the less degenerate sample (more normal cartilage surface and glycosaminoglycans distribution) and develops larger and more dispersed pores in comparison to the degenerate sample (Compare Figure 9.1 and 9.2).

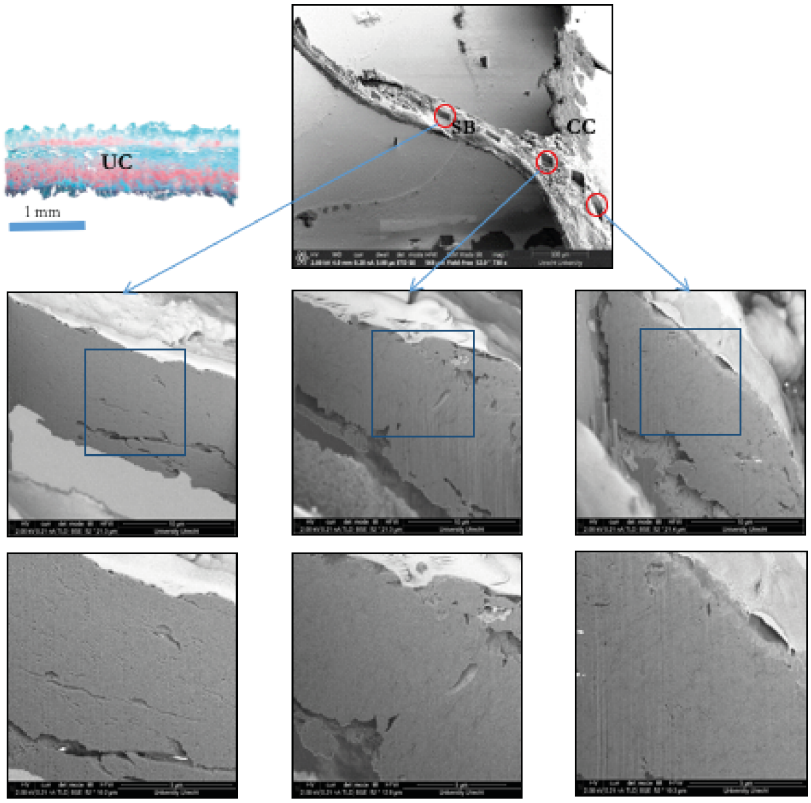

Figure 9.2. Nano-topographic features of calcified cartilage (CC)-subchondral bone plate interface (SB) of the more degenerated human sample, highlighting the transition from calcified cartilage to the subchondral bone plate.

This observation is confirmed by the obtained grey values from the micro-CT showing a thicker calcified cartilage in the degenerate sample (Figure 9.3). Close to the subchondral bone plate region, the pores are larger (200% larger near the subchondral bone plate), reaching a maximum pore size within the bone region (Figure 9.1 and Figure 9.2).

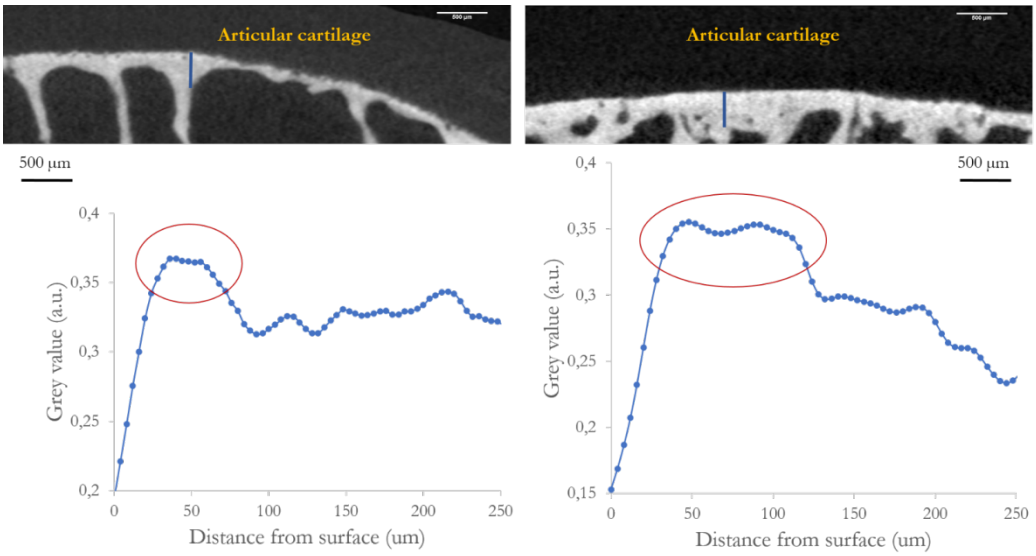

Figure 9.3. micro-CT image of the samples used in the current study (left image depicting healthier sample) showing higher density of the calcified cartilage as compared to the subchondral bone plate.

To capture the sub-micrometer porous network in the calcified cartilage and subchondral bone plate, we employed a focused ion beam-scanning electron microscope (FIB-SEM tomography). Doing so, site-specific cross sections can be directly imaged with nanometer resolution by the SEM. Moreover, the successive FIB cross sectioning and SEM imaging during the FIB-SEM tomography provides three-dimensional volumetric representations with nanometer resolution across the micrometer lengths [11-13].

The FIB-SEM tomography-based 3D reconstruction of the pore space in the healthier sample led to the characterization of the pore structures within the calcified cartilage and subchondral bone plate. The analyzed volumes were 10 µm x 4 µm x 2.5 µm for calcified cartilage and 4 µm x 4 µm x 3 µm for subchondral bone plate. The porosity of the calcified cartilage and subchondral bone plate were found to be 1.6 % and

9.7 %, respectively. The average pore diameter of the extracellular matrix of calcified cartilage (i.e. non-mineralized collagen fibrils) and subchondral bone plate (canalicular space and non-mineralized collagen fibrils) were 10.71 ± 6.45 nm and 39.1 ± 26.17 nm, respectively (see Figure 9.4).

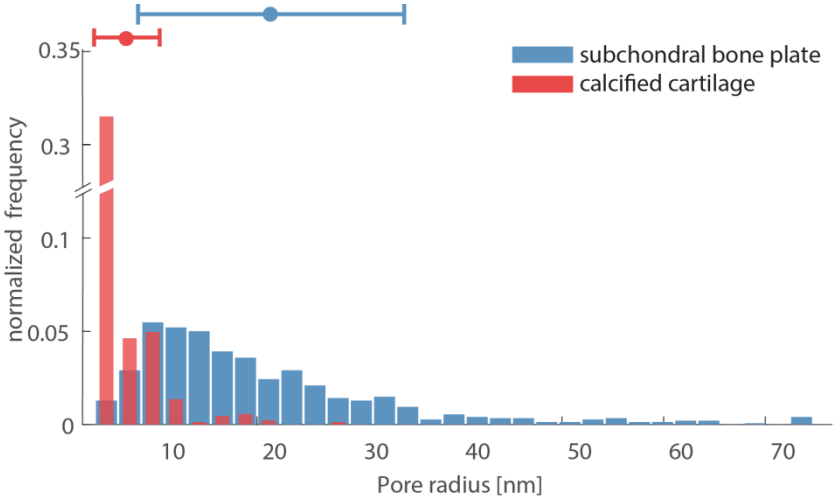

Figure 9.4. pore size distribution for subchondral bone plate and calcified cartilage.

The calcified cartilage in fact blocks all solutes larger than 10 nm in diameter. However, our findings confirm presence of pore spaces in the calcified cartilage, even in the almost completely calcified region near the subchondral bone plate. The probability of finding an interconnected network of pores decreases as a function of length in the calcified cartilage (Figure 9.5). As a result, diffusion across the osteochondral interface naturally vanishes at the larger thicknesses of calcified cartilage.

Numerical flow and solute transport simulations are performed employing the 3D-reconstructed FIB-SEM pore spaces in the healthy region to obtain the diffusivity and permeability values. A transport hindrance coefficient, τ [-], is defined as the ratio of calculated diffusivity ($D_{Calculated}$) through the pore network over the diffusivity ($D_{Unhindered}$) through a straight tube across the same length and with the same porosity:

$$\tau = D_{Calculated} / D_{Unhindered}$$

The breakthrough curves were obtained at several locations across the subchondral bone plate to investigate the length effect (Figure 9.5A).

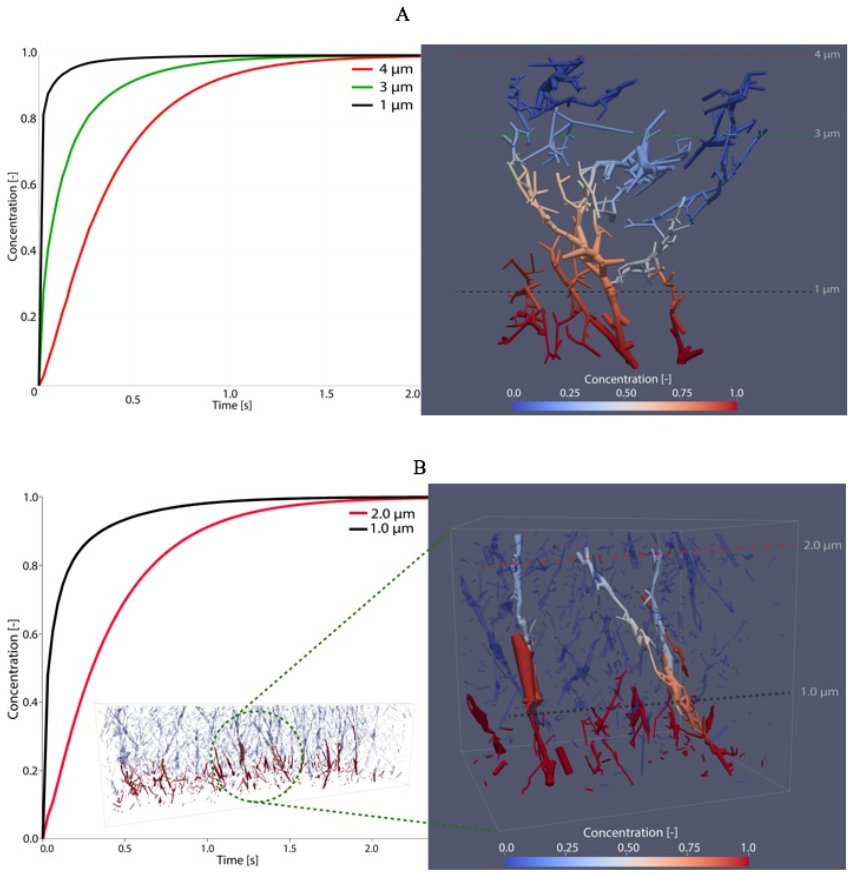

Figure 9.5. Right image: Pore structure in the subchondral bone plate. Left image: Normalized concentration vs. time in different length scales perpendicular to the osteochondral interface (free diffusivity = 2.5E-10). (B) Right image: Pore structure in the calcified cartilage. Left image: Normalized concentration vs. time in different length scales parallel to the osteochondral interface (free diffusivity = 2.5E-10).

In calcified cartilage, τ for the half of the 3D FIB-SEM volume (d = 1 μm) was 0.16 which decreased to 0.13 for the entire 3D FIB-SEM volume (d = 2 μm). Perpendicular to osteochondral interface direction (with d = 0.7 μm), τ was found to be 0.05, showing that the calcified cartilage is more conductive parallel to osteochondral interface than perpendicular to it.

It can then be inferred that calcified cartilage mainly acts as a solute distributor in its entire volume rather than a cross passage for solutes towards the subchondral bone plate. Previous research found local pathways across the interface where non-calcified cartilage meets the subchondral bone plate [10], suggesting that the solutes preserved in the matrix of (calcified) cartilage can be made available at the subchondral bone plate. Previously reported diffusivities in the calcified cartilage of mice between the chondrocytes were much lower than our diffusivity values [3]. Our observations indicate and the insight from our pore-scale model suggests the length dependent diffusivity in the calcified cartilage. The previously reported values have been obtained merely in the region of calcified cartilage close to non-calcified cartilage where non-mineralized patches may facilitate the transport. The justification for the variations between the values reported earlier and here majorly originates from the length-scale differences; our results have been obtained within the pore domain, whereas the previously obtained results are driven using the larger continuum scale formulations (the so-called tissue level) [2, 3, 14]. Using the numerical fluid flow modeling (see Materials and Methods), we found a permeability value of 1.9×10^{-23} m^2 perpendicular to osteochondral interface within the connected region (d = 0.7 μm). The fraction of the domain occupied by the disconnected pores hinders the fluid motion to potentially reduce the calculated value, indicative of anisotropic matrix permeability. The anisotropic permeability found using here is attributed to the non-uniform orientation of collagen fibrils in the calcified cartilage region [9]. Therefore, permeability predominantly facilitates convective solute and

fluid transport in short ranges to the passages where non-calcified cartilage directly touches the subchondral bone plate.

In the subchondral bone plate, parallel to osteochondral interface, τ was found to be 0.21. Perpendicular to osteochondral interface, τ showed a decreasing trend by distance from 1 to 4 μm (Figure 9.6).

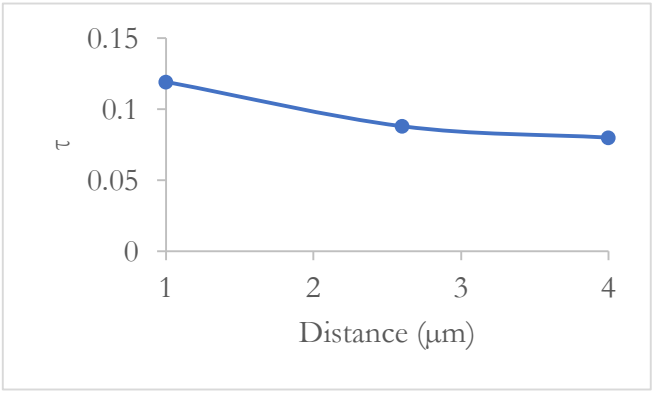

Figure 9.6. Length dependency of ratio of the transport hindrance (τ) in the subchondral bone plate perpendicular to the osteochondral interface.

The pore-scale diffusivity in the subchondral bone plate can be 16-fold higher than that in the tissue level (homogenized), which is consistent with the earlier study [15]. Higher diffusivities in the pore-scale are attributed to the higher freedom of solutes to distribute, as they do not encounter the highly impermeable solid mineralized phase. Furthermore, pore-scale analysis allows exact determination of diffusivity in subchondral bone plate and calcified cartilage separately, as opposed to contrast enhanced micro-CT which cannot discriminate between these two mineralized compartments. It is important to note that the computed values here were obtained at the extracellular matrix region, as the added cellular space would potentially affect those. In the course of osteoarthritis, an initial drop in density of calcified tissue is followed by its increase [16, 17], which potentially affects solute transport and thereby cartilage-bone cross-talk due to structural alterations. The breakthrough curves (concentration versus time) were obtained at several locations

across the subchondral bone plate to investigate the length effect (Figure 9.5B). Permeability showed an anisotropic behavior with values of 3.9×10^{-19} m^2 and 3.2×10^{-20} m^2, parallel and perpendicular to osteochondral interface, respectively. This provides the first pore-scale reported permeability based on the real subchondral bone plate pericellular architecture at the nano-scale. Our obtained values lie in the range of previously reported values. Perpendicular to osteochondral interface, the permeability in the subchondral bone plate was 1000-fold higher compared to the overlaying calcified cartilage. The range of permeability's of a region involving the bone canalicular region in the present study agrees with that of the previous study based on an analytical approach [18]. Obviously, we expected larger permeability's when incorporating the contribution of lacunae and vessels.

The essential microscopic pore sizes manifest themselves at the macroscopic level though bulk parameters of diffusivity and permeability. To explore the pore size effects, we have performed simulations using the obtained real pore sizes as well as using a uniform pore size equal to the average value of the real pore sizes. Solute showed slower penetration into the subchondral bone plate with the real pore size distribution compared to the bone with uniform pore sizes (Figure 9.7). This analysis showed the contribution of insulated, or dead-end, pore clusters (shown by the dotted circle in Figure 9.7) located along the flux of solutes which act as a sink for solute to delay its penetration and therefor its arrival at the longer distances. A later arrival, in turn, provides smaller effective diffusion values for bone.

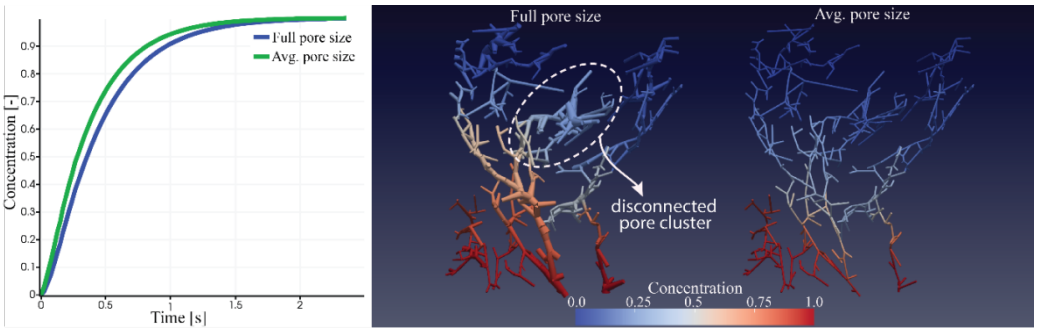

Figure 9.7. Left plot: Time arrival of solute concentration for two pore structures. Right image: pore structure with real pore size distribution, and the pore structure with pores having the average size.

The domain with the intrinsic pore distribution showed 89% higher permeability value compared to its corresponding uniform media. Analyzing the pore sizes and their connectivity, this is because in the real pore network pores with different sizes are distributed non-uniformly and are spatially correlated where a main branch with a larger pore size dominates the flow (as shown in Figure 9.8).

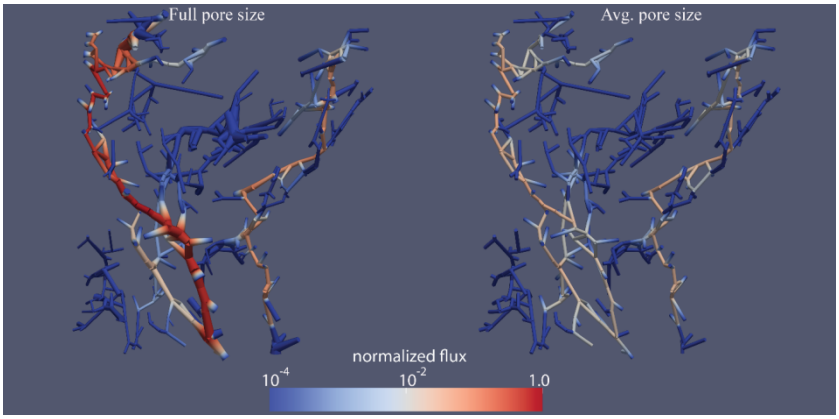

Figure 9.8: Flux of fluid for real pore size distribution (left plot), and the pore structure with pores having the average size (right plot). The flux values are normalized using the maximum flux value. The pore network with the uniform pore size also shows a domain flow pathway, although being weaker compared the dominant flow path within network with the real pore size distribution.

This analysis reveals that the occurrence of flow pathway in the subchondral bone plate is not only due to the presence of the larger pore sizes (i.e., geometrical properties of the bone) but is also controlled by the connectivity pattern between the pores (i.e., a topological property of the bone) and the pore size correlation. Another major conclusion using Figures 9.7 and 9.8 is that a bone with higher permeability values does not necessarily have a larger diffusivity – as is the case here. This is because pathways of conductive pores with their larger sizes control bone permeability, while presence of isolated pore clusters branching out from such a pathway regulates the effective diffusivity. The larger pores in the subchondral bone plate are believed to be the osteocyte processes as opposed to the smaller pores that form due to partial mineralization of the collagen fibrils.

In short, the results of the present study shed light on the topographic features at the primary interface between articular cartilage and subchondral bone plate. As opposed to the conventional and strict separation between non-calcified and calcified cartilage as well as calcified cartilage and subchondral bone plate, we found a nano-scale continuous and transitional architectural pattern across the boundaries. Applying advanced FIB-SEM tomography and pore-network modeling allowed accurate prediction of the solute and fluid transport properties in both calcified cartilage and subchondral bone plate. These techniques applied at pore-scale within the extracellular matrix are believed to successfully quantify mass and momentum transport at the interface of cartilage and bone.

MATERIALS AND METHODS

Sample harvest

Osteochondral plugs (diameter=8.5 mm) were harvested from human cadaveric femoral condyles using a custom-made drill bit [19] The drilling was performed while continuously spraying the drilling site using phosphate buffer solution (PBS) enriched with protease inhibitor (cOmplete, Germany). The osteochondral plugs were put in a plastic vial. The vials were placed in a container which was sealed in a bag and stored at -20 °C.

Micro-computed tomography (micro-CT)

The entire osteochondral plugs were scanned at a resolution of 10 μm (Tube voltage = 60 kV and Tube current = 200 μA, MILabs, The Netherlands) using a micro-CT (MILabs, The Netherlands). The scans were then reconstructed to quantify the grey values at the osteochondral interface.

Cryo-sectioning

Post-micro-CT, the osteochondral plugs were embedded in an resin (Cryo-Gel, Leica) within the chamber of cryo-microtome (Leica CM3600 XP, Germany, -25 °C) and serial sectioning (alternating sections for FIB-SEM and histology) was performed perpendicular to the interface of cartilage and bone. The sections (10 μm) were collected on coated glass slides (SuperfrostTM Plus, ThermoFisher). After immersion in ethanol series (100%, 90%, 70%) for five minutes, the sections were incubated for 45 minutes in the oven at 60 °C to ensure stable attachment of the sections to the glass slide surface.

Histology

To locate the calcified cartilage and subchondral bone plate within the slides and to assess the healthiness of the osteochondral plugs, Safranin-O/Fast green staining was performed to a number of sections that would not undergo FIB/SEM.

Focused-ion-beam scanning electron microscopy (FIB/SEM)

After freeze-drying (Christ alpha 1-2 LD plus) the sections for 24 hours, Glass slides containing one or more sections were attached to a standard SEM aluminum stubs with adhesive carbon tape. A small strip of the tape was stuck to the edge of the section and led to the SEM stub to improve electrical conductivity. Subsequently, the glass slide was sputter coated with 5 nm Pt/Pd (Cressington 208HR). FIB-SEM operations were performed on a Helios Nanolab UC-G3 (FEI). A small strip of Pt deposition was deposited from the bone region to the uncalcified cartilage region (thickness approximately 1 μm). Subsequent FIB milling (30 kV, stepwise reducing the ion current from 21 nA – 24 pA) resulted in a wide cross section. Backscatter Electron (BSE) imaging (2 kV, 0.2 nA) with the through the lens detector in immersion mode revealed the pore structure.

FIB-SEM tomography [12] was performed with Slice & ViewTM G3 v1.7.3 (FEI). Slices of 20 nm were milled with 30 kV, 24 pA and imaged in BSE mode (2 kV, 0.2 nA) with the through the lens detector in immersion mode.

Pore-scale modelling

The FIB-SEM tomography data was further treated with Avizo (FEI). The pore space was segmented, resulting in binary data (pore space versus solid). Subsequently, the pore space was converted into a pore network model consisting of pore junctions connected by pore segments (Figure 1S).

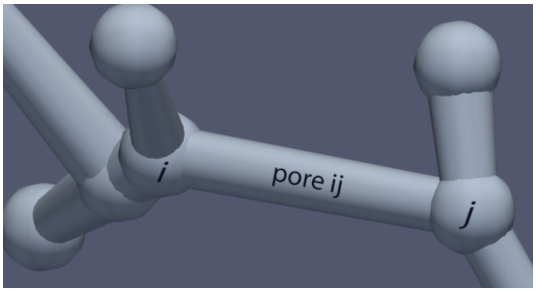

Figure 1S. An example of interconnected pores, ij, and pore junctions, i and j, obtained from the bone sample.

The fluid flow and the overall permeability can be determined by simulations [20]. Each pore segment obtains a conductance depending on its size. The resulting flow through a particular pore segment is calculated by:

$$q_{ij} = \frac{\pi R_{ij}^4}{8\mu l_{ij}}\left(P_j - P_i\right) \quad (1)$$

where qij is volumetric flow through a given pore segment ij, Rij and lij are the radius and length of pore throat, respectively. μ is dynamic viscosity, Pi and Pj are pressures at pore junctions i and j, respectively. Equation (1) can be defined for each and every pore segment together.

The solute transport across the pore segment can be calculated by solving mass balance equation (2) which describes change of concentration for a given pore, cij, as a result of advection and diffusion transport processes.

$$V_{ij}\frac{dc_{ij}}{dt} = \underbrace{q_{ij}\left(\overline{c_j}^{t+\Delta t} - \overline{c_{ij}}^{t+\Delta t}\right)}_{\text{advection process}} + \underbrace{DA_{ij}\frac{\left(\overline{c_j}^{t+\Delta t} - \overline{c_{ij}}^{t+\Delta t}\right)}{l_{ij}} + DA_{ij}\frac{\left(\overline{c_i}^{t+\Delta t} - \overline{c_{ij}}^{t+\Delta t}\right)}{l_{ij}}}_{\text{diffusion process}} \quad (2)$$

where Vij, Aij are volume and pore cross-sectional area respectively, cij and ci are concentrations belonging to the upstream pore junction i and pore ij itself and D is molecular diffusion.

Another mass balance equation is written for each pore junction, ci, where solutes from connected pores to it may exchange mass:

$$V_i\frac{dc_i}{dt} = \underbrace{\sum_{j=1}^{j=z_{i,\text{inflow}}} q_j\overline{c_j}^{t+\Delta t} - Q_i\overline{c_i}^{t+\Delta t}}_{\text{advection process}} + \underbrace{\sum_{j=1}^{Z_i} DA_{ij}\frac{\overline{c_j}^{t+\Delta t} - \overline{c_i}^{t+\Delta t}}{l}}_{\text{diffusion process}}, \text{ where } \sum_{j=1}^{j=z_{i,\text{inflow}}} q_j = Q_i = \text{total flux} \quad (3)$$

where Vi is the pore junction volume and zi is the pore connectivity, showing the number of pores connected at the junction i.

Finally, the overall solute transport can be determined for a given concentration gradient across the pore space by iteratively solving equation (2) and equation (3) for all pore segments and pore volumes (Jacobi's method), which converges to a stable concentration distribution across the pore space. The time step for each iteration is determined by:

REFERENCES

1. Pouran, B., et al., *Solute transport at the interface of cartilage and subchondral bone plate: Effect of micro-architecture.* J Biomech, 2016.
2. Pan, J., et al., *Elevated cross-talk between subchondral bone and cartilage in osteoarthritic joints.* Bone, 2012. **51**(2): p. 212-7.
3. Pan, J., et al., *In situ measurement of transport between subchondral bone and articular cartilage.* J Orthop Res, 2009. **27**(10): p. 1347-52.
4. Burstein, D., et al., *Protocol issues for delayed Gd(DTPA)(2-)-enhanced MRI (dGEMRIC) for clinical evaluation of articular cartilage.* Magn Reson Med, 2001. **45**(1): p. 36-41.
5. Weinans, H., *Periarticular bone changes in osteoarthritis.* HSS J, 2012. **8**(1): p. 10-2.
6. Benalla, M., et al., *Dynamic permeability of the lacunar-canalicular system in human cortical bone.* Biomech Model Mechanobiol, 2014. **13**(4): p. 801-12.
7. Wang, L., et al., *Modeling tracer transport in an osteon under cyclic loading.* Ann Biomed Eng, 2000. **28**(10): p. 1200-9.
8. Sophia Fox, A.J., A. Bedi, and S.A. Rodeo, *The basic science of articular cartilage: structure, composition, and function.* Sports Health, 2009. **1**(6): p. 461-8.
9. Khanarian, N.T., et al., *FTIR-I compositional mapping of the cartilage-to-bone interface as a function of tissue region and age.* J Bone Miner Res, 2014. **29**(12): p. 2643-52.
10. Lyons, T.J., et al., *The normal human chondro-osseous junctional region: evidence for contact of uncalcified cartilage with subchondral bone and marrow spaces.* BMC Musculoskelet Disord, 2006. **7**: p. 52.
11. de Winter, D.A.M., F. Meirer, and B.M. Weckhuysen, *FIB-SEM Tomography Probes the Mesoscale Pore Space of an Individual Catalytic Cracking Particle.* Acs Catalysis, 2016. **6**(5): p. 3158-3167.
12. De Winter, D.A.M., et al., *Tomography of insulating biological and geological materials using focused ion beam (FIB) sectioning and low-kV BSE imaging.* Journal of Microscopy, 2009. **233**(3): p. 372-383.
13. Narayan, K. and S. Subramaniam, *Focused ion beams in biology.* Nat Methods, 2015. **12**(11): p. 1021-31.
14. Arbabi, V., et al., *Neutral solute transport across osteochondral interface: A finite element approach.* J Biomech, 2016. **49**(16): p. 3833-3839.
15. Fan, L., et al., *A multiscale 3D finite element analysis of fluid/solute transport in mechanically loaded bone.* Bone Res, 2016. **4**: p. 16032.
16. Intema, F., et al., *In early OA, thinning of the subchondral plate is directly related to cartilage damage: results from a canine ACLT-meniscectomy model.* Osteoarthritis Cartilage, 2010. **18**(5): p. 691-8.
17. Day, J.S., et al., *Adaptation of subchondral bone in osteoarthritis.* Biorheology, 2004. **41**(3-4): p. 359-68.
18. Beno, T., et al., *Estimation of bone permeability using accurate microstructural measurements.* J Biomech, 2006. **39**(13): p. 2378-87.

19. Arbabi, V., et al., *An Experimental and Finite Element Protocol to Investigate the Transport of Neutral and Charged Solutes across Articular Cartilage.* J Vis Exp, 2017(122).
20. Raoof, A., et al., *PoreFlow: A complex pore-network model for simulation of reactive transport in variably saturated porous media.* Computers & Geosciences, 2013. **61**: p. 160-174.

CHAPTER 10

NON-ENZYMATIC CROSS-LINKING OF COLLAGEN TYPE II FIBRILS IS TUNED VIA OSMOLALITY SWITCH

This chapter is submitted as a scientific paper:

B. Pouran, PR. Moshtagh, V. Arbabi, J. Snabel, R. Stoop, J. Ruberti, J. Malda, A. A. Zadpoor, H. Weinans.

ABSTRACT

Objective: An important aspect in cartilage ageing is accumulation of advanced glycation end products (AGEs) after exposure to sugars. Advanced glycation results in crosslinks formation between the collagen fibrils in articular cartilage, hampering their flexibility and making cartilage more brittle. In the current study, we investigate whether collagen crosslinking after exposure to sugars depends on the stretching condition of the collagen fibrils.

Design: Healthy equine cartilage specimens were exposed to L-threose sugar and placed in hypo-, iso- or hyper-osmolal conditions that expanded or shrank the tissue and changed the 3D conformation of collagen fibrils. We applied micro-indentation tests, contrast enhanced micro-computed tomography, biochemical measurement of pentosidine cross-links, and cartilage surface color analysis to assess the effects of advanced glycation cross-linking under these different conditions.

Results: Swelling of ECM due to hypo-osmolality made cartilage less susceptible to advanced glycation, namely, the increase in effective Young's modulus was approximately 80% lower in hypo-osmolality compared to hyper-osmolality and pentosidine content per collagen was 47% lower.

Conclusions: These results indicate that healthy levels of glycosaminoglycans not only keep cartilage stiffness at appropriate levels by swelling and pre-stressed collagen fibrils, but also protect collagen fibrils from adverse effects of advanced glycation. These findings highlight the fact that collagen fibrils and therefore cartilage can be protected from further advanced glycation ('ageing') by maintaining the joint environment at sufficiently low osmolality. Understanding of mechanochemistry of collagen fibrils provided here might evoke potential ageing prohibiting strategies against cartilage deterioration.

Chapter 10

10.1. INTRODUCTION

In normal articular cartilage, the extracellular matrix (ECM) includes structured collagen type II fibrils, depth-wise distributed glycosaminoglycan macromolecules (GAGs), and interstitial water [1]. In osteoarthritis (OA), proteolytic activity initiates marked changes in the ECM of cartilage [2]. The depletion of GAGs is often considered as early signs of OA, whereas irreversible degradation of collagen fibrils can be observed in the developing stages of OA followed by macroscopic degeneration of ECM in the late stage OA [3, 4]. Contrary to OA, normal ageing does often not affect the major constituents, nor the organization of ECM, but rather contributes to formation and accumulation of so-called advanced glycation end-products (AGEs) including pentosidine cross-links, which chemically affect the collagen molecules [5]. The AGEs are formed by a chain of irreversible reactions between two adjacent amino acids of Arginin and Lysin found as the repeating units in the triple-helix tropocollagen molecules [6]. Not only is their production augmented due to increased systemic sugar levels, e.g. in diabetes, but is also observed in the turnover processes of the ECM [5]. Apart from obvious biomechanical effects of AGEs due to the impaired function of the collagen fibrils and increased brittleness [5], at the cellular level they interact with the surface receptors of chondrocytes [5]. In short, AGEs stimulate catabolic pathways leading to upregulation of matrix metalloproteinases (MMPs) that are responsible for degrading the ECM components.

The three-dimensional (3D) spatial orientation of collagen either in single molecular state or fibrillar state has been shown to affect enzymatic degradation of collagen [7-9]. There is some evidence that stretching of collagen fibrils decelerates MMPs enzymatic activity [7, 9-11]. This could be due to the 3D orientation of the amino acids that form the cleavage sites in the backbone of collagen fibrils, which might only interact with enzymes in a specific (low stretched) conformation. Similarly, the essential amino acids involved in advanced glycation, namely arginine and lysin [12], may need a specific 3D conformation to interact with sugars and create crosslinks.

Here, we investigate the effects of osmotically-driven mechanical conditioning of collagen fibrils within equine articular cartilage samples on their

chemical response to the non-enzymatic cross-linking, in other words "artificial ageing". This "artificial ageing" is induced by using L-threose as the glycating agent under various osmotic conditions of hypo-, normal and hyper-osmoality, thereby creating water outflow or inflow [13] and consequent shrinkage or stretching of the collagen fibers. The micro-scale effective elastic modulus, pentosidine level, surface color, and fixed charge density were then characterized to determine whether or not osmotic stretching of collagen fibrils protects them against non-enzymatic glycation.

10.2. **METHODOLOGY**

Sample

Equine osteochondral plugs (n = 5, φ = 8.5 mm) were extracted from visually-intact femoral condyle (~ 7 years old) using a custom-made drill bit while care was taken to avoid overheating of the drilling site by constantly spraying phosphate buffer solution (PBS, Gibco, UK). Post-extraction, the samples were stored at -20 °C until further use. The full cartilage layer (~ 2 mm) was then carefully cut from the osteochondral plug followed by splitting it into four quarter disks. Each quarter disk was then equilibrated in a separate solution containing the required amount of NaCl and protease inhibitors (cOmplete, Roche, Mannheim, Germany) at an osmolality of 400 mOsm/kg water (0.2 M NaCl) at room temperature before performing micro-indentation tests (Figure 10.1).

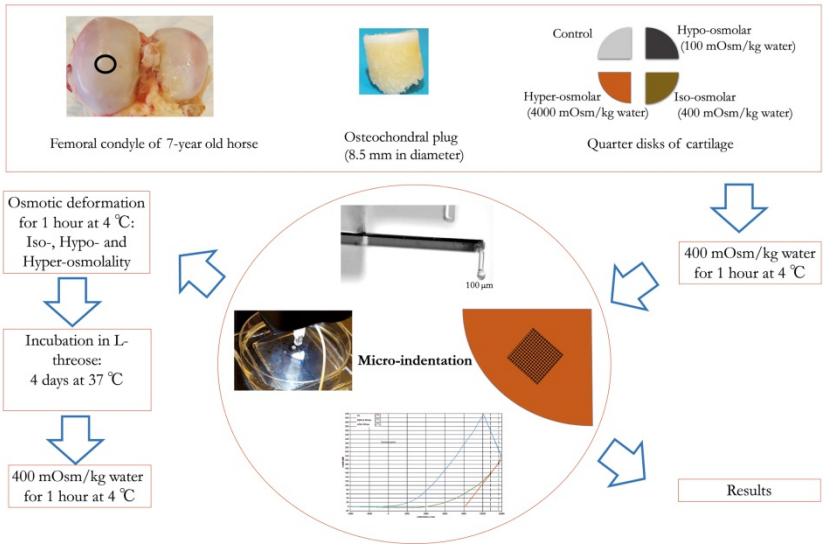

Figure 10.1. Schematic of the osmotic deformation, L-threose incubation and micro-indentation experiments. Osteochondral plugs are extracted from Equine femoral condyle of 7-year old horse using custom-made drill bits. Full thickness of cartilage is then removed from the subchondral bone using razor blade and split into four quarter disks. Three disks undergo their corresponding osmotic deformations, whereas one serves as control negative (no incubation with L-threose). The cartilage specimens are equilibrated at 4 ºC in a 400 mOsm/kg water bath and therefore are prepared for the micro-indentation tests. Matrix micro-indentation is performed on each specimen in an area of 1.5 mm×1.5 mm containing 81 equally-spaced indentation points. Thereafter, samples are treated osmotically corresponding to our desired conditions and then L-threose (50 mM) is added to each solution. Following the L-threose incubation at 37 ºC, specimens are equilibrated in 400 mOsm/kg water for an hour before matrix micro-indentation. The change of the effective Young's modulus is reported as the result.

Mechanical conditioning

External osmotic pressure of the solution to which cartilage is exposed controls its swelling state due to the in-/out-flux of water [13-15]. Articular cartilage loses water when exposed to hyper-osmolar solution, gains water when exposed to hypo-osmolar solution, while exposure to iso-osmolar solution is not expected to alter its shape. Four-quarter disks were obtained from each osteochondral plug, where each underwent different mechanical conditioning by adjusting the osmotic pressure of the external bath to hypo- (100 mOsm/kg water

or 0.05 M), iso- (400 mOsm/kg water or 0.2 M) and hyper- (4000 mOsm/kg water or 2 M) osmolalities using NaCl. Prior to incubation with L-threose (50 mM, Sigma-Aldrich, Slovakia), each quarter disk was placed in its respective solution (2 mL), i.e. hypo-, iso- or hyper-osmolal, for one hour (pre-conditioning of collagen fibrils). Then, each quarter disk was transferred to 50 mM L-threose solution having the same osmolality as in the pre-conditioning step, except one quarter disk which functions as a non-L-threose control sample (400 mOsm/kg). Two quarter disks under hypo-osmolality and two quarter disks under hyper-osmolality (from a cartilage disk) served as the controls to check for possible effects of osmolality on cross-linking process. The vials containing the samples were then placed in an incubator at 37 °C for 96 hours to induce cross-linking of the collagen fibrils (Figure 10.1).

Micro-indentation

Before and after incubation with L-threose, cartilage quarter disks were allowed to reach equilibrium at 400 mOsm/kg water enriched with protease inhibitor for 1 hour at 4 ºC, while glued to the bottom of a petri-dish with the cartilage surface facing upward. Using a permanent marker with fine tip, a reference point was specified on the cartilage surface as the starting point of the micro-indentation process. Micro-indentation was performed following the protocol determined in a previous study [14] within a 1.5×1.5 mm2 area on the cartilage surface using an array of 81 equally spaced (9×9) contact points (Figure 10.1). For this purpose, a displacement-controlled indenter (Piuma, The Netherlands) was used which consisted of a controller, optical fiber, and spherical probes with diameters of ~ 100 μm and stiffness values of ~ 50 N/m (Optics, The Netherlands). The force-displacement curves were obtained after indenting each contact point with the applied indentation depth (Piezo movement) of 18 μm. The actual indentation depth in the cartilage tissue varied based on the stiffness of each contact point, which can be calculated by subtracting the cantilever deflection from the Piezo movement. Indentation protocol at each contact point consisted of three consecutive steps of loading with Piezo movement of 18 μm for the second, holding time of 7 seconds, and unloading for 20 seconds. The effective Young's modulus at each contact point was calculated based on the Oliver-Pharr theory, i.e. calculating the slope of the initial portion of

the unloading curve. See Moshtagh et al. [14] for a more detailed description of this optimized indentation protocol.

For each sample, the average of the Young's modulus in 81 contact points was calculated before and after incubation in L-threose. The difference between the moduli measured before and after the cross-linking process was used as a measure of the cross-linking efficiency:

$$\text{Change in effective Young's modulus } (\%) = \frac{E_{after} - E_{before}}{E_{before}} \times 100 \quad (1)$$

where E_{after} and E_{before} are respectively the effective Young's moduli after and before incubation in L-threose.

Contrast enhanced micro-CT

To check the enhanced fixed charge density (FCD) of the samples, the samples were scanned with micro-computed tomography (Quantum FX, Perkin Elmer, USA) at 90 kV tube voltage and 180 μA tube current and voxel size of 20 μm3 after 24-hour incubation in Hexabrix solution (40 v/v% GE Healthcare, The Netherlands, 320 mgI/ml, MW=1269 g/mol, charge= -1) enriched with Protease inhibitor (complete, Roche, Mannheim, Germany) before and after incubation with L-threose. To eliminate the possible effects of Hexabrix on the cross-linking process, samples were washed out in a saline bath (400 mOsm/kg water, protease inhibitor) according to a previous study [15]. The average of the grey scale values was calculated in 10 mid-slices using imageJ (public domain, NIH, version 1.47).

Colorimetry of cartilage surface

Depending on the intensity of the cross-linking i.e. ageing, the color of cartilage undergoes alterations from white (normal cartilage) to brown (cross-linked cartilage) [16]. To quantify possible color changes as an indication of the cross-linking following incubation with L-threose, samples were placed side-by-side and digital images from the cartilage surface were captured (vertical, Samsung Galaxy S6, 12 Megapixels) in absence of ambient light. The resulting RGB images were then converted to 32-bit images and the average pixel intensity was calculated with imageJ.

Collagen and pentosidine content

Each quarter disk was first weighed before freeze-drying (Christ alpha 1-2 LD plus) for 48 hours. The dry weight of the samples was measured after freeze-drying. 800 μL HCL (Sigma-Aldrich) was added to the dried samples before placement in screw cap vials and subsequently in an oven at 95 °C. After 20 hours, the liquid phase of the digested samples was allowed to completely evaporate at 60 °C under a fume hood. After adding 500 μL mQ water to the vials, they were vortexed, centrifuged, and prepared for hydroxyproline measurement. Measuring the hydroxyproline allowed for calculating the collagen content of each quarter disk. The complete procedure for the hydroxyproline assay can be found elsewhere [17].

Pentosidine cross-linking level within the digested samples was determined based on high performance liquid chromatography (HPLC) [18]. The peak representative of the pentosidine cross-links was found for all samples, while care was taken to exclude the interference of other peaks as much as possible.

Statistical analysis

Statistical analysis was performed using one-way ANOVA followed by post hoc analysis using MATLAB and p-values less than 0.05 were taken as indicators of statistical significance.

10.3. **RESULTS**

Micro-indentation

The effective Young's modulus increased after cross-linking, as captured using micro-indentation before and after cross-linking with L-threose (Figure 10.1). The change in the effective Young's modulus (Eq. 1) was -21.5±32.6% for non-treated specimens, 10.0±33.2% for hypo-osmolal specimens, 10.1±47.9% for iso-osmolal specimens, and 92.5±62.1% for hyper-osmolal samples. Our results showed that, within each group, the effective Young's modulus was substantially higher for cartilage specimens that were exposed to high osmolality (shrunk samples) during the L-threose treatment as compared to those exposed to either

low or iso-osmolality conditions (Figure 10.2A). Moreover, a decrease in the effective Young's modulus of non-treated samples was observed. The effective Young's modulus of the non-treated samples decreased from 1.1±0.3 MPa to 0.8±0.3 MPa for hyper-osmotic group and from 1.1±0.3 MPa to 0.6±0.2 MPa for hypo-osmotic group suggesting only little chemical effect of osmolality itself on the cross-linking (Figure 10.2B).

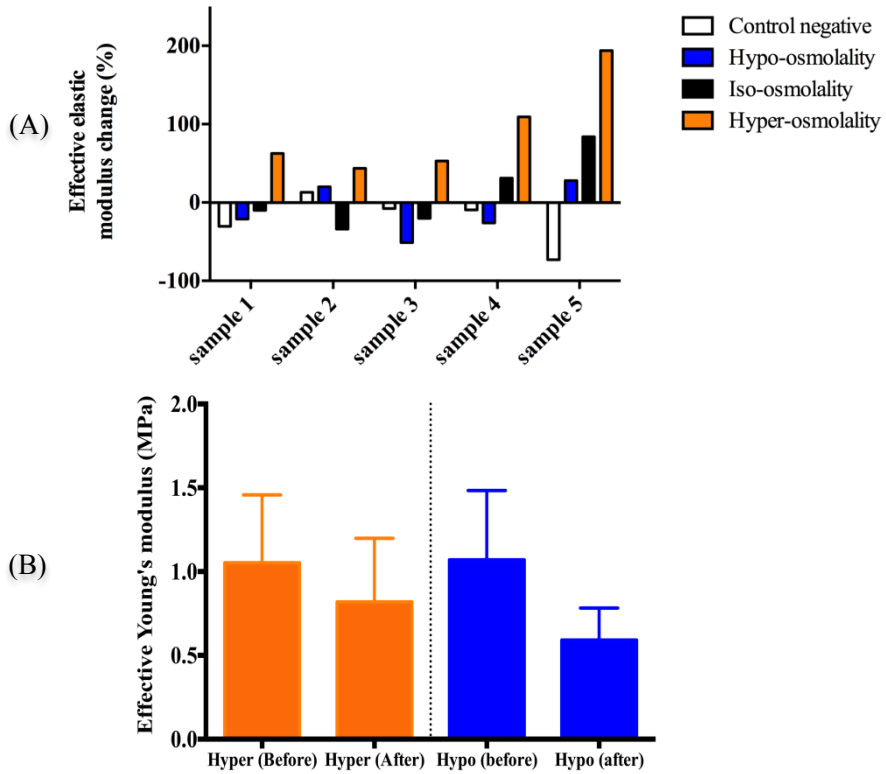

Figure 10.2. (A) Alterations in the effective Young's modulus following the incubation with L-threose compared to sample's intrinsic effective Young's modulus before incubation with L-threose. The change of effective Young's modulus of hyper-osmolal vs. control negative as well as hypo-osmolal vs. hyper-osmolal was statistically significant (p-value<0.005). (B) Effective Young's modulus change before and after incubation in Hypo- and Hyper-osmolality solutions without L-threose.

Contrast enhanced micro-CT

Previous studies showed that cross-linking is associated with the formation of free negative groups on the collagen molecules, which leads to increased density of net negative charges within the extracellular matrix [19]. Determination of possible increase in the negative charge within the extracellular matrix was achieved using contrast-enhanced micro-CT. However, increase in negative charge density due to cross-linking is counteracted by possible leakage of negatively charged GAGs due to enzymatic activity within the matrix particularly during prolonged incubation with L-threose. Our experiments on the negative control samples (iso-osmolality and no L-threose) confirmed tangible GAG loss in those samples (Figure 10.3). Therefore, average grey values obtained before and after incubation with L-threose indicate the effects of both aforementioned phenomena. The increased penetration of Hexabrix followed a rising trend toward decreasing the osmolality within each group of samples (Figure 10.3, p-value=0.12).

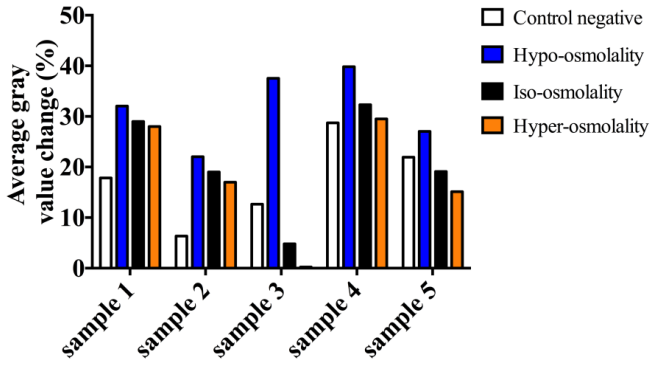

Figure 10.3. Increase in average grey value indicating the Hexabrix penetration depending on the net negative charges in the ECM. The equilibrium penetration of Hexabrix is inversely related to the amount of matrix fixed charge density.

Cartilage surface color analysis

Non-enzymatic cross-linking causes the white surface of normal articular cartilage to turn brown. Our cartilage surface color analysis allowed us to clearly identify differences in the intensity of the brown color between treated and non-treated normal specimens. The intensity of the color is an indicator of efficacy of the cross-linking process as the trend suggests (Figure 10.4).

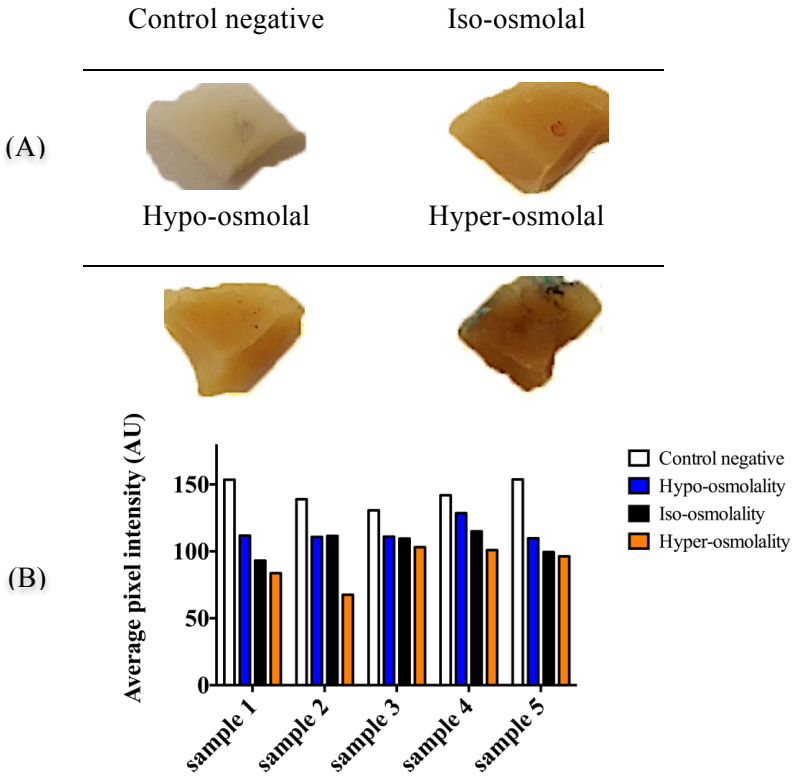

Figure 10.4. (A) Changes in the color of horse cartilage for negative control, iso-osmolal, hypo-osmolal and hyper-osmolal specimens after 4 days incubation. (B) Cartilage surface color analysis: Brighter color represents higher average pixel intensity, while dark yellow/brown represents lower average pixel intensity.

Pentosidine level

In general, the pentosidine level per collagen (pmol/pmol) increases with the level of osmolality during the L-threose treatment (Figure 10.5A). The amount of pentosidine per collagen (mol/mol) increased 47% from hypo-osmolality toward hyper-osmolality (average difference over the 5 samples). Plotting the amounts of pentosidine per collagen molecules versus surface color reveals a decreasing trend as expected (Figure 10.5B).

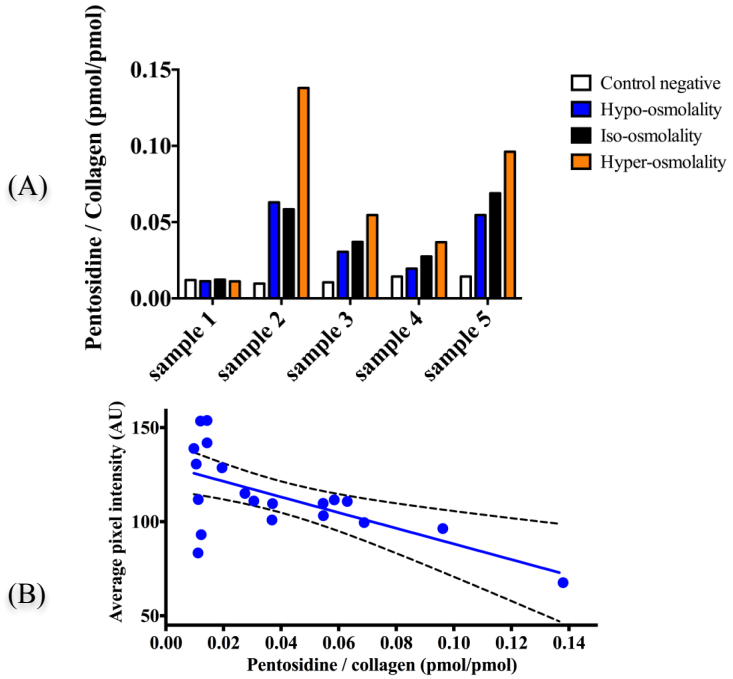

Figure 10.5. (A) Amount of pentosidine per collagen (mol/mol) is reported for different osmolality conditions. In average, the hyper-osmolality led to higher accumulation of pentosidine per collagen molecule (mol/mol) (p-value>0.05). The difference was higher between hyper-osmolality and control negative (p-value=0.067). (B) Average pixel value of the cartilage surface vs. pentosidine per collagen molecules (r=-0.63 and p-value=0.0027).

10.4. **DISCUSSION**

We investigated the effects of the mechanical strain experienced by collagen fibrils on their chemical response to non-enzymatic glycation, leading to pentosidine cross-linking. Due to the fixed charges of the glycosaminoglycan molecules enmeshed within fibrillary network of collagen molecules, articular cartilage allows for the exchange of water from/to the external bath. To maintain osmotic balance, normal articular cartilage swells when exposed to hypo-osmolality, while it shrinks under hyper-osmolality. Different joint diseases have been shown to cause a decrease in the osmolality of the synovial fluid, particularly in osteoarthritic and rheumatoid arthritis [20, 21]. In this study, osmolality was adopted as a means to induce expansion and shrinkage of the articular cartilage and its collagen fibers. Measurements of the effective Young's modulus of cartilage (stiffness) at several locations within a prescribed indentation matrix before and after L-threose incubation were performed. Our data indicated that incubation with L-threose as the reducing sugar results in stiffened cartilage matrix, which agrees with the findings of a previous study [22]. Our micro-indentation data illustrated that L-threose treatment under hyper-osmolality enhances the formation of advanced glycation end-products (Figure 10.2). In contrast to hyper-osmolality, hypo-osmolality showed restrictive effects on the non-enzymatic glycation cross-linking, indicating that expanded collagen fibrils are less susceptible to react with L-threose. Our observations are in line with findings of previous research that underscored the importance of stretching the collagen molecules in various forms of molecular, fibrillary and tissue level, to protect them against enzymatic activity [7-10]. Sufficient compressive strain of the extracellular matrix, i.e. 25% strain, has been shown to buckle the collagen fibrils [23] and consequently affect the conformation of collagen building blocks, i.e. amino acids, which is believed to affect the susceptibility to enzymatic degradation. Our micro-indentation data suggest that expansion protects the ECM against glycation or the so-called 'artificial ageing', whereas shrinkage makes it prone to glycation, although in our study the induced shrinkage and expansion were below 25% of the original cartilage thickness. Using a bath containing a neutral contrast agent (iodixanol), we determined the swelling behavior of equine cartilage at the osmolalities applied in this study when articular cartilage was kept attached to the subchondral bone. Those experiments showed; post free swelling, less than 4% at

hypo-osmolality (100 mOsm/kg water) which is consistent with a previous study [23], whereas hyper-osmolality (4000 mOsm/kg water) resulted in less than 3% shrinkage (data not shown). This infers that relatively mild matrix deformations are enough to affect the cross-linking efficiency. Moreover, it is well established [23, 24] that high salt concentration in the bath modulates up ions flux through the cartilage matrix, shielding the negatively charged proteoglycans from further ionic interactions, which results in more relaxing state of the collagen fibrils (less pre-stress).In addition, higher ionic concentration in the extrafibrillar region than the intrafibrillar region expels the intrafibrillar water [23], causing denser collagen fibril network (crushed collagen fibrils), which obviously alters the spatial conformation of the lysin and arginine, mainly responsible for non-enzymatic cross-linking. Moreover, the intrafibrillar water normally follows an exponential decay function of the applied external osmotic pressure [23], which has likely influenced our cross-linking efficiency the most.

Previous studies have shown that the osmolality of the synovial fluid decreases in the patients with osteoarthritis and rheumatoid arthritis [20, 21]. As this will create increased swelling of the cartilage (in an early phase of the disease) it might be a protective strategy from advanced glycation in the diseased joint. Moreover, exercise has been shown to be associated with decreased osmolality of the synovial fluid [25]. Our data, although not exactly in-line with the physiologic osmolalities, suggest that by maintaining the osmolality of the environment surrounding the cartilage sufficiently yet wisely low, the chance of cross-linking of the collagen fibrils can be minimized.

It is well-known that non-enzymatic glycation results in accumulation of net negative charge generated by the additional group on the collagen molecules [19]. To identify increased net negative charge post L-threose treatment, negatively charged contrast agent (Hexabrix) was used, which its equilibrium concentration inversely correlates with the amount of formed negatively charged groups. The penetration of Hexabrix was shown to follow an osmolality-dependent trend (Figure 10.3) which means higher osmolality results in less penetration of Hexabrix, likely due to direct electrostatic interaction between glycation-driven negatively charged groups and Hexabrix. Furthermore, in highly cross-linked collagens, steric hindrance, which slows the diffusion rate down, also plays a role as a barrier against Hexabrix transport [15, 19].

The color of the cartilage surface undergoes a shift from white toward yellow/brown in non-enzymatic cross-linking [26]. Therefore, the pixel intensity of cartilage surface could provide potential indication of the intensity of the cross-linking process. The pixel intensity was significantly different between the control and other samples indicating the efficacy of the cross-linking process. Similar to the above-mentioned analyses, pixel intensity varied according to the osmolality of the external bath with the highest difference observed between the hypo- and hyper-osmolality conditions among all L-threose treated samples (26.6% based on hyper-osmolality). Similar to the observations regarding the surface color, pentosidine per collagen molecule values also confirm that increasing the osmolality leads to increased non-enzymatic cross-linking (Figure 10.5A).

We have found that hypo-osmolality and the related stretching of collagen molecules, lowers the glycation (ageing) efficiency in collagen fibrils. We believe that this is due to the micro-unfolding of the triple helix [27]. Another study suggested that cross-linked collagen fibrils are more susceptible to enzymatic degradation when stretched in tendon tissue [28], which again sheds light on the importance of underlying forces that regulate chemical processes in connective tissues.

It is widely believed that the superficial layer of articular cartilage represents a highly inhomogeneous distribution of collagen fibrils and glycosaminoglycans, which creates heterogeneous mechanical behavior [1]. Due to this fact, slight differences between iso-osmolality (400 mOsm/kg water or 0.2 M NaCl) and hypo-osmolality (100 mOsm/kg water or 0.05 M NaCl), which are relatively similar conditions as compared to the hyper-osmolality condition (4000 mOsm/kg water or 2 M NaCl), may not be fully captured. The elastic properties calculated here indicate the pre-stress in the collagen fibrils [13], but as articular cartilage is intrinsically a poroelastic material its hydraulic permeability could provide additional information about the possible restrictions against fluid flow due to cross-linking. As cartilage properties changes across its thickness, one could apply deep indentations to obtain details regarding depth-wise mechanical and physical properties. Solute features such as permeability through extracelluar matrix could also affect the cross-linking efficacy as accumulation of small ions in the extrafibrillar region causes exudation of the intrafibrillar water, which potentially restricts the accessibility of L-threose to the collagen molecules and is therefore worth investigating.

In conclusion, we have shown that non-enzymatic cross-linking of collagen fibrils of articular cartilage can be controlled through shrinking or stretching of the cartilage tissue, which we applied through adjustment of the bath osmolality. Our micro-indentation data, colorimetry of the cartilage surface, pentosidine level measurement, and contrast-enhanced computed tomography data all show that increased osmolality accelerates advanced glycation and the 'ageing' of articular cartilage.

Our findings contribute towards understanding how the mechanical environment of the articular cartilage influences the chemical reactions between sugars and collagen building blocks at micro-scale, which undergo micro-unfolding of the triple helix in the hyper-osmolal and glycation sensitive conditions. We believe that more advanced understanding of collagen fibrils mechanochemistry provided here, evokes potential ageing prohibiting strategies against cartilage deterioration.

10.5. **REFERENCES**

1. Sophia Fox, A.J., A. Bedi, and S.A. Rodeo, *The Basic Science of Articular Cartilage: Structure, Composition, and Function*. Sports Health, 2009. **1**(6): p. 461-8.
2. Grushko, G., R. Schneiderman, and A. Maroudas, *Some biochemical and biophysical parameters for the study of the pathogenesis of osteoarthritis: a comparison between the processes of ageing and degeneration in human hip cartilage*. Connect Tissue Res, 1989. **19**(2-4): p. 149-76.
3. Weinans, H., et al., *Pathophysiology of peri-articular bone changes in osteoarthritis*. Bone, 2012. **51**(2): p. 190-6.
4. Wachtel, E., A. Maroudas, and R. Schneiderman, *Age-related changes in collagen packing of human articular cartilage*. Biochim Biophys Acta, 1995. **1243**(2): p. 239-43.
5. Lotz, M. and R.F. Loeser, *Effects of aging on articular cartilage homeostasis*. Bone, 2012. **51**(2): p. 241-8.
6. Sell, D.R. and V.M. Monnier, *Structure elucidation of a senescence cross-link from human extracellular matrix. Implication of pentoses in the aging process*. J Biol Chem, 1989. **264**(36): p. 21597-602.
7. Bhole, A.P., et al., *Mechanical strain enhances survivability of collagen micronetworks in the presence of collagenase: implications for load-bearing matrix growth and stability*. Philos Trans A Math Phys Eng Sci, 2009. **367**(1902): p. 3339-62.
8. Chang, S.-W., et al., *Molecular mechanism of force induced stabilization of collagen against enzymatic breakdown*. Biomaterials, 2012. **33**(15): p. 3852-3859.
9. Camp, R.J., et al., *Molecular mechanochemistry: low force switch slows enzymatic cleavage of human type I collagen monomer*. J Am Chem Soc, 2011. **133**(11): p. 4073-8.
10. Tonge, T.K., J.W. Ruberti, and T.D. Nguyen, *Micromechanical Modeling Study of Mechanical Inhibition of Enzymatic Degradation of Collagen Tissues*. Biophys J, 2015. **109**(12): p. 2689-700.
11. Dittmore, A., et al., *Internal strain drives spontaneous periodic buckling in collagen and regulates remodeling*. Proc Natl Acad Sci U S A, 2016. **113**(30): p. 8436-41.
12. Hardin, J.A., N. Cobelli, and L. Santambrogio, *Consequences of metabolic and oxidative modifications of cartilage tissue*. Nat Rev Rheumatol, 2015. **11**(9): p. 521-9.
13. Moshtagh, P.R., et al., *Micro- and nano-mechanics of osteoarthritic cartilage: The effects of tonicity and disease severity*. J Mech Behav Biomed Mater, 2016. **59**: p. 561-71.
14. Maroudas, A. and C. Bannon, *Measurement of swelling pressure in cartilage and comparison with the osmotic pressure of constituent proteoglycans*. Biorheology, 1981. **18**(3-6): p. 619-32.
15. Pouran, B., et al., *Isolated effects of external bath osmolality, solute concentration, and electrical charge on solute transport across articular cartilage*. Med Eng Phys, 2016. **38**(12): p. 1399-1407.
16. Bae, W.C., et al., *Indentation testing of human cartilage: sensitivity to articular surface degeneration*. Arthritis Rheum, 2003. **48**(12): p. 3382-94.
17. Sondergaard, B.C., et al., *Relative contribution of matrix metalloprotease and cysteine protease activities to cytokine-stimulated articular cartilage degradation*. Osteoarthritis Cartilage, 2006. **14**(8): p. 738-48.

18. Bank, R.A., et al., *Amino Acid Analysis by Reverse-Phase High-Performance Liquid Chromatography: Improved Derivatization and Detection Conditions with 9-Fluorenylmethyl Chloroformate.* Analytical Biochemistry, 1996. **240**(2): p. 167-176.
19. Kokkonen, H.T., et al., *Computed tomography detects changes in contrast agent diffusion after collagen cross-linking typical to natural aging of articular cartilage.* Osteoarthritis Cartilage, 2011. **19**(10): p. 1190-8.
20. Bertram, K.L. and R.J. Krawetz, *Osmolarity regulates chondrogenic differentiation potential of synovial fluid derived mesenchymal progenitor cells.* Biochem Biophys Res Commun, 2012. **422**(3): p. 455-61.
21. Shanfield, S., et al., *Synovial fluid osmolality in osteoarthritis and rheumatoid arthritis.* Clin Orthop Relat Res, 1988(235): p. 289-95.
22. Verzijl, N., et al., *Crosslinking by advanced glycation end products increases the stiffness of the collagen network in human articular cartilage: a possible mechanism through which age is a risk factor for osteoarthritis.* Arthritis Rheum, 2002. **46**(1): p. 114-23.
23. Basser, P.J., et al., *Mechanical properties of the collagen network in human articular cartilage as measured by osmotic stress technique.* Arch Biochem Biophys, 1998. **351**(2): p. 207-19.
24. Setton, L.A., H. Tohyama, and V.C. Mow, *Swelling and curling behaviors of articular cartilage.* J Biomech Eng, 1998. **120**(3): p. 355-61.
25. Baumgarten, M., et al., *Normal human synovial fluid: osmolality and exercise-induced changes.* The Journal of Bone & Joint Surgery, 1985. **67**(9): p. 1336-1339.
26. Chen, A.C., et al., *Induction of advanced glycation end products and alterations of the tensile properties of articular cartilage.* Arthritis Rheum, 2002. **46**(12): p. 3212-7.
27. Bourne, J.W. and P.A. Torzilli, *Molecular simulations predict novel collagen conformations during cross-link loading.* Matrix biology : journal of the International Society for Matrix Biology, 2011. **30**(5-6): p. 356-360.
28. Bourne, J.W., J.M. Lippell, and P.A. Torzilli, *Glycation Cross-Linking Induced Mechanical-Enzymatic Cleavage of Microscale Tendon Fibers.* Matrix biology : journal of the International Society for Matrix Biology, 2014. **34**: p. 179-184.

CHAPTER 11

CONCLUDING REMARKS AND FUTURE DIRECTIONS

Physico-chemical phenomena, namely molecular and convective transport as well as chemical reactions play a crucial role in proper metabolic, anabolic and physiological functioning of articular cartilage and the subchondral bone plate. In the current thesis, novel experimental and finite element platforms assisted to enhance the understanding of the solute transport across articular cartilage and the osteochondral interface using a multi-scale approach. Moreover, the effects of chemical reactions that generate advanced glycated cross-links which prevail during ageing were investigated under different osmotic conditions. The multiphysics phenomena behind those processes are highly complicated due to the interplay of a multitude of parameters such as the non-uniform distribution of negatively charged proteoglycans, varying thickness of collagen fibrils, the water content gradient in cartilage and the complex pore structure of calcified cartilage and the subchondral bone plate. To accurately address the effect of each parameter, specific experimental setups, i.e. contrast-enhanced micro-computed tomography, micro-indentation, histology, biochemical tests and advanced microscopy, have been designed to form the basis for the development of sophisticated computational methods i.e. finite element models and pore-network modeling. The key conclusions extracted from the individual chapters in this thesis will enhance our insight in this complex matter.

Chapter 2: Choosing the appropriate imaging tool to study the diffusion process in cartilage is not trivial. The selection criteria include, but are not limited to, achievable resolution, acquisition time, bath attributes and cartilage thickness. Computed Tomography (CT) techniques feature high resolution and low acquisition time and are therefore suitable to study the diffusion of radiopaque molecules in various zones of the tissue. Magnetic Resonance Imaging (MRI) techniques are often capable of capturing diffusion of water and some small molecules, but the long acquisition time, low out-of-plane resolution and high costs limit their wide application. Fluorescent microscopy allows high in-plane resolution when used to image the extracellular matrix of the excised explants and is ideal to study the diffusion in the pericellular matrix.

Chapter 3: Three types of intertwined physical phenomena, mechanical, electrical and chemical, complicate the transport processes in articular cartilage. The separate effects of external bath osmolality, bath concentration and solute's charge were investigated in this chapter using a combination of experimental and

biphasic-solute computational techniques. Bath concentration and osmolality had little effect on the diffusion in different zones of cartilage, suggesting that the diffusion of neutral contrast agent follows Fickian behavior. On the other hand, diffusion of negatively charged solute, strongly deviated from idealized Fickian behavior, revealing much lower flux compared to that of the neutral solutes.

Chapter 4: A novel biphasic-solute finite element model was developed to calculate the diffusion coefficient of neutral solutes diffusing axially in different zones of articular cartilage, based on contrast-enhanced micro-computed tomographic experiments. The diffusion coefficient of the superficial zone was one order of magnitude larger than in the middle zone. The higher compactness of proteoglycans and the lower water content in the middle zone are likely the primary reasons of lower diffusion coefficient in this zone.

Chapter 5: A multi-zone multiphasic finite element model was developed based on the contrast-enhanced micro-computed tomographic experiments to describe the transport of charged solutes. The model not only allowed calculation of the diffusion coefficient in different cartilage zones, but also estimation of the fixed charge density (FCD) in different zones. The diffusion coefficient of the superficial zone was ten times higher than in the middle zone while the FCD of the middle zone was about two times higher in the middle zone.

Chapter 6: The overlying solute-containing bath in contact with the cartilage surface continuously interacts with the tissue and might therefore alter the diffusion characteristics. The size of the bath, stirring of the bath and the possible formation of a stagnant layer are among the most likely influential factors affecting the transport across cartilage. Using advanced biphasic-solute finite element models, the well-stirred condition could be attained when the ratio of diffusivity of bath to cartilage was at least 1000. Unlike the thickness of the stagnant layer at the cartilage-bath interface, its concentration substantially affects the diffusion characteristics. Stirring showed promise in attenuating the stability of the stagnant layer, hence mitigating its effect. This multiphysics platform could be employed to design efficient diffusion experiments when using soft hydrated tissues.

Chapter 7: Diffusion at the interface of cartilage and subchondral bone has long been debated. Contrast-enhanced micro-computed tomographic experiments on human and equine samples not only confirmed the existence of such diffusion at the osteochondral interface, but also showed the importance of thickness and

porosity of the subchondral bone plate and of cartilage thickness on solute transport.

Chapter 8: A multi-zone biphasic-solute platform was developed to capture the diffusion of neutral solutes in cartilage and subchondral bone plate simultaneously. The findings confirmed the decrease in diffusion coefficient when traveling from the superficial zone to the deep zone of cartilage and that the diffusion coefficient of the deep cartilage zone is 1.5-fold higher than of the subchondral bone plate.

Chapter 9: The pathways by which solutes transfer across the osteochondral interface were investigated in this chapter. Nano-structural observations revealed a continuous and gradual transition of mineralization architecture from the non-calcified cartilage region towards the calcified cartilage, revoking the textbook picture of the so-called tidemark; a well-defined discontinuity at the osteochondral interface zone. The 3D structure of the pores was obtained using the FIB-SEM technique that showed that pores were larger and more connected in the subchondral bone plate than in the calcified cartilage. A pore-network model was created from this data and applied to determine the diffusion coefficient and hydraulic permeability of calcified cartilage and of the subchondral bone plate. Perpendicular to the osteochondral interface, the diffusion coefficient and hydraulic permeability were respectively 1.5 and 1000 times higher in the subchondral bone plate.

Chapter 10: Non-enzymatic (advanced) glycation in the collagen fibrils within articular cartilage (i.e. a form of artificial ageing) was induced under external hypo-, iso- and hyper-osmolality conditions. Tuning the extent of collagen pre-stress and inter-fibrillar spacing via osmolality-switch altered the efficiency of collagen fibril cross-linking. The hypo-osmolality condition (swelling) made cartilage less susceptible to advanced glycation. These findings indicate that timely adjusted joint osmolality may decelerate the efficiency of the ageing process and thus possibly prolong the functionality of the tissue.

This thesis provides an in-depth understanding of various physical phenomena involved in solute transport in cartilage and underlying bone, as well as of the effect of the advanced glycation (ageing) process in articular cartilage using a combination of experiments and numerical techniques. Practical extensions to the solute transport part are suggested through designing efficacious diffusion platforms to enhance diffusion of therapeutic compounds or promote

contrast agent delivery to cartilage. Simultaneous transport of multiple contrast agents with various charges to acquire more detailed information regarding the health state of cartilage could be a future step as an extension to the findings of the current thesis. Furthermore, it is proposed that on-line investigation of diffusion of biologically relevant solutes such as cytokines across the osteochondral interface in healthy and degenerate tissues may lead to a better understanding of the cross-talk between cartilage and bone during disease, e.g. in osteoarthritis progression. Study of transport of charged solutes across the osteochondral interface and development of pore-scale models to describe their interactions with the pore wall is suggested.

Regarding the degeneration of cartilage, future experiments could be set up to investigate the enzymatic degradation (e.g. Matrix metalloprotease-driven) of collagen fibrils within the aged tissue to understand the degeneration of cartilage when aging and osteoarthritis act together. Efficient delivery tools based on enhanced transport of anti-aging compounds can then be designed to treat the susceptible aged cartilage.

SUMMARY

Articular cartilage and its connecting subchondral bone plate are main compartments that play an important role in proper mechanical functioning of diarthrodial joints. However, in ageing and osteoarthritis structural changes propagate in these tissues, which impairs them for proper functioning. One way to characterize the structural alterations during different stages of degeneration and disease is to perform solute transport tests in an experimental set-up and quantify the parameters such as diffusivity (diffusion rate) and permeability (fluid ability to pass through a porous solid) that represent the quality of the tissue. Therefore, common imaging techniques to investigate diffusion across cartilage have been reviewed and suggestions to select appropriate tools to determine diffusion parameters were made.

The primary aim of this thesis is to setup a set of experiments that can capture the transport (diffusion) properties of cartilage and its underlying bone. To this end we designed experiments that used contrast-enhanced micro-computed tomography to measure diffusion through cartilage and subchondral bone and applied computational models of these experiments to quantify the physical parameters such as diffusivity and permeability of the tissues concerned. The individual role of the bath osmolality, concentration and solute's charge on the diffusion in articular cartilage was successfully studied and solute's charge was identified as the dominant factor. Biphasic-solute and multiphasic finite element models were subsequently developed to precisely simulate the transport of neutral and charged solutes in various cartilage zones, respectively. As the cartilage-bone interface experiences morphological alterations after joint degeneration and during progression of osteoarthritis, characterization of the transport properties of the interface becomes of paramount importance. Therefore, experiments based on contrast-enhanced micro-computed tomography were first conducted and a correlation was found between the extent of diffusion and the micro-architecture of the subchondral bone plate and articular cartilage. Multi-zone biphasic-solute finite element models then assisted in determination of diffusion coefficients in different cartilage layers and the subchondral bone plate. To identify the pathways between cartilage and bone responsible for transport, focused-ion-beam scanning electron microscopy (FIB-SEM) imaging was employed. Using the 3D data of the

pore structure at the osteochondral interface and with the aid of advanced pore-network modeling, the diffusive and permeability attributes of the extracellular matrices were successfully determined.

The next theme of this thesis was to assess the effects of collagen fibril conformation under different environmental osmotic pressure on advanced non-enzymatic glycation, a process, responsible for cartilage deterioration during ageing. Sugars were added under different external bath osmotic pressures to study the glycation process when collagen fibrils are either stretched or shrunk. Using micro-indentation, biochemical assays, contrast-enhanced micro-computed tomography and cartilage surface colorimetry, the stretching of the collagen fibrils was found to minimize the degenerative effects of sugar-induced glycation.

The author believes that the current findings contribute to solve the yet-challenging physico-chemical problems involved in the cartilage and its related joint disease. The current work will lead to new techniques that aim to not only understand the fundamental physico-chemical aspects of cartilage, but also might suggest methods for efficient delivery of drugs into the cartilage tissue and visualizing agents that could better follow and diagnose joint disease.

SAMENVATTING

Articulair kraakbeen en het verbindende subchondrale bot zijn de hoofdbestanddelen die een rol spelen bij het mechanisch goed functioneren van synoviale gewrichten. Echter, bij veroudering en artrose ontstaan structurele veranderingen in deze weefsels, die hen belemmeren in het functioneren. Een manier om de structurele veranderingen tijdens de verschillende fasen van weefseldegeneratie en ziekte te bestuderen is het uitvoeren van experimenten die de transport van vloeistof door het kraakbeen en bot testen in een experimentele opstelling, om daarmee fysische parameters zoals diffusie en permeabiliteit te kwantificeren die ons iets vertellen over de kwaliteit van het weefsel. Allereerst is er een review gemaakt van algemene beeldvormingstechnieken voor diffusie in kraakbeen. Hieruit komen suggesties voor de beste gereedschappen voor het bepalen van diffusie gerelateerde parameters in kraakbeen.

Het belangrijkste doel van dit proefschrift is het opzetten van een reeks experimenten die de transporteigenschappen door het kraakbeen en het onderliggende bot kunnen vastleggen. Daartoe hebben we experimenten ontwikkeld die gebruik maken van een contrastvloeistof in combinatie met micro-computertomografie om diffusie door kraakbeen en subchondraal bot te meten. Daarnaast hebben we gebruik gemaakt van computermodellen die deze experimenten simuleren, zodat fysische parameters zoals diffusie en permeabiliteit van de betrokken weefsels gekwantificeerd konden worden.

De individuele rol van osmolaliteit, concentratie en elektrische lading in de vloeistof werd nader bestudeerd. Hierbij werd de elektrische lading geïdentificeerd als de belangrijkste factor voor het transport. Deze elektrische lading zorgt ervoor dat vloeistoffen zich in kraakbeen niet standaard gedragen volgens de reguliere diffusiewetten. Vervolgens werden twee-fase en multi-fase eindige elementen modellen ontwikkeld om het transport van ongeladen en elektrisch geladen vloeistoffen in verschillende kraakbeenzones nauwkeurig te simuleren. Aangezien de kraakbeen-bot interface morfologische veranderingen ondervindt tijdens de gewrichtsdegeneratie is dit een belangrijke structuur die gevolgen heeft voor de transport van moleculen en vloeistoffen en derhalve is karakterisering van deze transporteigenschappen door de kraakbeen-bot interface van groot belang. Daarom werden experimenten uitgevoerd met contrast-houdende vloeistoffen

zodat m.b.v. micro-computertomografie het transport van vloeistof nauwkeurig gemeten kon worden. Hierbij werd er een correlatie gevonden tussen de mate van diffusie en de micro-architectuur van de subchondrale botplaat. Met behulp van de bifasische eindige element modellen (vaste en vloeistof fase) konden vervolgens de diffusiecoëfficiënten in verschillende kraakbeenlagen en de subchondrale botplaat worden bepaald. Om meer details van de morfologie en de microarchitectuur op het overgangsgebied tussen kraakbeen en bot te identificeren, werd gebruik gemaakt van beeldvorming m.b.v. gefocusseerde-ion-beam-scanning-elektronenmicroscopie (FIB-SEM). Met deze methode wordt een deel van het weefsel met een laserstraal verwijderd en kunnen zeer nauwkeurige 3D-gegevens van de poriestructuur worden verkregen. Aldus werden bij enkele osteochondrale preparaten nauwkeurig de bot-kraakbeen interface in kaart gebracht en vervolgens met behulp van geavanceerde computermodellen, die de porie-structuur exact weergeven, de diffusie en permeabiliteit van het weefsel bepaald.

Het volgende thema van dit proefschrift was het bepalen van de effecten van de conformatie van de collageenfibrillen op 'versuikering' (niet-enzymatische glycatie) van het kraakbeen. Deze glycatie verzwakt het kraakbeen en wordt gezien als een belangrijke component bij het verouderingsproces van kraakbeen. Om dit glycatieproces te induceren, werden suikers toegevoegd onder hypo-osmotische druk van de vloeistof, waardoor het kraakbeen vocht aanzuigt en het collageen derhalve verder uitrekt. Met behulp van micro-indentatie proeven, biochemische analysen, micro-computertomografie van contraststoffen en het meten van de verkleuring van het kraakbeenoppervlak, bleek het oprekken van de collageenfibrillen de mate van suiker-geïnduceerde glycatie te minimaliseren.

De auteur is van mening dat de bevindingen in dit proefschrift kunnen bijdragen tot het verkrijgen van meer inzicht in de fysisch-chemische aspecten van kraakbeen en de daarmee samenhangende ziektebeelden. Op basis van het huidige werk kunnen nieuwe technieken geïnduceerd worden die niet alleen de fundamentele fysisch-chemische aspecten van kraakbeen onderbouwen, maar ook methoden kunnen genereren voor een efficiëntere afgifte van geneesmiddelen in het moeilijk doordringbare kraakbeen of voor het beter visualiseren van kraakbeenweefsel ten behoeve van de diagnostiek van artrose

APPENDIX A

AN EXPERIMENTAL AND FINITE ELEMENT PROTOCOL TO INVESTIGATE TRANSPORT OF NEUTRAL AND CHARGED SOLUTES ACROSS ARTICULAR CARTILAGE

This appendix is submitted as a scientific video journal (Invited):

V. Arbabi*, **B. Pouran***, A.A. Zadpoor, H. Weinans. *Experimental and finite element protocol to investigate transport of charged and neutral solutes across articular cartilage*. Journal of Visualized Experiments, 23, 2017, 122.

*These authors contributed equally.

Appendix A

ABSTRACT

Osteoarthritis (OA) is a debilitating disease that is associated with degeneration of articular cartilage and subchondral bone. Degeneration of articular cartilage impairs its load-bearing function substantially as it experiences tremendous chemical degradation, i.e. proteoglycan loss and collagen fibril disruption. One promising way to investigate chemical damage mechanisms during OA is to expose the cartilage specimens to an external solute and monitor the diffusion of the molecules. The degree of cartilage damage (i.e. concentration and configuration of essential macromolecules) is associated with collisional energy loss of external solutes while moving across articular cartilage creates different diffusion characteristics compared to healthy cartilage. In this study, we introduce a protocol, which consists of several steps and is based on previously developed experimental micro-computed tomography and finite element modeling. The transport of charged and uncharged iodinated molecules is first recorded using micro-computed tomography, which is followed by applying biphasic-solute and multiphasic finite element models to obtain diffusion coefficients and fixed charge densities across cartilage zones.

Appendix A

INTRODUCTION

Molecular transport plays a vital role in the homeostasis of articulating joints, delivery of therapeutics to articular cartilage and contrast-enhanced cartilage imaging [1-3]. Factors such as cartilage integration and intactness, solute charge and size as well as osmolality and concentration of bath in contact with cartilage may influence the transport rate [4-6]. The transport of solutes, either neutral or charged, can be different between articular cartilage zones, because each zone consists of different concentrations and orientations of major extracellular matrix molecules, namely proteoglycans (PGs) and collagen type II [1, 7-11]. More importantly, the transport of charged solutes can be highly dependent on the concentration of proteoglycans comprising negative fixed charges within the extracellular matrix which increases across articular cartilage [8, 9]. Those parameters particularly fixed charge density (FCD), orientation of collagen fibrils and water content variation across cartilage may undergo alterations as osteoarthritis (OA) progresses, thereby signifying the importance of studying diffusion across cartilage.

In the current study, a protocol based on previously established experimental and computational studies [6, 8, 9] is proposed to accurately investigate diffusion under various boundary conditions using neutral and charged solutes in a finite-bath model of diffusion. The proposed methods are composed of micro-computed tomography imaging (micro-CT) of a system including cartilage and a finite-bath supported by advanced biphasic-solute and multiphasic finite element models. These models enable obtaining the diffusion coefficients of neutral and charged molecules as well as FCDs across various zones of articular cartilage. Using these models, one can gain better understanding of the behavior of the diffusing neutral and charged molecules that could be used to investigate the interactions between cartilage and overlaying finite-bath.

Appendix A

PROTOCOL

Note: The protocol presented here is adopted from the experimental and computational procedures of recent research papers [8, 9, 12]. The protocol is illustrated in Figure 1.
The cadaveric materials were collected with permission from veterinary faculty of Utrecht University.

1. SAMPLE AND BATH PREPARATION

1.1. Drill out cylindrical osteochondral plugs (diameter of 8.5 mm) from cadaveric equine femoral condyles using custom-made drill bit (Figure 1) while spraying cool phosphate buffer serum (PBS) to prevent overheating and subsequent cartilage damage.

1.2. Heat-shrink the osteochondral plugs with a plastic shrinking sleeve to minimize the lateral diffusion of the overlaying bath.

1.2.1. Mount the osteochondral plug with cartilage at the top initially inside the plastic shrinking sleeve and follow by blowing hot air to it. Add wet cotton pieces on the surface of cartilage to prevent heat-related damage

1.3. Prepare finite-baths of charged (650 μL, 420 mM, ioxaglate, molecular weight (MW) = 1269 Da, charge=-1) and neutral (650 μL, 420 mM, iodixanol, MW= 1550 Da) solutes separately.

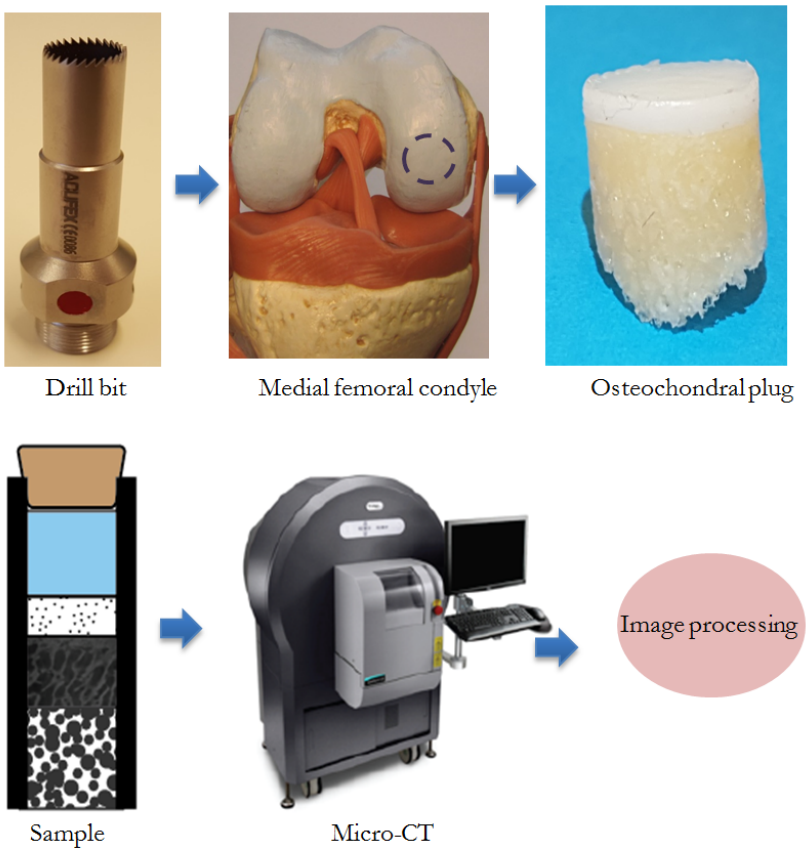

Figure 1. A) Sample extraction procedure using a custom-made drill bit, B) Micro-CT imaging procedure to monitor diffusion process.

1.4. Load the prepared finite-baths on the surface of cartilage using a syringe and place a cork plug on the wrapped sample to prevent evaporation during experiments at room temperature (Figure 2A). To study the neutral solute transport, place the iodixanol bath and to study the negatively charged solute transport place ioxaglate bath onto the cartilage surface.

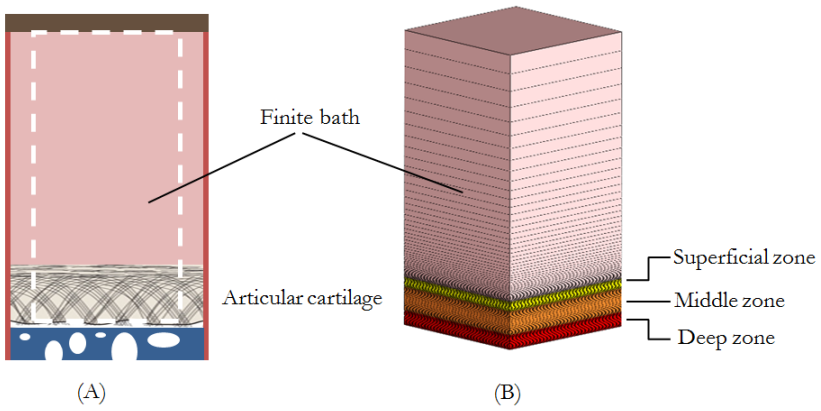

Figure 2. A) Schematic of experimental sample design B) multi-zone computational model consisting of the finite bath, superficial, middle and deep zones of cartilage and associated mesh.

2. IMAGING AND IMAGE PROCESSING

2.1. Place the wrapped samples isolated with cork plug on a custom-made holder attached to the motorized stage of a micro-CT. Place the sample so that cartilage surface covered with contrast agent solution is facing upward.

2.2. Scan using the micro-CT (voxel size of 40×40×40 μm^3, scan time of 2 minutes, tube voltage of 90 kV and tube current of 180 μA) a field of view consisting of cartilage, subchondral plate, and finite-bath in several time points until equilibrium state (48 hours) is reached (Figure 2A). The equilibrium state is achieved when concentration values do not change over time.

2.3. Register the 3D images in different time points based on the initial image to facilitate positioning of the region of interest (ROI) using manufacturer's software (e.g., Analyze).

2.4. Convert the 3D reconstructed micro-CT images into 2D tagged image file format (TIFF) stack before processing them using manufacturer's software.

2.5. Globally segment (ImageJ>Adjust>Threshold) the cartilage from the subchondral bone and overlying bath in the software.

2.6. Obtain the average grey value of cartilage at different time points (ImageJ>Analyze>Measure) using the generated cartilage mask in the previous step.

2.7. Given the initial bath concentration and initial contrast agent concentration in the cartilage, use a linear calibration curve to convert the average grey values to the actual concentration of solutes. Previous data support the fact that grey values maintain a linear relationship with the concentration of contrast agents.

2.8. Plot the solute concentrations versus experimental time points.

3. COMPUTATIONAL MODELING

Note: The diffusion in this problem is assumed to take place in 1D (along the z-axis), which complies with the experimental boundary condition. Therefore, the geometry could be arbitrarily created.

3.1. Build finite-bath based cartilage multi-zone models: 1) cartilage consisting of superficial zone (20% of the total cartilage thickness), middle zone (50% of the total cartilage thickness) and deep zone (30% of the total cartilage thickness) [13] and 2) finite-bath in FEBio[14, 15] (Figure 2B).

3.2. Assign the mechanical and physical properties of different zones of cartilage and bath in FEBio. Young's modulus (10 MPa) was assumed to be high enough to resist the osmotic pressure exerted by the overlying bath and therefore protect the cartilage from excessive deformations.

3.2.1. Use a hydraulic permeability of 10^{-3} mm^4/Ns and Poisson's ratio of 0. Use actual solute diffusion coefficient of the bath in the simulations[8, 9].

3.3. Generate mesh (8-node trilinear hexahedral elements) and refine it near the boundaries (Figure 2B)[8, 9].

3.4. Biphasic-solute model

3.4.1. Apply initial solute concentration in the bath and effective pressure corresponding to it. Look at the description of effective pressure in [9, 16].

3.4.2. Run the model in transient mode to obtain solute concentration versus time curves according to the prescribed diffusion coefficients in different cartilage zones.

3.5. Multiphasic model

Note: The electric fluctuation between bath and tissue can be circumvented by adding two monovalent counter-ions to both the bath and tissue.

3.5.1. For steady-state models: use the same effective fluid pressures and concentrations in cartilage and overlying bath while increasing FCD to its desired value.

3.5.2. For transient models: create a well-stirred finite-bath by keeping the diffusion coefficient in the bath sufficiently high. Inject the solute from the bath-air interface into the bath to reach its desired concentration value.

3.5.3. Transient: remove the prescribed solute concentration boundary condition in the previous step and revert the diffusion coefficient of the finite-bath to its actual diffusion coefficient.

3.5.4. Run the model to obtain solute concentration-time curves based on applied FCDs and diffusion coefficients in different cartilage zones.

3.6. FEBio-MATLAB interface

3.6.1. Develop a MATLAB code to automatically perform simulation in FEBio and plot concentration-time curves (FEBio-MATLAB interface)[8, 9].

3.6.2. Change diffusion coefficients and FCDs in cartilage zones using FEBio-MATLAB interface. Run models in FEBio and extract solute concentration-time curves[8, 9].

3.6.3. Compare the obtained solute concentration-time curves with the experimental data and obtain sets of diffusion coefficients and FCDs in different cartilage zones based on minimum root mean square error (RMSE)[8, 9].

REPRESENTATIVE RESULTS

The representative results provided here are adopted from previous research papers [6, 8, 9, 17].

In OA, articular cartilage undergoes significant changes most importantly GAG loss, and collagen fibril damage [18-20]. Those changes may affect the diffusive behavior of solutes through articular cartilage [21, 22]. We studied axial

diffusion of two iodinated contrast agents, i.e. iodixanol (charge=0) and ioxaglate (charge=-1), in cadaveric equine osteochondral plugs using micro-computed tomography. To quantify the diffusion process of a neutral solute (iodixanol), a biphasic-solute model and a charged solute (ioxaglate) multiphasic model were developed in FEBio that considered the zonal structure of cartilage. The biphasic-solute and multiphasic models could predict the diffusion of iodixanol and ioxaglate across articular cartilage (Figure 3). These models enabled obtaining diffusion coefficient of iodixanol (biphasic-solute) and diffusion coefficient as well as FCD (ioxaglate) in different cartilage zones [8, 9].

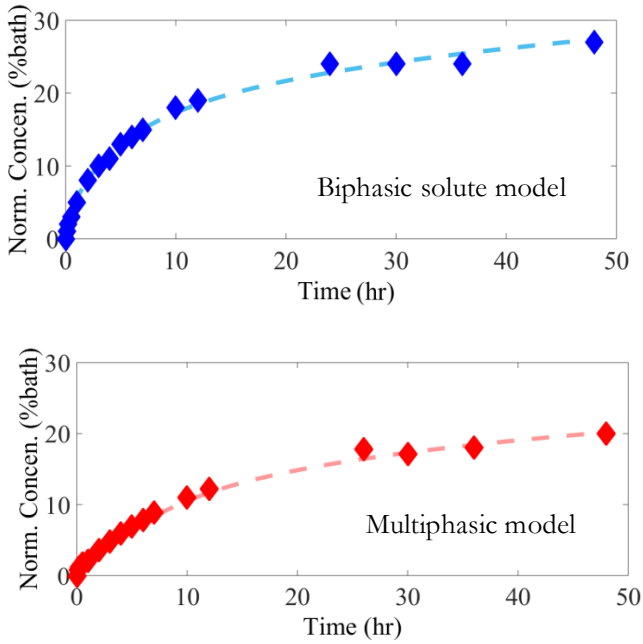

Figure 3. Computationally curve-fitted data A) Multi-zone biphasic-solute (dashed) versus experimental data and B) multiphasic models fits (dashed) versus experimental data (symbol) [8, 9].

DISCUSSION

We presented an experimental protocol combined with a finite element modeling procedure to study the diffusion of neutral and charged solutes across articular cartilage. According to our recent studies, the proposed models could accurately describe the transport of both neutral (biphasic-solute) and negatively charged (multiphasic) solutes across different zones of articular cartilage [8, 9]. It is widely believed that articular cartilage becomes functionally limited through loss of its vital components such as negatively charged GAG macromolecules as well as collagen fibrils during OA progression [22-25]. Using the technique proposed in this study, one can potentially examine the healthiness of articular cartilage. The transport of neutral solute may be augmented in OA primarily because of lower interactions between the solute as well as GAGs and collagens. On the other hand, the transport of negatively charged solutes could help acquire information with respect to the concentration of fixed charges of proteoglycans, thereby giving some indication of the level of OA progression.

The biphasic-solute and multiphasic models that were developed based on the emergence of finite-bath concept according to the previous studies could serve as platforms by which accurate estimation of zonal properties of articular cartilage could be provided. Limitations associated with large baths of contrast agents, namely possible beam-hardening artifacts, and assigning a single diffusion coefficient to articular cartilage[7, 21, 26-31] drove the motivation to develop the current study. In the future OA research, our developed models might potentially find applications for early OA diagnosis.

There are some critical steps required both in experiments and computational simulations. To preserve cartilage integrity during experiments, one would require adding sufficient amounts of protease inhibitors to prevent subsequent enzymatic activities. In case of using one sample for more than one experiment, wash-out time for the penetrated solutes after equilibration was approximately 48 hours. The wash-out efficiency needs to be checked using micro-CT. When using our set up employing equine cartilage, the minimum volume of the overlying bath equivalent to an infinite bath was calculated to be five times higher than cartilage volume. Moreover, to perform finite element modeling of diffusion, it is critical to apply actual solute diffusion coefficient in the bath since deviation from that could affect the outcomes.

In the underlying finite element models, solute size effect was not implemented and therefore could not be studied. Our proposed finite-bath model offers some advantages, namely understanding diffusion process in the articulating joints more appropriately, and reducing beam hardening artefacts. Our proposed technique combining experiments and computational models enables scrutinizing the diffusion attributes of cartilage when positively charged contrast agents are applied. The knowledge of actual solute diffusion coefficient in the bath seems to be crucial as that might significantly affect the accuracy of the obtained diffusion coefficients across articular cartilage. This would require either obtaining the diffusion coefficient of bath experimentally or readily using literature values.

In conclusion, we proposed a general protocol consisting of experiments and computations to investigate the transport of charged and uncharged solutes across articular cartilage. Using the protocol, one can successfully obtain diffusion coefficients and fixed charged densities in different cartilage layers.

ACKNOWLEDGMENTS

The authors would like to express their gratitude to Mr. Jeroen van den Berg and Mr. Matthijs Wassink from the development mechanics group at UMC Utrecht for their help in wrapping process of the osteochondral plugs. This work was supported by a Grant from Dutch Arthritis Foundation.

REFERENCES

1. Arkill, K.P. and C.P. Winlove, *Solute transport in the deep and calcified zones of articular cartilage.* Osteoarthritis Cartilage, 2008. **16**(6): p. 708-14.
2. Chin, H.C., M. Moeini, and T.M. Quinn, *Solute transport across the articular surface of injured cartilage.* Arch Biochem Biophys, 2013. **535**(2): p. 241-7.
3. Leddy, H.A. and F. Guilak, *Site-specific effects of compression on macromolecular diffusion in articular cartilage.* Biophys J, 2008. **95**(10): p. 4890-5.
4. Leddy, H.A. and F. Guilak, *Site-Specific Molecular Diffusion in Articular Cartilage Measured using Fluorescence Recovery after Photobleaching.* Annals of Biomedical Engineering, 2003. **31**(7): p. 753-760.
5. Gu, W.Y. and H. Yao, *Effects of hydration and fixed charge density on fluid transport in charged hydrated soft tissues.* Ann Biomed Eng, 2003. **31**(10): p. 1162-70.
6. Pouran, B., et al., *Isolated effects of external bath osmolality, solute concentration, and electrical charge on solute transport across articular cartilage.* Medical Engineering and Physics, 2016. **38**(12): p. 1399-1407.
7. Kulmala, K.A.M., et al., *Diffusion coefficients of articular cartilage for different CT and MRI contrast agents.* Medical Engineering & Physics, 2010. **32**(8): p. 878-882.
8. Arbabi, V., et al., *Transport of Neutral Solute Across Articular Cartilage: The Role of Zonal Diffusivities.* Journal of Biomechanical Engineering, 2015. **137**(7): p. 071001-071001.
9. Arbabi, V., et al., *Multiphasic modeling of charged solute transport across articular cartilage: Application of multi-zone finite-bath model.* J Biomech, 2016. **49**(9): p. 1510-7.
10. Arbabi, V., et al., *Combined artificial neural networks for robust estimation of the diffusion coefficients across cartilage.* 22nd Congress of the European Society of Biomechanics, Lyon, France, 2016.
11. Arbabi, V., et al., *Combined inverse-forward artificial neural networks for fast and accurate estimation of the diffusion coefficients of cartilage based on multi-physics models.* Journal of Biomechanics, 2016.
12. Pouran, B., et al., *Isolated effects of external bath osmolality, solute concentration, and electrical charge on solute transport across articular cartilage.* (under review), 2016.
13. Sophia Fox, A.J., A. Bedi, and S.A. Rodeo, *The Basic Science of Articular Cartilage: Structure, Composition, and Function.* Sports Health, 2009. **1**(6): p. 461-468.
14. Ateshian, G. and J. Weiss, *Finite Element Modeling of Solutes in Hydrated Deformable Biological Tissues*, in *Computer Models in Biomechanics*, G.A. Holzapfel and E. Kuhl, Editors. 2013, Springer Netherlands. p. 231-249.
15. Ateshian, G.A., S. Maas, and J.A. Weiss, *Multiphasic Finite Element Framework for Modeling Hydrated Mixtures With Multiple Neutral and Charged Solutes.* Journal of Biomechanical Engineering, 2013. **135**(11): p. 111001-111001.
16. Arbabi, V., et al., *Transport of neutral solute across articular cartilage and subchondral plate.* 22nd Congress of the European Society of Biomechanics, Lyon, France, 2016.
17. Pouran, B., et al., *Application of multiphysics models to efficient design of experiments of solute transport across articular cartilage.* Comput Biol Med, 2016. **78**: p. 91-96.

18. Hosseini, S.M., et al., *The importance of superficial collagen fibrils for the function of articular cartilage.* Biomechanics and Modeling in Mechanobiology, 2013. **13**(1): p. 41-51.
19. Alexopoulos, L.G., et al., *Osteoarthritic changes in the biphasic mechanical properties of the chondrocyte pericellular matrix in articular cartilage.* Journal of Biomechanics, 2005. **38**(3): p. 509-517.
20. Felson, D.T., et al., *Osteoarthritis: new insights. Part 1: the disease and its risk factors.* Ann Intern Med, 2000. **133**(8): p. 635-46.
21. Kokkonen, H.T., et al., *Detection of mechanical injury of articular cartilage using contrast enhanced computed tomography.* Osteoarthritis Cartilage, 2011. **19**(3): p. 295-301.
22. Raya, J.G., et al., *Diffusion-tensor imaging of human articular cartilage specimens with early signs of cartilage damage.* Radiology, 2013. **266**(3): p. 831-41.
23. Tavakoli Nia, H., et al., *Aggrecan Nanoscale Solid–Fluid Interactions Are a Primary Determinant of Cartilage Dynamic Mechanical Properties.* ACS Nano, 2015. **9**(3): p. 2614-2625.
24. Arbabi, V., et al., *Estimation of cartilage properties using indentation tests, finite element models, and artificial neural networks.* 11th World Congress on Computational Mechanics & 5th European Conference on Computational Mechanics, Barcelona, Spain, 2014.
25. Arbabi, V., et al., *Determination of the mechanical and physical properties of cartilage by coupling poroelastic-based finite element models of indentation with artificial neural networks.* Journal of Biomechanics, 2016. **49**(5): p. 631-637.
26. Kokkonen, H.T., et al., *Computed tomography detects changes in contrast agent diffusion after collagen cross-linking typical to natural aging of articular cartilage.* Osteoarthritis and Cartilage, 2011. **19**(10): p. 1190-1198.
27. Decker, Sarah G.A., et al., *Adsorption and Distribution of Fluorescent Solutes near the Articular Surface of Mechanically Injured Cartilage.* Biophysical Journal, 2013. **105**(10): p. 2427-2436.
28. Tuomo S. Silvast, J.S.J., Virpi Tiitu, Thomas M. Quinn and Juha Töyräs, *Bath Concentration of Anionic Contrast Agents Does Not Affect Their Diffusion and Distribution in Articular cartilage In Vitro.* Cartilage, 2013. **4**(1): p. 42-51.
29. Silvast, T.S., et al., *pQCT study on diffusion and equilibrium distribution of iodinated anionic contrast agent in human articular cartilage – associations to matrix composition and integrity.* Osteoarthritis and Cartilage, 2009. **17**(1): p. 26-32.
30. Pouran, B., et al., *Contrast agent's transport across healthy articular cartilage under various bath conditions.* Orthopaedic Research Society Annual Meeting, Las Vegas, Nevada, 2015.
31. Arbabi, V., et al., *Application of a biphasic-solute model in predicting diffusive properties of osteochondral interface.* International Workshop on Osteoarthritis Imaging (IWOAI), Oulo, Finland, 2016.

ACKNOWLEDGEMENTS

Inspiration sparks in the mind but only expands and blooms when several factors come together and make a scientific achievement possible to emerge. On my scientific growth path, I was privileged to have all those factors including creativity, possessing motivated, inspirational, expert and supportive mentors, ever-lasting support of the family, luxury of being surrounded by understanding and collaborative friends and colleagues. I would therefore like to express my sincere and special gratitude to my role-model and supportive mentor 'Prof. Harrie Weinans' who not only was my scientific supervisor but also was encouraging and helping me pass the hardship and circumvent the obstacles through my PhD life. My thanks go to 'Prof. Jos Malda' for his scientific inputs and remarks and remarkably preparing me to organize my academic work. I thank 'Dr. Amir Abbas Zadpoor' who was from the beginning of my PhD journey helpful and well-organized and made me benefit from his tips throughout my scientific work.

I wish to extend my wholehearted appreciation to my lovely and supportive family: my lovely mother, my lovely father, my lovely brother, my sweet grandmother and my inspirational grandfather whom I have sorrowfully lost lately. You have always encouraged me and listened to my scientific discussions in person or remotely. I am blessed for having a lovely aunt (Khale Gila) whose support and kindness are unique.

Sanaz Malaei, my fiancé, thank you so much for your company, support and patience during this adventure.

Dr. Vahid Arbabi, you have always been a unique friend and scientific partner and I am thankful for being assiduous during our collaborative work, which resulted in stunning progress. Mrs. Firuzeh Farrokhzad, thank you very much for your wonderful support during my PhD time. I never forget you being so kind to me.

Dr. Nasim Salehi-Nik, my wonderful friend and collaborator, thanks for constantly injecting a great sense of true friendship since 2009. It is awesome that your arrival in The Netherlands as a Post-doctoral Fellow has been realised.

Asimina Glynou, I am proud of you as my former student who has taken the steps forward to become a very successful individual. Thanks for all the hospitality and nice time we had together.

I would like to thank Dr. Amir Raoof and Dr. Matthijs de Winter who have always been a great motive for my progress and spirit source. Dr. Ambika Goel Bajpayee and Prof. Jeffrey Ruberti, Dr. Jeffrey Paten and Mohammad Siadat, thank you very much for hosting me at Northeastern University during my visit in Boston: I learned a lot during our discussion sessions.

Prof. Juha Töyräs, Prof. Jukka Jurvelin, I am so grateful for your hospitality and for providing me with the unique opportunity to work together on the multi-contrast agent project. Prof. Rami Korhonen and Dr. Mikko Nissi, you have always inspired me and been so hospitable during my visit at Biophysics of Bone and Cartilage group. Mohammad Hossein Ebrahimi, Ali Mohammadi and Amir Esrafilian (and your wife), thank you so much for treating me the best possible way in Kuopio. I am thankful to Annina Saukko, Katariina Myler, Abhisek Bhattarai, Dr. Petri Tanska for providing such an excellenet environement at Biophysics of Bone and Cartilage group.

We had wonderful time generating ideas together. Dr. Hadi Tavakoli Nia, thank you very much for your insights regarding scientific career development.

Thank you, Dr. Khoon Lee, Dr. Tim Woodfield, Mohsen Ramyar, Dr. Nigel Anderson, and Gabriella Brown for having me among you during my visit at Christchurch.

I was honored to have such wonderful past and current colleagues and friends at Orthopaedics and Maxillofacial Departments of UMC Utrecht and faculty of Veterinary Medicine of Utrecht University:

Prof. René Castelein, Prof. Cumhur Öner, Prof. René van Weeren, Dr. Laura Creemers, Dr. Jacqueline Alblas, Dr. Debby Gawlitta, Dr. Marianna Tryfonidou, Dr. Vivian Mouser, Dr. Jetze Visser, Dr. Parisa Rahnamay Moshtagh, Anita Krouwels, Dr. Saber Amin Yavari, Joao Garcia, Michiel Croes, Mattie van Reijn, Dr. Riccardo Levato, Dr. Miguel Castilho, Kim van Dorenmalen, Dr. Lucienne vonk, Koen Dijkstra, Iris Otto, Iris Pennings, Irina Mancini, Lotte Groen, Mylene de Ruijter, Anneloes Mensinga, Flor Abinzano, Jonneke Kuperus, Mechteld Lehr, Maaike Braham, Chella Hagemeijer, Koen Willemsen, Willemijn Boot, Barbara Klotz, Alessia Longoni, Imke Jansen, Anna Tellegen, Razmara

Nizak, Huub de Visser, Marianne Koolen, Rob Brink, Willem Paul Gielis, Dr. Nicoline Korthagen, Said Sadiqi, Dino Colo etc.

Special thanks to Leili Ghazizadeh who has been a great friend and colleague. I am certain that you will stay at the apex of your scientific success in future.

BIOGRAPHICAL SKETCH

NAME: Pouran, Behdad

EDUCATION

INSTITUTION AND LOCATION	DEGREE	START DATE	END DATE	FIELD OF STUDY
Engineering, Tehran	BS	09/2005	09/2009	Chemical Engineering
Engineering, Tehran	MS	09/2009	09/2012	Chemical Engineering-Biotechnology
University of Eastern Finland, Kuopio	Fellow	05/2017	09/2017	Biophysics of bone and cartilage
University Medical Center Utrecht, Utrecht	Graduate Student	04/2013	Present	Orthopaedic biomechanics

B. Positions and Honors

Positions and Employment

2013 - PhD researcher, University Medical Center Utrecht, Utrecht, The Netherlands

2016 - 2016 Visiting scholar, University of Otago, Christchurch, New Zealand

2017 - Visiting scholar, University of Eastern Finland, Kuopio, Finland

Other Experience and Professional Memberships

- Member, European Society of Biomechanics

-	Member, Orthopaedic Research Society
2015 - 2016	Teaching assistant, TU Delft
2016 -	Instructor of Enabling technologies, University Medical Center Utrecht
2017 -	Reviewer, Osteoarthritis and Cartilage/Annals of Biomedical Engineering

Honors

2014	Most Active Young Investigator Award, 6th Nordic Meeting on Quantitative Imaging of Cartilage
2015	Organizer, 7th Nordic Meeting on Quantitative Imaging of Cartilage
2016	Presenter, European Society of Biomechanics
2016	Meritorious paper, Computers in Biology and Medicine
2017	Highlighted paper, Journal of Biomechanics
2017	Presenter, 9th International Conference on Porous Media & Annual Meeting, Rotterdam, The Netherlands

C. Publications

1: Croes M, Boot W, Kruyt MC, Weinans H, **Pouran B**, van der Helm YJM, Gawlitta D, Vogely HC, Alblas J, Dhert WJA, Öner FC. Inflammation-Induced Osteogenesis in a Rabbit Tibia Model. Tissue Eng Part C Methods. 2017 Aug 21.

2: **Pouran B***, Arbabi V*, Zadpoor AA, Weinans H. An Experimental and Finite Element Protocol to Investigate the Transport of Neutral and Charged Solutes across Articular Cartilage. J Vis Exp. 2017 Apr 23;(122). (* co-first authors).

3: Gorgin Karaji Z, Hedayati R, **Pouran B**, Apachitei I, Zadpoor AA. Effects of plasma electrolytic oxidation process on the mechanical

properties of additively manufactured porous biomaterials. Mater Sci Eng C Mater Biol Appl. 2017 Jul 1; 76:406-416.

4: Boot W, Gawlitta D, Nikkels PGJ, **Pouran B**, van Rijen MHP, Dhert WJA, Vogely HC. Hyaluronic Acid-Based Hydrogel Coating Does Not Affect Bone Apposition at the Implant Surface in a Rabbit Model. Clin Orthop Relat Res. 2017 Jul;475(7):1911-1919.

5: Otto IA, van Doremalen RF, Melchels FP, Kolodzynski MN, **Pouran B**, Malda J, Kon M, Breugem CC. Accurate Measurements of the Skin Surface Area of the Healthy Auricle and Skin Deficiency in Microtia Patients. Plast Reconstr Surg Glob Open. 2016 Dec 22;4(12):e1146.

6: Bobbert FSL, Lietaert K, Eftekhari AA, **Pouran B**, Ahmadi SM, Weinans H, Zadpoor AA. Additively manufactured metallic porous biomaterials based on minimal surfaces: A unique combination of topological, mechanical, and mass transport properties. Acta Biomater. 2017 Apr 15;53:572-584.

7: **Pouran B**, Arbabi V, Bleys RL, René van Weeren P, Zadpoor AA, Weinans H. Solute transport at the interface of cartilage and subchondral bone plate: Effect of micro-architecture. J Biomech. 2017 Feb 8;52:148-154.

8: de Krijger J, Rans C, Van Hooreweder B, Lietaert K, **Pouran B**, Zadpoor AA. Effects of applied stress ratio on the fatigue behavior of additively manufactured porous biomaterials under compressive loading. J Mech Behav Biomed Mater. 2017 Jun;70:7-16.

9: Arbabi V, **Pouran B**, Weinans H, Zadpoor AA. Neutral solute transport across osteochondral interface: A finite element approach. J Biomech. 2016 Dec 8;49(16):3833-3839.

10: **Pouran B**, Arbabi V, Weinans H, Zadpoor AA. Application of multiphysics models to efficient design of experiments of solute transport across articular cartilage. Comput Biol Med. 2016 Nov 1;78:91-96.

11: Moshtagh PR, **Pouran B**, Korthagen NM, Zadpoor AA, Weinans H. Guidelines for an optimized indentation protocol for measurement of cartilage stiffness: The effects of spatial variation and indentation parameters. J Biomech. 2016 Oct 3;49(14):3602-3607.

12: **Pouran B**, Arbabi V, Zadpoor AA, Weinans H. Isolated effects of external bath osmolality, solute concentration, and electrical charge on solute transport across articular cartilage. Med Eng Phys. 2016 Dec;38(12):1399-1407.

13: Salehi-Nik N, Banikarimi SP, Amoabediny G, **Pouran B**, Shokrgozar MA, Zandieh-Doulabi B, Klein-Nulend J. Flow Preconditioning of Endothelial Cells on Collagen-Immobilized Silicone Fibers Enhances Cell Retention and Antithrombotic Function. Artif Organs. 2017 Jun;41(6):556-567.

14: Arbabi V, **Pouran B**, Weinans H, Zadpoor AA. Combined inverse-forward artificial neural networks for fast and accurate estimation of the diffusion coefficients of cartilage based on multi-physics models. J Biomech. 2016 Sep 6;49(13):2799-2805.

15: Moerman A, Zadpoor AA, Oostlander A, Schoeman M, Rahnamay Moshtagh P, **Pouran B**, Valstar E. Structural and mechanical characterisation of the peri-prosthetic tissue surrounding loosened hip prostheses. An explorative study. J Mech Behav Biomed Mater. 2016 Sep;62:456-467.

16: Moshtagh PR, **Pouran B**, van Tiel J, Rauker J, Zuiddam MR, Arbabi V, Korthagen NM, Weinans H, Zadpoor AA. Micro- and nano-mechanics of osteoarthritic cartilage: The effects of tonicity and disease severity. J Mech Behav Biomed Mater. 2016 Jun;59:561-571. 27043052.

17: Arbabi V, **Pouran B**, Weinans H, Zadpoor AA. Multiphasic modeling of charged solute transport across articular cartilage: Application of multi-zone finite-bath model. J Biomech. 2016 Jun 14;49(9):1510-7.

18: Arbabi V, **Pouran B**, Campoli G, Weinans H, Zadpoor AA. Determination of the mechanical and physical properties of cartilage by coupling poroelastic-based finite element models of indentation with artificial neural networks. J Biomech. 2016 Mar 21;49(5):631-7.

19: Salehi-Nik N, Amoabediny G, Banikarimi SP, **Pouran B**, Malaie-Balasi Z, Zandieh-Doulabi B, Klein-Nulend J. Nanoliposomal Growth Hormone and Sodium Nitrite Release from Silicone Fibers Reduces

Thrombus Formation Under Flow. Ann Biomed Eng. 2016 Aug;44(8):2417-30.

20: Harteveld AA, Denswil NP, Siero JC, Zwanenburg JJ, Vink A, **Pouran B**, Spliet WG, Klomp DW, Luijten PR, Daemen MJ, Hendrikse J, van der Kolk AG. Quantitative Intracranial Atherosclerotic Plaque Characterization at 7T MRI: An Ex Vivo Study with Histologic Validation. AJNR Am J Neuroradiol. 2016 May;37(5):802-10.

21: Ahmadi SM, Yavari SA, Wauthle R, **Pouran B**, Schrooten J, Weinans H, Zadpoor AA. Additively Manufactured Open-Cell Porous Biomaterials Made from Six Different Space-Filling Unit Cells: The Mechanical and Morphological Properties. Materials (Basel). 2015 Apr 21;8(4):1871-1896.

22: Arbabi V, **Pouran B**, Weinans H, Zadpoor AA. Transport of neutral solute across articular cartilage: the role of zonal diffusivities. J Biomech Eng. 2015 Jul;137(7).

23: Amin Yavari S, Ahmadi SM, Wauthle R, **Pouran B**, Schrooten J, Weinans H, Zadpoor AA. Relationship between unit cell type and porosity and the fatigue behavior of selective laser melted meta-biomaterials. J Mech Behav Biomed Mater. 2015 Mar;43:91-100.

24: Visser J, Gawlitta D, Benders KE, Toma SM, **Pouran B**, van Weeren PR, Dhert WJ, Malda J. Endochondral bone formation in gelatin methacrylamide hydrogel with embedded cartilage-derived matrix particles. Biomaterials. 2015 Jan;37:174-82.

25: Anisi F, Salehi-Nik N, Amoabediny G, **Pouran B**, Haghighipour N, Zandieh-Doulabi B. Applying shear stress to endothelial cells in a new perfusion chamber: hydrodynamic analysis. J Artif Organs. 2014 Dec;17(4):329-36.

26: Salehi-Nik N, Amoabediny G, **Pouran B**, Tabesh H, Shokrgozar MA, Haghighipour N, Khatibi N, Anisi F, Mottaghy K, Zandieh-Doulabi B. Engineering parameters in bioreactor's design: a critical aspect in tissue engineering. Biomed Res Int. 2013;2013:762132.

ABOUT THE AUTHOR

Behdad Pouran was born on 18th of December 1986 in Tehran, Iran. In 2009, he completed his B.Sc in Chemical Engineering from University of Tehran, Iran. In 2012, he graduated from his Master's degree in Chemical Engineering-Biotechnology at University of Tehran, Iran. His Master's thesis was entitled "Modeling and simulation of hydrodynamics and mass transfer in micro-bioreactors". His passion and interest in academic area led to his enrolment in the Regenerative Medicine doctoral program at Utrecht University, Utrecht, The Netherlands. He joined the department of Orthopaedics at University Medical Center (UMC) Utrecht in April 2013 as a PhD researcher where he was supervised by Prof. Harrie Weinans, Prof. Jos Malda and Dr. Amir Abbas Zadpoor. During his PhD, he remained affiliated with the department of Biomechanical Engineering at Delft University of Technology, Delft, The Netherlands. His main interest has been soft tissue biomechanics, transport phenomena in biological systems, biomedical image processing, micro-computed tomography (micro-CT) and orthopaedic scaffold design and characterization. In November 2016, he served as a visiting scholar working on MARS CT project at University of Otago, Christchurch, New Zealand. In the summer of 2017, he served as a visiting scholar at the department of Applied Physics, University of Eastern Finland, to work on multi-contrast agent imaging of cartilage. He contributed to more than 25 peer-reviewed journal papers and several conference papers and presented his work in several international conferences. In April 2017, since he finished preparing all the required materials for his PhD thesis, he was appointed as a post-doctoral researcher at UMC Utrecht. His will be working on advanced cartilage and bone imaging, mechano-chemistry and mechano-biology of cartilage and bone as well as therapeutics delivery to the diseased cartilage.